The Dissertation Committee for Noah Harold Smith Certifies that this is the approved version of the following dissertation:

Alignment Filtering of ICESat Flight Data

Committee:

Bob Schutz, Supervisor

Glenn Lightsey

Todd Humphreys

Peter Shelus

Sungkoo Bae

Alignment Filtering of ICESat Flight Data

by

Noah Harold Smith, B.A.; M.S.E.

Dissertation

Presented to the Faculty of the Graduate School of

The University of Texas at Austin

in Partial Fulfillment

of the Requirements

for the Degree of

Doctor of Philosophy

The University of Texas at Austin

December 2012

Alignment Filtering of ICESat Flight Data

Noah Harold Smith, Ph.D.

The University of Texas at Austin, 2012

Supervisor: Bob E. Schutz

ICESat consisted of the Geoscience Laser Altimeter System (GLAS) and a commercial spacecraft bus. The stability of the GLAS to bus alignment was unknown and significant for GLAS pointing. Pointing control was performed by the bus, and variations of the GLAS alignment were effectively pointing control errors. There were four star trackers making measurements sensitive to this alignment, two on GLAS and two on the bus. Tracker pointing variations during samples from seven years of flight data were estimated using an alignment filter. The states of an alignment filter represent multiple independent attitudes, enabling the fusion of measurements from an arbitrary number of trackers and gyro units. The ICESat alignment filter states were equivalent to four tracker pointing vectors, expressed in both the body and celestial frames. Together with a star catalog, the four pointing vectors were equivalent to predictions of the tracker measurements. The stars provided nearly ideal reference points, but filter performance was improved by detecting and handling deterministic star errors. The primary result was evidence for relatively large pointing variations of the two GLAS trackers, on the order of fifty arcseconds, with both periodic orbital variations and trends on long time scales. There was also evidence of correlations between the variations of the two GLAS trackers, suggesting that they reflected GLAS to bus alignment variations.

Table of Contents

I. Introduction

ICESat consisted of the Geoscience Laser Altimeter System (GLAS) and a commercial spacecraft bus. The stability of the GLAS to bus alignment was unknown and significant for GLAS pointing. Pointing control was performed by the bus, and variations of the GLAS alignment were effectively pointing control errors. There were four star trackers making measurements sensitive to the GLAS alignment, two on GLAS and two on the bus. Tracker pointing variations during samples from seven years of flight data were estimated using an alignment filter. The states of an alignment filter represent multiple independent attitudes, enabling the fusion of measurements from an arbitrary number of trackers and gyro units. Tracker pointing in the body frame was represented using latitude and longitude-like body north and body west coordinates, as shown in Figure 1. These coordinates aided physical interpretation of tracker pointing variations in terms of GLAS alignment, and were independent of the relatively inaccurate estimated rotations of the trackers about their pointing vectors. Correlations in the pointing of the two GLAS trackers suggest that there were significant variations of the GLAS alignment.

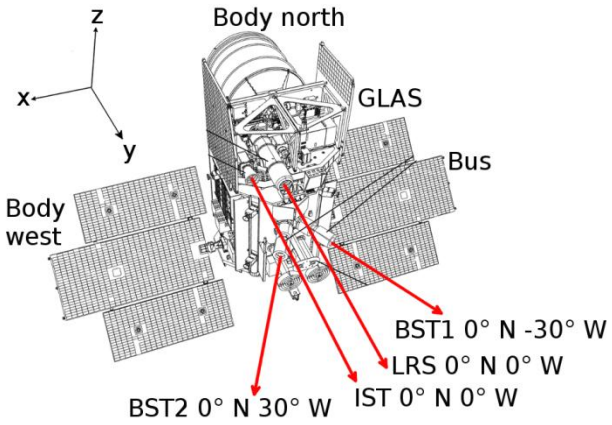

Figure 1. ICESat, body north and body west coordinates, and approximate tracker pointing vectors.

The combined states of the alignment filter represented the individual attitudes of all four ICESat trackers, relative to both the body and celestial frames. Individual filter states

included alignment rotations for each of the four tracker frames, and an attitude rotation for the body frame. For each tracker, a tracker pointing vector represented the tracker optical axis relative to the celestial frame based on three frame rotations: from the celestial frame to the body frame (attitude state), from the body frame to the reference tracker frame (constant), and from the reference tracker frame to the estimated tracker frame (alignment state). Star tracker measurements are less sensitive to rotations about the tracker optical axis. The sensitivity to rotation about the optical axis for a star on the axis is zero. Representing the tracker attitudes as pointing vectors made the results independent of the less sensitive tracker axes, and aided physical interpretation. Together with a star catalog, the tracker attitudes were equivalent to predictions of the tracker measurements. If the differences between tracker measurements and filter predictions were small, then the estimated tracker pointing vectors were accurate. For the primary results presented here, the BST1 tracker frame was tied to the body frame by holding the BST1 alignment states constant. In others words, there was a constant rotation between the body frame and the BST1 frame. The body frame was identified with the gyro unit. The individual tracker alignment states were small variations from a set of reference alignments. The alignment filter could run with the all of the tracker alignment states held constant at the reference values, but this resulted in relatively large star measurement residuals on the order of tens of arcseconds. With the tracker alignment states updating to follow alignment variations, the filter residuals were an order of magnitude smaller.

The stars provided nearly ideal reference points to compare with the filter states via tracker measurements. In the flight data sample used here, the spacecraft was normally rotating at a constant rate about the GLAS to bus axis and the four star tracker pointing vectors followed one another along a great-circle around the celestial sphere, from near the celestial north pole to near the celestial south pole and then back. The same stars passed through all four tracker fields of view within a sixteen minute period. Variations of the tracker alignments and pointing vectors directly affected the predicted star unit vectors. Deterministic and stochastic errors affected the measured star unit vectors.

Detecting and handling deterministic star errors was a practical method for improving filter performance. The filter reduced the effects of these errors by averaging over multiple stars, but ultimately stochastic and deterministic errors in the measurements were the limiting factor for the accuracy of the tracker pointing vectors and individual filter states. The reference values in the star catalogs are more accurate than the tracker measurements, so in all cases the errors were in the measurements. The errors were often identified with the stars, particularly in the cases referred to as bad stars, but were always a result of the measurement process. The interaction between the alignment filter and the celestial reference frame via tracker measurements was a unifying theme throughout this research.

Alternatives to alignment filtering are often based on batch processing and estimation of alignments at a point in time. Alignment batch processing has a similar relationship to alignment filtering as single-frame attitude determination does to attitude filtering, and more generally as least squares parameter estimation does to Kalman filtering. The batch, single-frame, and least squares methods for attitude and alignment estimation tend to be deterministic. They are oriented towards taking a set of measurements as input, and outputting an estimate that minimizes a performance parameter at a particular point in time. Alignment filtering is less deterministic in the sense that it is natural to view the alignment states as stochastic processes with variations and uncertainties that change over time and depend on how the system, measurement, and noise processes are modeled. The literature review is meant to show how the evolution from batch methods towards filtering methods for alignment estimation paralleled a similar but earlier evolution of attitude estimation. ICESat was well suited for alignment filtering. There were four trackers and their alignment variations had strongly differing characteristics for comparison. Attitude maneuvers were generally relatively small, and the pointing requirements emphasized two rotational degrees of freedom rather than three. Pointing, attitude, and alignments primarily involved roll and pitch rotations. This constraint was fundamentally why the latitude and longitude-like body north and body west coordinate

system used here was useful. Roughly speaking, ICESat had two primary degrees of rotational freedom rather than three. These two degrees of freedom could have been referred to as roll and pitch, or body north and body west. Both sets of terminology had advantages and disadvantages.

a. Contributions to the Field

The contributions made by this dissertation are in several areas: star measurement processing and flight star catalogs; ICESat gyro attitude propagation; and ICESat GLAS to bus alignment and more generally spacecraft alignment estimation using indirect measurements where direct measurements are not available. These areas combine in a practical objective: simultaneously predict the star measurements from all four ICESat star trackers. The contributions described here are incorporated in data processing software that is in operational use reprocessing ICESat data and is adaptable to future missions.

In the area of star measurements and flight catalogs, there are a range of contributions. There is a new method for detecting and characterizing stars with biased position measurements.[1] The results are specific to a star tracker and independent from other sensors or estimates. Results for the ICESat trackers are given. There is an evaluation of a large group of models for star instrument magnitude prediction, with a study of prediction performance and errors for the ICESat trackers, and a large set of reduced instrument magnitude results.[2] There are methods for empirically estimating star tracker measurement noise and distortion, with an analysis of the noise and distortion characteristics of the ICESat trackers. These empirical flight results are a significant reference for anyone dealing with star tracker measurements: not only are the methods and results unique in the open literature, it is unique that the flight data is publicly available and easily accessible from the National Snow and Ice Data Center (NSIDC).[1]

The discussion of biased star position measurements in the open literature generally concerns analytic approaches for pre-launch creation of flight catalogs. This is often

referred to as the center of light problem: predict the apparent center of light for a small area of sky as measured by a particular tracker. A new empirical approach to the center of light problem is introduced here.[1] There is a wide range of possible methods for detecting and characterizing stars with biased position measurements. A fundamental decision is whether to utilize data from one star tracker alone, or to incorporate information from multiple sensors, particularly gyros. For example, in the alignment filter described here, star position measurements and predictions are compared in order to detect and reject biased stars before they are used in a measurement update. A decision was made to develop a fundamentally different method to compliment and validate the Kalman filtering results. This new method has been referred to as a gyro-free or filtering-free method. It is meant to provide independent results that can validate the Kalman filtering results, and to serve as a basis for independent data mining studies of flight data. Reduced results for a sample of ICESat data are provided here. The results demonstrate that the new method contributes an effective way to detect and characterize small position measurement biases.

One of the primary challenges in the center of light problem is the initial step of predicting the response or instrument magnitude for each object in an area of sky. Instrument magnitude prediction has been called the most delicate step in constructing a flight catalog.[2] It also plays a central role in star identification, where the difference between the measured and predicted instrument magnitude of an object are commonly a criteria for positive identification. For both of these reasons, empirical results reduced from flight data are valuable. They validate current prediction models, act as training data for developing new models, and improve operational star identification routines. There are several contributions here: a study of prediction models, results concerning prediction performance and errors for the ICESat trackers, and a major new set of publicly available reduced instrument magnitudes from ICESat flight data.[2] These contributions expand on work done in the 1990s and 2000s using flight data from the RXTE mission.[3-5] Reduced instrument magnitudes from RXTE were used to augment the NASA SKY2000 Master

Catalog and have been the primary public set of flight instrument magnitudes. The contributions here are part of an ongoing effort, in cooperation with the SKY2000 group, to coordinate and standardize the reduced ICESat and RXTE results and form an expanded public set of flight instrument magnitudes, including multiple types of star trackers. Joining the ICESat and RXTE instrument magnitude results provides a significantly expanded number of unique stars, measured using three distinct types of trackers.

In the area of spacecraft alignment estimation and GLAS to bus alignment, the contributions are answers for a specific question about GLAS alignment, and a method for arriving at the answers despite the lack of direct measurements. The results are of immediate interest to spacecraft designers, and contribute to the fields of pointing control and knowledge by demonstrating that the variations can be tracked by an onboard filter, and that the measurements from multiple star trackers are a practical basis for tracking small structural variations. Though there were no sensors making direct measurements of GLAS alignment and only conventional star tracker measurements were available, the results demonstrate that software alone was needed to extract the desired information from the available sensors. There are gyro calibration results for the ICESat SIRU using a full gyro measurement model and alternative gyro propagation methods, including a higher-order method from inertial navigation systems. There is a contribution to the overall topic of alignment filtering. It is possible to define the gyro measurement frame as the body frame and simultaneously estimate all star tracker alignments relative to it. This approach has been advocated in the literature and may become important for some applications.[6, 7] An empirical evaluation of the gyro body frame approach is given for ICESat flight data and shows that, while practical, gyro propagation accuracy and filter tuning become critical. For all of the processing here, outside of the gyro body frame evaluation, the body frame was identified with one of the star tracker frames.

These contributions span a range of topics involved in going from star tracker measurements to information about spacecraft alignment. The differences between measured and predicted star measurements can have multiple causes and interpretations: measurement error in star tracker horizontal and vertical coordinates, attitude estimate and alignment estimate error in spacecraft body north and west coordinates, and center of light error due to multiple astronomical objects in celestial right ascension and declination coordinates. A unifying perspective is introduced and emphasized here: the use of two-component scaled tangent coordinates to represent and interpret three-component unit vectors in multiple reference frames. This perspective enables a natural progression from lower level measurements through higher levels of estimated information to arrive at answers for a difficult question. Initially it was not clear if it was possible to say anything significant about GLAS alignment. The results here demonstrate that it is possible and that the answers represent significant new information about the spacecraft.

II. Literature Review

The evolution of attitude and alignment estimation is described here in roughly chronological order. Star tracker errors and calibration are then reviewed separately organized by topic rather than chronologically. Up to the 2000s, attitude and alignment estimation were often performed separately and typically involved batch processing on the ground for at least the alignments. Alignment filtering tends to unify attitude and alignment estimation and adapt them for real-time and autonomous systems.

The evolution of attitude estimation from single-frame attitude determination to attitude filtering is discussed in Section IIa. Attitude filtering and the standard Multiplicative Extended Kalman Filter (MEKF) are the basis for alignment filtering. Similarly, alignment estimation has evolved from batch processing methods to alignment filtering. Batch processing of flight data to estimate alignments using both attitude independent and attitude dependent methods has been a common approach. Methods for augmenting the MEKF with alignment states have been discussed from the 1990s. The state of an alignment filter represents the individual attitudes of multiple trackers. Evolution of the alignment filter is discussed in Section IIb. The stars are nearly ideal reference points. Star tracker measurements however are affected by a variety of errors. Star measurements and error sources are discussed in Section IIc.

a. Attitude Estimation

Up to the 1980s, attitude estimation was commonly based on deterministic methods analogous to classical least squares. These methods are often referred to as single-frame attitude estimation or attitude determination. They are solutions of the Wahba problem, posed by Grace Wahba in 1965: find the rotation that minimizes the differences between measured and reference unit vectors at a single point in time.[8] The solution is the attitude rotation, usually represented as a rotation matrix or quaternion. The inputs are a set of measured unit vectors, a corresponding set of reference vectors from a star catalog, and optional measurement noises for the unit vectors.

The need for onboard real-time attitude estimation led naturally to filtering. A 1982 paper on attitude filtering from a group associated with GSFC became a standard review of the problem.[9] One of the attitude filters described in the 1982 paper has become standard and is known as the Multiplicative Extended Kalman Filter (MEKF).[10] Earlier papers had been published on attitude filtering.[11-17] Markley[10] has identified a 1967 paper by Farrell[15] as the earliest application of the EKF to attitude estimation (the 1970 journal version is cited here). The 1982 paper describes the earlier work with the statement "The application of Kalman filtering to attitude estimation had not shown impressive results up to 1967. Aside from insufficient study, the lack of real success in applying optimal estimation was caused by the inability to model the system dynamics accurately."[9] The difficulty in modeling system dynamics was addressed by using gyro measurements in model replacement mode.[13, 14]

One of the significant characteristics of the MEKF was that it estimated the attitude error in the measurement update phase as a three-component rotation vector. The attitude error was then converted to a rotation matrix or quaternion and multiplied with the attitude state. This measurement update by multiplication was emphasized by the title Multiplicative EKF.[10] In the MEKF the state error vector has six components and the state error covariance is six by six. A result of this design has been the introduction of a third phase into the filter cycle for clarity, in addition to the standard propagation and measurement update phases. The third phase has been called the reset phase and acts as the link between the three-component attitude error and the attitude state, which is represented using rotation matrices or quaternions as convenient.[10, 18] Markley, one of the original authors of the 1982 paper, has noted that this aspect of the MEKF has raised questions. In a 2003 review he states "The main aim of this paper is to dispel the lingering suspicion that there is something amiss with the MEKF. We show that the MEKF is not really a quaternion estimator; it performs an unconstrained estimation of a three-component attitude error, with the quaternion playing the role of a reference about which the errors are defined."[10]

Gyro propagation of the attitude state between star tracker measurements is an important practical topic that has not been emphasized in the attitude filtering literature. Propagation methods designed to handle high-frequency motion and rapid maneuvers are generally found in the Inertial Navigation Systems (INS) literature. A 1998 paper by Savage reviewed the history and standard methods in strapdown INS.[18] A dual cycle structure (fast-cycle and slow-cycle) was evolved for attitude integration. The fast-cycle performs rapid lower-order integration and periodically outputs to the slow-cycle, which uses more exact higher-order representations. This INS heritage is apparent in the ICESat gyro unit. Its integrated rate outputs are identical to the INS propagation fast-cycle outputs.

b. Alignment Estimation

Two late 1960s papers by desJardins at GSFC may be the earliest to describe batch calibration for alignments and gyros.[19, 20] From at least the early 1990s a group associated with GSFC published a series of papers on the same topic.[21-33] Alignment calibration initially used a batch method that did not involve attitude estimates.[21] Later a batch method involving the Wahba problem and single-frame attitude determination was introduced.[24, 25] Gyro calibration was performed using batch methods coupled with calibration maneuvers.[21, 28] Some filtering, particularly for gyros, was introduced from the early 2000s.[28, 32, 33]

A 1978 paper by Murrell may be the earliest description of a filter for simultaneous attitude and alignment estimation.[16] It appears that little else was published on alignment filtering until 1990 when a group at The Aerospace Corporation and Boeing published a description of a filter for alignment and gyro calibration.[34] From the mid 2000s a Boeing group has published papers and acquired patents related to a commercial filter including alignment and gyro calibration.[35-37] These developments may have been related to work at Hughes Space described in the next section.

In the early 1990s a JPL group published a paper discussing hybrid batch and filter estimation of alignment and gyro parameters for TOPEX.[38] The processor operated in a batch mode but included some characteristics of a filter such as a gain matrix, measurement updates, and covariance propagation.[38] Another example of hybrid batch and filter calibration for alignments alone was published in 2003.[39]

From the early 2000s Pittelkau published a series of papers describing a filter for alignment and gyro calibration and discussing related topics. The foundation of the filter evolved over a sequence of three papers from 2001 to 2005.[40-42] A 2008 paper provided a useful summary of typical alignment representations.[43] A unique aspect of the Pittelkau filter is its generalization for gyros with more than three sense-axes (redundant inertial measurement units or RIMUs).[6, 42, 44-49]

From the early 2000s a JPL group published a series of papers discussing calibration filters for the SIRTF mission.[50-54] Star tracker alignment was estimated by a six state filter with measurement updates every eight hours.[51] Attitude estimation used a fast observer rather than a Kalman filter to avoid long settling times.[51] Gyro calibration used an 18 state filter including 9 linear scale factors and alignments, 3 attitude states, 3 bias states, and 3 absolute scale factor parameters. Gyro calibration was performed during 1.5 hours of calibration maneuvers, matched with additional maneuvers to estimate alignments, distortions, and gyro biases. A combination of a special 37 state filter and calibration maneuvers was used to calibrate the science instruments. The filter was explicitly designed to estimate alignment and distortion without interference between the two types of parameters.[26] Iterative passes of the filter over a calibration maneuver were made until the parameters converged fully. The system achieved arcsecond pointing accuracy and sub-arcsecond jitter.[54]

A 2003 paper from another group associated with GSFC described an alignment calibration filter using an unscented filter.[55] The state and measurement equations are similar to those in the Pittelkau papers.

c. Star Measurements

A 2003 paper from Boeing is a clear review of star tracker errors from an end-user perspective.[37] The same classifications and terminology were used in a 2002 paper from Swales Aerospace, GSFC, and Boeing.[56] A common factor in these groups appears to be work in the mid 1990s at Hughes Space (merged with Boeing in 2000) in support of the GOES program.[57] The discussion here uses the error classifications defined in the Boeing paper and reproduced here in Figure 2. A 2002 review paper from JPL used essentially the same classification scheme with different labels.[58] In the late 1990s a group at Johns Hopkins APL published at least two papers on star tracker errors.[59, 60] The focus of the APL papers was on the fact that some star trackers errors are not white noise (they are correlated in time).

Star tracker error classification first separates noise from systematic errors, or equivalently stochastic from deterministic errors. The term noise equivalent angle is sometimes used equivalently for what is labeled temporal noise in Figure 2.[58] Within fixed pattern error there is a further separation of low spatial frequency error from high spatial frequency error. The term distortion is used here for low spatial frequency error, and the term centroiding error is used for high spatial frequency error. Distortion becomes significant on large spatial scales such as the field of view as a whole. Centroiding error is significant on small spatial scales, primarily the scale of individual pixels. As stars move across the field of view they cross pixel boundaries with a frequency determined by the pixel size. Another term for centroiding error is S-curve error.[58]

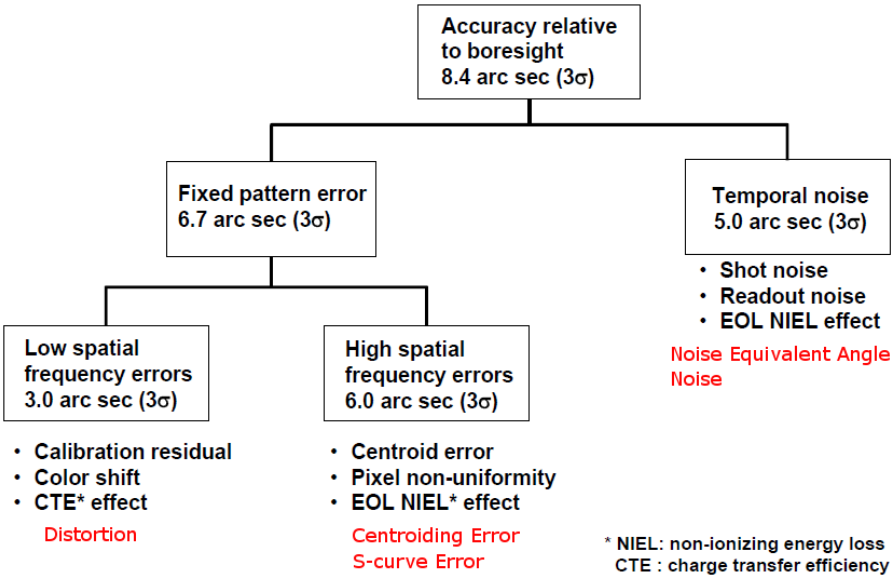

Figure 2. Error classifications and error budget for a Ball CT-602 star tracker, adapted from Wu.[37]

In practice star tracker error parameters enter filter processing in two ways. First, a correction is applied to measured star positions. The correction typically includes the effects of distortion, and more sophisticated corrections for centroiding error are possible. The corrected measurements are used to calculate measured minus predicted residuals in the filter measurement update phase. Second, distortion, centroiding error, and noise effect the filter measurement noise covariance matrix *R*.[37] Star tracker errors are not white noise (uncorrelated in time) as explicitly assumed for the Kalman filter *R* matrix.[37, 56, 59, 60] The practice at Boeing was to add distortion and centroiding corrections to the *R* matrix and then treat the errors as white noise.[37] An alternative as described by the Boeing group is "A colored noise model can be used to more faithfully describe the characteristics of the star-tracker errors but it is very difficult to determine the parameters in a robust and reliable way. In addition, a colored noise model used in a Kalman filter formulation leads to higher order designs, which is often undesirable."[37]

A 1999 APL paper discusses distortion for the MSX mission star tracker and gives an example quiver plot of distortion estimated from flight data.[59] This may be the earliest

public reduced flight data for a CCD star tracker. Earlier examples of reduced flight data concerned photomultiplier tube single-star trackers.[23] The corrections for the MSX tracker were described as less than an arcminute.

From the early 2000s the Junkins group at Texas A&M published a series of papers concerning star tracker geometric calibration, including distortion correction.[61-63] The group was designing the hardware and software for a new tracker and some of the discussion is of more interest to tracker builders than end-users. For example they needed to estimate the focal length and principle point (the intersection of the optical axis with the CCD array defining the origin of the tracker frame). The measurements output to end-users by a commercial tracker are reduced internally by the tracker processor using estimates of these geometric parameters, higher-order geometric effects, and temperature. End-users treat the tracker as a black-box and estimate their own additional corrections. The straightforward approach is a batch least-squares fit of polynomials to the observed minus predicted star position residuals.[61] The Junkins group extended their work on geometric calibration to include applications of neural networking and machine learning.[63] The early 2000s papers from Boeing and JPL described distortion correction using least-squares fits of polynomials.[37, 56, 58] The overall impression from these papers is that distortion was corrected in a straightforward manner and that attention was focused on centroiding errors and noise.

A 2009 paper from the Indian Institute of Science describes an unconventional approach to geometric calibration.[64] It requires at least six simultaneously measured stars and uses the additional information to estimate both attitude and lower-order geometric parameters. Given this estimate, radial distortion is then estimated using least-squares. Both steps are then iterated as necessary. This method demonstrates the potential inherent in larger numbers of measured stars. More stars increase the information throughput or bandwidth of the tracker, which can be put to practical use in estimation. The use of a

radial term to describe distortion, rather than a two dimensional polynomial, is a common feature of methods rooted in photogrammetry and machine vision.

Star trackers achieve sub-pixel centroiding accuracy using defocused optics that spread a star image over multiple pixels. If the image is focused and falls within a single pixel, sub-pixel accuracy is not possible. Software centroiding uses the defocused light detected by multiple pixels to estimate a sub-pixel centroid. The centroid estimate is sensitive to both the geometry and the relative responsiveness of the pixels.[58] Hardware factors such as varying pixel responses, dark currents, and charge transfer efficiencies contribute to centroiding error.

Centroiding error is demonstrated by moving a star image over an equally spaced ten by ten grid within a single pixel. The output measurements are not an equally space grid. It is possible to map a correction, termed an S-curve correction.[58] Centroiding error is also demonstrated by a star moving at a uniform rate across rows of pixels. The rate calculated from the output measurements is not constant and the variations contain a signal with the frequency at which the pixel rows are crossed.[37] The 2003 Boeing paper has some discussion of centroiding error characteristics.[37] The 1990s APL papers also discuss centroiding error, including a figure from Ball Aerospace.[59, 60]

A quantity commonly used to describe star tracker noise is an angular measure of the ability to reproduce the same attitude estimate over time given the same constant and ideal starlight input. This quantity is termed noise equivalent angle, the attitude angular uncertainty caused by noise.[58] This type of noise estimate is not adequate for direct use in filtering of individual star measurements. It is of more relevance to filtering if the tracker is sending attitude quaternions to the filter rather than star unit vector measurements.

For filtering with star unit vector measurements, independent noise measures for each star appear in the filter measurement noise covariance matrix *R*. Noise can depend on magnitude, color, background light from the sun or moon, temperature, etc.[1, 65] A 2007

paper from an ESA group describes a method for estimating star unit vector noise directly from simultaneous measurements of stars.[66] The method uses triangles of stars to form three equations with the position covariances as unknowns. For ICESat, the method was used to estimate individual noises for a large number of stars. The noise estimates were then fit as a function of magnitude for use as an empirical noise model. Further work is needed on other possible parameters such as star color. In an experiment, the method also was implemented with a sequential design, making it suitable for use in a more autonomous and adaptive filter.

Typically more than one flight catalog is created for a mission, for example onboard catalogs for the flight computer and ground catalogs for ground-based processing. The term flight catalog refers here to any mission-specific star catalog. Most of the information used to create a star tracker flight catalog was not measured and reduced for that purpose. Generally the information was intended for astronomical science. There are some exceptions, primarily where star tracker users have measured, reduced, and released flight data.[3, 5, 67, 68] Here all of the discussion concerns star trackers using charge-coupled devices or more recent imaging technology. These are referred to as second generation (or later) star trackers. The situation for first generation star trackers using photomultiplier tubes and other early technologies was more complex due to larger measurement nonlinearities and other technical issues.[69]

The standard process for creating a flight catalog begins with astronomical position and brightness data taken by telescopes with sub-arcsecond level resolution through standard astronomical narrow-passband color filters.[70] For a flight catalog, it is better to know how the sky appears to star trackers, which are deliberately defocused to several arcminutes resolution and are sensitive over a broad color passband.[68] Methods with various levels of sophistication are used to compensate for these differences and the final results are not entirely satisfactory.[68] Flight catalogs are adapted to specific tracker models and individual physical units. Some of the important tracker characteristics are spectral

response, field of view, pixel size, and maximum instrument magnitude.[70] The generalized approach taken by the French national space agency CNES was summarized in a three page flowchart by Manon.[70] A paper by Kudva has a simpler flowchart describing the approach taken for the Earth Observation System AM1 spacecraft.[71] Bezooijen described the development of a flight catalog with 196,087 guide stars for the Spitzer Space Telescope.[72] For the Spitzer catalog, which included guide stars as faint as magnitude eleven, many catalogs were used including Hipparcos, the Tycho double star catalogs, the 2 Micron All Sky Survey Point Source Catalog, the US Naval Observatory A2.0 catalog, the 2MASS Extended Source Catalog, the 2003 Principal Galaxy Catalog, and the Digital Sky Survey.[72] The European Space Operations Centre proposed using the Hipparcos and Tycho catalogs as the primary sources for creating flight catalogs, together with the Hubble Guide Star Catalog and an independent master catalog of extended celestial objects.[73]

NASA flight catalogs are often based on the SKY2000 Master Catalog.[3-5, 74, 75] The SKY2000 Version 5 Master Catalog was developed as a source catalog from which to create flight star catalogs. It contains instrument magnitude data reduced from RXTE mission Ball CT-601 flight data. Within SKY2000 the empirical instrument magnitudes are referred to as Passband 3 magnitudes.[3, 68] SKY2000 Version 5 does not contain all of the stars that typical trackers can acquire, or all of the neighboring stars that can affect the apparent positions of acquirable stars when measured by a tracker.[68] It is believed to be missing some stars that are acquirable by a Ball CT-602 tracker.[68] In practice it is also significant that SKY2000 does not contain reduced flight data concerning variability of instrument magnitudes.[68, 76] SKY2000 has sometimes been augmented with the Tycho catalog.[70]

A flight catalog consists of at least three values for each star. Two values define a position on the sky, and a third value defines the brightness. In theory the two position values are sufficient for an attitude filter since only position is needed in attitude

estimation. In practice the brightness values are needed for star identification and position corrections. Often multiple stars are close enough together on the sky that it is necessary to validate identifications using brightness and to correct positions for complex light distributions. Additional values beyond the minimum three such as brightness in multiple passbands, color, and variability are also useful. Generating the brightness values for a flight catalog is a complex process. The ultimate objective is to assist in predicting the brightness measurements from a particular tracker. Ideally a flight catalog would simply contain actual brightness measurements for a given tracker, including time-varying values for variable stars. In practice a flight catalog could contain various brightness values for input into prediction models at run-time. The question is both what brightness values to include in the flight catalog (how many and what definitions), and how to generate them. Due to the uneven nature of information about regions of the sky and particular stars, in practice different methods and different prediction models are used for different stars. Overall, characterizing star position is relatively straightforward compared to characterizing star brightness.

The term blended stars is used here for cases where two or more sources contribute to a measured position and magnitude. Blended stars commonly meet mission requirements and are used as flight catalog stars and tracker guide stars. For the RXTE mission Ball CT-601 tracker flight catalog, NASA blended all sources within a 120 arcseconds radius of a given catalog star.[77] If some of the blended sources are variable, then the blended centroid changes with the magnitudes of the variable sources. A paper by Sande discussed this situation in detail for the NASA Aura spacecraft star SKYMAP 17310145. It was a blended source which was affected by the initially overlooked long term variable near-neighbor V04835 Sco.[68] The paper describes the center of light calculations used to predict the positions of blended catalog stars, and the blended instrument magnitude predictions generated by the Multi-Mission Catalog generation program (MMSCAT). Another type of blended star was discussed in the literature. It involved multiple sources where one or more of the sources were intermittently resolved by the

tracker. This effect was caused by the geometry of the sources and the tracker hardware, particularly characteristics such as image size, pixel size, and background noise. The effect was that the measured position for the blended source switched intermittently between several values.[78] Star number 1717 from the Rosetta onboard flight catalog was an example.[78] It was a known blended star involving HIP77052 and the faint neighbors HIP77034 and HIP77043. The measured position switched between three values related to the predicted blended position and the blended positions for two of the three possible star-pair combinations.[78] Another example illustrates a class of stars that were termed Ping-Pong bad stars in the literature. Figure 3 shows an example involving HIP74778 and HIP74750.[66] They were measured individually or as a blended star depending on noise and pixel phase, the measured centroid switched between three positions over time.

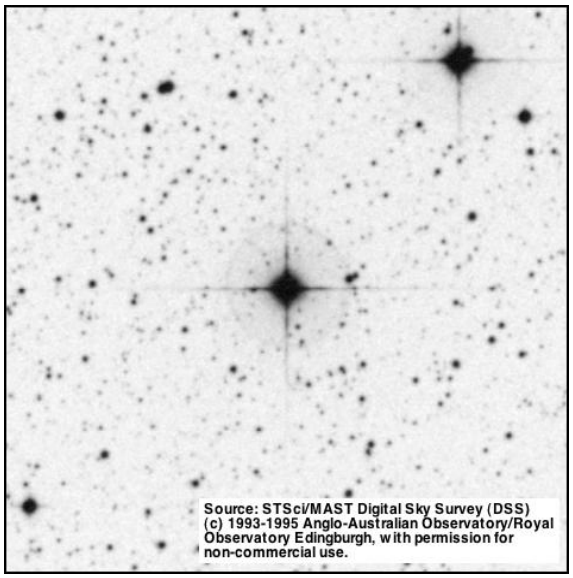

Figure 3. Ping-pong bad stars HIP74778 and HIP74750.

When considering flight catalog stars whose neighbors can safely be predicted to be resolvable, so not a blended star, the concern is misidentification.[70] If a neighbor is near enough in position and brightness, then there is the danger that the star tracker can acquire the neighbor, or equivalently that the attitude filter can misidentify the acquired star.[70] Such neighbors have been called spoilers.[79] Filter residual checking for position

and brightness are responsible for preventing misidentifications from affecting the filter results.

Star brightness is expressed using the astronomical magnitude system. Absolute brightness measurements such as counts from a sensor are converted to magnitudes expressed relative to a reference star. Magnitude m is defined by the ratio of a measured brightness b and a reference brightness b_0 as shown in Equation (1).

$$m = -2.5 \log_{10} \left(b / b_0 \right) \tag{1}$$

Astronomical magnitudes are measured through color filters or passbands. There are multiple systems of filters and associated reduction methods, for example the Johnson and Cousins system.[80, 81] Standard astronomical passband magnitude types used here are ultraviolet U, blue B, visual V, red R, and infrared I.[81] Measurements in multiple passbands are used to determine spectral class, which characterizes star color. The standard astronomical spectral classes are O, B, A, F, G, K, M ranging from blue stars to red stars. Reference stars are used to define passband magnitudes and spectral classes. For example Vega has been used as the reference star for V magnitudes and the A spectral class. For star trackers, the magnitude passband is unique to a particular instrument and is commonly termed an instrument magnitude. Every model and individual unit has a unique passband and sensitivity and the term instrument magnitude stresses that the values are instrument dependent. The reference star chosen to define instrument magnitudes varies from mission to mission.[65] The use of different reference stars can lead to biases between instrument magnitudes from different spacecraft. This was the case for the instrument magnitudes from ICESat and RXTE.

Calculating instrument magnitudes has been called the most delicate step in constructing a flight catalog.[70] Magnitudes in star catalogs for the various passbands are incomplete, inconsistent, and often include groups of stars that appear to be single stars (blended stars) at the resolution of a tracker.[68] Stars are often multiple, variable, or both, which

increases the difficulty of predicting the apparent brightness in the tracker passband from data in other passbands. The astronomical data that are available was generally measured in different bandwidths, and at different angular resolutions, than that of a typical star tracker.[3, 68, 70]

If both the star spectral curve and the tracker response curve are available, they can be convolved to predict the instrument magnitude.[70, 82] Full spectral curves are available for a relatively small number of stars. Some examples are the 13-color photometry of 1380 bright stars by Johnson and Mitchell, and the 180 stars in the Gunn and Stryker catalog.[70, 82] Flight measurements of reference stars from a similar instrument have also been used.[83-85] It has been noted in the literature that there are noticeable differences in response between even nominally identical star trackers.[83, 86] Every tracker has a slightly different response curve, even trackers of the same make and model. Some examples are available in the literature: two Ball CT-601 star trackers on EOS-AM1[71], a nominal and actual response curve for a SED-12 star tracker[70], and the response curve for the Indian Resourcesat-1 star tracker.[82] Comparing these response curves, the Ball CT-601 curves are clearly distinct, and the two non-Ball curves are distinctly different from each other and from the Ball curves. Shuttle flight data from two Ball CT-611 trackers showed instrument magnitude differences of 0.14 for blue stars and 0.27 for red stars.[83]

Many instrument magnitude prediction models and empirical fits have been published in the literature. Manon suggested that a color index be calculated from the spectral type and luminosity class and a first or second order polynomial be fitted to differences of astronomical passband magnitudes.[2] Differences of visual and infrared passband magnitudes were used for the French SED-12 star tracker.[2] Sande suggests using the most favorable available astronomical magnitude together with a color correction calculated from the Morgan-Keenan stellar class, subclass, and luminosity.[3] For the Ball CT-601 star tracker the astronomical magnitudes are ranked in descending order as: red, visual, photovisual, infrared, blue, photographic, and ultraviolet.[3] Davenport suggests a quadratic

fit to the astronomical ultraviolet, blue, and visual magnitudes.[8] Singh used a linear fit in the SKY2000 Passband 1 and Passband 2 magnitudes.[4] These correspond to astronomical red R and infrared I magnitudes. A quadratic fit to blue and visual magnitudes was used for stars lacking this SKY2000 data.[4] Strunz used a fourth order polynomial fit to blue and visual magnitudes and noted that the fit quality degraded for red stars.[5] Barry used a second order polynomial in blue and visual magnitudes for flight data from two Ball CT-631 trackers.[6] It was noted that the fit was poor for blue stars, there was a mean difference of 0.236 magnitudes between the trackers, and the difference varied with star color by up to 0.14 magnitudes.[6] Schmidt gave a computed curve of the offset between instrument magnitudes from an active pixel star tracker and the Hipparcos mission instrument magnitudes.[9] Two Ball CT-611s were modeled using $B-V$.[83] A STAR1000 active pixel sensor was modeled using stellar class or $B-V$.[87] It was noted that faint stars tend to have dimmer instrument magnitudes than predicted due to thresholding of the star image during processing. Another paper noted the same effect and characterized it as up to 0.5 instrument magnitudes for faint stars.[78] Another paper used $B-V$ and noted that the prediction quality decreased rapidly for bluer stars.[85] The Ball CT-601 on RXTE were modeled using $B-V$.[77] Two of these papers concluded that some of the instrument magnitudes were associated with misidentified stars.[83, 86]

The usual method for predicting instrument magnitudes is to use a training set as the basis for various models. Before launch the training set consists of analytical predictions from convolving star spectral curves and tracker response curves, or actual instrument magnitudes reduced from the flight data of other spacecraft. After launch the training set contains flight data. The model inputs are various passband magnitudes, spectral class, luminosity class, etc. In practice the significant astronomical passbands are blue B, visual V, red R, and infrared I. Deep infrared J and K were also used for the Spitzer flight catalog.[72] Two other important passbands are Passband 1 and Passband 2. They were defined locally within the SKY2000 catalog and usually corresponded to astronomical R and I. Often the differences of passband magnitudes are significant

because of their relationship to star color and spectral class. Some common magnitude differences are $B-V$, $V-R$, and $V-I$. Second order polynomial fits on magnitude differences, spectral class, luminosity class, and a linear combination of Passband 1 and Passband 2 from Sky2000 have all been used.[70, 82] These empirical fits tend to have a significant number of outliers.[73] Batten states that "there were many instances of stars being more than 0.3 magnitudes fainter than predicted from the ISO guide star catalog, resulting in a failure to acquire the guide star".[73]

Computing instrument magnitudes for variable stars and optical doubles by this approach is particularly difficult.[70, 82, 86] Undetected variables are one concern. The problem is that though it takes only a few measurements to establish the brightness of a non-variable star, it takes many more to even detect that a star is variable. An example of an undetected variable involved the Galileo spacecraft and Delta Velorum. It is one of the 50 brightest stars in the sky (brighter than Polaris) and was one of the approximately 150 stars included in the Galileo flight catalog. The Galileo tracker periodically lost track due to its undetected variability, which was not published until 2001. The conclusion was that it is an Algol-type eclipsing binary and variable during a few hours every 45 days.[88] The frequency of undetected variables is naturally higher for fainter stars. Once detected, it takes many measurements to characterize the range of brightness of a variable star. This task is complicated by the fact that not all variable stars are periodic and that some have periods of years.[68, 70] The color and spectrum of a variable star often fluctuates together with its magnitude making secondary characteristics like $B-V$ vary as well.[70] The result is that even when a star is known to be variable and its variability is characterized by astronomers, the variability of predicted and measured instrument magnitudes may be unknown.[68]

Once instrument magnitude predictions are available, they can be used as criteria in the selection of stars for a flight catalog. This step is particularly important when the flight catalog is used to actively specify what stars a tracker should acquire. In this case the

stars can be termed guide stars. The criteria are often that the guide stars not be too faint for the tracker to acquire, or too bright for measurement without saturating the detector.[70] An attempt was often made to exclude variable stars as well.[68, 77, 83, 85, 86] Alternative types of flight catalogs can include additional stars beyond what would be considered ideal guide stars, for example flight catalogs for ground processing where there can be other considerations besides star acquisition.

After predicted instrument magnitudes are dealt with, the next step in creating a flight catalog is often to exclude stars with relatively bright near-neighbors.[67] Near-neighbors have also been called polluting stars.[70] This situation is inherently more common for dimmer stars. Standard star trackers with defocused optics do not resolve near-neighbor stars, so instrument magnitudes and positions are determined by multiple sources. Sometimes no single neighbor is bright enough to create a significant disturbance, but the composite effect is significant. Such cases have been called integrated magnitude spoilers.[67] The neighbors need not be stars. They can be open clusters, globular clusters, bright galaxies, or nebulae.[70, 79] For example, the star SKYMAP 15190039 was placed on the Hubble bad stars list for problems attributed to the M5 globular cluster.[79]

There are several examples in the literature of stars that have caused practical problems for spacecraft. Star which are capable of causing a problem are referred to here as bad stars. The term bad star dates back to at least May 1992 and a Hubble Space Telescope program list of guide stars that could not be acquired or that resulted in the star tracker reporting a different position than expected.[67, 79] By October 2000 there were thirty-two stars on the bad stars list and three candidates for addition.[67] In March 2001, after eleven years of operation, five of ninety-eight Fixed Head Star Tracker attitude updates attempted by the Hubble Space Telescope failed due to bad stars .[89] On November 27, 2001 after six years of operation the NASA RXTE satellite went into inertial hold mode due to an attitude anomaly attributed to a bad star.[90, 91] A similar loss of star lock had occurred a year previously on September 6, 2000.[76, 91] On July 30, 2003 the primary star

tracker on Mars Express lost star lock, failed automatic reacquisition, and switched over to the secondary tracker due to a bad star.[92] From 2000 to 2004 there were 444 attitude disturbances on the Chandra spacecraft attributed to bad stars.[93]

Table 1 shows some examples of bad stars reported in the literature. Only a few examples were included from the Hubble bad star list because it is long and freely available.[67] Similarly, thirteen stars from the RXTE list that had dimmer instrument magnitudes than expected were not included.[76] The star catalog abbreviations are HIP for Hipparcos, SM for SKYMAP, and HD for Henry Draper. The acronyms for types of bad stars are:

- NN, Near-neighbor stars where a nearby star affected the measured position and brightness.
- IMS, Integrated magnitude spoiler where multiple nearby stars affected the measured position.
- NSO, Non-stellar objects where measurements were affected by nebulae or galaxies.
- PP, Ping-pong where intermittently resolved neighbors affected measurements.
- SP, Spoiler where a near-neighbor was acquired and misidentified.
- MD, Magnitude too dim where instrument magnitude was smaller than predicted.
- MB, Magnitude too bright where instrument magnitude was higher than predicted.
- VD, Variable too dim where a variable star was dimmer than expected.
- VB, Variable too bright where a variable star was too bright.

Table 1. Bad stars reported in the literature.

Primary ID	Secondary ID	Type	Date	Reference
SM 15190039	M5	NSO	1992.5.11	[67]
SM 4370037		IMS	1992.11.17	[67]
SM 9370022		IMS	1993.04.26	[67]
SM 17380016	NGC 6397	NSO/NN	1994.12.17	[67]
SM 200104	SM 200127	NN	1998	[67]
HIP 26220	Trapezium	SP/IMS/NSO	1999.05	[94]
SM 19220121	SM 19230045	PP	1999.10.01	[67]
Not stated	M8 variable	NN/VB	2000.09	[76]
SM 16040108	SM 16040128	NN	2000.05.03	[67]
Delta Velorum		VD	2001	[88]
SM 1070042	Variable	NN/VB	2001.11	[76]
214 suspected		Various	2002.03.15	[76]
13 stars		MD	2002.03.15	[76]
V 5.43 $B-V$ 1.9	-	MD	2003.07.30	[92]
SM 17310145	HD 158619	NN/VB	2004.07.20	[68]
HIP 77072	HIP 77034	PP	2005.10.17	[78]
HIP 74778	HIP 74750	PP	2007.09.26	[66]
HIP 52009	-	MD	2007.09.26	[66]
97-106 stars	-	MD	2007.09.26	[66]

III. ICESat Characteristics

ICESat was launched on January 13, 2003 and deorbited on August 30, 2010. It consisted of the Geoscience Laser Altimeter System (GLAS) and a Ball BCP2000 spacecraft bus, shown below in Figure 4. There were five attitude instruments. The IST was a Raytheon Optical Systems (later Goodrich) HD-1003 star tracker. In the nominal attitude the IST was pitched at 0.3° from the zenith. It had an $8^\circ \times 8^\circ$ field of view, instrument magnitude 6.2 sensitivity, a 512×512 pixel CCD, and tracked up to 6 stars with 10 Hz output.[95] The IST acquired and tracked any available objects in its field of view. The LRS was a second, modified 10 Hz HD-1003 with third-party optics and baffle reducing the field of view to $0.5^\circ \times 0.5^\circ$ and increasing the sensitivity to instrument magnitude 7.5. The LRS was deactivated on the day side of the orbit due to problems with glare. The gyro unit was a Litton (later Northrop Grumman) Space Inertial Reference Unit (SIRU) sampled at 10 Hz and was mounted on the GLAS optical bench beside the IST and LRS. The BSTs were 10 Hz Ball CT-602 trackers mounted on the bus and pointing 30° to either side of the IST pointing vector. They had the same CCD and optics as the CT-601 used on RXTE. The BSTs had an $8^\circ \times 8^\circ$ field of view, instrument magnitude 7.1 sensitivity, a 512×512 pixel CCD, and tracked up to 5 stars simultaneously. They used position predicts from the flight computer to acquire stars specified in a flight catalog stored in the flight computer.

Because of the geometry of the spacecraft and trackers, there were advantages to using a special body frame coordinate system described in Section IIIa. The flight data and attitude instruments are discussed in Section IIIb. There were two primary attitude modes and intermittent maneuvers during science operations and their significance for tracker alignment estimation are discussed in Sections IIIc and IIId.

a. Body North and Body West Coordinate System

The geometry of the spacecraft and trackers meant that, in order to study the GLAS to bus alignment, it was useful to focus on the pointing of the trackers. When tracker

pointing was expressed in a consistent way that corresponded with the possible variations of the GLAS to bus alignment, the results were easier to interpret physically. Representing the tracker attitudes as pointing vectors also made the results independent of the less sensitive tracker axes. Star tracker measurements are less sensitive to rotations about the tracker optical axis. The sensitivity to rotation about the optical axis for a star on the axis is zero.

Tracker pointing vectors represented the tracker optical axes in both the body and celestial frames. The unit vector constraint meant that two coordinates were sufficient. Right ascension and declination coordinates were used in the celestial frame. In the body frame, the relationship between GLAS alignment and tracker pointing was emphasized by a body north and body west coordinate system derived from latitude and longitude.

Individual filter states included alignment rotations for each of the four tracker frames, and an attitude rotation for the body frame. For each tracker, a tracker pointing vector represented the tracker optical axis relative to the celestial frame based on three frame rotations: from the celestial frame to the body frame (attitude state), from the body frame to the reference tracker frame (constant), and from the reference tracker frame to the estimated tracker frame (alignment state). The alignment states for the four trackers were three-component rotation vectors. The rotation vectors were small and expressed relative to reference alignments, which were usually stored as rotation matrices. For a particular tracker, the combination of its alignment state and reference alignment specified the orientation of the tracker frame relative to the body frame. The z axis of the tracker frame was the tracker pointing vector, and the body north and body west coordinates were calculated directly from it. Body north and body west coordinates represented the tracker pointing vector in the body frame and, with a rotation by the body frame attitude, in the celestial frame.

GLAS was defined as body north. All four trackers pointed near the body equator. The tracker pointing vectors shown below in Figure 4 are simplified approximations. When

the exact pointing vectors were calculated from the reference alignments, there were small differences. The LRS reference pointing vector differed by -424 arcseconds north and -1205 arcseconds west. The IST difference was 166 arcseconds north and 176 arcseconds west, the BST1 difference was 442 arcseconds north and -1249 arcseconds west, and the BST2 difference was 479 arcseconds north and 465 arcseconds west. Tracker pointing variations were expressed in a similar fashion as differences from the reference pointing vectors.

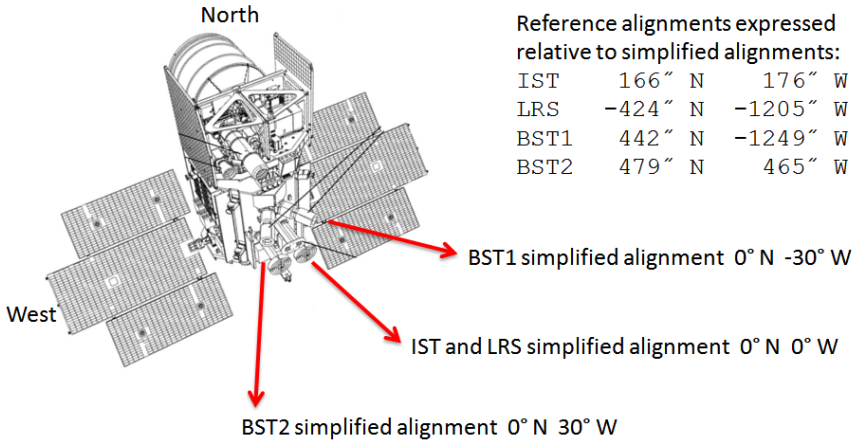

Figure 4. Body north and body west coordinate system.

ICESat was a nadir pointing spacecraft and there was a fundamental asymmetry or difference between the nadir and horizontal directions. The orientation relative to the nadir or zenith was nearly constant, with only small roll and pitch rotations for science pointing. The alignments of the trackers reflected this. They were pointed towards or near the zenith so that their measurements were most sensitive to roll and pitch rotations. Body north and body west coordinates also reflected this difference and were in sense analogous to roll and pitch. The emphasis on roll and pitch was increased by the characteristics of the science being performed. Yaw rotation about the GLAS pointing vector, or the nadir or zenith direction, was not significant for ICESat science.

Because the trackers were pointed vertically, their north and west alignment states were more sensitive to measurements than their yaw alignment states. The position of a star image on a tracker imager is more sensitive to rotation about the two axes in the image plane than about the tracker pointing vector (the axis orthogonal to the image plane). At the origin of the tracker frame, image position is independent of rotation about the tracker pointing vector. The IST and LRS were both pointed vertically so had little sensitivity to yaw. BST1 and BST2 were pointed thirty degrees from vertical along the equator, so increased yaw sensitivity was coupled into their measurements. This appeared as increased noise and uncertainty in BST measurements in the body west direction.

b. Flight Data

The term survey is used here for all of the ICESat flight data that was processed and reduced for the various results. One of the criteria in selecting the survey data was maximizing sky coverage for investigating practical aspects of using the stars as reference points. The sample used for the alignment filter results in Chapter VI was a subset of the survey. Other characteristics besides sky coverage were significant for the alignment results, in particular the attitude mode.

The survey was limited to data publicly available from the National Snow and Ice Data Center (NSIDC), which meant only data from periods when GLAS was operating. These periods were referred to as laser campaigns. Table 2 summarizes the laser campaigns, with the campaigns included in the survey shaded. The identifiers for survey campaigns were 2A, 2B, 2C, 3B, 3F, 3G, 3H, 3J, and 2E. In total they covered 327 days from 2003 to 2009.

Table 2. ICESat laser campaigns with survey campaigns shaded.

Start date	End date	Day count	Laser campaign
2/20/2003	3/29/2003	38	1AB
9/24/2003	11/19/2003	55	2A
2/17/2004	3/21/2004	34	2B
5/18/2004	6/21/2004	35	2C
10/3/2004	11/8/2004	37	3A
2/17/2005	3/24/2005	36	3B
5/20/2005	6/23/2005	35	3C
10/21/2005	11/24/2005	35	3D
2/22/2006	3/27/2006	34	3E
5/24/2006	6/26/2006	33	3F
10/25/2006	11/27/2006	34	3G
3/12/2007	4/14/2007	34	3H
10/2/2007	11/5/2007	37	3I
2/17/2008	3/21/2008	34	3J
10/4/2008	10/19/2008	16	3K
11/25/2008	12/17/2008	23	2D
3/9/2009	4/11/2009	34	2E
9/30/2009	10/11/2009	12	2F

Figure 5 is a projection of the sky showing stars that were measured by the ICESat trackers and analyzed as part of the survey. 90% of the sky was covered. With the $8^{\circ} \times 8^{\circ}$ field of view of the IST and BSTs and the normal ICESat rotation rate of 223 arcseconds per second, the mean length of a star pass was 78.3 ± 27.7 seconds. The term pass is used here to refer to a set of measurements of a star as it travelled across a tracker field of view. Stars were often acquired by the trackers after they had already travelled across a significant fraction of the field of view. This led to a lower mean pass length than

predicted from the size of the field of view and the rotation rate alone. In general very short passes were edited out because of small sample sizes. This also rejected some unusual cases such as transients (dust, debris, satellites) that could have been mistaken for stars, or biased stars that were only marginally being identified. After editing, the survey data included 3.4 million passes of 10,472 unique stars.

ICESat was in a near-circular, frozen orbit with 94^{o} inclination, 590 km altitude, 96.5 minute period, and 183 day nodal regression period (0.5° per day sidereal precession rate).[95-98] The sun was near the orbit plane during campaigns 2C and 3F, creating the gap in coverage at 100° right ascension. The two vertical gaps at 20° and 200° right ascension are areas that were not covered by the survey data. If additional data were included in the survey all three gaps would be filled.

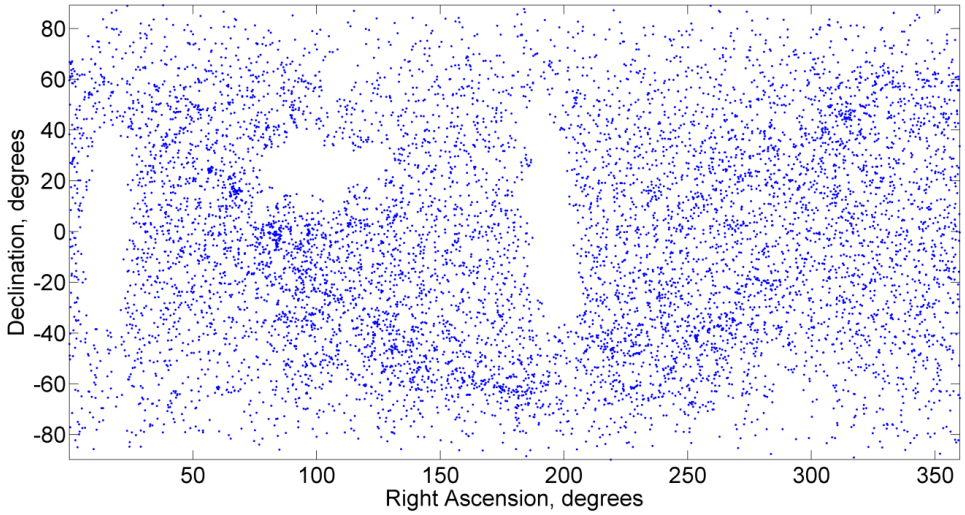

Figure 5. Projection of the sky showing stars that were measured by the ICESat trackers and analyzed as part of the survey.

In the dataset used for the alignment filter results, the spacecraft was normally rotating at 223 arcseconds per second about its long axis, which was always approximately parallel to the celestial equator. The four star tracker pointing vectors followed one another along a great-circle around the celestial sphere, from near the celestial north pole to near the

celestial south pole and then back. The same stars passed through all four tracker fields of view within a sixteen minute period.

The ICESat data at NSIDC was organized into fifteen types of files. The type of concern here was referred to as GLA04 and covered attitude and pointing. The GLA04 files were divided into granules covering two orbits. Since ICESat made about fifteen orbital revolutions per day, there were seven or eight GLA04 granules per day. GLA04 used a big-endian binary format that stored all values as integers. Defined scaling factors were applied by the end user to convert the integer values where appropriate. Summary plots of the events in particular granule were also available from NSIDC.[99]

A GLA04 granule was composed of six physical files, five of which contained information directly related to attitude and alignment. GLA04-01 contained data from the Laser Profile Array (LPA) instrument.[100] The LPA output a high resolution image of the laser beam and was indirectly related to attitude. GLA04-02 contained data from the LRS.[101] GLA04-03 contained date from the gyro unit.[102] GLA04-04 and GLA04-05 contained data from the IST and BSTs.[103, 104] GLA04-06 contained data from the flight computer concerning spacecraft position, velocity, attitude, and solar array angles.[105] The flight computer attitude was important in practice for filter initialization, particularly star identification. The spacecraft velocity was essential for performing aberration correction of star position predictions.

Within each file the data was organized in one second records. Each record had an integer identifier that provided a rough but not exact alignment in time between the six files. The IST data records were 1620 bytes long and contained 35 fields. Of these, 24 fields were at 10 Hz with 10 samples per record. For each of the six IST virtual trackers, a virtual tracker state, star valid flag, magnitude, encircled energy, h and v coordinates, and background bias were output at 10 Hz. The IST time to center of integration, CCD temperature, lens cell temperature, effective focal length, boresight row, boresight column were also output at 10 Hz.[103]

The BST data records were 2196 bytes long and contained 56 fields. For each of the five virtual trackers per BST, Θ_h and Θ_v angles and instrument magnitudes were output at 10 Hz. Sample time, background reading, CCD temperature, baseplate temperature and lens temperature were also output at 10 Hz.[104] The spacecraft sampled the IST and BSTs at 10 Hz but the clocks were asynchronous and there was relative clock drift so that some tracker measurement frames were dropped.[96]

Star measurements were represented in the GLA04 data as unit vectors in one of the four tracker reference frames. Two methods were used to express the unit vectors. BST1 and BST2 output two scaled angles $k\theta_h$ and $k\theta_v$ where the scaling factor k converted from radians to arcseconds. To convert the angles to a unit vector y, an intermediate vector $x = [x_1 \quad x_2 \quad x_3]^T$ was calculated with x_3 defined equal to one, x_1 defined as the horizontal coordinate h, and x_2 defined as the vertical coordinate v, so that $x = [h \quad v \quad 1]^T$ where

$$h \equiv x_1 / x_3 = x_1 / 1 = \tan\theta_h \tag{2}$$

$$v \equiv x_2 / x_3 = x_2 / 1 = \tan\theta_v \tag{3}$$

The unit vector y was then the normalized version of x

$$y = \left[h \quad v \quad 1\right]^T \Big/ \left(h^2 + v^2 + 1\right)^{1/2} \tag{4}$$

The native outputs of the IST and LRS were kh and kv. The IST and LRS performed the trigonometric calculations $h = \tan\theta_h$ and $v = \tan\theta_v$ internally. Because θ_h and θ_v were small angles, kh and kv were nearly equal to $k\theta_h$ and $k\theta_v$, but confusing the two types of output produced errors on the order of thirty arcseconds across an eight degree field of view. From GLA04 Release 24 (2005.12.21) onwards the IST values were converted from kh and kv to $k\theta_h$ and $k\theta_v$. In all GLA04 releases the LRS output was kh and kv but a special calculation was used to convert to unit vectors

$$y = \left[3.388v / 3.42 \quad -3.388h / 3.42 \quad 1\right]^T \Big/ \left(\left(3.388v / 3.42\right)^2 + \left(-3.388h / 3.42\right)^2 + 1\right)^{1/2} \tag{5}$$

c. Attitude Modes and Alignment Filter Dataset

ICESat had two primary attitude modes which were selected depending on the sign and magnitude of the angle from the orbit plane to the sun vector (beta prime angle).[95] Within each attitude mode a 180 degree rotation was also specified for four total possibilities. When the sun was within 32 degrees of the orbit plane airplane mode was selected. In airplane mode the solar array drive axes were perpendicular to the orbit plane. Otherwise sailboat mode was selected. In sailboat mode the solar array drive axes were parallel to the orbit plane. The IST and LRS were aligned so that star motion was roughly parallel to the pixel rows or columns. The BSTs were aligned so that star motion was diagonal across the pixel rows and columns. Commanded rotations or stepping of the solar arrays caused 1 Hz oscillations of the tracker pointing vectors. This oscillation had an amplitude of up to 20 arcseconds peat-to-peak in sailboat mode, and up to 2.5 arcseconds in airplane mode.[97] There were twice per day 5° off-nadir ocean scan calibration maneuvers over the Pacific Ocean near the equator, on both ascending and descending passes. These were 20 minute octagonal roll-pitch scans with a 3-5° radius. Additionally, targets of opportunity at angles up to 5° off-nadir were pointed at intermittently.[95]

Alignment results are given in chapter VI for seven of the nine laser campaigns in the survey. They included one campaign per year from 2003 to 2009 as shown inTable 3. The seven campaigns took place in the spring or fall when the orbit plane was far from the sun and the spacecraft was in sailboat mode. The sun did not approach the tracker pointing vectors and there was no sun blinding.

Table 3. Dataset for the Chapter VI alignment results.

Year	Campaign	Days	First day	Last day
2003	2A	55	2003.09.25	2003.11.18
2004	2B	34	2004.02.17	2004.03.21
2005	3B	36	2005.02.17	2005.03.24
2006	3G	34	2006.10.25	2006.11.27
2007	3H	34	2007.03.12	2007.04.14
2008	3J	34	2008.02.17	2008.03.21
2009	2E	33	2009.03.09	2009.04.11

The seven sailboat mode campaigns had similar characteristics except for 2003 campaign 2A. It was longer and included two commanded temperature changes that caused step changes in the alignments, demonstrating the sensitivity of the alignments to temperature. The 2A campaign is a useful test case because the two commanded temperature changes divide it into three roughly steady state periods separated by step changes.

During airplane mode campaigns, sunlight caused tracker blinding periods and temperature spikes. Only sailboat mode campaigns were included in the dataset in order to focus on steady state baseline characteristics. Airplane mode campaigns were set aside for later study.

The disk files for the dataset were composed of one GLA04 granule from each day of the seven campaigns. The campaigns covered 260 days, so there were 260 GLA04 granules containing 520 orbital revolutions and approximately 832 minutes of flight data. Sixteen of the granules were found to have abnormal filter results, leaving 244 normal granules. The problem granules are discussed in Chapter VI.

d. Maneuvers

Table 4 is a summary of the 260 granules in the dataset. The granules represent 260 unique days in seven laser campaigns from 2003 to 2009. The fourth column shows the number of problem granules per campaign with the ratio to the total in parenthesis. The fifth column shows the number of maneuver granules. These were normal granules containing an ocean scan maneuver. The table indicates that the later campaigns contained a higher proportion of maneuver granules than the earlier campaigns. In the final campaign 82% of the normal granules contained a maneuver. In the first two campaigns only 16% and 18% of normal granules contained a maneuver.

Table 4. Counts of dataset granules where problems or maneuvers were detected.

Year	Campaign	Granules	Problem granules	Maneuver granules
2003	2A	55	3 (0.05)	9 (0.16)
2004	2B	34	2 (0.06)	6 (0.18)
2005	3B	36	7 (0.19)	14 (0.39)
2006	3G	34	0 (0.00)	2 (0.06)
2007	3H	34	3 (0.09)	18 (0.53)
2008	3J	34	1 (0.03)	15 (0.44)
2009	2E	33	0 (0.00)	27 (0.82)

Ocean scan maneuvers occurred in 91 of the 244 normal granules. They were performed near the day or night equator crossing. Because the LRS was deactivated on the day side of the orbit due to glare, ocean scans took place near the middle of periods where the LRS was deactivated or activated. A related and less frequent type of maneuver referred to as an around the world scan had larger rate variations than ocean scans and covered a complete orbital revolution. Portions of seven around the world scans were present in the dataset, and as shown in Chapter VI they were the direct cause of seven of the sixteen problem granules.

The filter alignments and residuals were affected by ocean scan maneuvers and showed variations that were correlated with the angular rate variations. Minimizing the effects of oceans scans and improving filter performance during oceans scans was a primary research objective. Briefly, gyro data became much more important during maneuvers. It was desirable to use the alignment filter for the types of star results discussed in Chapter V, but caution was required during ocean scans. The fact that ocean scans correlated with variations in the filter residuals indicated that the predicted star unit vectors in the filter were degraded. Tracker pointing vector errors during ocean scans were generally found to be on the order of two or three arcseconds, which was relatively large for the purposes of investigating star measurement errors. Position biases due to near-neighbor stars were of particular interest and could be difficult to distinguish from the effects of ocean scans in individual cases. As a result, maneuver detection was implemented and ocean scans were flagged in the filter output.

Figure 6 superimposes the magnitudes of the angular rates for 244 of the dataset granules. The timing of ocean scans near 2000, 5000, and 8000 seconds is clear. The 244 granules spanned seven laser campaigns from 2003 to 2009 and the relative timing of the ocean scans varied from campaign to campaign. This variation is apparent in the ocean scans at 2000 and 8000 seconds where the final rate spikes appear as two discrete spikes corresponding to two subsets of campaigns. The rates vary about the orbital rate of 223 arcseconds per second.

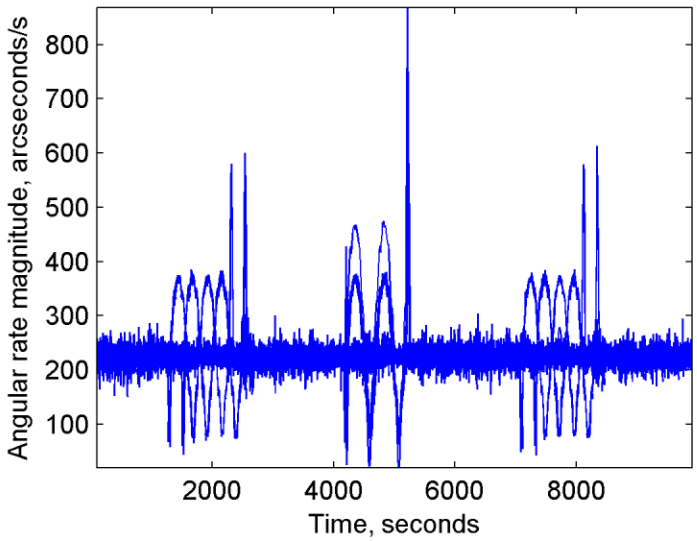

Figure 6. Superimposed angular rate magnitudes for 244 dataset granules.

Figure 7 superimposes the magnitudes of the deviations away from the orbital rate. This quantity was useful for automated maneuver detection. The objective was to detect the beginning and end of maneuvers. Figure 7 suggests that a practical criterion for detecting maneuver boundaries is when the deviation magnitude exceeds 100 arcseconds per second. An empirical check confirmed that there were either zero or one maneuvers per granule. The beginning and end points of maneuvers were defined as the first and last crossings of the 100 arcseconds per second threshold. Each of the 91 maneuver granules contained one ocean scan near either 2000, 5000, or 8000 seconds. They began and ended abruptly with sharp transitions from the normal orbital rate to ocean scan and vice versa.

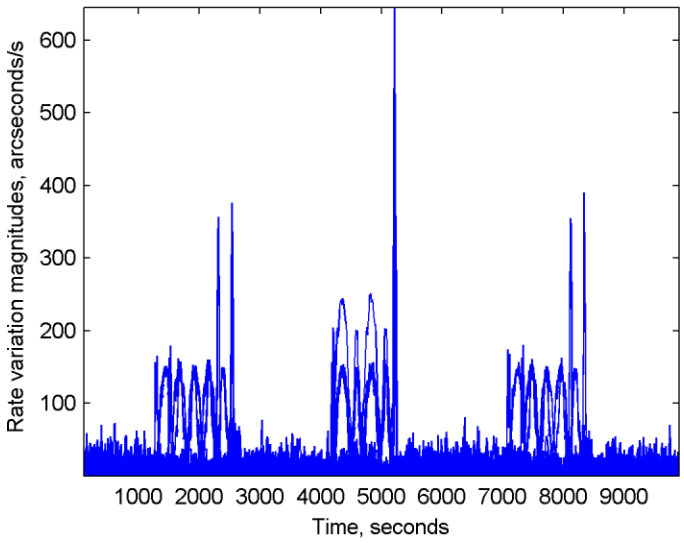

Figure 7. Magnitudes of deviations away from the orbital rate.

An interface to the alignment filter results was implemented that distinguished normal periods and maneuver periods using the maneuver detection method. The filter results were physically represented as two types of data structures. One represented the filter state results and the other represented the star results. The interfaces to these two data structures automatically classified the alignment and star results as being from either a normal or maneuver period.

For the state results, the effects of maneuvers were relatively small. The characteristic effect was an oscillation of the alignment and attitude states, with a magnitude of a few arcseconds and duration of approximately a thousand seconds. The orbital variations of the GLAS tracker alignments were an order of magnitude larger. The orbital variations of the bus tracker alignments were comparable in magnitude to the maneuver effects, and there were a few cases with unusual results due to ocean scans. These cases are discussed in Chapter VI. For the star measurement results, the effects of maneuvers were more significant because the objective was arcsecond level positional accuracy. Since a typical star pass was shorter than a typical maneuver, a few hundred seconds versus a thousand

seconds, systematic differences were possible between passes measured during maneuvers and passes measured during normal periods.

IV. Alignment Filtering

The quantities estimated by an alignment filter represent the individual attitudes of multiple trackers. The filter unifies attitude and alignment estimation, makes them adaptable for real-time and autonomous systems, and fuses the measurements from an arbitrary number of trackers. For ICESat the estimated quantities included alignment estimates for each of the four tracker frames and an attitude estimate for the body frame, as described in Section IVa. The filter phases and their implementation are described in Sections IVb and IVc.

For studying the GLAS to bus alignment, the practical outputs from the filter were time-series of tracker pointing vectors and star residuals. The tracker pointing vectors combined the filter alignment and attitude states and emphasized their physical meaning as positions on the celestial sphere. A tracker pointing vector represented a tracker optical axis expressed relative to the celestial frame using two frame rotations: from the tracker frame to the body frame using the tracker alignment state, then from the body frame to the celestial frame using the body attitude state. The pointing vectors could also be expressed in the body frame by a frame rotation back from the celestial frame to the body frame. In the ideal filter, the body frame was defined as the gyro frame and the tracker pointing vectors were sensitive to alignment variations between the gyro unit and the trackers. In practice, the body frame could be redefined as one of the tracker frames by holding its alignment constant, effectively removing it from the filter state.

The star residuals were differences between measured and predicted star unit vectors. The predicted star vectors were in a sense equivalent to the tracker pointing vectors. Both were deterministic functions of the filter alignment and attitude states. The most significant difference between the filter states, tracker pointing vectors, and predicted star vectors was that there were direct measurements to compare with the predicted star vectors. The stars and star catalogs were nearly ideal inertial references, so if the

predicted star vectors were near the measured star vectors, then the tracker pointing vectors and combined states were accurate.

The time-series of pointing vectors and residuals were reduced to descriptive statistics and interpreted as alignment variations and tracker errors. A practical method for evaluating filter performance is based on descriptive statistics for individual stars as they cross a tracker field of view. Each crossing is referred to as a pass, and pass residuals were smoothed to generate error signals for the filter. The filter output and evaluation methods are discussed in Section IVd.

a. Filter Structure

Attitude and alignments are estimated using the multiplicative extended Kalman filter (MEKF)[9, 10] augmented with alignments for the four ICESat trackers. The overall structure is summarized by Figure 8 on the next page. The attitude estimate is a rotation from the inertial frame to the spacecraft body frame. Any rotation representation can be used as convenient.[10, 18] Here the attitude estimate is represented by a rotation matrix $\hat{A}_i^b$. It is maintained separately from other estimated quantities throughout the filter. This aids in keeping $\hat{A}_i^b$ a proper rotation matrix while allowing unconstrained estimation of a three-component rotation vector attitude error estimate in the measurement update. Markley, an author of the original MEKF description[9], states "the MEKF is not really an attitude estimator; it performs an unconstrained estimation of a three-component attitude error, with the attitude playing the role of a reference about which the errors are defined."[10] Other estimated quantities are a three-component gyro bias estimate $\hat{b}$, and three-component rotation vector tracker alignment estimates $\hat{a}_j$ for each of the four star trackers, $j = 1, 2, 3, 4$.

During the propagation phase, gyro measurements are used to propagate the attitude estimate $\hat{A}_i^b$ and covariance P from t_k to t_{k+1}. The gyro bias estimate $\hat{b}$ and tracker alignment estimates $\hat{a}_j$ are constant during the propagation phase.

In the measurement update phase, star tracker measurements are used to estimate: a three-component rotation vector attitude error estimate $\tilde{a}_{\phi}$, a three-component gyro bias error estimate $\tilde{b}$, and three-component rotation vector tracker alignment error estimates $\tilde{a}_j$. The error estimate $\tilde{x}$ and covariance P are defined in Equations (6) and (7), where x are the true values and $\hat{x}$ are the estimated values. The vector y represents star tracker unit vector measurements.

$$\tilde{x} \equiv E\{x - \hat{x} \mid y\} \equiv [\tilde{a}_{\phi}^T \quad \tilde{b}^T \quad \tilde{a}_1^T \quad \tilde{a}_2^T \quad \tilde{a}_3^T \quad \tilde{a}_4^T]^T \tag{6}$$

$$P \equiv E\{(\tilde{x} - E\{\tilde{x}\})(\tilde{x} - E\{\tilde{x}\})^T\} \tag{7}$$

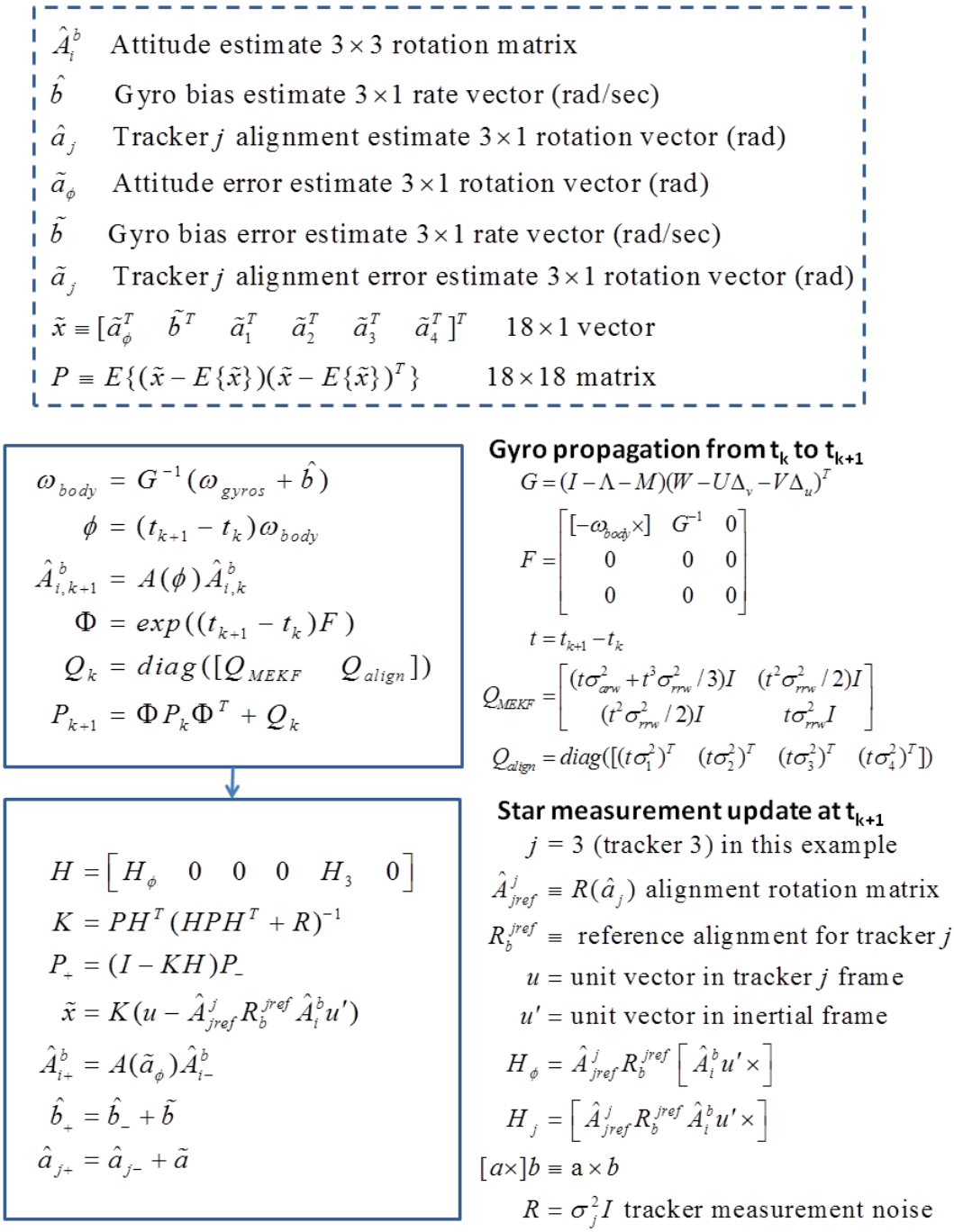

Figure 8. Structure of the alignment filter.

During a measurement update from star tracker j, the tracker alignment estimate rotation vector $\hat{a}_j$ is represented as a rotation matrix $\hat{A}^j_{jref}$. $\hat{A}^b_i$ and $\hat{A}^j_{jref}$ are used to predict the unit vector star tracker measurements and form measured minus predicted innovations for estimating $\tilde{x}$. The first three components of $\tilde{x}$ are the attitude error estimate $\tilde{a}_\phi$. It is converted to a rotation matrix $A(\tilde{a}_\phi)$ and used to update the attitude estimate $\hat{A}^b_i$ by multiplication (hence the name Multiplicative EKF).

$$\hat{A}^b_{i,+} = A(\tilde{a}_\phi)\hat{A}^b_{i,-} \tag{8}$$

The gyro bias error estimate $\tilde{b}$ is used to update the gyro bias estimate $\hat{b}$

$$\hat{b}_+ = \hat{b}_- + \tilde{b} \tag{9}$$

and the tracker alignment error estimate $\tilde{a}_j$ is used to update the tracker alignment estimate $\hat{a}_j$.

$$\hat{a}_{j+} = \hat{a}_{j-} + \tilde{a}_j \tag{10}$$

One objective of the alignment filter is to simultaneously predict the star position measurements from all four trackers. Measurement predictions are used during the measurement update phase to form the innovations, measurement sensitivity matrix H, and residuals. The predictions are a function of the tracker attitude estimate $\hat{A}^j_i$ alone. The alignment estimate $\hat{a}_j$ for tracker j is a three-component rotation vector expressed relative to $R^{jref}_b \hat{A}^b_i$, the product of the tracker j reference alignment rotation matrix R^{jref}_b and the attitude estimate $\hat{A}^b_i$. The tracker attitude estimate $\hat{A}^j_i$ for tracker j is then

$$\hat{A}^j_i = \hat{A}^j_{jref} R^{jref}_b \hat{A}^b_i \tag{11}$$

Where $\hat{A}^j_{jref} \equiv R(\hat{a}_j)$ is the rotation matrix representation of the alignment estimate rotation vector $\hat{a}_j$. The reference alignments R^{jref}_b were determined after launch from flight data and their accuracy was judged by how well they performed as initial values and the behavior of the alignment updates. They were very good for the bus trackers,

within a few arcseconds, and adequate for the GLAS trackers, which had large alignment variations. Given a star unit vector measurement in the tracker frame u, and the unit vector for the same star in the inertial frame u' from a star catalog, the measured minus predicted innovation or residual $\tilde{y}$ is

$$\tilde{y} = u - \hat{A}^{j}_{jref} R^{jref}_{b} \hat{A}^{b}_{i} u' \tag{12}$$

The star catalog unit vector u' and the reference alignment R^{jref}_{b} are constant. The measurement u, tracker alignment estimate $\hat{A}^{j}_{jref}$, and attitude estimate $\hat{A}^{b}_{i}$ contain errors and represent physical characteristics that are normally time-varying. There is measurement noise in u and process noise in $\hat{A}^{j}_{jref}$ and $\hat{A}^{b}_{i}$, therefore a time series of residuals $\tilde{y}_k$ is a random process.

An example involving two trackers demonstrates some aspects of the estimates, predictions, and residuals. Assume that tracker 1 is tracking the star u_1, and tracker 2 is tracking the star u_2. The residuals from the two trackers are

$$\tilde{y}_1 = u_1 - \hat{A}^{1}_{1ref} R^{1ref}_{b} \hat{A}^{b}_{i} u'_1 \tag{13}$$

$$\tilde{y}_2 = u_2 - \hat{A}^{2}_{2ref} R^{2ref}_{b} \hat{A}^{b}_{i} u'_2 \tag{14}$$

The time series of residuals $\tilde{y}_{1,k}$ and $\tilde{y}_{2,k}$ are random processes. If the predictions $\hat{A}^{1}_{1ref} R^{1ref}_{b} \hat{A}^{b}_{i} u'_1$ and $\hat{A}^{2}_{2ref} R^{2ref}_{b} \hat{A}^{b}_{i} u'_2$ are accurate, then $\tilde{y}_{1,k}$ and $\tilde{y}_{2,k}$ are approximately zero mean Gaussian. Now assume that there is strong evidence that the alignments of both trackers are nearly constant, and that there are accurate alignment estimates $\hat{a}_1$ and $\hat{a}_2$. A test to validate these results is to configure the filter with $\hat{a}_1$ and $\hat{a}_2$ effectively held constant at their reference values by setting their initial covariance values and process noise values small. This is equivalent to holding $\hat{A}^{1}_{1ref}$ and $\hat{A}^{2}_{2ref}$ constant, in which case they can be absorbed into the reference alignments R^{1ref}_{b} and R^{2ref}_{b} and the residuals become

$$\tilde{y}_1 = u_1 - R^{1ref}_{b} \hat{A}^{b}_{i} u'_1 \tag{15}$$

$$\tilde{y}_2 = u_2 - R_b^{2ref} \hat{A}_i^b u_2' \tag{16}$$

Here the measurements from both trackers are predicted using the attitude estimate $\hat{A}_i^b$ alone. If the alignments of both trackers truly are nearly constant, then the measurement predictions will be good and the time series of residuals $\tilde{y}_{1,k}$ and $\tilde{y}_{2,k}$ will be approximately zero mean Gaussian. If either or both time series of residuals $\tilde{y}_{1,k}$ and $\tilde{y}_{2,k}$ depart from approximately zero mean Gaussian, then the attitude estimate $\hat{A}_i^b$ alone is not sufficient for predicting the measurements because at least one of the tracker alignments is not constant.

The standard MEKF was a special case of the alignment filter. The alignment filter could be configured with the tracker alignment estimates effectively constant, to use any combination of the trackers, or to have the attitude error estimate respond more or less strongly to star measurement updates. Two types of sensors and measurements were combined by the filter. Star tracker unit vectors were used to make corrections during the measurement update phase via a measurement equation as in a typical filter. Gyro unit rate vectors were used to replace the dynamics in the propagation phase state equation. This is termed model replacement.[9] A dynamical model of accelerations usually present in the state-equation was replaced by empirical measurements of rates. The practical effect was that the gyro measurements dominated the prediction phase, but did not appear in the measurement update phase. A fundamental difference or asymmetry in the filter was that gyros affected propagation and trackers affected measurement updates. In the ideal situation, the gyros would play another special role defining the body frame. The sensors are summarized in Table 5.

Table 5. Sensors and the ideal filter.

	Gyro unit	Star tracker
Measurement type	Angular rate vector (rad / s)	Units vectors (*unitless*)
Filter phase	Propagation	Measurement update
Estimates	Attitude estimate	Alignment estimate
Reference frame	The body frame	An alignment frame
Expressed relative to	Celestial frame	Body frame

The filter cycle was composed of two phases: propagation, and measurement update.[9, 10, 18] The propagation phase advanced the attitude estimate $\hat{A}_i^b$ and covariance P from t_k to the next tracker measurements at t_{k+1} and was viewed as the prediction phase, in which the tracker attitude $\hat{A}_{jref}^{j} R_b^{jref} \hat{A}_i^b$ was predicted for the next measurement. The measurement update phase incorporated new information and was viewed as the filtering phase, in which new information was filtered or reduced by comparing it to the prediction.

b. Gyro Propagation

Propagation used gyro measurements to advance the attitude estimate $\hat{A}_i^k$ and covariance P from t_k to t_{k+1}. All estimated quantities other than the attitude estimate were constant during the propagation phase. The angular rates used for propagation came from gyro measurements, corrected using a gyro measurement model that included various gyro calibration parameters. The process noise matrix Q was a function of the gyro noise characteristics and gyro error model. The term gyro error model is associated here with stochastic processes and random noise, whereas the term gyro measurement model is associated with deterministic errors and corrections.

In practice, the gyro noise parameters and Q matrix were a critical factor in filter performance. The Q matrix effectively decided how strongly the filter responded to the gyros versus the trackers, in other words the size of the attitude error estimates $\tilde{a}_{\phi}$ during the measurement update phase. With perfect gyros the attitude error estimates during measurement update would approach zero.

The attitude estimate was maintained separately throughout the filter and represented by a rotation matrix or quaternion as convenient. Attitude propagation for both representations is shown in Equations (17) and (18). Here ϕ is a rotation vector and the rotation matrix function $A(\phi)$ and quaternion function $q(\phi)$ are discussed in the Appendix.

$$A_{inertial,k+1}^{body} = A(\phi) A_{inertial,k}^{body} \tag{17}$$

$$q_{inertial,k+1}^{body} = q(\phi) \otimes q_{inertial,k}^{body} \tag{18}$$

Attitude propagation reduced in practice to estimating the rotation vector ϕ over the time interval $t_{k+1} - t_k$.

A basic method for estimating ϕ over short time intervals was implemented as shown in Equations (19) to (20). The 10 Hz gyro data was used to propagate between 10 Hz tracker measurements from four trackers, so the time intervals were generally at most 0.1 seconds. Equation (19) for the estimated body rates is discussed below in the section concerning the gyro measurement model.

$$\omega_{body,k} = G_k^{-1}\left(\omega_{gyros,k} + b_k\right) \tag{19}$$

$$\phi = \left(t_{k+1} - t_k\right)\omega_{body,k} \tag{20}$$

This method was based on the kinematic equation describing the time rate of change of the rotation vector ϕ, known as the Bortz equation.[106] The Bortz equation is shown to second-order accuracy in Equations (21) to (23). Here α is called the integrated angular rate and β is called the coning attitude motion.[106] Integrated angular rate α was

particularly significant because the ICESat gyro unit contained rate-integrating gyros outputting angles, rather than rates.

$$\dot{\phi} \approx \omega_{body} + \frac{1}{2}\alpha \times \omega_{body} \equiv \dot{\alpha} + \dot{\beta} \tag{21}$$

$$\dot{\alpha} \equiv \omega_{body} \Rightarrow \alpha \equiv \int \omega_{body} dt \tag{22}$$

$$\dot{\beta} \equiv \frac{1}{2}\alpha \times \omega_{body} \Rightarrow \beta \equiv \int \frac{1}{2}\alpha \times \omega_{body} dt \tag{23}$$

For basic propagation equation (21) was expressed as Equation (24).[106]

$$\phi = \alpha + \beta \tag{24}$$

The coning motion β was assumed negligible and the rotation vector reduced to Equation (25).

$$\phi = \alpha = \int \omega_{body} dt \tag{25}$$

This is equivalent to Equation (20) over short time intervals.

A standard propagation method for Inertial Navigation Systems (INS) was also used and is referred to here as INS propagation.[18, 106] It was designed for high-rate gyro measurements and was structured with a fast cycle accumulating the gyro measurements and a slow cycle outputting a rotation vector ϕ for use in Equations (17) and (18).

The INS method was designed with high-frequency jitter in mind and is a relatively accurate way to calculate ϕ. Jitter and rapid maneuvers can cause an unwanted effect termed coning during attitude propagation, represented by the β term in Equation (24). High-rate gyro measurements for ICESat would mean 100 Hz gyro data used to propagate between 10 Hz tracker measurements from four trackers. Since the ICESat gyro output rate was 10 Hz, this meant interpolating the gyro data from 10 Hz to 100 Hz. The interpolated 100 Hz gyro data did not contain the jitter information in true 100 Hz data but did make the INS method practical for implementation and testing.

The objective is to calculate a rotation vector ϕ_m after a time interval t_m. The initial rotation vector ϕ_0 and time t_0 are assumed to be zero. The time interval t_0 to t_m is termed the slow-cycle and in practice t_m corresponds to a filter cycle, the time between two measurement updates. There are a number of sub-intervals termed the fast-cycle and defined by gyro measurements. The index l indicates which fast-cycle is currently being processed beginning with $l = 0$ at $t_0 = 0$. The calculations in each fast-cycle starting with $l = 1$ are shown in Equations (26) to (29) where $\alpha_0 = 0$ and $\beta_0 = 0$. In practice $\Delta\alpha_l$ in Equation (26) is a gyro measurement (assuming rate-integrating gyros).

$$\Delta\alpha_l = \int_{t_{l-1}}^{t_l} d\alpha \tag{26}$$

$$\Delta\beta_l = \frac{1}{2}\left(\alpha_{l-1} + \frac{1}{6}\Delta\alpha_{l-1}\right) \times \Delta\alpha_l \tag{27}$$

$$\alpha_l = \alpha_{l-1} + \Delta\alpha_l \tag{28}$$

$$\beta_l = \beta_{l-1} + \Delta\beta_l \tag{29}$$

When $t_l = t_m$ the fast-cycle calculations are complete and ϕ_m is shown in Equation (30).

$$\phi_m = \alpha_l + \beta_l \tag{30}$$

What the INS propagation of Equation (30) provides that the basic propagation of Equation (25) does not is the effect of the coning term β_l.

The covariance was propagated as shown in Equation (31). Practical values for the initial covariance P_0 are discussed below in conjunction with the process noise.

$$P_{k+1} = \Phi_k P_k \Phi_k^T + Q_k \tag{31}$$

The discrete-time state transition matrix Φ_k in Equation (31) was only used for covariance propagation. The continuous-time state-equation for $\tilde{x}$ is shown in Equations (32) and (33).[107] The process noise vector w represented a random process $w \sim N(0, Q)$

in the continuous-time case and a random sequence $w_k \sim N(0, Q_k)$ in the discrete-time case.[108]

$$\frac{d}{dt}\tilde{x} = F\tilde{x} + w \tag{32}$$

$$F = \begin{bmatrix} [-\omega_{body}\times] & G^{-1} & 0 \\ 0 & 0 & 0 \\ 0 & 0 & 0 \end{bmatrix} \tag{33}$$

The discrete-time state equation is shown in Equations (34) and (35).[107]

$$\tilde{x}_{k+1} = \Phi_k \tilde{x}_k + w_k \tag{34}$$

$$\Phi_k = \exp\left(\left(t_{k+1} - t_k\right)F\right) \tag{35}$$

Φ_k was calculated using the matrix exponential function. Various implementations of the matrix exponential with different accuracies and computational performance were available and evaluated.[109]

The set of noise parameters shown in Table 6 characterized the gyro noise sources and were used in the gyro error model equations. The error model equations were applied in computing the filter process noise matrix Q. Additional parameters and more sophisticated error models were possible. The term random walk is commonly associated with two types of quantities with different units, both a white noise and an error value. The white noise integrates over time to generate the error values, and the error values perform a random walk. In other words, random walk is integrated white noise. For example, a noise x with units $rad/s^{1/2}$ causes the error $t^{1/2}x$ with units rad. The noise units can be made more intuitive by defining a sample time t_s and multiplying the noise by the scaling factor $1/t_s^{1/2}$. The noise x becomes $y = x/t_s^{1/2}$ with units rad/s and the error over the sample time is $t_s y$ with units rad.

Table 6. Gyro noise parameters.

Gyro noise parameter	Units	Symbols
Angle noise (angle white noise)	rad	σ_{awn}
Rate noise (angular random walk noise)	$rad/\mathrm{s}^{1/2}$	σ_{arw}
Acceleration noise (rate random walk noise)	$rad/s^{3/2}$	σ_{rrw}

The discrete-time gyro error model for angular error θ, angular random walk u, and rate random walk v was given by Equations (36) to (38) for $t = t_{k+1} - t_k$.[110]

$$\theta_k = u_k + \sigma_{awn} \tag{36}$$

$$u_{k+1} = u_k + tv_k + \left(t\sigma_{arw}^2 + \frac{1}{3}t^3\sigma_{rrw}^2 \right)^{1/2} + \frac{1}{2}t\left(t\sigma_{rrw}^2\right)^{1/2} \tag{37}$$

$$v_{k+1} = v_k + \left(t\sigma_{rrw}^2\right)^{1/2} \tag{38}$$

For initial values the angular random walk u_0 was set to zero and the rate random walk v_0 was set to the current estimate of the gyro rate bias *b*.

The gyro error model was applied in the discrete-time process noise matrix Q implemented in the filter. The discussion here concerns the first six states in $\tilde{x}$. They were the attitude error $\tilde{a}_\phi$ with units of radians, and the gyro rate bias error $\tilde{b}$ with units of radians per second. In practical terms only the upper-left 6×6 block of Q was affected by the gyro error model. This upper-left 6×6 block is the complete Q matrix for the standard MEKF.

Q was the covariance of the process noise vector $w_k \sim N\left(0, Q_k\right)$ as shown in Equation (39).[53, 54]

$$Q_k = E\left(w_k w_k^T\right) \tag{39}$$

The first three components of w_k were associated with u_k from Equation (37) and represented angular noise affecting the attitude states. The last three components were associated with v_k from Equation (38) and represented rate noise affecting the rate states.

The gyro process noise model Q_{gyro} is shown in Equation (40) for $t = t_{k+1} - t_k$.[107, 111, 112] It is also identified as Q_{MEKF} because it is the complete process noise matrix Q_k for the MEKF.

$$Q_{gyro} = Q_{MEKF} = \begin{bmatrix} (t\sigma_{arw}^2 + t^3\sigma_{rrw}^2/3)I & (t^2\sigma_{rrw}^2/2)I \\ (t^2\sigma_{rrw}^2/2)I & t\sigma_{rrw}^2 I \end{bmatrix} \tag{40}$$

The gyro angular random walk value and rate random walk value specified in the ICESat documentation were $\sigma_{arw} = .01$ arcseconds/s$^{1/2}$ and $\sigma_{rrw} = .0000319$ arcseconds/s$^{3/2}$. Angular random walk is dominant on short time scales, and rate random walk is dominant on long time scales. With updates from four 10 Hz star trackers, the normal gyro propagation length was less than a tenth of a second and Q_{gyro} was dominated by the angular random walk value. In MEKF-based filters, gyro measurements replace a dynamical model and Q_{gyro} represents uncertainty associated with gyro propagation of the attitude estimate $\hat{A}_i^b$.

During normal science operations, gyro propagation of $\hat{A}_i^b$ using the specified angular random walk value and Equation (40) was adequate. The propagated $\hat{A}_i^b$ predicted the tracker measurements well enough that the time series of residuals $\tilde{y} = u - \hat{A}_{jref}^{j} R_b^{jref} \hat{A}_i^b u'$ from all four trackers were approximately zero mean Gaussian. Propagation was validated by calculating the measured minus predicted innovations for the star tracker measurements while using gyro propagation alone, without star measurement updates of $\hat{A}_i^b$. Gyro propagation alone did an adequate job of predicting the tracker measurements until the gyro rate bias instability errors, represented by rate random walk in Equation (40), became significant over hundreds or thousands of seconds. Monitoring the

measured minus predicted innovations while using gyro propagation alone is a practical method for estimating the empirical uncertainties represented by Q_{gyro}.

During ocean scan maneuvers, gyro propagation of $\hat{A}_i^b$ using the specified angular random walk value and Equation (40) was not adequate. The differences between measured and predicted star positions grew to tens of arcseconds during periods of relatively high angular rates and accelerations. This level of pointing knowledge degradation during maneuvers is not a problem for many spacecraft, but the ICESat pointing knowledge objective is arcsecond level accuracy. Figure 9 shows the rate about one axis during an ocean scan maneuver in the bottom row of plots, and the residuals from three of the trackers in the top three rows of plots. Trends and peaks in the residuals $\tilde{y} = u - \hat{A}_{jref}^{j} R_b^{jref} \hat{A}_i^b u'$ reflect the rate variations of the maneuver. This is evidence of increased empirical uncertainty in gyro propagation of the attitude estimate $\hat{A}_i^b$ during ocean scan maneuvers.

Rather than modify the form of the gyro process noise, Equation (40), the angular random walk value was increased to reflect the higher empirical uncertainty. The plots on the left side of Figure 9 are for the specified angular random walk value, the plots on the right are for a value three times larger. The larger angular random walk value results in smaller trends and peaks in the residuals because the attitude error estimates $\tilde{a}_\phi$ and resulting updates to the attitude estimate $\hat{A}_i^b$, shown in the fourth row of plots, are larger. The star measurements are relied on more and used to make stronger corrections to the attitude estimate.

An objective of the MEKF is to improve gyro propagation of the attitude estimate $\hat{A}_i^b$ by estimating and correcting the gyro measurement errors, represented by the gyro bias estimate $\hat{b}$. At the same time, the gyro measurement model G corrects gyro measurement errors due to scale factors and sense-axes misalignments. The estimated body rate ω_{body} used to propagate $\hat{A}_i^b$ depends only on the gyro measurements ω_{gyros}, gyro bias estimate $\hat{b}$, and gyro measurement model G

$$\omega_{body} = G^{-1}(\omega_{gyros} + \hat{b}) \tag{41}$$

Improved estimates of $\hat{b}$ and G mean reduced errors in ω_{body}, resulting in smaller measured minus predicted star position innovations, and smaller attitude error estimates $\tilde{a}_{\phi}$ and corrections to the attitude estimate $\hat{A}_i^b$.

For ICESat during normal science operations, the uncorrected errors in ω_{body} were small and gyro propagation of $\hat{A}_i^b$ predicted the tracker measurements well enough that the time series of residuals $\tilde{y} = u - \hat{A}_{jref}^{j} R_b^{jref} \hat{A}_i^b u'$ from all four trackers were approximately zero mean Gaussian. Figure 9 demonstrates that this was no longer true during ocean scan maneuvers. In response, the gyro error corrections represented by $\hat{b}$ and G can be improved, resulting in a reduction of both the residuals and the corrections to the attitude estimate $\hat{A}_i^b$. Or the gyro process noise Q_{gyro} can be increased to reflect the increased empirical uncertainty in gyro propagation of $\hat{A}_i^b$, resulting in reduced residuals due to stronger corrections to $\hat{A}_i^b$.

.

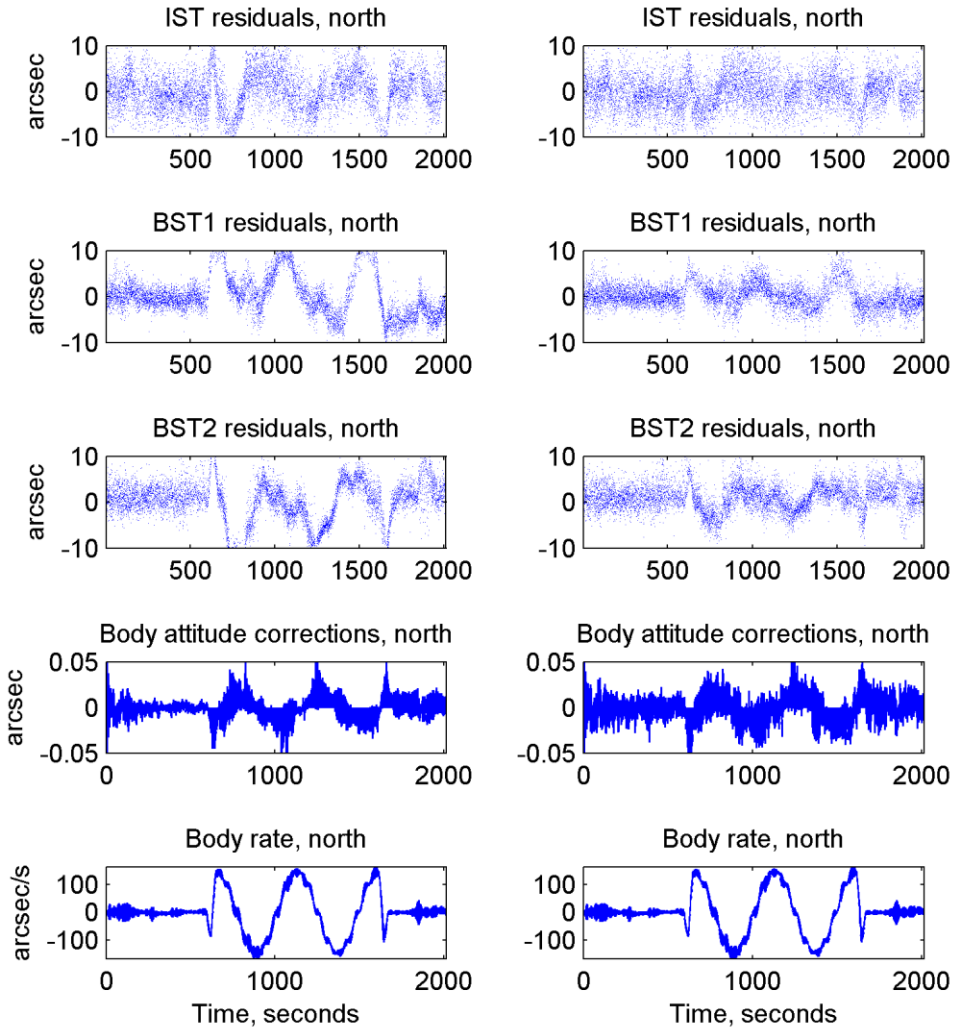

Figure 9. Results for an ocean scan maneuver using the specified angular random walk value (left), and a value three times larger (right).

The gyro measurement model transformed gyro sense-axis rate measurements ω_{gyros} into body frame rates ω_{body}. More sophisticated measurement models correct deterministic errors in the sense-axes measurements using calibration parameters such as scale factor errors and sense-axes misalignments. The measurement model was implemented as the matrix G in Equation (42).[6]

$$\omega_{gyros} + b = G\omega_{body} \tag{42}$$

Here b was a vector of rate biases estimated for each of the gyro sense-axes as part of the filter state. For a gyro unit with n sense-axes, G was a $n \times 3$ matrix. In practice ω_{body} was the unknown computed from ω_{gyros} using Equation (43) where the pseudo-inverse $G^{-1} \equiv \left(G^T G\right)^{-1} G^T$ was used when G was not square.

$$\omega_{body} = G^{-1}\left(\omega_{gyros} + b\right) \tag{43}$$

The simplest gyro measurement model did not include corrections for scale factor errors or sense-axes misalignments. In this special case G only represented geometric information. The ideal geometry matrix W was the only description of the gyro unit needed and $G = W^T$. The need for a separate geometry matrix W becomes apparent below in more sophisticated measurement models. For ICESat the W matrix defined the nominal directions of the four sense-axes A, B, C, D in the gyro frame. The sense-axes were associated with four hemispherical resonator gyros arranged with three forming an orthogonal triad and the fourth along the central axis. Each sense-axis direction was represented by a unit vector in the W matrix. For the simple case with no scale factor errors or sense-axis misalignments, the ICESat gyro measurement model was given by Equations (44) to (46).[42, 45, 113]

$$G = W^T = \begin{bmatrix} 0 & \sqrt{2/4} & -\sqrt{2/4} & 0 \\ -\sqrt{2/3} & \sqrt{2/12} & \sqrt{2/12} & 0 \\ -\sqrt{1/3} & -\sqrt{1/3} & -\sqrt{1/3} & 1 \end{bmatrix}^T \tag{44}$$

$$\omega_{gyros} + b = G\omega_{body} = W^T \omega_{body} \tag{45}$$

$$\omega_{body} = \left(G^T G\right)^{-1} G^T \left(\omega_{gyros} + b\right) = \left(WW^T\right)^{-1} W \left(\omega_{gyros} + b\right) \tag{46}$$

Sense-axis D was never active so in practice the gyro measurement model for the simple case was Equations (47) to (49). For the three axes *A*, *B*, and *C* of the orthogonal triad $\left(W^T\right)^{-1} = W$.

$$G = W^T = \begin{bmatrix} 0 & \sqrt{2/4} & -\sqrt{2/4} \\ -\sqrt{2/3} & \sqrt{2/12} & \sqrt{2/12} \\ -\sqrt{1/3} & -\sqrt{1/3} & -\sqrt{1/3} \end{bmatrix}^T \tag{47}$$

$$\omega_{gyros} + b = G\omega_{body} = W^T \omega_{body} \tag{48}$$

$$\omega_{body} = G^{-1}\left(\omega_{gyros} + b\right) = \left(W^T\right)^{-1}\left(\omega_{gyros} + b\right) = W\left(\omega_{gyros} + b\right) \tag{49}$$

The measurement model implemented in the filter was Equation (50). It included calibration parameters for symmetric scale factor errors Λ, asymmetric scale factor errors M, and sense-axes misalignments Δ_u, Δ_v.[6] If all calibration parameters were equal to zero then Equation (50) reduced to the simple model $G = W^T$ of Equation (45).

$$G = \left(I - \Lambda - M\right)\left(W - U\Delta_v - V\Delta_u\right)^T \tag{50}$$

$$\omega_{gyros} + b = G\omega_{body} \tag{51}$$

$$\omega_{body} = \left(G^T G\right)^{-1} G^T \left(\omega_{gyros} + b\right) \tag{52}$$

W, U, V were geometry matrices defining the ideal sense-axes geometry relative to the gyro unit reference frame. They defined orthogonal coordinate frames with *w*, *u*, and *v* unit vectors at each of the gyro sense-axes. The W matrix was the same as in Equation (44) and defined the directions of the sense-axes. The U and V matrices defined the other two orthogonal unit vectors for each sense-axis. The essentially arbitrary U and V matrices were computed using matrix decomposition methods.[42, 45]

The symmetric scale factor matrix Λ and asymmetric scale factor matrix M were defined by Equations (53) and (54).[42] λ_i and m_i were vectors of scale factor parameters, one for each gyro sense-axis. These parameters were dimensionless real numbers within the filter, but for input and output were converted to units of parts per million ($ppm = 10^{-6}$).

$$\Lambda = diag\left(\lambda_i\right) \tag{53}$$

$$M = diag\left(sign\left(\omega_{gyro}\right) m_i\right) \tag{54}$$

The Δ_u, Δ_v sense-axes misalignment matrices were defined by equations (55) and (56). Within the filter u_i and v_i were vectors of angles with units of radians and were converted to arcseconds for input and output.

$$\Delta_u = diag\left(u_i\right) \tag{55}$$

$$\Delta_v = diag\left(v_i\right) \tag{56}$$

The rate biases for the sense-axes b were filter states. This left four calibration parameters per sense-axis λ, m, u, v. When the body rate vector was constant, effects on the filter due to these four parameters were gradually absorbed by the rate bias b.[42] This was clear in practice as the filter had no difficulty maintaining small zero-mean residuals and small state corrections when the rates were nearly constant.

When the rates spiked due to vibrations or maneuvers the full gyro measurement model and the λ, m, u, v parameters became significant. Figure 10 compares the filter results using the simple (left) and full (right) gyro measurement models during the same time period as in Figure 9. The bottom row of Figure 10 shows the angular rates and the attitude maneuver. The top three rows show the filter residuals from three of the ICESat star trackers. The fourth row shows the attitude estimate changes. The simple gyro measurement model resulted in larger residuals and larger attitude corrections. The full gyro measurement model simultaneously reduced the residuals and attitude corrections.

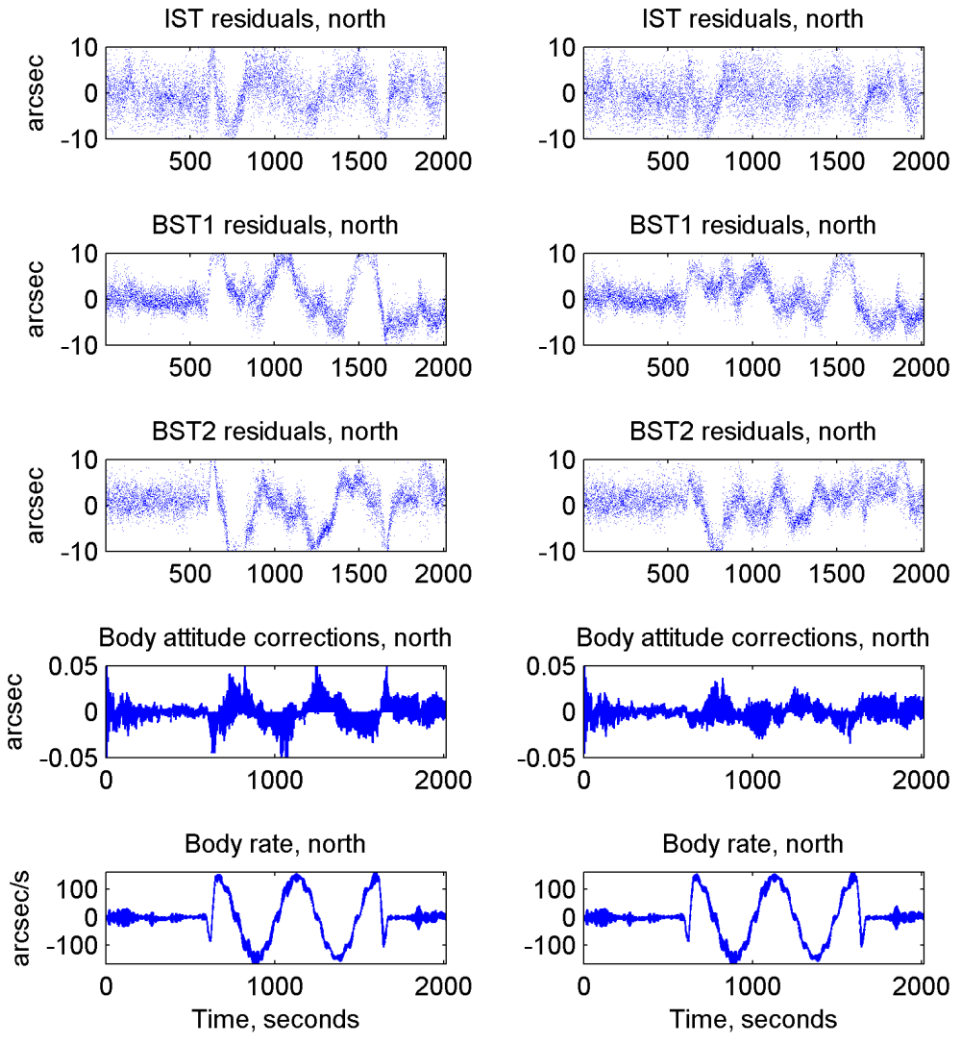

Figure 10. Results for an ocean scan maneuver using the simple (left) and full (right) gyro measurement models.

Table 7 shows the gyro calibration parameter estimates used for the full model results on the right side of Figure 10.

Table 7. Gyro calibration parameter estimates used in the full gyro measurement model.

Sense-axis	λ, *ppm*	*m, ppm*	*u, arcsec*	*v, arcsec*
Sense-axis A	-366	361	6	-51
Sense-axis B	-1696	14	-49	-14
Sense-axis C	1547	-147	-2	-31

The parameters in Table 7 were estimated using a gyro calibration maneuver performed on May 7, 2010. Two other calibration maneuvers were performed on February 25, 2003 and July 1, 2008.

c. Star Tracker Alignment Process Noise

The discrete-time process noise matrix Q_k for $t = t_{k+1} - t_k$ was composed of MEKF and star tracker alignment blocks

$$Q_k = \begin{bmatrix} Q_{MEKF} & 0 \\ 0 & Q_{align} \end{bmatrix} \tag{57}$$

where

$$Q_{MEKF} = \begin{bmatrix} (t\sigma_{arw}^2 + t^3\sigma_{rrw}^2/3)I_{3\times3} & (t^2\sigma_{rrw}^2/2)I_{3\times3} \\ (t^2\sigma_{rrw}^2/2)I_{3\times3} & t\sigma_{rrw}^2 I_{3\times3} \end{bmatrix} \tag{58}$$

$$Q_{align} = \begin{bmatrix} t\sigma_{align,1}^2 I_{3\times3} & 0 & 0 & 0 \\ 0 & t\sigma_{align,2}^2 I_{3\times3} & 0 & 0 \\ 0 & 0 & t\sigma_{align,3}^2 I_{3\times3} & 0 \\ 0 & 0 & 0 & t\sigma_{align,4}^2 I_{3\times3} \end{bmatrix} \tag{59}$$

The alignment process noise values σ_{align} are the subject of this section.

The objective was to use hypothesis testing to select the most correct star tracker alignment process noise value σ_{align} from a set of possible values. Each value was associated with a hypothesis and filter. To choose between seven process noise values, seven filters were run in a parallel filter bank. Hypothesis testing to select the most correct value involved determining which of the seven filters was most consistent.

The filters were evaluated using measurements generated by a simulation where the truth was known and could be compared with the filter results. The simulation represented a star tracker as a rotation A_i^t from the inertial frame to the tracker frame

$$A_i^t = A_{t0}^t(x)A_i^{t0} \tag{60}$$

where A_i^{t0} was the nominal attitude, and A_{t0}^t was a small alignment rotation relative to the nominal attitude. The nominal attitude A_i^{t0} was given as an input and varied with the ICESat orbital rate of 223 arcseconds per second resulting in realistic motion of the stars through the tracker field of view. The alignment rotation A_{t0}^t was a function of the simulation state x. It was equivalent to a three-component rotation vector $x = [x_1 \quad x_2 \quad x_3]^T$ where x_j was a small rotation about the *j*th axis of the nominal tracker frame and the third axis was associated with the tracker optical axis. When simulated measurements were used as input to a filter, x was the true state for comparison with the estimated state $\hat{x}$.

The simulation represented the orbital variation of x as a sinusoid with amplitude a

$$x = [a\sin(2\pi t / t_p + \theta_0) \quad 0 \quad 0]^T \tag{61}$$

where t_p was the ICESat orbital period and θ_0 was a random initial phase. Two simulation cases were considered, with a equal to two arcseconds and ten arcseconds. These two cases were representative of the orbital variations of the trackers mounted on the spacecraft bus and GLAS respectively. Simulated measurements of star unit vectors y were generated from star catalog unit vectors y'

$$y = A_i^t y' \tag{62}$$

Simulated zero-mean Gaussian measurement noise was applied to the y vectors.

For filtering, the discrete-time state x was modeled as a function of zero-mean Gaussian noise w

$$x_{k+1} = x_k + w_k \tag{63}$$

$$E\{w_k w_j^T\} = Q_k \delta_{jk} \tag{64}$$

where the process noise matrix Q_k was a function of the alignment process noise value σ_{align}

$$Q_k = (t_{k+1} - t_k)\sigma_{align}^2 I \tag{65}$$

During filter propagation the state estimate $\hat{x}$ was constant. If $\hat{x}_k^+$ and P_k^+ were the state estimate and covariance after update at time t_k, then after propagation to t_{k+1} and before update they were

$$\hat{x}_{k+1}^- = \hat{x}_k^+ \tag{66}$$

$$P_{k+1}^- = P_k^+ + Q_k \tag{67}$$

The measurement model h for a star unit vector in the tracker frame was

$$h = A(\delta x)A_i^t(x)y' = A(\delta x)\bar{h} \tag{68}$$

where δx was a small rotation vector perturbing the state, y' was a star catalog unit vector in the inertial frame, and $\bar{h} = A_i^t(x)y'$ was the vector in the tracker frame predicted by the state. To first-order $A(\delta x) = I - [\delta x \times]$,[10] so

$$\begin{aligned} h &= (I - [\delta x \times])\bar{h} \\ &= \bar{h} + [\bar{h} \times]\delta x \end{aligned} \tag{69}$$

and the measurement sensitivity matrix H was

$$H = \frac{\partial h}{\partial \delta x} = [\bar{h}\times] = [A_i^t(x)y'\times] \tag{70}$$

Measurement uncertainty was modeled as zero-mean Gaussian noise v

$$E\{v_{k+1}v_j^T\} = R_{k+1}\delta_{jk+1} \tag{71}$$

where the measurement noise covariance matrix R_{k+1} was a function of the noise σ_{star} for a particular star

$$R_{k+1} = \sigma_{star}^2 I \tag{72}$$

For the filter update at time t_{k+1} the Kalman gain was

$$K = P_{k+1}^- H^T (HP_{k+1}^- H^T + R_{k+1})^{-1} \tag{73}$$

and the state estimate and covariance after update were

$$\hat{x}_{k+1}^+ = \hat{x}_{k+1}^- + K(y - A_i^t(\hat{x}_{k+1}^-)y') \tag{74}$$

$$P_{k+1}^+ = (I - KH)P_{k+1}^- \tag{75}$$

The initial state estimate and covariance were $\hat{x}_0 = [x \quad 0 \quad 0]^T$ and $P_0 = (1\text{ arcsecond})^2 I$.

A hypothesis test for the consistency of an individual filter was based on the normalized estimation error squared ε

$$\varepsilon_k = (x_k - \hat{x}_k)^T P_k^{-1}(x_k - \hat{x}_k) \tag{76}$$

If the filter was consistent, ε had a chi-squared distribution with three degrees of freedom. For N simulations, if the filter was consistent then

$$N\bar{\varepsilon}_k = \sum_{j=1}^{N} \varepsilon_{k,j} \tag{77}$$

had a chi-squared distribution with $3N$ degrees of freedom. If $N\bar{\varepsilon}_k$ was within the bounds $N\bar{\varepsilon}_{k,lower} = F^{-1}(p = 0.005 | 3N)$ and $N\bar{\varepsilon}_{k,upper} = F^{-1}(p = 0.995 | 3N)$ where F^{-1}

was the inverse of the chi-squared cumulative distribution function, then there was not sufficient evidence to reject the null hypothesis that the filter was consistent.

To select the most correct alignment process noise value σ_{align} from a set of seven possible values, each value was associated with a hypothesis and filter $H_1, H_2, \ldots, H_7$. The seven filters were run in parallel and the measurement probabilities $p(y_k \mid H_i)$ for each filter were a measure of consistency

$$p(y_k \mid H_i) = (1/((2\pi)^{3/2} \mid S \mid^{1/2})) \exp\{(-1/2) r_k^T S^{-1} r_k\} \tag{78}$$

where $r_k = y_k - A_i^t(\hat{x}_k^-)y'$ and $S = HP_k^- H^T + R_k$. At the beginning of a simulation run each of the seven hypotheses was assigned the same probability $p_0(H_i) = 1/7$ of being correct. The hypothesis probabilities were reevaluated at each measurement update.[114]

$$p_k(H_i) = \frac{p(y_k \mid H_i)\, p_{k-1}(H_i)}{\sum_{j=1}^{7} p(y_k \mid H_j)\, p_{k-1}(H_j)} \tag{79}$$

If a hypothesis probability $p_k(H_i)$ approached one as t_k increased, it was evidence that the associated hypothesis H_i was more consistent than the others, and that the associated alignment process noise value σ_{align} was the most correct.

Two cases were considered, with simulated alignment variation amplitudes of two and ten arcseconds. Results for the case with an amplitude of two arcseconds are shown in Table 8 and Figure 11, results for the case with an amplitude of ten arcseconds are shown in Table 9 and Figure 12. In both cases, seven hypotheses $H_1, H_2, \ldots, H_7$ were tested. The alignment process noise values σ_{align} associated with the seven hypotheses H_i are shown in the second columns of Table 8 and Table 9.

Ten simulation runs were performed for each case, resulting in the bounds $N\bar{\varepsilon}_{k,lower} = 13.8$ and $N\bar{\varepsilon}_{k,upper} = 53.7$ for the hypothesis test of an individual filter's consistency. The third columns of Table 8 and Table 9 contain the mean values of $N\bar{\varepsilon}_k$ where there were n measurement updates $t_k = t_1, t_2, \ldots, t_n$.

$$mean(N\bar{\varepsilon}_k) = \frac{1}{n}\sum_{k=1}^{n} N\bar{\varepsilon}_k \tag{80}$$

For all but two hypotheses, $mean(N\bar{\varepsilon}_k)$ was within the bounds. The exceptions were H_1 and H_2 for the case with an amplitude of two arcseconds (Table 8). These two hypotheses were the smallest σ_{align} values that were tested.

The final hypothesis probabilities $p_{final}(H_i)$ were used to select the most correct hypothesis. The fourth columns of Table 8 and Table 9 contain the mean values of $p_{final}(H_i)$

$$mean(p_{final}(H_i)) = \frac{1}{10}\sum_{sim=1}^{10} p_{final,sim}(H_i) \tag{81}$$

Figure 11 and Figure 12 show the time series $p_{k,sim}$ for the ten simulations in blue, and the mean time series

$$mean(p_k(H_i)) = \frac{1}{10}\sum_{sim=1}^{10} p_{k,sim}(H_i) \tag{82}$$

in red. For the case with an amplitude of two arcseconds, $mean(p_{final}(H_4)) = 1$ so H_4 with $\sigma_{align} = 0.01$ arcseconds/seconds$^{1/2}$ was selected as the most correct hypothesis. For the case with an amplitude of ten arcseconds, $mean(p_{final}(H_4)) = .985$ so H_4 with $\sigma_{align} = 0.032$ arcseconds/seconds$^{1/2}$ was selected.

Table 8. Hypothesis testing results for ten simulations with alignment variation amplitude $a = 2$ arcseconds.

Hypothesis H_i	σ_{align}, arcseconds/seconds$^{1/2}$	$mean(N\bar{\varepsilon}_k)$	$mean(p_{final}(H_i))$
H_1	.002	91.0	2.6E-59
H_2	.005	54.5	1.9E-29
H_3	.007	31.9	7.2E-9
H_4	.01	20.3	1
H_5	.015	16.8	3.7E-6
H_6	.02	15.9	7.5E-15
H_7	.025	15.7	1.1E-29

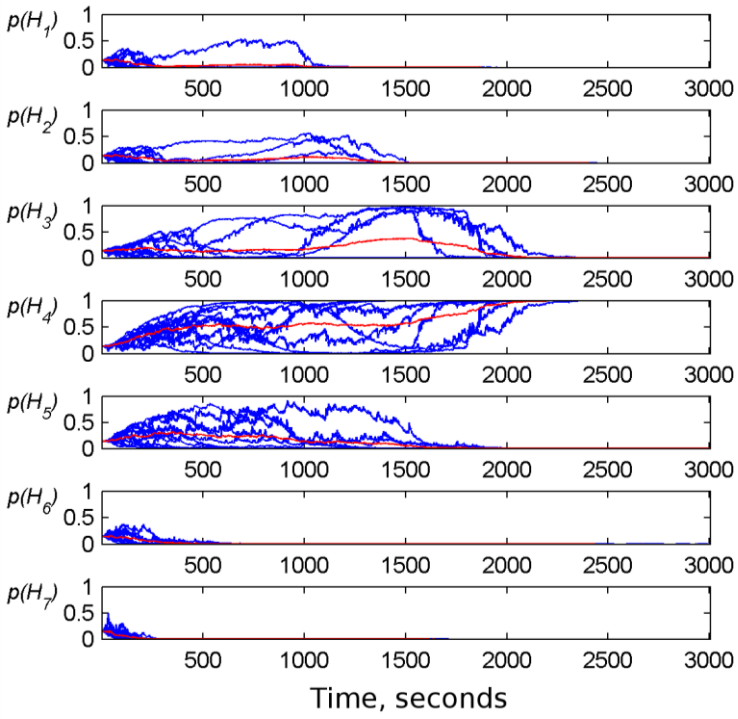

Figure 11. Hypothesis probabilities $p(H_i)$ for ten simulations with alignment variation amplitude $a = 2$ arcseconds. $mean(p_k(H_i))$ is shown in red.

Table 9. Hypothesis testing results for ten simulations with alignment variation amplitude $a = 10$ arcseconds.

Hypothesis H_i	σ_{align}, arcseconds/seconds$^{1/2}$	$mean(N\bar{\varepsilon}_k)$	$mean(p_{final}(H_i))$
H_1	.017	48.8	5.7E-53
H_2	.022	31.6	3.2E-16
H_3	.027	24.6	0.001
H_4	.032	21.2	0.985
H_5	.037	19.3	0.014
H_6	.042	18.2	1.6E-7
H_7	.047	17.5	2.2E-14

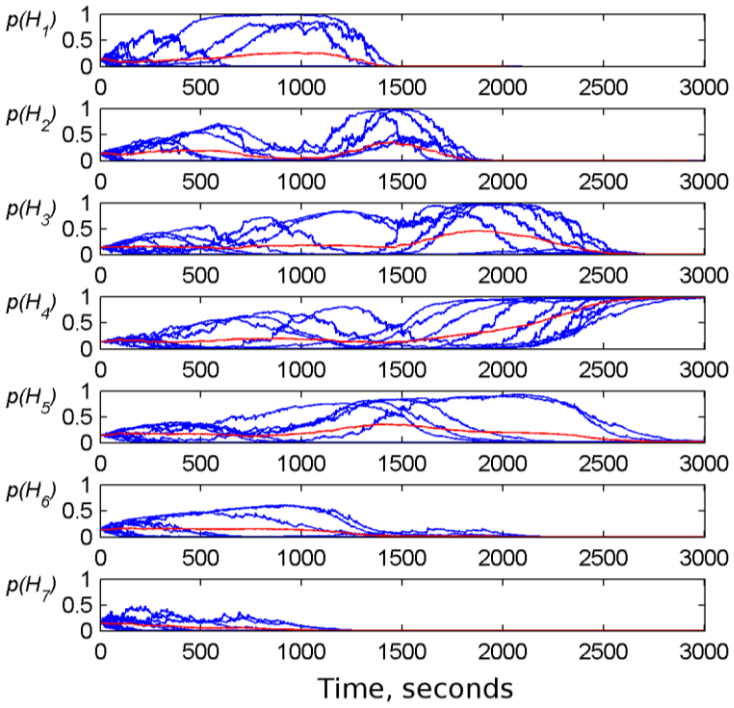

Figure 12. Hypothesis probabilities $p(H_i)$ for ten simulations with alignment variation amplitude $a = 10$ arcseconds. $mean(p_k(H_i))$ is shown in red.

The σ_{align} values used to produce the results in chapter VI were 0.01 arcseconds/seconds$^{1/2}$ for the IST and 0.002 arcseconds/seconds$^{1/2}$ for BST2. The second value has been used for other missions and simulations and was treated as the default.[7, 41, 42, 44, 49] When the ICESat alignment filter became operational, trends in the IST residuals over orbital time periods showed that the IST alignment variations were large. The estimated IST alignment was not tracking the true IST alignment. The IST value of 0.01 arcseconds/seconds$^{1/2}$ was arrived at by increasing from the default until the IST residuals were consistently zero-mean Gaussian.

The hypothesis testing described in this section was performed later. It provided evidence for larger σ_{align} values of 0.032 arcseconds/seconds$^{1/2}$ for the IST and 0.01 arcseconds/seconds$^{1/2}$ for BST2. Figure 13 and Figure 14 show the estimated alignment variations for the IST and BST2 during a typical orbit using the two sets of values. Figure 13 shows the results when using the smaller values and is representative of the chapter IV results. Figure 14 shows the results for the same orbit but using the larger values. Qualitatively the results are similar. The larger values introduce more high-frequency variation in the estimates, but this may effectively be noise. Further work on hypothesis testing of σ_{align} values and its operational significance for ICESat-2 is called for.

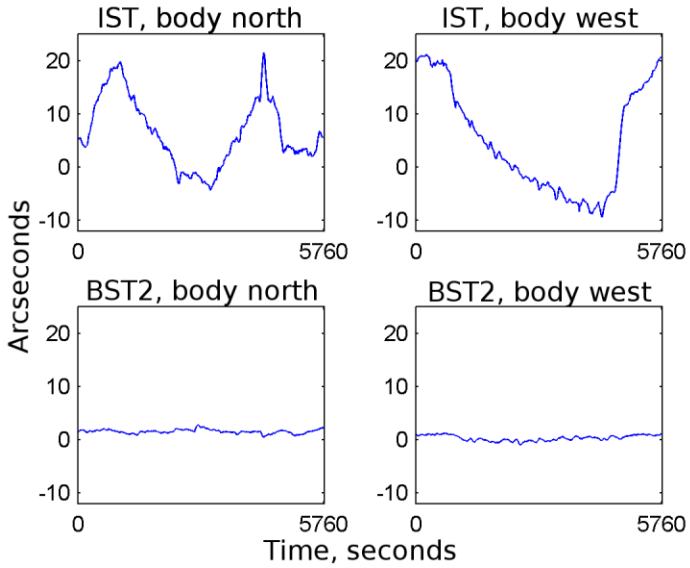

Figure 13. IST and BST2 alignment results for one orbit and the σ_{align} values 0.01 and 0.002 arcseconds/seconds$^{1/2}$.

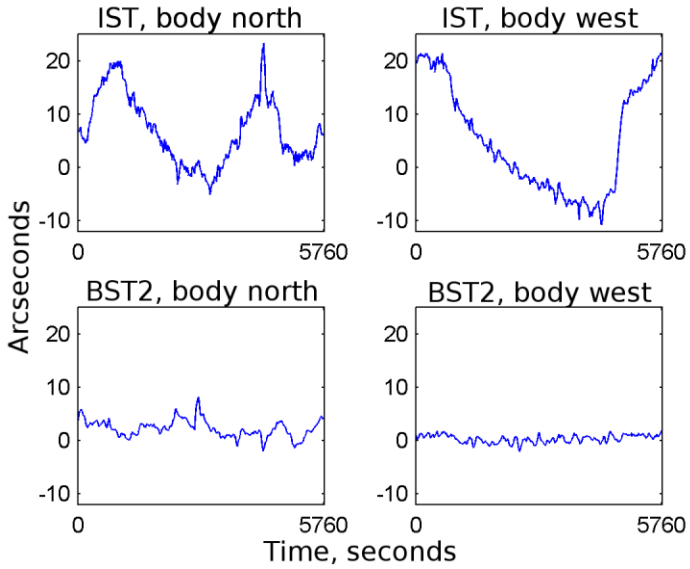

Figure 14. IST and BST2 alignment results for one orbit and the σ_{align} values from hypothesis testing, 0.032 and 0.01 arcseconds/seconds$^{1/2}$.

d. Star Measurement Update

Each measurement update phase corresponded to a tracker output record containing from one to six measured unit vectors u expressed in the tracker coordinate frame, defined with the z axis along the tracker optical axis and the x and y axes in the image plane.

$$u = \begin{bmatrix} u_1 & u_2 & u_3 \end{bmatrix}^T = \begin{bmatrix} x & y & z \end{bmatrix}^T \Big/ \left(x^2 + y^2 + z^2 \right)^{1/2} \tag{83}$$

The tracker attitude $\hat{A}_i^j = \hat{A}_{jref}^j R_b^{jref} \hat{A}_i^b$ was the orientation of this frame with respect to the celestial frame. Scaled tangent h and v coordinates were also used to represent the measured unit vectors. A hardware dependent definition of h and v uses the tracker focal length f and the x and y position of the star image in the image plane.

$$k = 648000 / \pi \ \left[arcseconds / radian \right] \tag{84}$$

$$h = k\left(x / f \right) = k \tan \Theta_h \tag{85}$$

$$v = k\left(y / f \right) = k \tan \Theta_v \tag{86}$$

An equivalent definition of h and v is hardware independent, replacing the hardware dependent parameters with similar triangles and the components of the unit vector representation.

$$h = k\left(u_1 / u_3 \right) \tag{87}$$

$$v = k\left(u_2 / u_3 \right) \tag{88}$$

An angular representation Θ_h and Θ_v was used as the output format of the Ball CT-602 star trackers.

$$\Theta_h = \tan^{-1}\left(u_1 / u_3 \right) = \tan^{-1}\left(h / k \right) \tag{89}$$

$$\Theta_v = \tan^{-1}\left(u_2 / u_3 \right) = \tan^{-1}\left(v / k \right) \tag{90}$$

The unit vector representation had a simple expression in terms of h and v coordinates, as shown in Equation (91). In effect, an intermediate vector whose third component was defined equal to one was calculated and then normalized. This was equivalent to setting u_3 equal to one in Equations (87) and (88) leaving two equations for u_1 and u_2 and then normalizing.

$$u = \begin{bmatrix} h/k & v/k & 1 \end{bmatrix}^T \Big/ \left((h/k)^2 + (v/k)^2 + 1 \right)^{1/2} \tag{91}$$

Tracker errors were classified as distortion, centroiding error, and noise.[115] Distortion errors and corrections were estimated using functions of position in the tracker frame. The functions were fitted to the filter residuals for large numbers of star measurements using least-squares and third-order polynomials.[116] Distortion correction is described as part of the star results in Chapter V. Centroiding error covers variations on the scale of the image pixels. For the ICESat trackers this was a 3 to 4 Hz zero-mean variation with an amplitude of about an arcsecond, as shown in Chapter V, and was not explicitly corrected. Noise estimation was based on the measured variations of the angular separations between pairs of stars.[66] It is described with the star results in Chapter V. Within the filter, noise estimation using fit curves like those shown in Figure 24 was not the only option. Adaptive noise estimation with an iterative implementation of the triangle method was also used. The primary advantage of the triangle method is that it is independent of the attitude estimate. The attitude does not appear in the equations, only unit vectors in the tracker frame are needed. Another advantage is that it is independent of star identification. Reference unit vectors from a star catalog do not appear in the equations. Another method for estimating noise was termed the residuals method and was based on analyzing high frequency variations of the filter residuals for individual stars. The residuals method is dependent on the attitude estimate. If the attitude estimate contained high frequency errors they would appear directly in the variations of the filter residuals. In an alignment filter, high frequency alignment estimate variations would also appear in the filter residuals. The overall uncertainty σ of a measured unit vector u was

used to form the measurement noise covariance $R = \sigma^2 I$. In practice σ was a noise value estimated using one of the methods described above.

A star tracker measurement was composed of a unit vector u expressed in the tracker frame and an instrument magnitude m. To use a measurement, there must be a positive identification of u with a star catalog unit vector u' expressed in the inertial frame. Many problem measurements were detected and flagged during identification. Both predicted position $\hat{A}^j_{jref} R^{jref}_b \hat{A}^b_i u'$ and predicted instrument magnitude m' were compared with the measurement u and m. Instrument magnitude predictions were based on empirical values from flight data when they were available in the reduced instrument magnitude results for RXTE and ICESat, otherwise they were based on astronomical passband magnitudes and spectral type. If the measured minus predicted instrument magnitude residual and the position innovation were less than tracker dependent criteria, a positive identification was made.

The attitude estimate $\hat{A}^b_i$, tracker alignment estimate $\hat{A}^j_{jref}$, reference alignment R^{jref}_b, and star catalog unit vector u' were used to calculate predicted unit vectors $\hat{A}^j_{jref} R^{jref}_b \hat{A}^b_i u'$ and form measured minus predicted innovations $\tilde{y} = u - \hat{A}^j_{jref} R^{jref}_b \hat{A}^b_i u'$. The innovations were used to accept or reject u for use as a measurement update. The criterion for acceptance was adaptive. If the tracker alignment estimate had not been updated recently the criterion was progressively increased up to a tracker dependent upper-limit. This allowed updates to begin at the start of a filter run or after the tracker has been blinded. In these cases the tracker alignment estimate $\hat{A}^j_{jref}$ and the resulting prediction $\hat{A}^j_{jref} R^{jref}_b \hat{A}^b_i u'$ could be poor. If the tracker alignment estimate had been updated consistently and recently, the criterion for acceptance was progressively decreased down to a tracker dependent lower-limit to reject stars with position measurement biases.

In practice the two bus trackers, the IST, and the LRS had different characteristics and criteria. Two of the most important characteristics were the amount of alignment variation, and the method used to acquire new stars. The two bus trackers had stable

alignments and acquired selected stars using an onboard catalog. The IST and LRS had large alignment variations and acquired any detectable objects. The LRS tracked one object at a time and was blinded during half of each orbit.

Equation (92) was the vector measurement model h for a unit vector u measured in the tracker j frame.[10]

$$h(u) = h(\hat{A}^{j}_{jref} R^{jref}_{b} \hat{A}^{b}_{i} u') + H_{\phi}\tilde{a}_{\phi} + H_{j}\tilde{a}_{j} \tag{92}$$

where

$$H_{\phi} = \hat{A}^{j}_{jref} R^{jref}_{b} [\hat{A}^{b}_{i} u' \times] \tag{93}$$

$$H_{j} = [\hat{A}^{j}_{jref} R^{jref}_{b} \hat{A}^{b}_{i} u' \times] \tag{94}$$

and

$$[x\times] \equiv \begin{bmatrix} 0 & x_3 & -x_2 \\ -x_3 & 0 & x_1 \\ x_2 & -x_1 & 0 \end{bmatrix} \tag{95}$$

The measurement sensitivity matrix was

$$H = \begin{bmatrix} \frac{\partial h}{\partial \tilde{a}_{\phi}} & \frac{\partial h}{\partial \tilde{b}} & \frac{\partial h}{\partial \tilde{a}_1} & \frac{\partial h}{\partial \tilde{a}_2} & \frac{\partial h}{\partial \tilde{a}_3} & \frac{\partial h}{\partial \tilde{a}_4} \end{bmatrix} \tag{96}$$

and because the measurement did not depend on the gyro bias or the alignments of the other trackers, only

$$\frac{\partial h}{\partial \tilde{a}_{\phi}} = H_{\phi} \tag{97}$$

and

$$\frac{\partial h}{\partial \tilde{a}_{j}} = H_{j} \tag{98}$$

were non-zero.

The error estimate $\tilde{x}$ was an eighteen component vector consisting of the attitude error estimate $\tilde{a}_\phi$, gyro bias error estimate $\tilde{b}$, and tracker alignment error estimate $\tilde{a}_j$.

$$\tilde{x} \equiv E\left(x - \hat{x} \mid y\right) \equiv \left[\begin{array}{cccccc} \tilde{a}_\phi^T & \tilde{b}^T & \tilde{a}_1^T & \tilde{a}_2^T & \tilde{a}_3^T & \tilde{a}_4^T \end{array}\right]^T \tag{99}$$

$$P = E\{(\tilde{x} - E\{\tilde{x}\})(\tilde{x} - E\{\tilde{x}\})^T\} \tag{100}$$

The measured minus predicted innovations $\tilde{y} = u - \hat{A}_{jref}^{j} R_b^{jref} \hat{A}_i^b u'$ were used to calculate $\tilde{x}$ and P_+ using the standard Kalman update equations.

$$K = P_- H^T \left(HP_- H^T + R\right)^{-1} \tag{101}$$

$$\tilde{x} = K(u - \hat{A}_{jref}^{j} R_b^{jref} \hat{A}_i^b u') \tag{102}$$

$$P_+ = \left(I - KH\right) P_- \tag{103}$$

The attitude estimate, gyro bias estimate, and tracker alignment estimate were then updated.

$$\hat{A}_{i+}^b = A(\tilde{a}_\phi)\hat{A}_{i-}^b \tag{104}$$

$$\hat{b}_+ = \hat{b}_- + \tilde{b} \tag{105}$$

$$\hat{a}_{j+} = \hat{a}_{j-} + \tilde{a}_j \tag{106}$$

e. Output and Star Pass Residuals

Output took place immediately after each update phase. There were two types of filter output: state results, and star results. The state results included information that in some ways duplicated information in the star results, but there were significant differences. The information in the state results focused strictly on the innovations used to update the state, and they were sub-sampled because the quantities of interest were the tracker alignments, which varied on orbital time scales of hundreds and thousands of seconds.

The characteristic filter time scale was tenths of seconds. Sub-sampling by approximately a factor of ten provided good resolution for investigating the alignments, and significant performance and resource advantages. The star results included information on both position and brightness measurements for every star measurement without sub-sampling and regardless of whether they were used to update the filter state or rejected. They contained less information per record, but many more records than the sub-sampled state results. The sizes of the state and stars results for a granule were 11 MB and 25 MB respectively, reflecting the difference in output bandwidth.

Filter residuals were used to evaluate the tracker pointing vectors and the individual alignment and attitude states. Residuals with a zero mean and small variation were evidence that the tracker pointing vectors were accurate. This was equivalent to evidence that the combination of the filter alignment and attitude states was accurate, but not that particular alignment states alone or the attitude state alone were accurate, because the attitude state could have errors that were counteracted by errors in the alignment states.

The residuals did provide information about specific errors. For the systematic component of the time-series of residuals of normal stars (the deterministic component as opposed to the stochastic noise component), biases away from zero were related to systematic errors in the filter alignment and attitude states. For example, if the residuals for the IST were biased while the residuals of BST1, BST2, and the LRS were zero, then the IST residual bias equaled the IST tracker frame alignment error. Similarly, if the residuals for all four trackers were biased identically, then the bias equaled the attitude error for the body frame.

A method was developed to sample and statistically reduce the time-series of residuals based on the passes of individual stars across a tracker field of view. These samples were termed passes and were treated as the fundamental unit of organization in the residuals. Every residual had three tags: a time tag, a star identifier tag, and a tag designating one of the four trackers. The practical definition of a pass was a set of residuals with the same

star identifier and tracker tags, and time tags nearby in time. Generally a pass sample consisted of several hundred residuals, all with similar characteristics that were suitable for reduction to a set of descriptive statistics. These reduced pass statistics were the basis for interpretation of the filter output.

Several representations were used for the residuals. The simplest was radial separations between measured and predicted star vectors. Another defined the predicted unit vector as the z axis of a coordinate frame and then expressed the measured unit vector using two-component scaled tangents. An advantage of scaled tangents was that the x and y axes could be defined locally parallel to other reference frames and emphasize physically significant information. In a tracker, h and v coordinates were used to represent the residuals relative to the tracker image plane. In the body frame, body north and body west coordinates were used to represent the residuals relative to the body and the spacecraft roll and pitch axes. In the celestial frame, right ascension and declination were used to represent the residuals relative to the celestial sphere.

As an example, consider the case where the residuals for one of the trackers were biased while the residuals of the other trackers were nearly zero, so that the bias equaled the tracker frame alignment error. Expressed using scaled tangents oriented to the tracker frame, the two components of the residuals gave the h and v error of the predicted star vectors on the tracker image plane. Expressed using scaled tangents oriented to the body frame, the two components of the residuals gave the body north and body west error of the predicted star vectors and therefore the tracker frame alignment. Expressed using scaled tangents oriented to the celestial frame, the two components gave the right ascension and declination error of the predicted star vectors and tracker frame alignment. For the alignment results in Chapter VI, the spacecraft was in sailboat attitude mode with body north coordinates equivalent to celestial frame right ascension coordinates, and body west coordinates equivalent to celestial frame declination coordinates. The

discussion here is generally in terms of celestial frame coordinates, but can also be expressed in terms of the body frame.

The filter residuals were differences between measured and predicted star unit vectors and could be represented in a variety of ways: radial separations, various rotation representations, and three or two component vector differences. Figure 15 shows the standard deviations of the filter residuals versus star brightness for each of the four trackers. This is a measure of overall variability or noise including the effects of measurement noise and errors in the filter attitude and alignments states. The attitude and alignment states directly affect both bias (changes of the mean, median, and mode) and noise (variation and standard deviation) in the residuals. The root mean square or quadratic mean is a measure of the overall error including both bias and noise. If the residuals for a star have a mean $\bar{x}$ (bias) and standard deviation σ_x (noise) then x_{rms} is given by Equation (107).[117]

$$x_{rms}^2 = \bar{x}^2 + \sigma_x^2 \tag{107}$$

Figure 15 shows the σ_x terms from Equation (107) for 9,114 stars found in the dataset. The overall structure as a function of star brightness reflects tracker measurement noise. This is clear from a comparison with plots of measurement noise alone (Section Va). The effects of errors in the filter alignment states are also apparent, particularly for the LRS. The primary structure for the LRS is the nearly constant two arcsecond measurement noise, but there is another group of points rising above the measurement noise points. They reflect the fact that the alignment of the LRS was less certain than the alignments of the other trackers due to the sparse LRS measurements. The LRS measured one star at a time in a small field of view, stars were only acquired intermittently, and the LRS was deactivated during the daylight part of each orbit due to problems with glare. The LRS alignments and residuals jumped at the beginning and end of the periods when the LRS was active, at the transitions between the daylight and night parts of the orbit. Stars

measured during these transition periods had larger variations of their residuals, as reflected in Figure 15.

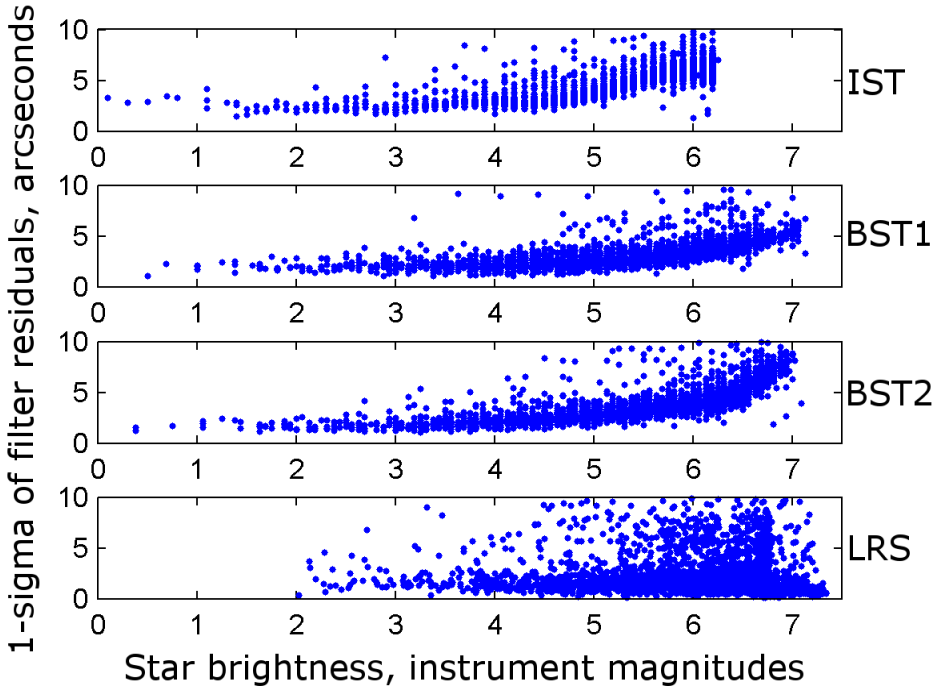

Figure 15. Standard deviations of filter residuals for the four trackers.

Another useful representation of the filter residuals was based on the right ascension and declination coordinate system, so that the residuals reflected the apparent positions of the stars on the sky (apparent to the combination of the trackers and the filter). Celestial frame residuals define a plane tangent to the sky at the catalog position of a star, with linear coordinate axes on the plane locally parallel to right ascension and declination. The stars residuals are expressed using linear coordinates in the tangent plane. The two components, right ascension-like and declination-like, of the residuals for a star near the north pole can be directly compared to the residuals for a star near the equator, while the apparent positions of each star on the sky are also uniquely defined. This is an advantage because true right ascension is highly nonlinear away from the equator (lines of right ascension converge at the poles). Celestial frame residual coordinates are referred to here

as right ascension and declination, but in fact are right ascension-like and declination-like locally linear approximations.

To define the tangent plane axes for a star, a catalog unit vector for the star $u_{catalog}$ and a unit vector pointing to the celestial north pole $u_{north} = \begin{bmatrix} 0 & 0 & 1 \end{bmatrix}^T$ were used. The u_x and u_y axes of the tangent plane were then calculated using vector cross-products as shown in Equations (108) and (109).

$$u_x = u_{north} \times u_{catalog} \tag{108}$$

$$u_y = u_{catalog} \times u_x \tag{109}$$

$$u_z = u_{catalog} \tag{110}$$

Measured unit vectors for the star were then rotated from the tracker frame to the celestial frame using the filter attitude and alignment states and expressed relative to the tangent plane axes. If the measured unit vectors all pointed along the $u_{catalog}$ axis, then the measured minus predicted residuals were zero. The x and y plane was scaled so that at the origin a unit of distance was equivalent to a one arcsecond change in direction of a measured unit vector. If a measured unit vector was $u \equiv \begin{bmatrix} u_1 & u_2 & u_3 \end{bmatrix}^T$ relative to the tangent plane axes, then the corresponding residual components r and d (right ascension-like and declination-like) are given by Equations (112) and (113).

$$k = 648000 / \pi \ \left[arcseconds / radian \right] \tag{111}$$

$$r = k\left(u_1 / u_3\right) \tag{112}$$

$$d = k\left(u_2 / u_3\right) \tag{113}$$

A time-series of celestial residuals for every star measurement from all four trackers was output by the filter. Computationally this type of output is relatively expensive because for every star measurement several operations are required: a frame rotation from the tracker frame to the inertial frame, calculation of the tangent plane axes, and calculation

of the residuals components. No editing was performed on the output. For each measurement the catalog star and resulting tangent plane was simply the nearest star available in the run-time catalog. For example, a dust particle moving with respect to the sky could appear in the time-series of residuals paired with various catalog stars, generating large and quickly changing residuals as it moved past each.

Figure 16 shows an example of tangent plane residuals, in this case for BST1 (2003 campaign 2A, 2003.09.25, GLA04_031 _1102_028_0087 _0_01_000). Several objects are apparent that were moving with respect to the sky. Their celestial residuals are changing with time. The line near 1000 seconds is a good example. Its rapid motion relative to the sky is typical of transient objects such as dust particles, satellites, etc. Several objects have relatively large residuals, near 3500 and 9000 seconds for example. These could be transients that were tracked for short periods, misidentified stars, or stars with position biases due to near-neighbors. Most of the residuals are clustered near zero and that part of Figure 16 is expanded in Figure 17.

Figure 17 shows an expanded view of the residuals near zero in Figure 16. These are generally the residuals for normal stars, not transient objects or stars with position biases. The two primary error sources causing non-zero residuals are measurement noise, and errors in the filter attitude and alignment states. The combined effects of these two error sources are also apparent above in Figure 15, where the effects of variation with time are reduced by averaging. Here it is the variation with time that is of primary interest. An objective was to use the time variations of these residuals to investigate errors in the filter states. For example, near 8000 seconds there was an ocean scan maneuver and the residuals show correlated structure.

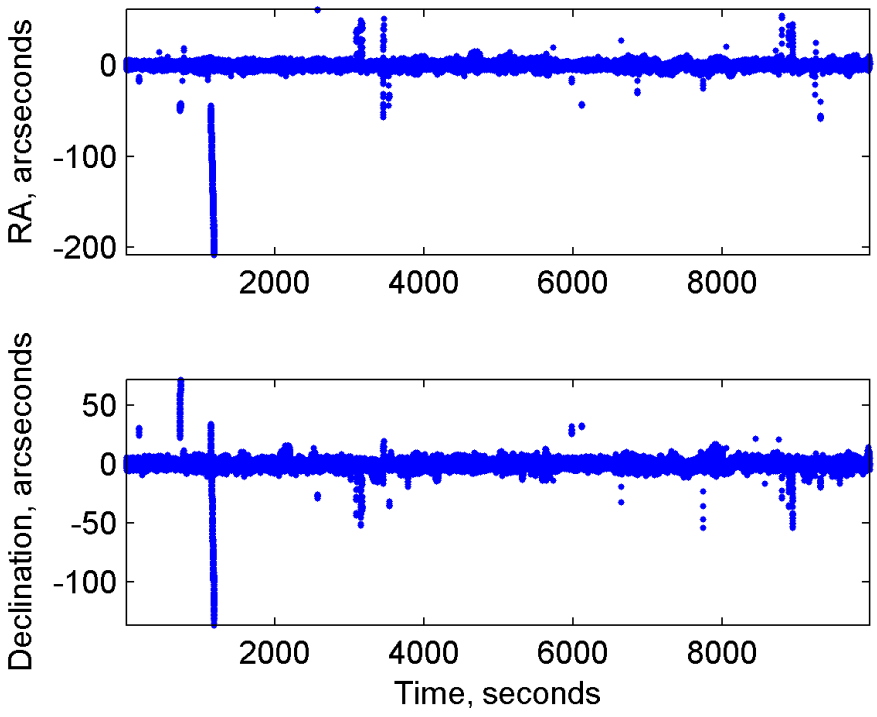

Figure 16. Celestial frame residuals from BST1.

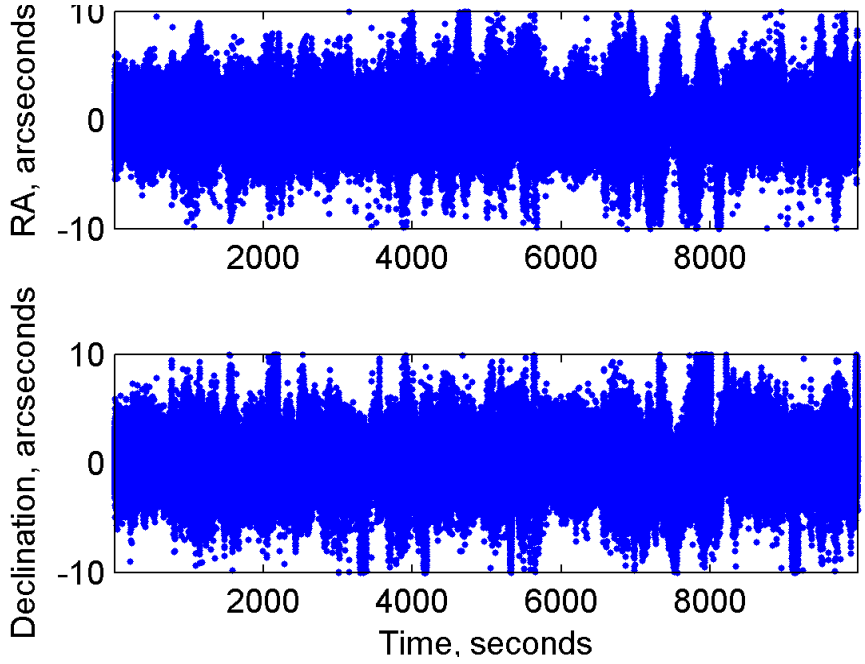

Figure 17. Celestial residuals near zero from Figure 16.

A method was developed to sample and statistically reduce the time-series of residuals based on samples defined by individual stars moving across a tracker field of view. These samples were termed passes and were treated as the fundamental unit of organization in the residuals. Every residual had three tags: a time-tag, a star identifier tag, and a tag designating one of the four trackers. The practical definition of a pass was a set of residuals with the same star identifier and tracker tags, and time-tags nearby in time. The longest pass for the normal orbital rate of 223 arcseconds per second and an 8° field of view was 130 seconds. To allow for maneuvers, nearness in time was defined as a time difference less than 500 seconds. This definition can result in a single physical object being processed as multiple objects if it is moving with respect to the sky. For example, while crossing a tracker field of view a dust particle can move past two stars. In this case the dust particle would receive two star identifiers and therefore be processed as two objects.

The following two figures demonstrate some characteristics of passes for the same granule used in Figure 16 and Figure 17. The first shows a blow-up of a 1000 second sub-interval (4,600 seconds to 5,600 seconds). The second figure shows 10,000 seconds (0 seconds to 10,000 seconds) from the granule. The figures show object declination on the vertical axis and time on the horizontal axis. Each object was assigned a unique declination (from its star identification tag and star catalog record), so all points in a horizontal row are from the same star. The tracker pointing vectors are moving at roughly 223 arcseconds per second in declination, so declinations versus time shows a strong rotational (orbital) signal. The points are color coded by tracker: red for IST, green for BST1, blue for BST2, and black for LRS. A star measured by all four trackers appears as a horizontal row of points with strong clustering in time by tracker. Each cluster is a pass. It is apparent from the color coding that in this case stars were acquired first by BST2, then the IST, LRS, and BST1. In this granule 691 unique star identifiers were used to tag the passes. This means that 691 unique declinations and rows of points are present in the

second figure. Some of these identifiers may have been applied to non-stellar objects, so at most 691 unique stars were measured.

Figure 18 shows passes of approximately thirty stars between declinations 0 degrees and 25 degrees as they move through the tracker fields of view over a period of about 1000 seconds. For example the star at the top of the figure, near declination 25 degrees, makes a BST2 pass at about 4800 seconds, an IST pass at about 5300 seconds, and a BST1 pass at about 5800 seconds. The LRS passes (color coded black) are much shorter because of the small LRS field of view.

Figure 19 shows passes of all 691 objects through the four tracker fields of view over a period of 10,000 seconds. Almost two orbital revolutions are apparent as the star declinations oscillate twice between +90 and -90 degrees declination. Between 7000 and 8000 seconds the effects of an ocean scan maneuver are apparent as slight variations from the dominant structure. The daylight sides of the orbits, when the LRS was deactivated, have no LRS passes.

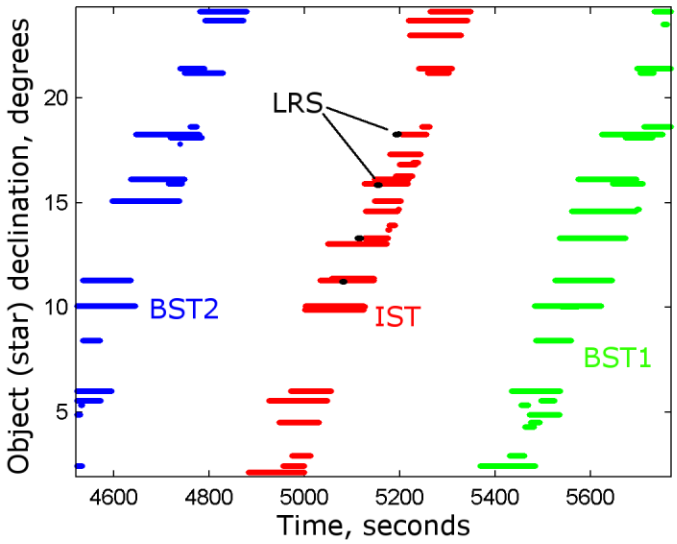

Figure 18. Passes of stars measured moving through the four tracker fields of view during roughly 1000 seconds.

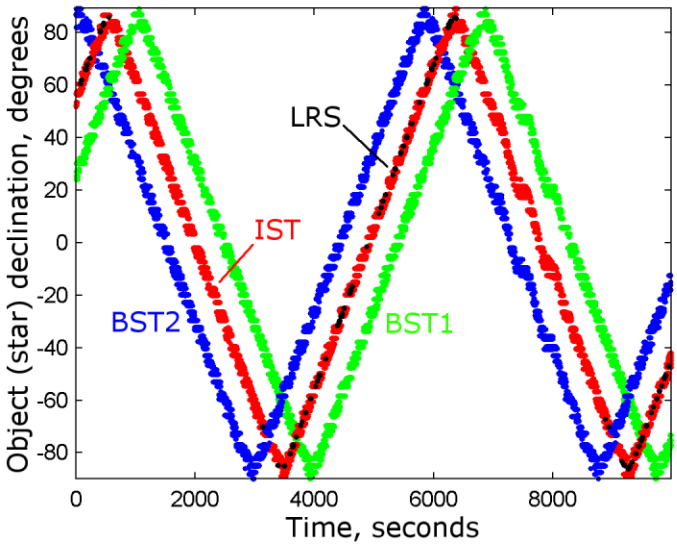

Figure 19. Passes of stars measured moving through the four tracker fields of view during nearly two orbital revolutions.

The residuals for each pass were reduced to descriptive statistics. The primary concerns for implementing the statistical reduction were sample sizes, outliers, and uncertainty statistics for relative weighting of pass statistics for multiple passes. Passes with residuals containing a trend due to transient objects moving with respect to the sky were also a special consideration. The basic approach was to describe a pass using the sample mean μ and the standard deviation of the sample mean σ_{mean} (also referred to as the standard error of the sample mean). For a pass with n residuals, sample mean μ, and sample standard deviation σ, the standard deviation of the sample mean σ_{mean} is given by Equation (114).[118]

$$\sigma_{mean} = \sigma / \sqrt{n} \tag{114}$$

The pass residuals were described by the expression $\mu \pm \sigma_{mean}$ where σ_{mean} gives an estimate of relative precision for comparison with other passes.

Outliers did not follow the pattern of other residuals, they were qualitatively different and indicated errors in the output tracker measurements, data handling and processing, or the filter. Adaptive methods based on quantile statistics were used for outlier detection. This was a problem for small samples where there were not enough values to meaningfully apply quantiles. An early decision was to use adaptive methods for normal passes, and static methods with constant cutoffs or thresholds for small passes.

It was assumed that the right ascension and declination coordinates of the residuals were independent, and that the values were approximately normally distributed. In practice a pass was represented by two vectors with the same length: a vector of right ascension residuals, and a vector of declination residuals. The values in each vector were assumed to have an approximately normal distribution, and to be independent of the other vector. The normality assumption was based on the central limit theorem which states that the sum of many independent random variables tends towards a normal distribution.[118] For celestial residuals the independent random variables included a large number of error

sources such as temperature variations, instrument electronics noise, spacecraft jitter, small alignment variations, timing, star catalog, and computational errors, etc.

Outlier detection for normal passes was based on quantiles, which divide ordered data into q equal-sized subsets. In particular the common $q = 4$ form, referred to as quartiles, was used. Quartiles produced four subsets each containing 25% of the data. The three boundaries between the subsets were Q1 (25% of the data is less than Q1 and 75% is greater), Q2 (50% of the data is less and 50% is greater), and Q3 (75% of the data is less and 25% is greater). Q2 is the median value. A useful parameter for expressing the variability of the data is the interquartile range (IQR) which is equal to Q3 minus Q1 as shown in Equation (115).

$$IQR = Q3 - Q1 \tag{115}$$

A standard method for detecting outliers is to use the lower and upper cutoffs shown in Equations (116) and (117).

$$\text{lower cutoff} = Q1 - 1.5(IQR) \tag{116}$$

$$\text{upper cutoff} = Q3 + 1.5(IQR) \tag{117}$$

Values less than the lower cutoff or greater than the upper cutoff are classified as outliers.

Figure 20 shows an example of outlier detection for the declination residuals from a BST1 pass of SKYMAP 18150090 containing 902 points. The median value of the residuals (Q2) is near zero as expected for a normal star and small filter errors. Measurement and filter noise errors generate residual variations which are described by the Q1 and Q3 values. The upper and lower cutoffs result in 17 residuals being classified as outliers.

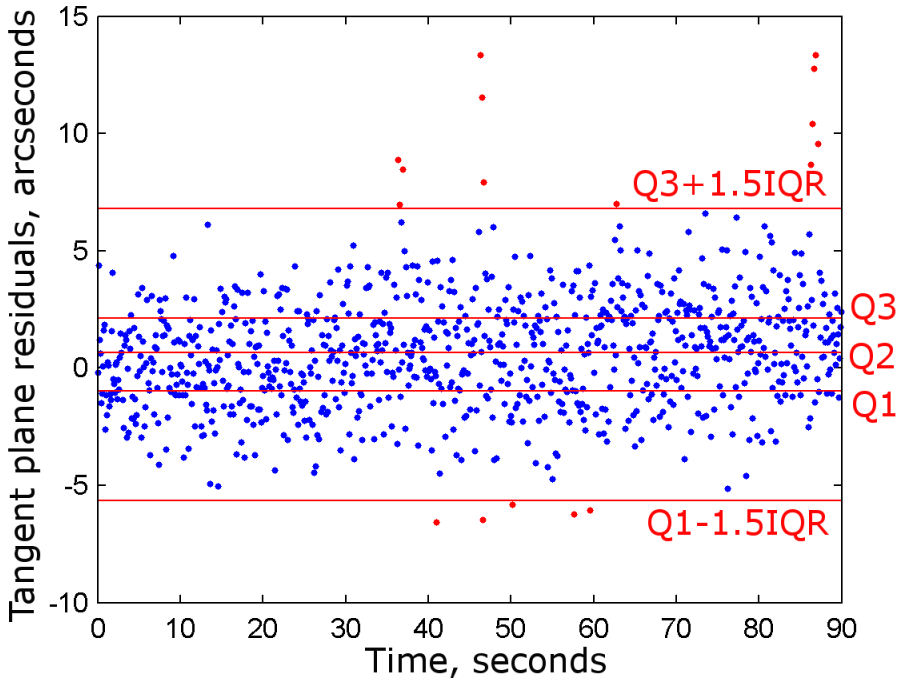

Figure 20. Outlier detection for declination residuals from a BST1 pass of SKYMAP 18150090.

The outputs from pass reduction were eight independent time-series of pass residuals, a right ascension time-series and a declination time-series for each tracker. These time-series were relatively noisy and complex. A robust method was needed to automate and generalize the process of extracting information. Smoothing was used to reduce the noisy pass residuals to curves. These smoothed curves were referred to as error signals. Deviations of the error signals away from zero represented errors in the tracker pointing vectors and the alignment and attitude states. Some practical concerns were the choice of smoothing method, smoothing parameters, and interpretation of the resulting error signals.

Figure 21 shows the declination pass residuals for 621 BST1 objects from the granule described above in Figure 16 through Figure 19. For each pass, the mean and standard deviation of the mean $\mu \pm \sigma_{mean}$ for the declination residuals are shown as a point and

error bar. Each pass residual was assigned a time tag calculated as the mean of the measurement time tags contained within the pass. The ocean scan maneuver near 8000 seconds is apparent in the sinusoidal variation of the pass residuals. The figure includes a red curve showing the error signal fit using locally weighted scatterplot smoothing (LOESS).[119, 120] LOESS generally uses local fits of first or second degree polynomials. Degree zero polynomials can also be used, in which case LOESS acts as a moving boxcar average. It has two tunable parameters. One specifies the degree of polynomial used for local fitting. The other specifies the relative weighting or width of the fitting. The weighting effectively defines what is meant by the term local, and is referred to here as the scale parameter α. In practice α was determined empirically based on the time scale of interest and whether the pass residuals were being under-fit or over-fit. A time scale of hundreds or thousands of seconds was of primary interest in order to study orbital variations of the alignments. This is referred to here as the orbital time scale and LOESS worked well using a range of α values. Using a different range of α values, LOESS also performed well for shorter time scales and higher frequency signals (due to ocean scan maneuvers for example).

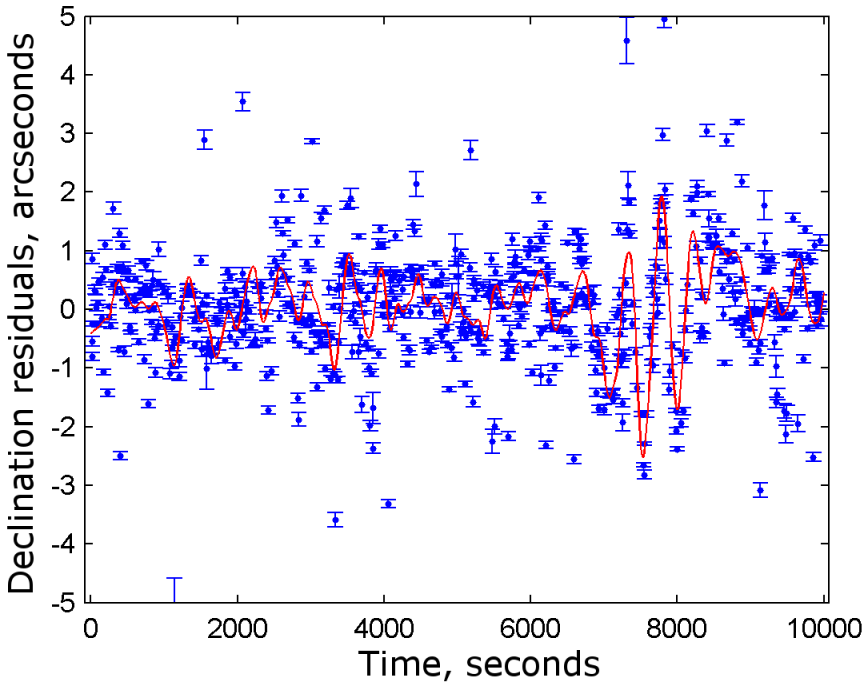

Figure 21. Pass residuals and error signal for BST1 declination.

A possible disadvantage to using pass residuals is that they have a lower effective sampling rate than the raw 10 Hz residuals from the trackers. This could be a concern for investigating short time scales and high frequency signals in the filter output. From Figure 21 it is apparent that the 10 Hz sampling rate of the raw data is reduced to a rate of roughly 0.1 Hz to 0.01 Hz for the pass residuals. This rate was sufficient for investigating signals on time scales of hundreds or thousands of seconds, which was the time scale of primary interest for structural variations due to orbital temperature changes, and between laser campaigns.

Figure 22 shows the pass residuals for all four trackers from the granule described above in Figure 16 through Figure 21. This figure is a good example of the two types of biased residuals. If the residuals for the IST were biased while the residuals of BST1, BST2, and the LRS were zero, then the IST residual bias equaled the IST tracker frame alignment error. This situation is apparent in the IST right ascension residuals near 3000 seconds. A

clear trend is visible that does not appear in the BST1 or BST2 residuals. Similarly, if the residuals for all four trackers were biased similarly, then the bias equaled the attitude error for the body frame. This situation is apparent near 8000 seconds for all trackers but the LRS, which was deactivated at the time because of sunlight. The sinusoidal oscillation of the residuals was caused by errors of a few arcseconds peak-to-peak in the filter attitude state due to an ocean scan maneuver. The oscillations in the residuals correlate with oscillations in the body rates and the attitude.

Figure 22 is an example where the LOESS α value was set small (0.025) for the error signals to track the high frequency oscillations caused by the ocean-scan maneuver near 8000 seconds. This is useful for studying the effects of maneuvers, but the noisy variations of the signals outside of the ocean scan suggest that on the orbital time scale the data may be over-fit. Figure 23 is the same as Figure 22 except a larger LOESS α value (0.1) was used. The error signals no longer track the high frequency oscillations during the ocean scan, but on the orbital time scale there is less evidence of over-fitting.

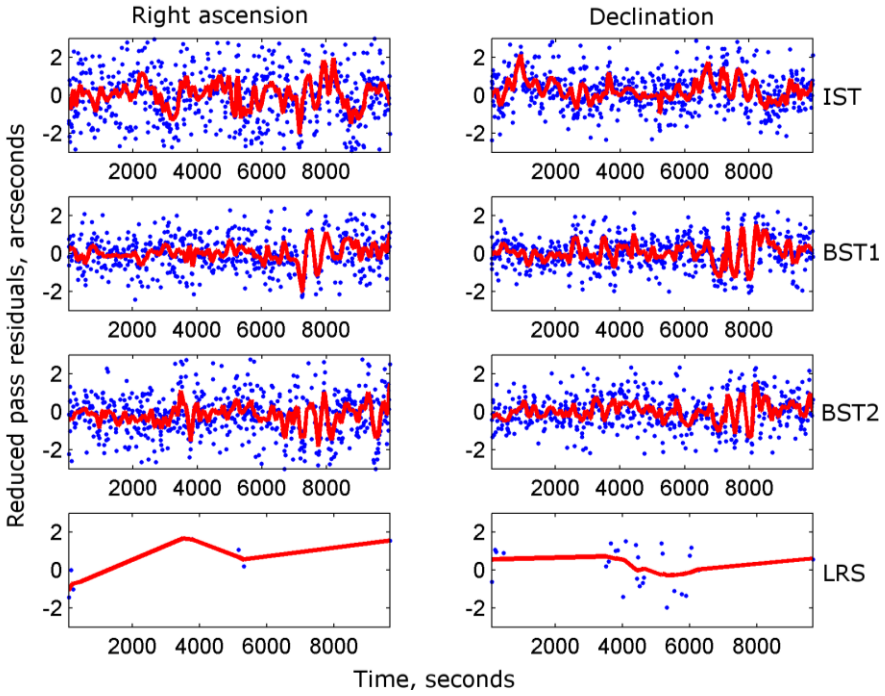

Figure 22. Pass residuals and error signals (LOESS alpha = 0.025).

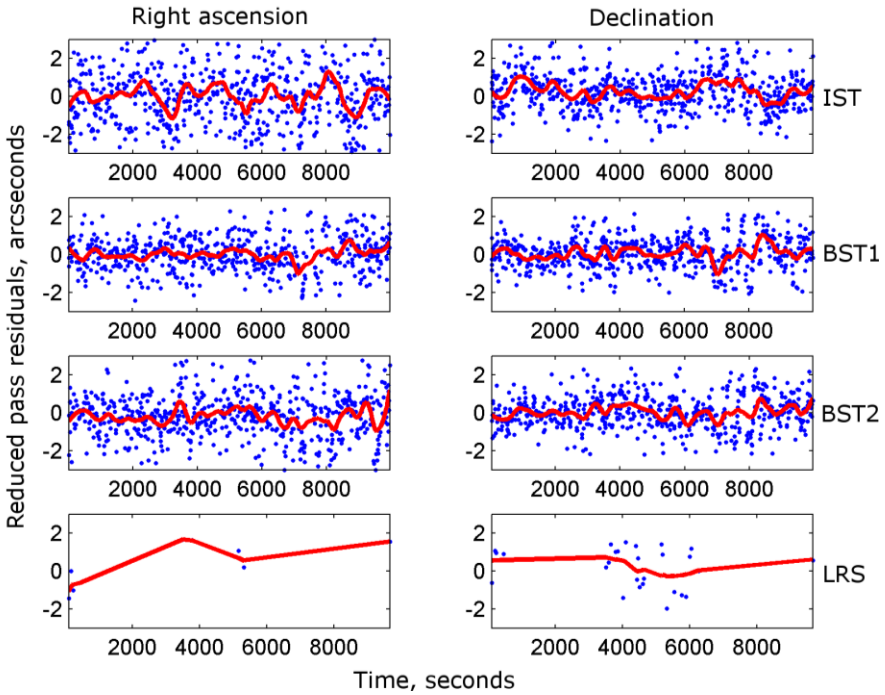

Figure 23. Reduced pass residuals and error signals (LOESS alpha = 0.1)

The error signals were interpreted as uncertainties and errors in the tracker pointing vectors and filter alignment and attitude states. Error signal variations affecting all the trackers were interpreted as attitude state errors. Error signal variations affecting a single tracker were interpreted as alignment state errors for that tracker. The error signals were usually generated using a small LOESS α value (0.025) so that they tracked high frequency errors due to maneuvers. Two approaches for extracting information from the error signals were investigated. The first approach was to interpolate error signal points to a constant sampling rate and use the relative counts and magnitudes of divergences from zero. Raw error signals did not have a constant sampling rate, they were vectors of smoothed points corresponding one-for-one with vectors of noisy pass residual points and vectors of non-constant rate time tags. The second approach was to use estimated analytic characteristics of raw error signals such as zero crossings, slopes, critical points, inflection points, etc. Setting LOESS to use first order polynomials generated an estimate of the slope of the error signal at each fit point and can effectively output both the error signal and its first derivative. Both approaches were implemented and tested. The interpolated error signal approach proved to be simple and robust.

V. Star Results

The stars provide nearly ideal reference points to compare with the filter states via tracker measurements. They are point sources due to their distance, and most also appear to be stationary for the same reason. If a star is near enough to have a significant proper motion, time-dependent corrections are available in the star catalogs. They are also an integral parts of the most inertial reference frame available, the International Celestial Reference Frame (ICRF). The fundamental measurements for the ICRF are of quasars, but the practical realization uses common stars. Measurements by star trackers introduce a variety of deterministic and stochastic errors. In all cases the errors are in the measurements and filter. The reference values in the star catalogs are more accurate than the tracker measurements. The errors are often identified with individual stars, bad stars for example, but the fact that the errors are in the tracker measurements and filter is implicit.

The primary tracker measurement errors are described in Section Va, including the noise and distortion results used in the alignment filter. Stars with position biases and bad stars are described in Section Vb. Tracker dependent instrument magnitude predictions and errors are described in Section Vc. Instrument magnitude prediction is important for star identification and for predicting apparent positions for blended stars.

The alignment filter made it possible to use the LRS in the same way as the other trackers. Because the LRS measured a single star, it was difficult to use in a stand-alone fashion. For example, single frame attitude determination requires at least two simultaneous star measurements. The data fusion inherent in the alignment filter made the LRS equivalent to the other trackers. The implementation of the filter demonstrated how significant this fusion was in practice. The filter was implemented using object oriented programming, with a single object class representing a generic star tracker. At run time, four instances of the tracker class were created for the IST, BST1, BST2, and LRS, and the four objects were treated identically by the filter.

The filtering dataset contained 307,817,169 measurements of 9,114 unique stars. 1,472 of these stars had measurements from all four trackers, with 133,311,558 total measurements. The fact that they accounted for 16% of the unique stars but 43% of the measurements demonstrates that they were easily acquired. The star results data structure output by the filter contained a record for every star measurement. Table 10 summarizes the information contained in each record. The position residuals were expressed using scaled tangent celestial frame coordinates. If a star had a position measurement bias, due to a near-neighbor for example, its position residuals were normally constant when represented using right ascension and declination. Exceptions generally involved variable stars. The brightness information was copied directly from the GLA04 data. The GLA04 data for the IST and LRS included encircled energy values. These were raw counts output by the tracker. The background brightness information was useful for determining when the sun and moon were effecting the other measurements.

Table 10. Filter star results record.

Quantity	Representation
Time tag	UTC time in seconds
Tracker identifier	Integer (1,2,3,4)
Star identifier	SKY2000 SKYMAP number
Right ascension residual	Arcseconds
Declination residual	Arcseconds
Brightness	Instrument magnitudes
Encircled energy (IST and LRS only)	Counts
Background brightness	Counts

a. Tracker Errors

Star tracker errors were classified as noise, distortion, or centroiding error.[56] The classification first separated noise or stochastic errors from systematic or deterministic

errors. Within systematic error there was a further separation of low spatial frequency error from high spatial frequency error. The term distortion is used for low spatial frequency error, and the term centroiding error is used for high spatial frequency error. Distortion becomes significant on large spatial scales such as the field of view as a whole. Centroiding error is significant on small spatial scales, primarily the scale of individual pixels.

The unit vectors representing star catalog positions were corrected for velocity aberration and proper motion.[121] Since the effect of stellar parallax is much less than one arcsecond except in a handful of cases it was not explicitly corrected.

Noise was defined as uncorrelated position variation and was estimated empirically from the tracker measurements for use in the filter R matrix. The estimate was based on the measured variations of the angular separations between pairs of stars.[66] The variance of the measured angular separation between two stars σ_{AB}^2 was equal to the sum of their noise variances σ_A^2 and σ_B^2 as shown in Equation (118).

$$\sigma_{AB}^2 = \sigma_A^2 + \sigma_B^2 \tag{118}$$

Given a series of simultaneous measurements of two stars, the variance of their separation σ_{AB}^2 was calculated directly.

For a series of simultaneous measurements of three stars, the variances of the separations σ_{AB}^2, σ_{AC}^2, σ_{BC}^2 were calculated directly from the measurements. Three equations were directly solvable for the three unknown noises σ_A^2, σ_B^2 and σ_C^2 as shown in Equations (119) to (121).

$$\sigma_{AB}^2 = \sigma_A^2 + \sigma_B^2 \tag{119}$$

$$\sigma_{AC}^2 = \sigma_A^2 + \sigma_C^2 \tag{120}$$

$$\sigma_{BC}^2 = \sigma_B^2 + \sigma_C^2 \tag{121}$$

This noise estimation method was termed the triangle method because of its dependence on triplets of stars. When there were $n > 3$ measured stars over a given time period, there was a variable number m of measured angular separations (simultaneously measured pairs). If $m > n$ then the resulting system of equations was solved using least-squares to estimate the individual star noises.

Figure 24 shows triangle method estimates of measurement noise versus star instrument magnitude for the IST and both BSTs. The noise was significantly higher for the IST. Third-order polynomial fit curves are also shown in the figure. In practice the fit curves were used to estimate noise values as a function of instrument magnitude during normal filter runs.

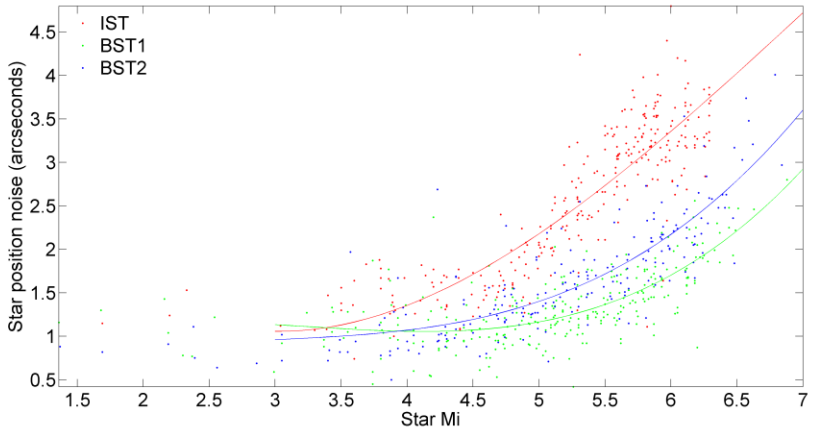

Figure 24. Triangle method estimates of measurement noise versus star magnitude.

Distortion errors were estimated for each tracker and used to correct the position measurements before use in the filter.[116] The correction map was a function of position in the tracker field of view. Time varying correction maps were generated and tested but in practice time variations were found to be small. Other potential factors in distortion correction, such as temperature, star brightness, and star color, have been discussed in the literature.[37, 56, 122]

Corrections were estimated using functions of position in the tracker frame. The functions were fitted to the filter residuals for large numbers of star measurements using least-squares and third-order polynomials.[116] An iterative method was used to accumulate the factors $H^T H$ and $H^T y$ for the least-squares solution. Here the matrix A represents $H^T H$ and the matrix B represents $H^T y$, where H is the measurement sensitivity matrix and y is the effective measurement vector. The iterative method was initialized as shown in Equations (122) and (123).

$$A_0 = 0_{20\times 20} \tag{122}$$

$$B_0 = 0_{20\times 1} \tag{123}$$

Calculating A_j and B_j for the jth measurement and iteration is demonstrated here. The input to the iteration was two unit vectors in the tracker frame, a measured unit vector $u_{measured}^{tracker}$ and a predicted unit vector $u_{predicted}^{tracker}$ as shown in Equations (124) and (125).

$$u_{measured}^{tracker} \equiv u = \begin{bmatrix} u_1 & u_2 & \left(u_1^2 + u_2^2\right)^{1/2} \end{bmatrix}^T \tag{124}$$

$$u_{predicted}^{tracker} \equiv u' = \begin{bmatrix} u_1' & u_2' & \left(u_1'^2 + u_2'^2\right)^{1/2} \end{bmatrix}^T \tag{125}$$

Within the iteration there were two effective measurements y_1 and y_2 as shown in Equations (126) and (127).

$$y_1 \equiv u_1 - u_1' \tag{126}$$

$$y_2 \equiv u_2 - u_2' \tag{127}$$

Two measurement models $y_1 \equiv h_1 x + \varepsilon_1$ and $y_2 \equiv h_2 x + \varepsilon_2$ were defined using a twenty-component vector of coefficients x and third-order polynomials for h_1 and h_2 as shown in Equations (128) and (129).

$$h_1 = \begin{bmatrix} 1 & u_1 & u_2 & u_1^2 & u_1u_2 & u_2^2 & u_1^3 & u_1^2u_2 & u_1u_2^2 & u_2^3 & 0_{1\times 10} \end{bmatrix} \tag{128}$$

$$h_2 = \begin{bmatrix} 0_{1\times 10} & 1 & u_1 & u_2 & u_1^{\,2} & u_1u_2 & u_2^{\,2} & u_1^{\,3} & u_1^{\,2}u_2 & u_1u_2^{\,2} & u_2^{\,3} \end{bmatrix} \tag{129}$$

A_j and B_j were accumulated as shown in Equations (130) and (131).

$$A_j = A_{j-1} + h_1^T h_1 + h_2^T h_2 \tag{130}$$

$$B_j = B_{j-1} + h_1^T y_1 + h_2^T y_2 \tag{131}$$

The estimated coefficients $\hat{x}$ were calculated as the least-squares solution using the normal equation as shown in Equation (132).

$$\hat{x} = \left(H^T H\right)^{-1} H^T y = A^{-1}B \tag{132}$$

The estimated coefficients $\hat{x}$ were also calculated as the least-squares solution using the singular value decomposition (SVD) as shown in Equations (133) and (134).

$$U, S, V = SVD\left(A\right) \tag{133}$$

$$\hat{x} = VS^{-1}U^T B \tag{134}$$

Given the estimated coefficients $\hat{x}$, a measured unit vector u was corrected to u' as shown in Equations (135) to (138).

$$h = \begin{bmatrix} 1 & u_1 & u_2 & u_1^2 & u_1u_2 & u_2^2 & u_1^3 & u_1^2u_2 & u_1u_2^2 & u_2^3 \end{bmatrix} \tag{135}$$

$$u_1' = u_1 - h\left[\hat{x}_1 \cdots \hat{x}_{10}\right]^T \tag{136}$$

$$u_2' = u_2 - h\left[\hat{x}_{11} \cdots \hat{x}_{20}\right]^T \tag{137}$$

$$u' = \begin{bmatrix} u_1' & u_2' & \left(\left(u_1'\right)^2 + \left(u_2'\right)^2\right)^{1/2} \end{bmatrix} \tag{138}$$

Figure 25 to Figure 27 shows the distortion corrections for the IST, BST1, and BST2. The corrections were approximately constant over the time-span of the mission. In these figures the field of view of a tracker is represented using h and v coordinates with units

of arcseconds. For each tracker the field of view was specified by the manufacturer as $8^{\circ} \times 8^{\circ}$. Here $9^{\circ} \times 9^{\circ}$ $(32000'' \times 32000'')$ fields of view are plotted.

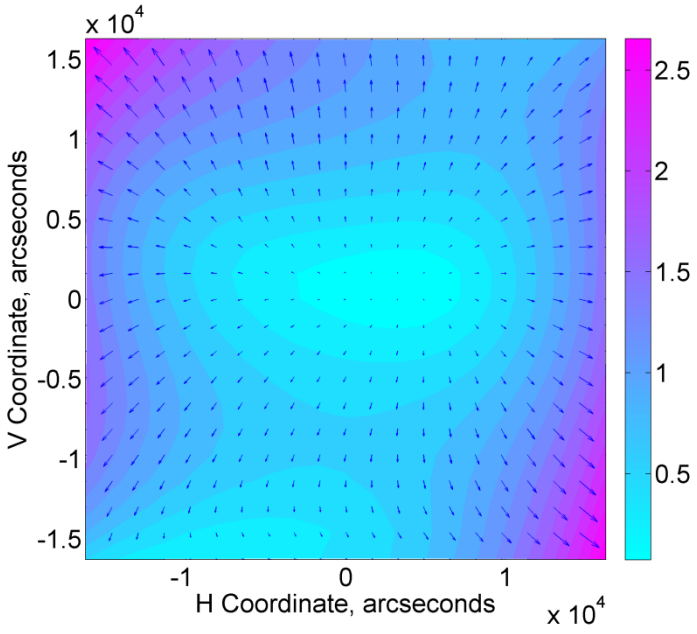

Figure 25. Distortion corrections of up to 2.5 arcseconds for the IST field of view.

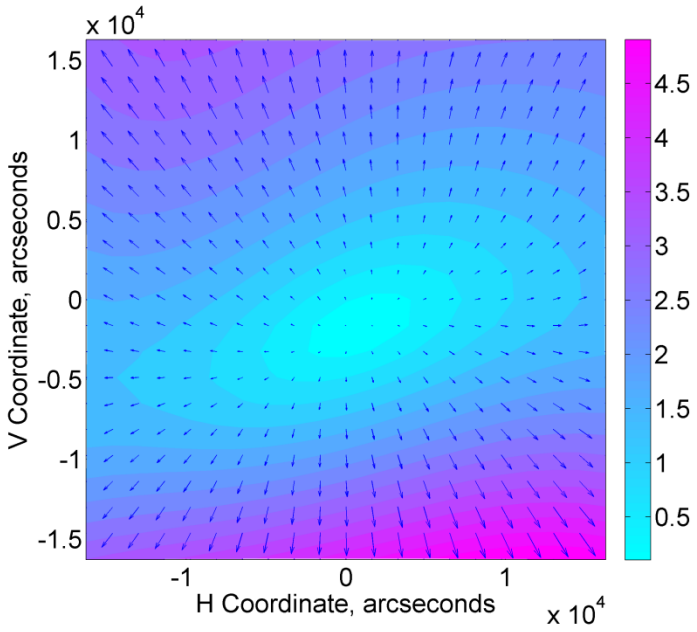

Figure 26. Distortion corrections of up to 4.5 arcseconds for the BST1 field of view.

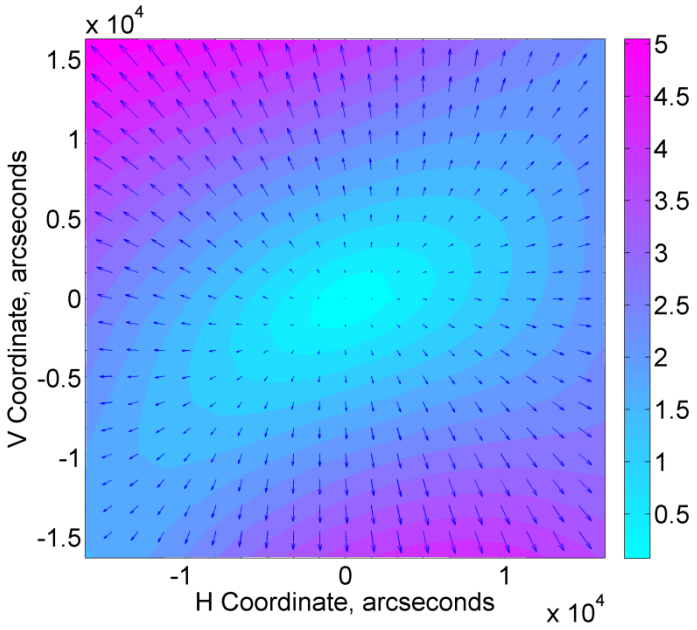

Figure 27. Distortion corrections of up to 5 arcseconds for the BST2 field of view.

Centroiding error or high spatial frequency error is primarily a result of stars moving across CCD pixel boundaries. It is typically a relatively small effect and in the literature it has been investigated using modeling and notch filtering.[37, 56] Here the effect was estimated and included in the measurement covariance. The effect was small in the along-track direction where pixel boundaries were crossed rapidly. Centroiding errors of around one arcsecond peak-to-peak at a frequency of several Hertz quickly averaged out to effectively become a small noise effect. The effect was of most concern in the IST data where the stars travelled along a row or column of the CCD. Occasionally a star image would slowly cross a pixel boundary in the cross-track direction, creating intermittent and unpredictable position step changes. The stars moved across the BST pixels diagonally, so crossed both row and column boundaries rapidly. Centroiding error was estimated using the Fourier transform of the measured minus predicted residuals. Figure 28 shows the frequency domain results for a typical case. The IST shows the strongest signal at 4 Hz and an amplitude of two arcseconds. For each BST there are two signals, corresponding to crossings of row or column boundaries.

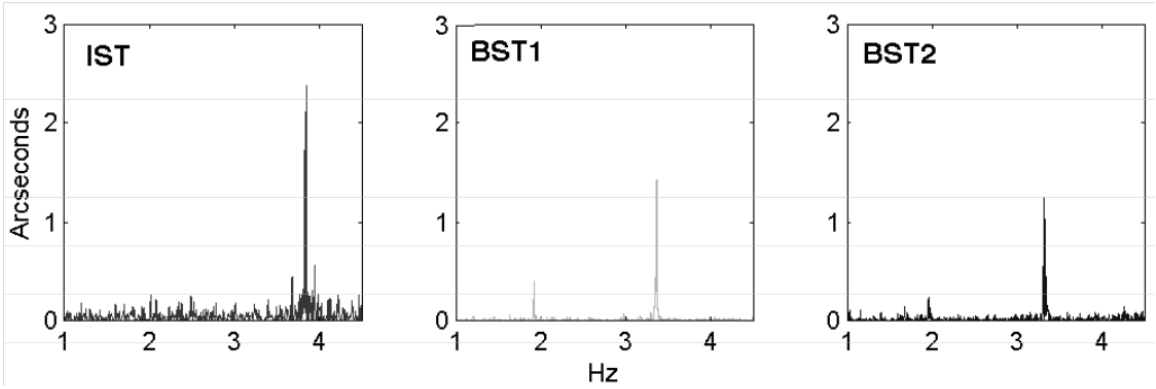

Figure 28. Centroiding error for a visual magnitude 5.87 star (SKYMAP 20500139).

b. Position Biases and Bad Stars

Certain types of errors were associated with individual stars. When these errors were significant the star was classified as a bad star. Stars with bright near-neighbors were the most common case.[67] Near-neighbors cause instrument dependent position biases because of the limited angular resolution of the trackers. Typically an attitude filter rejects some bad stars because of large position residuals. There are many bad stars with small biases however, particularly for faint stars. Since the number and density of stars increases with faintness, this is a concern. Methods were developed for detecting bad stars and estimating corrections where possible. Two approaches were taken. The fundamental difference between the two was whether or not filtering was used. The non-filtering approach used single frame attitude determination methods such as the q-method, QUEST, or SVD method to analyze individual tracker output frames. Statistics for each star were then built up over large numbers of frames. This is referred to here as the single frame method. The filtering approach was based on a detailed analysis of the filter residuals.

Similar preprocessing methods were used for all position measurements. The term blended star refers here to cases where two or more light sources contribute to the measured position, instrument magnitude, and possibly the catalog record representing the blended star. Blended stars have been used as tracker guide stars and flight catalog

stars. Both measurement and prediction accuracies for positions and instrument magnitudes are usually lower for blended stars, but they can meet filter requirements and be usable. The term transient refers to any light source that would not be expected to appear in a star catalog. Some examples are debris, dust, proton strikes, spacecraft, comets, asteroids, planets, hot pixels, etc. Transients have also been termed spurious measurements in the literature. Slowly varying transients such as planets, comets, and asteroids have typically been handled by ephemeris based stay-out zones in which tracker measurements are rejected.[71] Transients due to debris, dust, or spacecraft were detected by checking for motion relative to the stars.

The single frame method is a relatively simple approach for detecting and estimating bad stars and position measurement biases. Combining information from multiple trackers and the gyro unit is intentionally avoided during the processing. The focus is on a frame of simultaneous measurements from a single tracker, though after processing and reduction it is useful to compare the independent results between the different trackers. Very good accuracy was achievable with the single frame method. It has been argued that a similar approach to precision astrometry using block adjustment or iterative conventional adjustment is the best alternative.[123] The average number of tracker measurements per star in the publicly available ICESat data was greater than 250,000. Assuming that the tracker measurement errors were independent from frame to frame so that the position accuracy is proportional to $1/\sqrt{n}$, the accuracy would be approximately 0.05 arcseconds 1σ. Correlated tracker errors decrease the achievable accuracy but with three trackers and most stars making over 300 passes per tracker in the dataset, even brute force averaging could achieve an accuracy of 0.16 arcseconds. This is not impressive compared to the 0.002 arcsecond accuracy achieved by the Hipparcos spacecraft and catalog, but the Hipparcos position measurement and estimation method was fundamentally different (large angle astrometry rather than small angle imaging).[65]

Flight catalog designs and practical implementations have implicitly tolerated near-neighbor blended position uncertainties of 1.5 arcseconds or more.[68] Improved blended position centroiding and prediction using more sophisticated methods are an active research topic referred to as center of light estimation.[68] Center of light estimation is analogous to the centroiding, but for multiple light sources. The limiting factor for improved blended positions is believed to be the uncertainties in the instrument magnitudes of the blended light sources. An instrument magnitude uncertainty of 0.1 magnitudes 1σ is typical. Sophisticated center of light estimation is believed to be capable of an order of magnitude reduction in blended position uncertainty, from 1.5 arcseconds to 0.15 arcseconds, for typical blended stars (not cases involving bad stars).[68] Based on these numbers, the single frame method described here was capable of improving blended positions by roughly a factor of thirty over the simplest methods and a factor of three over more advanced center of light methods.[65]

Each star was individually examined to see if its measured positions were biased. In practice this meant examining measured minus predicted position residuals. One difficulty was that the residuals themselves could be biased by the presence of a bad star. This problem was dealt with using a method referred to here as everyone is a suspect. Some other terms used in the literature for this method are leave one out, and the Quenouille-Tukey jackknife. An alternative method is to use all possible combinations of the measured stars to generate a set of attitude estimates, and then do a statistical analysis of this set to arrive at an overall attitude estimate. This method has been referred to as the cloud method and the bootstrap method.[78, 87] Assuming that there are n measured stars in a tracker frame available for attitude estimation, jackknife methods use samples with $n-1$ stars and bootstrap methods use samples with less than $n-1$ stars.[65]

Each star took its turn as the suspect. The attitude and the attitude covariance of each star tracker frame containing the suspect star was estimated using the measurements of the other stars. The other stars were termed the jury. For each frame the estimated attitude

was used to calculate the predicted position of the suspect. The measured minus predicted residual was then computed and stored along with the attitude covariance. The result was that a suspect pass was converted from a set of position measurements to a set of independent position residuals and attitude uncertainties. The residuals of all the frames of the pass were then combined in an overall mean residual, and the overall attitude uncertainty was calculated from the attitude covariances. Finally, a scalar value representing the statistical significance of the overall residual was calculated using a method referred to in the literature as the Mahalanobis distance. Similar Mahalanobis distance methods have been used for searching and matching between multiple star catalogs.[124]

Using an iterative scheme, a segment of data was independently reprocessed for each star. Each star became the suspect star in turn. The set of measurements of the suspect as it moved through the tracker field of view was defined as a star pass or simply pass. Measurements of the suspect were set aside and attitude estimation was performed using measurements of the other stars in the field of view during the pass. Predicted measurements for the suspect star were calculated using the attitude estimates. Measured minus predicted position residuals and covariances were then calculated. Stars were classified using the Mahalanobis distance parameter, which scaled the residuals by the covariances to indicate the statistical significance of the residuals.

Position covariances were estimated using attitude estimate covariances and the position noise of the target star. Attitude covariances were transformed from 3×3 matrices with units of radians-squared to 2×2 matrices with units of arcseconds-squared representing tracker frame h and v coordinate uncertainties for the suspect. The sensitivity matrix used in this transformation is derived here. The position measurement noise of the target star was estimated using the triangle method discussed in Section Va.

The suspect star measurements, predictions, and covariances were expressed in a fixed coordinate frame where they could be directly compared. In the fixed frame both the

measured and predicted positions were ideally constant. The predicted positions were a function of the fixed frame attitude and the suspects catalog position so were in fact constant. Errors in the suspect measurements and attitude estimates produced variations of the measured positions. For each suspect measurement there was an estimated attitude defining a measurement coordinate frame. The attitudes and measurement coordinate frames were estimated using the other stars observed by the tracker, excluding the suspect. The fixed frame was arbitrary, but a specified measurement coordinate frame from the middle of the suspect pass was used in practice.

Each suspect measurement was first expressed as a unit vector in its measurement coordinate frame. The measurement coordinate frame was then rotated to the fixed frame while holding the measured unit vector constant in inertial space. The components of the unit vector were then recomputed relative to the fixed frame. The suspect star measurement in the fixed frame p_i was represented using h and v coordinates as shown in Equation (139).

$$p \equiv \left[k\left(u_1/u_3\right) \quad k\left(u_2/u_3\right) \right]^T \tag{139}$$

The prediction in the fixed frame $p_{predicted}$ was calculated similarly, giving the catalog unit vector of the suspect relative to the fixed frame as shown in Equation (140).

$$p_{predicted} \equiv star\ catalog\ \ position\ expressed\ in\ the\ \ fixed\ \ frame \tag{140}$$

The position residual vector r was defined as the difference of the measured and predicted positions as shown in Equation (141).

$$r \equiv p - p_{predicted} \tag{141}$$

The residual was expressed in h and v coordinates with units that corresponded to arcseconds near the center of the fixed frame. For a suspect without a position measurement bias the residuals were expected to cluster in a Gaussian distribution about zero.

For each two-component position residual vector r there was a corresponding 2×2 covariance matrix S, also expressed in h and v coordinates. S represented the uncertainty for the residual vector r. A residual vector with a small uncertainty was more statistically significant than one with a large uncertainty. S was calculated as the sum of the 2×2 measurement noise R and the 3×3 attitude covariance P transformed by a 2×3 sensitivity matrix H as shown in Equation (142). Because S, R, and P were expressed in h and v coordinates, their units were arcseconds squared.

$$S = R + HPH^T \tag{142}$$

The measurement noise R was a diagonal matrix with the suspect position noise variance $\sigma^2_{suspect}$ on the diagonal as shown in Equation (143). $\sigma^2_{suspect}$ was estimated during the preprocessing phase using the triangle method or a model fit to triangle method results.

$$R = \sigma^2_{suspect} I_{2\times2} \tag{143}$$

The attitude covariance P was calculated along with the attitude estimate using the SVD single frame attitude estimation method.[125] The measurements of the jury stars were weighted using their measurement noises. The sensitivity matrix H derived below was used to transform the attitude covariance P with units of radians squared to a covariance matrix in h and v coordinates with units of arcseconds squared.

The sensitivity matrix H gave the change of a position residual r resulting from a small change of the estimated attitude. The attitude change was represented by a three-component rotation vector $\tilde{\phi}$ as shown Equation (144).

$$\tilde{\phi} = \begin{bmatrix} \tilde{\phi}_1 & \tilde{\phi}_2 & \tilde{\phi}_3 \end{bmatrix}^T \tag{144}$$

It was equivalent to apply the attitude change to either the fixed frame or to the measurement frame. During the attitude change the measured suspect unit vector was held fixed. Multiplying the sensitivity matrix and the attitude change gave the small

change of the measured vector $\tilde{p} \equiv p_+ - p_-$ and the residual $\tilde{r} \equiv r_+ - r_-$ as shown in Equation (145) where a subscript minus sign indicates before the change and a subscript plus sign indicates after the change.

$$\tilde{r} = \tilde{p} = H\tilde{\phi} \tag{145}$$

The sensitivity matrix was formed as the product of two matrices. The first gave $\tilde{u} \equiv u_+ - u_-$ the change of the unit vector u. The second gave the resulting change $\tilde{r} \equiv r_+ - r_-$ of the h and v coordinates of the position residual r. The matrix giving $\tilde{u} \equiv u_+ - u_-$ was derived for the first two components as shown in Equation (146), the third component was redundant due to the unit vector constraint.

$$\begin{bmatrix} \tilde{u}_1 \\ \tilde{u}_2 \end{bmatrix} = \begin{bmatrix} \partial u_1/\partial\phi_1 & \partial u_1/\partial\phi_2 & \partial u_1/\partial\phi_3 \\ \partial u_2/\partial\phi_1 & \partial u_2/\partial\phi_2 & \partial u_2/\partial\phi_3 \end{bmatrix}\Bigg|_{u_-} \tilde{\phi} \tag{146}$$

The rotation matrix for a 1-2-3 rotation sequence shown in Equation (147) was used to derive expressions for $\tilde{u}_1$ and $\tilde{u}_2$.

$$u_+ = \begin{bmatrix} c\phi_2 c\phi_3 & c\phi_1 s\phi_3 + s\phi_1 s\phi_2 c\phi_3 & s\phi_1 s\phi_3 - c\phi_1 s\phi_2 c\phi_3 \\ -c\phi_2 s\phi_3 & c\phi_1 c\phi_3 - s\phi_1 s\phi_2 s\phi_3 & s\phi_1 c\phi_2 + c\phi_1 s\phi_2 s\phi_3 \\ s\phi_2 & -s\phi_1 c\phi_2 & c\phi_1 c\phi_2 \end{bmatrix} u_- \tag{147}$$

The change of the first unit vector component $\tilde{u}_1$ was derived by substituting in the small rotation $\tilde{\phi}$ as shown in Equations (148) to (150).

$$u_{1+} = \left(c\tilde{\phi}_2 c\tilde{\phi}_3\right)u_{1-} + \left(c\tilde{\phi}_1 s\tilde{\phi}_3 + s\tilde{\phi}_1 s\tilde{\phi}_2 c\tilde{\phi}_3\right)u_{2-} + \left(s\tilde{\phi}_1 s\tilde{\phi}_3 - c\tilde{\phi}_1 s\tilde{\phi}_2 c\tilde{\phi}_3\right)u_{3-} \tag{148}$$

$$u_{1+} = u_{1-} + \left(\tilde{\phi}_3 + \tilde{\phi}_1\tilde{\phi}_2\right)u_{2-} + \left(\tilde{\phi}_1\tilde{\phi}_3 - \tilde{\phi}_2\right)u_{3-} \tag{149}$$

$$\tilde{u}_1 = \begin{bmatrix} 0 & -u_{3-} & u_{2-} \end{bmatrix}\tilde{\phi} \tag{150}$$

The change of the second unit vector component $\tilde{u}_2$ was derived in the same way as shown in Equations (151) to (153).

$$u_{2+} = (-c\tilde{\phi}_2 s\tilde{\phi}_3)u_{1-} + (c\tilde{\phi}_1 c\tilde{\phi}_3 - s\tilde{\phi}_1 s\tilde{\phi}_2 s\tilde{\phi}_3)u_{2-} + \left(s\tilde{\phi}_1 c\tilde{\phi}_2 + c\tilde{\phi}_1 s\tilde{\phi}_2 s\tilde{\phi}_3\right)u_{3-} \tag{151}$$

$$u_{2+} = (-\tilde{\phi}_3)u_{1-} + (1 - \tilde{\phi}_1\tilde{\phi}_2\tilde{\phi}_3)u_{2-} + \left(\tilde{\phi}_1 + \tilde{\phi}_2\tilde{\phi}_3\right)u_{3-} \tag{152}$$

$$\tilde{u}_2 = \begin{bmatrix} u_{3-} & 0 & -u_{1-} \end{bmatrix}\tilde{\phi} \tag{153}$$

The two components were combined to form the sub-matrix giving the change of the first two components as shown in Equation (154).

$$\begin{bmatrix} \tilde{u}_1 \\ \tilde{u}_2 \end{bmatrix} = \begin{bmatrix} 0 & -u_{3-} & u_{2-} \\ u_{3-} & 0 & -u_{1-} \end{bmatrix}\tilde{\phi} \tag{154}$$

The matrix giving the change of the h and v coordinates of the position residual r was derived from the equations defining the h and v coordinates as shown in Equations (155) and (156).

$$h \equiv k\left(u_1/u_3\right) \tag{155}$$

$$v \equiv k\left(u_2/u_3\right) \tag{156}$$

The change $\tilde{h} \equiv h_+ - h_-$ was derived from the Taylor series as shown in Equations (157) to (158).

$$h_+ = h_- + \left.\frac{\partial h}{\partial u}\right|_{u_-} \left(u_+ - u_-\right) + \ldots \tag{157}$$

$$\tilde{h} = \left[\, k/u_3 + ku_1^2/u_3^3 \quad ku_1u_2/u_3^3 \,\right]\Big|_{u_-} \tilde{u} \tag{158}$$

The change $\tilde{v} \equiv v_+ - v_-$ was derived in the same way as shown in Equations (159) to (160)

.

$$v_+ = v_- + \left.\frac{\partial v}{\partial u}\right|_{u_-} \left(u_+ - u_-\right) + \ldots \tag{159}$$

$$\tilde{v} = \begin{bmatrix} ku_1u_2/u_3^3 & k/u_3 + ku_2^2/u_3^3 \end{bmatrix}\Big|_{u\_}\ \tilde{u} \tag{160}$$

The product of the change of the h and v coordinates with the change of the unit vector gave the sensitivity matrix as shown in Equation (161).

$$H = \begin{bmatrix} k/u_3 + ku_1^2/u_3^3 & ku_1u_2/u_3^3 \\ ku_1u_2/u_3^3 & k/u_3 + ku_2^2/u_3^3 \end{bmatrix} \begin{bmatrix} 0 & -u_3 & u_2 \\ u_3 & 0 & -u_1 \end{bmatrix} \tag{161}$$

This expression for the sensitivity matrix was evaluated using the measured unit vector $u\_$ expressed in the fixed frame.

A suspect's residual vectors r_i were described empirically by their distribution in the h and v coordinates of the fixed frame and analytically by their covariance matrices S_i. For a sample of n residual vectors all with the same covariances S, their distribution was approximately Gaussian by the central limit theorem and their sample covariance decreased with the square root of the sample size n.

$$sample\ distribution\ covariance = S/\sqrt{n} \tag{162}$$

This was demonstrated by plotting position residuals. Examples are shown below. As the number of measurements increased, the sample size increased and the distribution of residuals formed a narrower and sharper peak on the h and v coordinate plane. This principle of reducing positional uncertainty by increasing the sample size is important in astrometry.[123]

To classify a star as biased, its residuals and covariances were considered together. A useful scalar parameter that combined r and S was the Mahalanobis distance d defined in Equation (163).

$$d^2 \equiv r^T S^{-1} r \tag{163}$$

The parameter d was viewed as a ratio of the position residual and the position uncertainty. Position residuals with large uncertainties had smaller d values. Experience showed that d values greater than 1 to 1.5 indicated a significant position bias.

Two levels of statistics were computed: a lower-level set of pass statistics for each pass of a star, and a higher-level set of star statistics for each star. One version of star statistics was computed using all three trackers, and three additional versions used each tracker alone. The estimated position measurement biases were approximately the same for all three trackers. This was not surprising considering that all three trackers had the same basic characteristics of field of view and pixel size. The most significant differences between the trackers were sensitivity and noise and their overall effect on measurement biases was small. The statistics and plots below are for all three trackers unless noted. For a star that was measured in n passes there were n pass statistics for position residuals r_i and Mahalanobis distances d_i as shown in Equations (164) and (165).

$$r_i, i = 1, ..., n \tag{164}$$

$$d_i,\ i = 1, ..., n \tag{165}$$

Star statistics r_{star} and d_{star} were defined as the median values of the pass statistics as shown in Equations (166) and (167).

$$r_{star} = median\left(r_1, ..., r_n\right) \tag{166}$$

$$d_{star} = median\left(d_1, ..., d_n\right) \tag{167}$$

Median values were used to reduce the effects of outliers.

Two criteria were used to classify a star as unbiased. First if $r_{star} < 5$ arcseconds indicating that the residuals were relatively small in an absolute sense. And second if $d_{star} < 1$ indicating that the residuals were also small relative to their uncertainties. If $r_{star} < 5$ but $d_{star} > 1$ the star could have a small but statistically significant measurement bias. If a star did not meet these criteria it was flagged for further investigation.

Table 11 shows the numbers of unique stars examined while using the single frame method, grouped by tracker. The IST acquired any star in its field of view, resulting in a larger number of IST stars than BST stars. The BSTs operated in directed mode and acquired stars with help from the flight computer, which used an onboard attitude estimate and flight catalog of selected stars to direct the BST virtual trackers.

Table 11. Numbers of unique stars examined while using the single frame method.

Tracker	Number of stars	Exclusive	IST	BST1	BST2	All
IST	9410	4903	-	244	391	3872
BST1	4755	267	244	-	292	3872
BST2	4978	305	391	292	-	3872

Stars with large r_{star} and d_{star} values were automatically flagged for individual examination. The strongest evidence for position measurement bias was consistently large values of r_{star} and d_{star} over large numbers of passes, and particularly over passes in two or more of the trackers. Final confirmation was visual using astronomical imagery from the Aladin database.[126] If astronomical imagery showed a near-neighbor star corresponding to the position residuals r_{star} then the evidence became conclusive.

Figure 29 and Figure 30 show typical examples of bad stars with conclusive agreement between position measurement residuals and astronomical imagery. In each case an astronomical image is shown on the left and a plot of the residuals is shown on the right. The cross in the center of the residuals plots is the predicted position of the suspect star. The scattered points are the observed positions relative to the predicted position. The right ascension residuals have been scaled by the cosine of the star declination so that the axes scales are similar.

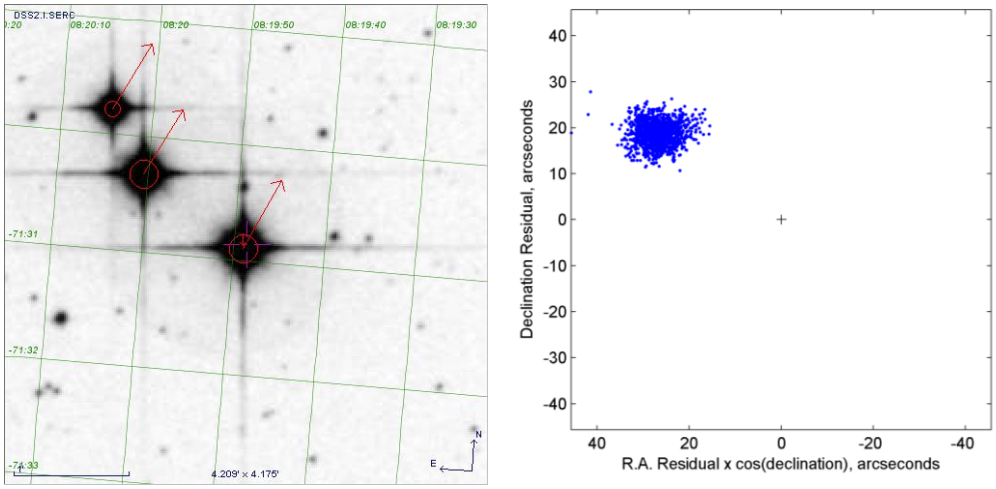

Figure 29. SKYMAP 8190190, 240" × 240" astronomical image (left) and measured minus predicted residual plot (right).

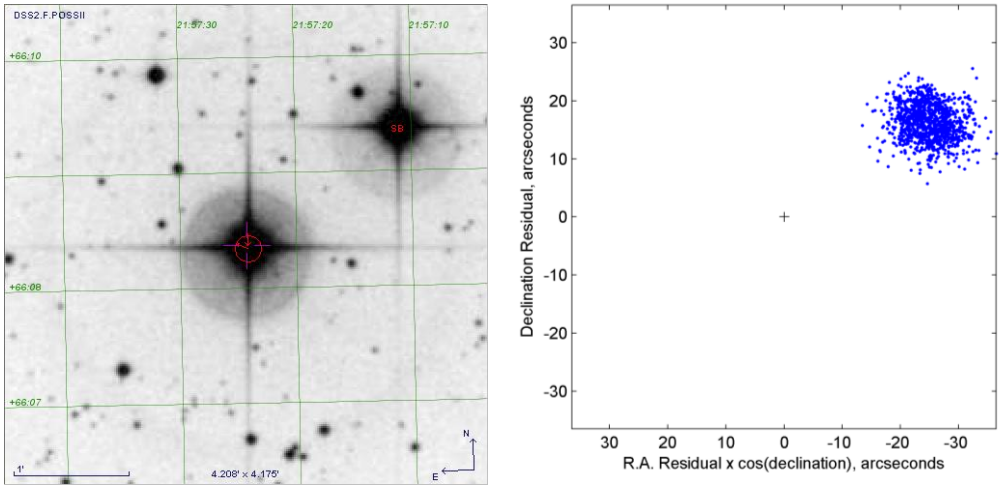

Figure 30. SKYMAP 21570079, 240" × 240" astronomical image (left) and measured minus predicted residual plot (right).

The next four example bad stars were of special interest because they were included in the 2004 NASA Aura spacecraft onboard flight catalog.[127-129] For the Aura flight catalog, work was done on blended stars involving near-neighbors, particularly the 3542 stars in the onboard flight catalog. The Aura documentation states that sophisticated center of light positions were not computed and some discrepancies were expected. The rule used

was that blended stars were computed and used for the Ball CT-601 star tracker when there was a near-neighbor within 120 arcseconds of the star in question.[77]

Table 12 summarizes the four stars. SKYMAP and Aura onboard catalog identifiers are given in the first two columns. The third column gives the number of passes of the star included in the analysis. The fourth column gives the number of passes for the BSTs alone. Two of the four stars were acquired by the BSTs, indicating that these two stars were included by Ball in their onboard flight catalog, since the BSTs were in directed field of view mode and acquired stars based on the onboard flight catalog. The final three columns gives means and sigmas for the Mahalanobis distance d, scaled right ascension residual $\tilde{\alpha} \equiv \hat{\alpha} - \alpha$ in arcseconds, and declination residual $\tilde{\delta} \equiv \hat{\delta} - \delta$ in arcseconds.

Table 12. Biased stars found in the survey that were also in the Aura onboard catalog.

SKYMAP	Aura	Passes	BST	d	$\tilde{\alpha}$ *(asec)*	$\tilde{\delta}$ *(asec)*
23190077	3025	238	-	15.51 ± 1.46	29.65 ± 1.92	34.99 ± 1.31
17310145	759	77	-	8.28 ± 1.75	17.76 ± 4.33	-17.05 ± 4.09
14290104	20	959	565	3.33 ± 0.91	-8.99 ± 1.81	2.88 ± 2.67
19370139	1204	144	144	2.74 ± 0.38	3.07 ± 0.74	-7.70 ± 1.25

Figure 31 to Figure 34 shows visual confirmation that the four stars in Table 12 have position measurement biases caused by near-neighbors. In each case an astronomical image is shown on the left and a plot of the residuals is shown on the right. The cross in the center of the residuals plots is the predicted position of the suspect star. The scattered points are the observed positions relative to the predicted position.

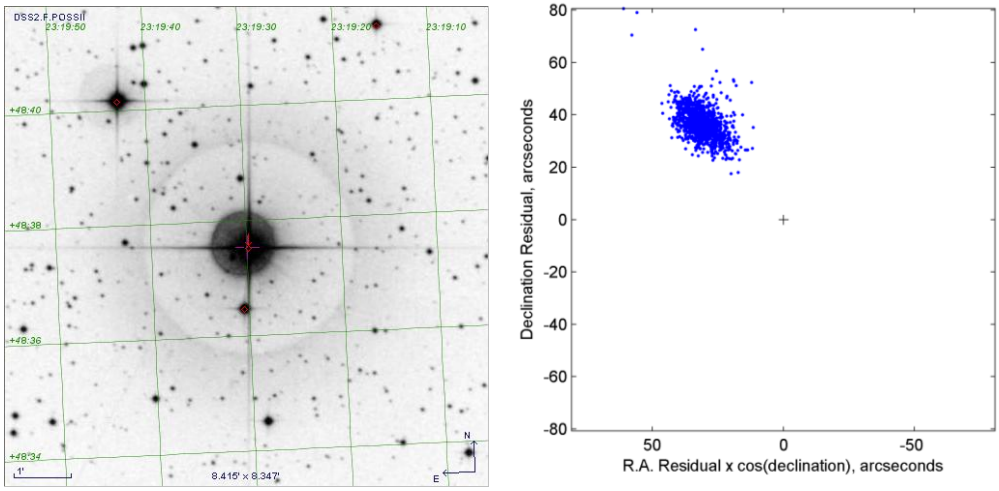

Figure 31. SKYMAP 23190077 Aura 3025, 300" × 300" astronomical image (left) and measured minus predicted residual plot (right).

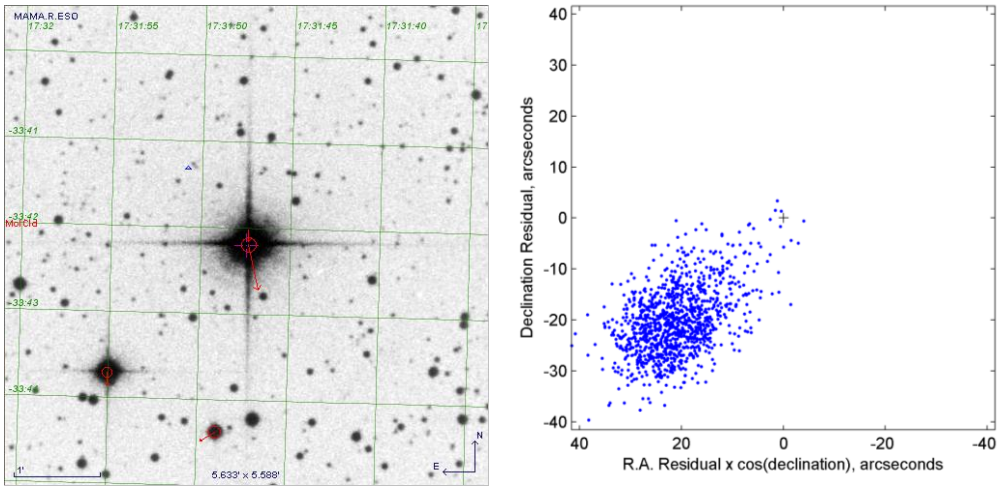

Figure 32. SKYMAP 17310145 Aura 759, 300" × 300" astronomical image (left) and measured minus predicted residual plot (right).

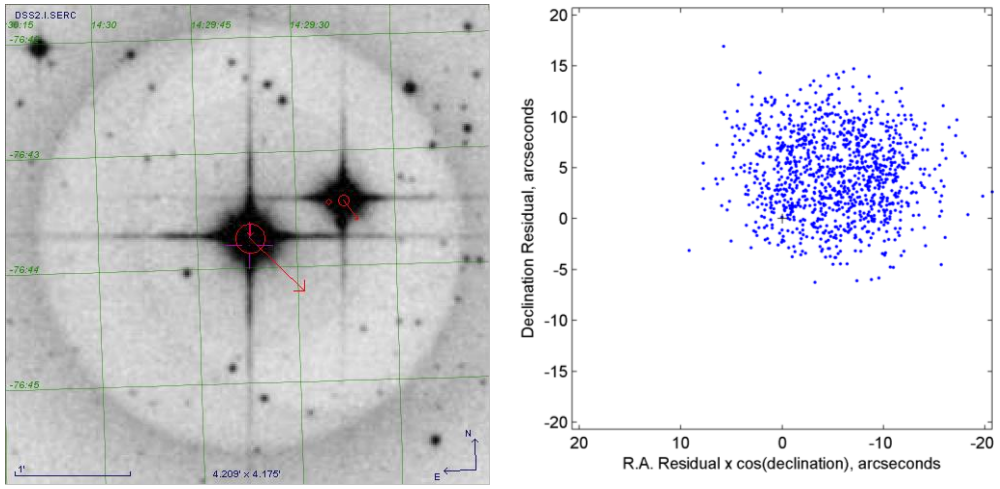

Figure 33. SKYMAP 14290104 Aura 70874, 240" × 240" astronomical image (left) and measured minus predicted residual plot (right).

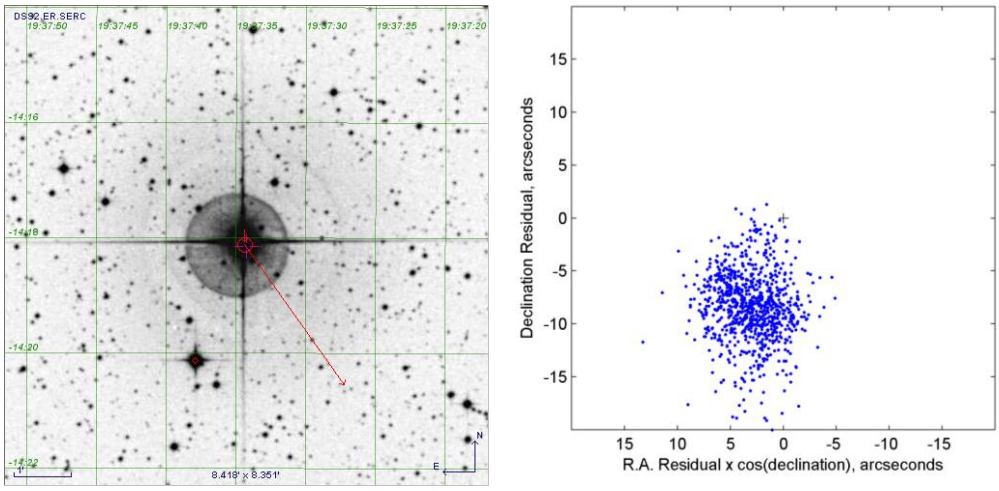

Figure 34. SKYMAP 19370139 Aura 1204, 300" × 300" astronomical image (left) and measured minus predicted residual plot (right).

Table 13 describes 45 stars with significant position measurement biases found using the single frame method (four more are described in Table 12). SKYMAP and Aura onboard catalog identifiers are given in the first two columns. The third column gives the number of passes of the star included in the analysis. The fourth column gives the number of passes for the BSTs alone. The final three columns gives means and sigmas for the

Mahalanobis distance d, scaled right ascension residual $\tilde{\alpha} \equiv \hat{\alpha} - \alpha$ in arcseconds, and declination residual $\tilde{\delta} \equiv \hat{\delta} - \delta$ in arcseconds.

Table 13. Stars with significant position measurement biases found using the single frame method.

SKYMAP	HIP	Passes	BST	d	$\tilde{\alpha}$ *(asec)*	$\tilde{\delta}$ *(asec)*
8190190	40817	598	-	11.50 ± 0.64	26.43 ± 1.39	18.05 ± 2.19
21570079	108378	224	2	9.41 ± 1.79	-20.99 ± 1.60	16.63 ± 5.10
21430083	107253	36	15	9.29 ± 2.45	23.82 ± 6.41	14.35 ± 2.46
21440193	107382	108	-	9.26 ± 0.74	-10.42 ± 0.90	24.96 ± 1.44
21020031	103814	415	-	9.18 ± 0.30	24.68 ± 1.51	7.36 ± 0.47
110134	967	145	14	8.74 ± 0.88	16.88 ± 1.53	19.39 ± 0.94
14240025	70400	280	21	8.39 ± 0.59	-23.90 ± 1.15	1.69 ± 0.65
16200091	80047	1925	7	7.06 ± 0.54	3.95 ± 1.80	19.85 ± 1.10
22220131	110478	513	169	6.88 ± 2.36	20.52 ± 6.61	7.50 ± 2.79
20180172	100122	57	9	6.19 ± 1.20	-7.19 ± 2.23	22.79 ± 3.57
9570131	48839	493	296	5.02 ± 0.84	14.79 ± 1.52	-4.06 ± 1.20
21440030	107310	269	14	4.52 ± 0.51	8.88 ± 1.25	10.62 ± 1.23
15240088	75411	215	-	4.43 ± 0.42	1.22 ± 0.79	-12.69 ± 0.45
310089	2484	880	880	4.30 ± 0.62	-3.14 ± 0.54	12.91 ± 1.00
14130055	69481	1331	931	3.77 ± 0.54	9.27 ± 0.98	6.15 ± 0.98
2540010	13518	1076	756	3.69 ± 0.77	3.07 ± 1.69	10.79 ± 3.10
16400088	81632	280	36	3.66 ± 0.69	-9.06 ± 2.22	5.27 ± 1.57
21420079	107162	10	-	3.64 ± 0.38	8.78 ± 1.25	-4.63 ± 1.06
3230087	15795	50	36	3.36 ± 0.47	-9.16 ± 1.25	2.79 ± 1.53
16160102	79757	348	274	3.32 ± 0.82	6.54 ± 2.49	6.33 ± 1.15
20220229	100515	43	1	3.23 ± 0.37	8.75 ± 1.24	3.47 ± 0.37
18560046	92946	26	-	3.17 ± 0.20	8.68 ± 0.65	-2.59 ± 0.37
18490160	92391	118	29	3.07 ± 0.49	2.73 ± 1.14	-8.56 ± 1.09

Table 13 (continued)

21010039	103734	1044	645	2.71 ± 0.68	5.51 ± 1.80	5.93 ± 2.23
4110075	19571	377	273	2.66 ± 0.46	-3.02 ± 1.58	7.21 ± 1.29
21440054	107323	1786	1317	2.53 ± 0.44	7.42 ± 1.21	0.49 ± 1.34
14260028	70574	144	84	2.52 ± 0.60	-3.09 ± 1.27	-6.89 ± 1.85
4500154	22534	117	2	2.49 ± 0.62	-5.05 ± 1.88	-4.10 ± 2.20
22550117	113222	277	180	2.43 ± 0.51	-6.72 ± 1.22	-3.62 ± 1.89
9510120	48374	1468	1223	2.28 ± 0.27	-0.80 ± 0.85	6.78 ± 0.58
19240223	95447	249	249	2.28 ± 0.37	-6.38 ± 0.95	1.70 ± 0.97
9290031	46509	319	218	2.23 ± 0.21	1.10 ± 0.98	6.30 ± 0.55
22080173	109332	478	471	2.11 ± 0.56	3.57 ± 1.29	5.00 ± 1.41
16080010	79043	261	26	2.09 ± 0.28	1.61 ± 0.72	6.07 ± 0.64
13510003	67589	1287	881	2.03 ± 0.51	5.73 ± 1.09	2.59 ± 0.92
17340102	85998	289	1	2.03 ± 0.38	-0.45 ± 1.60	-5.86 ± 1.06
20000063	98461	186	186	1.97 ± 0.37	4.53 ± 0.97	-4.48 ± 0.74
20370024	101716	201	163	1.90 ± 0.54	5.20 ± 1.67	1.69 ± 0.68
10550078	-	794	533	1.87 ± 0.24	-4.70 ± 0.81	2.40 ± 0.60
14190049	69996	1232	1104	1.85 ± 0.45	2.08 ± 0.78	-4.93 ± 1.23
21190179	-	2158	1705	1.82 ± 0.34	5.16 ± 1.02	-0.20 ± 0.85
19290088	95823	67	67	1.81 ± 0.15	4.12 ± 0.40	2.89 ± 0.24
9010159	44342	213	213	1.80 ± 0.28	-6.71 ± 2.03	1.50 ± 0.96
11270140	55945	598	411	1.79 ± 0.29	-0.08 ± 0.95	-5.34 ± 0.71
19150063	94624	262	262	1.79 ± 0.25	-5.07 ± 0.78	-0.41 ± 0.66

Stars were classified as normal if they had position residuals less than five arcseconds and Mahalanobis distances less than one. Statistics for large samples of normal stars were used to characterize the trackers. The samples were selected by tracker, by star brightness, and by observation time. The statistics combined the effects of measurement

errors and prediction errors, so they effectively described the overall accuracy of the single frame method. The distributions of position residuals r_{star} and Mahalanobis distances d_{star} were described using mean values and standard deviations. The criteria defining normal stars meant that the distributions were roughly Gaussian by the central limit theorem. The distributions of passes per star *n* were also described using mean values, though *n* is far from Gaussian. Many bright stars were tracked during every possible pass, while many dim stars were tracked in a handful of the possible passes. The two extremes dominated. The result was that the standard deviation of *n* was generally larger than its mean.

Table 14 contains statistics for unbiased stars grouped by tracker. BST1 had smaller position residuals than the other two trackers. This quantitative result agreed with other qualitative evidence. The mean position residual r_{star} was treated as the overall accuracy for the single frame method. Ideally it would be zero. The overall error described by this statistic comes from both the tracker measurements and the prediction process.

Table 14. Single frame method position residual statistics for normal stars grouped by tracker.

Tracker	Stars	n	r_{star} *(asec)*	d_{star}
IST	4894	210.1	1.63 ± 0.62	0.54 ± 0.19
BST1	4378	234.6	1.20 ± 0.62	0.39 ± 0.20
BST2	4217	248.9	1.37 ± 0.64	0.46 ± 0.21
All	6187	513.7	1.46 ± 0.61	0.49 ± 0.20

Table 15 shows statistics grouped by visual magnitude V . Position residuals generally increased with magnitude and were correlated with position noise. The number of stars increased with magnitude because of the increasing number and density of fainter stars. More passes of bright stars were observed, indicating that the trackers tended to acquire fainter stars less frequently.

Table 15. Single frame method position residual statistics for normal stars grouped by star brightness.

V	Stars	n	r_{star} *(asec)*	d_{star}
1 to 2	20	926.3	1.39 ± 0.78	0.47 ± 0.25
2 to 3	99	658.0	1.44 ± 0.60	0.47 ± 0.19
3 to 4	361	635.4	1.44 ± 0.65	0.48 ± 0.21
4 to 5	1028	637.3	1.34 ± 0.62	0.45 ± 0.19
5 to 6	2889	516.2	1.47 ± 0.63	0.49 ± 0.20
6 to 7	2792	252.1	1.56 ± 0.65	0.51 ± 0.20

Table 16 to Table 18 characterizes the distributions of r_{star} and d_{star} for each tracker during the six laser campaigns. The laser campaigns were taken from the first five years of the mission and there was not strong evidence of aging effects.

Table 16. Single frame method IST position residual statistics grouped by campaign.

Campaign	Stars	n	r_{star} *(asec)*	d_{star}
L2A 2003	1398	181.5	1.52 ± 0.61	0.50 ± 0.19
L2C 2004	1010	146.5	1.65 ± 0.62	0.54 ± 0.19
L3B 2005	1075	152.7	1.66 ± 0.63	0.53 ± 0.19
L3F 2006	1025	147.5	1.70 ± 0.61	0.57 ± 0.20
L3G 2006	1276	119.3	1.60 ± 0.70	0.53 ± 0.21
L3H 2007	1386	111.0	1.59 ± 0.67	0.52 ± 0.21

Table 17. Single frame method BST1 position residual statistics grouped by campaign.

Campaign	Stars	n	r_{star} *(asec)*	d_{star}
L2A 2003	1365	199.2	1.22 ± 0.65	0.40 ± 0.21
L2C 2004	913	139.8	1.16 ± 0.67	0.38 ± 0.21
L3B 2005	1146	153.8	1.23 ± 0.62	0.40 ± 0.20
L3F 2006	743	158.1	1.26 ± 0.67	0.41 ± 0.21
L3G 2006	1280	126.3	1.22 ± 0.65	0.40 ± 0.21
L3H 2007	1464	111.3	1.22 ± 0.65	0.40 ± 0.21

Table 18. Single frame method BST2 position residual statistics grouped by campaign.

Campaign	Stars	n	r_{star} *(asec)*	d_{star}
L2A 2003	1365	193.8	1.37 ± 0.67	0.44 ± 0.22
L2C 2004	987	142.3	1.40 ± 0.65	0.46 ± 0.21
L3B 2005	1063	168.4	1.40 ± 0.65	0.47 ± 0.21
L3F 2006	839	159.1	1.41 ± 0.66	0.47 ± 0.21
L3G 2006	1193	129.3	1.41 ± 0.66	0.48 ± 0.22
L3H 2007	1389	117.0	1.36 ± 0.67	0.46 ± 0.23

c. Instrument Magnitude Prediction

Instrument magnitude predictions are important for star identification, a step in forming the measured minus predicted star position residuals for the alignment filter. The predicted star unit vectors depend on star identification, star catalog reference values, and the filter states. Incorrect star identification causes errors in the filter residuals and measurement update phase. In theory, position measurements alone are adequate for identifying stars, but both star tracker measurements and the distribution of light on the sky complicate the situation. In practice, comparing an objects measured and predicted instrument magnitudes is an important step in identification. Every instrument has a

unique sensitivity and response, and the sky is complex with light from multiple objects blending together, variable stars, and transient nonstellar objects.

Flight data was used to evaluate various models for instrument magnitude prediction. The results show that models using flight instrument magnitudes from the SKY2000 catalog perform best.[2] The results agree with a NASA statement that "CT-6xx magnitude observations provide the best data for generating accurate instrumental magnitude predictions for charge-coupled device star trackers or other sensors with similar spectral response characteristics."[130] The results also agree with a statement that red passband magnitudes are the next best after flight instrument magnitudes.[3] This was expected since tracker response typically peaks in the red and infrared passbands.

The results include instrument magnitudes for 590 new stars that did not have RXTE or SKY2000 instrument magnitudes. The RXTE mission published flight data for 15,084 instrument magnitudes from the RXTE CT-601 star trackers in the early 2000s.[74] The RXTE results were included in the SKY2000 catalog as passband 3 magnitudes.[5] The results here include instrument magnitudes from at least one tracker for 6,317 stars, which is about 78% of the 8,107 stars analyzed. 2,090 of these stars have instrument magnitudes for all three trackers. Selection criteria included sample sizes, observed minus predicted position residuals, and magnitude measurement variations. The same selection criteria were used for all three trackers. The IST observed more stars than the BSTs because it was not in directed field of view mode, but fewer IST than BST stars met the selection criteria. The results were formatted as three text files, one for each tracker. The files have the same formatting as the RXTE file. They contain one line for each star. Each line contains a magnitude mean and standard deviation. If the star is classified as variable a magnitude maximum and minimum are also included.

Table 19 summarizes the instrument magnitude results. The first row shows the total number of stars in each file. The second row gives the number of stars in a file that also appear in the RXTE file and the ratio of this number to the total. Approximately 85% of

the stars were also in the RXTE file. The fifth row gives the instrument magnitude biases between ICESat and RXTE. These biases were approximately constant over the range of instrument magnitudes and were a result of the use of different reference stars to calibrate the ICESat and RXTE trackers. ICESat instrument magnitudes were evaluated by subtracting the tracker magnitude bias and RXTE magnitudes. Stars with magnitude differences larger than 3σ were classified as outliers. The fifth row gives the number of outliers and the ratio of this number to the total.

Table 19. Summary of instrument magnitude results.

	IST	BST1	BST2
ICESat stars	3827	4319	4395
Also RXTE stars	3285 (0.858)	3658 (0.847)	3683 (0.838)
Also SKY2000 passband 3 stars	3528 (0.922)	3907 (0.905)	3934 (0.895)
New ICESat only stars	299 (0.078)	412 (0.095)	461 (0.105)
ICESat to RXTE mean bias	0.548	0.544	0.619
ICESat magnitude outliers	32 (0.008)	35 (0.008)	27 (0.006)

Table 20 describes seven stars that were classified as outliers and appeared in all three files. These are examples of typical problems with instrument magnitudes encountered in practice. Pairs of magnitude differences are given for each star and tracker. The first number in each pair is the difference from the RXTE instrument magnitude. The second number is the difference from the predicted instrument magnitude. In all cases the RXTE magnitudes and predicted magnitudes were similar. For each star the values were approximately the same for all three trackers indicating agreement of the three ICESat magnitudes. Henry Draper (HD) identifiers are given for use with astronomical databases.

Table 20. Outlier stars appearing in all three files. The first number in each pair is the difference from the RXTE instrument magnitude, the second is the difference from the predicted instrument magnitude.

SKYMAP	HD	IST	BST1	BST2	Notes
510044	4817	+0.32, +0.24	+0.25, +0.21	+0.24, +0.20	variable, multiple
3470095	23878	-0.39, -0.24	-0.43, -0.42	-0.38, -0.40	variable
3550050	24534	-0.33, -0.19	-0.29, -0.32	-0.23, -0.29	variable, binary
4030090	25676	-0.32, -0.26	-0.49, -0.48	-0.46, -0.47	variable
15380095	139461	-0.85, -0.66	-0.82, -0.81	-0.85, -0.86	binary
16310033	149009	-1.70, -1.59	-1.75, -2.06	-1.80, -1.26	variable
21560069	208527	+0.31, +0.26	+0.24, +0.20	+0.34, +0.30	variable

Figure 35 shows the fifth star from Table 20 (SKYMAP 15380095). It is member of a binary system with a separation of 11.9 arcseconds and a magnitude difference of 0.1. There are two records in the SKY2000 catalog, one for each star, rather than a single blended record. In practice the attitude processor identified either member. The instrument magnitudes were significantly brighter than predicted due to the near-neighbor. In this situation flight catalog records for the binary pair can be combined into a single blended record.

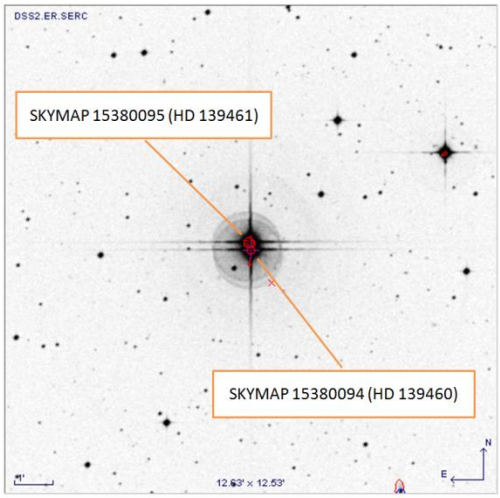

Figure 35. Astronomical image of the fifth star from Table 20 (SKYMAP 15380095).

For each unique star, varying amounts of information are available on magnitudes, spectral class, variability, multiplicity, near-neighbors, etc. The SKY2000 catalog contains records for 299,460 stars. The run-time catalog used for processing ICESat data consisted of the 45,394 SKY2000 stars with visual magnitudes less than eight. The results here concern 8,107 stars that were encountered in practice. These stars had instrument magnitude up to 7.1 (the maximum instrument magnitude of the BSTs). Figure 36 shows the counts of SKY2000 and ICESat stars versus magnitude. The number of stars increases exponentially with magnitude. The rapid drop-off of ICESat star counts occurs at the instrument magnitude limit of the trackers. The magnitude prediction and tracker response results can be used to create run-time catalogs based on predicted instrument magnitudes rather than visual magnitudes. This removes a large group of stars that are too dim to detect, and introduces a small group of detectable red stars with very dim visual magnitudes. The discussion of tracker response curves below shows that, for red stars with spectral class M, measured instrument magnitudes can be up to two magnitudes smaller (brighter) than visual magnitudes.

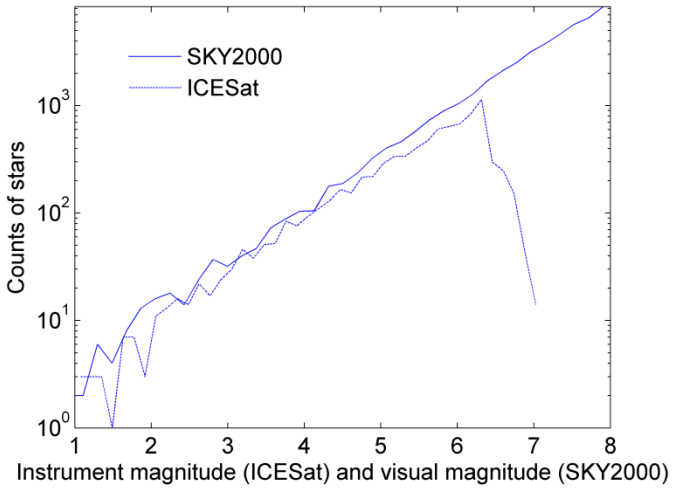

Figure 36. Counts of SKY2000 and ICESat stars versus magnitude.

SKY2000 includes information on astronomical ultraviolet U, blue B, and visual V magnitudes. It also includes information on special magnitudes termed passband 1, passband 2, and passband 3. Passband 1 and 2 magnitudes are effectively astronomical red R and infrared I magnitudes. Passband 3 magnitudes are instrument magnitudes, mostly from the RXTE mission CT-601 star trackers. Table 21 shows counts of ICESat stars for which the SKY2000 catalog includes particular magnitude types. The ratios of the counts to the numbers of ICESat stars are shown in parentheses. The counts are classified by star brightness into five columns with brighter stars to the left and dimmer stars to the right. The table shows that SKY2000 provides complete information for visual magnitudes and nearly complete information for blue magnitudes. Passband 1 and 2 information is above 89% for bright stars. Passband 3 availability is above 86% for all but the dimmest stars.

Table 21. Availability of passband magnitude information in SKY2000.

Passband	$V < 4$	$4 < V < 5$	$5 < V < 6$	$6 < V < 7$	$7 < V$
U	8 (0.01)	26 (0.01)	31 (0.01)	176 (0.05)	138 (0.20)
B	487 (0.99)	1508 (0.99)	2875 (0.99)	3035 (0.99)	678 (0.99)
V	490 (1.00)	1514 (1.00)	2877 (1.00)	3037 (1.00)	679 (1.00)
Passband 1	466 (0.95)	1398 (0.92)	1865 (0.64)	1874 (0.61)	172 (0.25)
Passband 2	461 (0.94)	1356 (0.89)	587 (0.20)	230 (0.07)	16 (0.02)
Passband 3	465 (0.94)	1414 (0.93)	2638 (0.91)	2632 (0.86)	462 (0.68)

Table 22 shows the availability and frequency of additional information for the ICESat stars. The standard astronomical spectral classes are O, B, A, F, G, K, M ranging from blue stars to red stars. Luminosity class represents a range from supergiant stars to dwarf stars. Spectral class and luminosity class were converted to integers for use as input variables to instrument magnitude prediction models. Variable stars were defined here as those whose catalog records included values for variability maximum and minimum magnitudes. A better definition for future use is stars with a non-empty variable name field, which gives a text variable star name for known variables and a numeric identifier for suspected variables. Bright neighbor stars had records that included an angular separation to a bright near-neighbor. SKY2000 defines a bright near-neighbor as having an angular separation of up to 0.6 degrees and a magnitude difference less than two. 0.6 degrees is a large separation for the ICESat trackers so more restricted criteria for bright near-neighbors are used in practice, but the frequencies shown here are a rough indicator. Blended position and blended visual magnitude stars had SKY2000 records that were calculated by combining more than one star. Both indicate cases where a near-neighbor has a significant effect on measurements.

Table 22. Availability and frequency of additional information in SKY2000.

Information	$V < 4$	$4 < V < 5$	$5 < V < 6$	$6 < V < 7$	$V > 7$
Spectral class	486 (0.99)	1506 (0.99)	2860 (0.99)	3026 (0.99)	664 (0.97)
Luminosity	489 (0.99)	1491 (0.98)	2672 (0.92)	2485 (0.81)	496 (0.73)
Variable	294 (0.60)	742 (0.49)	781 (0.27)	535 (0.17)	130 (0.19)
Multiple	271 (0.55)	702 (0.46)	855 (0.29)	637 (0.21)	133 (0.19)
Neighbor	82 (0.16)	437 (0.28)	1736 (0.60)	2485 (0.81)	666 (0.98)
Blended Pos.	46 (0.09)	96 (0.06)	45 (0.01)	35 (0.01)	17 (0.02)
Blended Mag.	19 (0.03)	53 (0.03)	69 (0.02)	23 (0.00)	6 (0.00)

The SKY2000 specification document has further details on available information.[5] Additional types of star identifiers for linking SKY2000 records to records in other star catalogs are of special interest. In particular, the Henry Draper (HD) identifiers in SKY2000 can be compared to the HD identifiers contained in the Hipparcos Main Catalog to link SKY2000 identifiers to Hipparcos identifiers for 82% of the 45,394 SKY2000 stars with visual magnitudes up to eight.

Star brightness and color are commonly characterized using a variety of astronomical quantities. Here visual magnitude is used for brightness, spectral class is used for color, and tracker response is defined as measured instrument magnitude minus visual magnitude. Figure 37 shows a typical scatter plot of tracker response versus visual magnitude for several thousand stars. Points higher in the plot have larger (dimmer) measured instrument magnitudes compared to visual magnitude. Points lower in the plot have smaller (brighter) measured instrument magnitudes compared to visual magnitudes. There are clear layers of the points corresponding to spectral class with blue stars in higher layers and red stars in lower layers. The layers are caused by the greater sensitivity of the detector to red light. The increased scatter within the layers for dim stars may be

due to thresholding by the tracker.[87] Dim stars have smaller signal to noise ratios and are more difficult to threshold and estimate encircled energy.

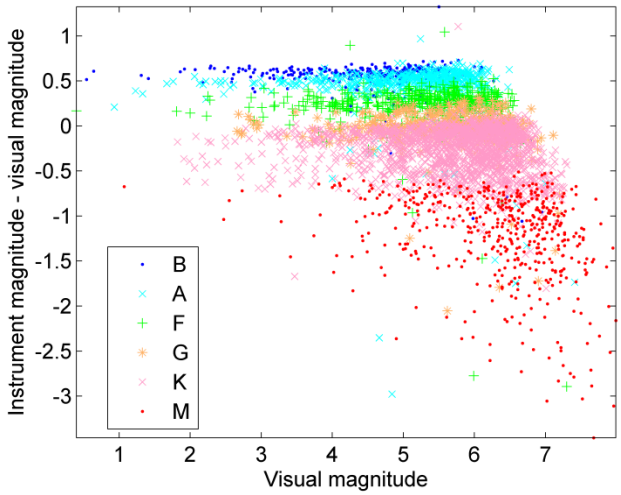

Figure 37. Tracker response to visual magnitude and spectral class.

The responses of multiple trackers can be compared by superimposed or side-by-side scatter plots. A similar method is used here. For each tracker, six curves were fit to the six layers of scatter plot points for the spectral classes. Between visual magnitudes three and six the layers of scatter plot points were roughly linear and linear fits in this region were used. The responses of multiple trackers were compared by superimposing their fit lines rather than their scatter plots. Figure 38 compares the fit lines for the ICESat and RXTE trackers. The responses of the three ICESat trackers to brightness and color are similar but have statistically significant differences. The response of the RXTE tracker shows the bias from the ICESat responses described above in Table 19.

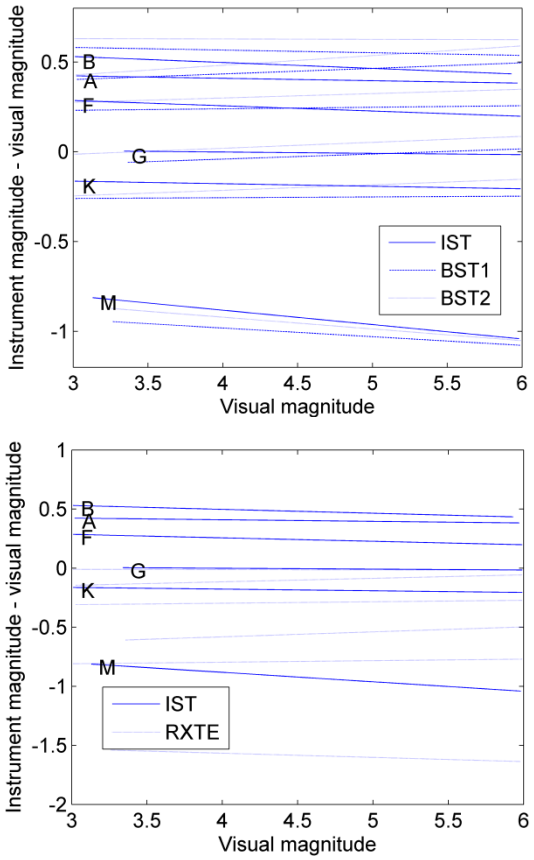

Figure 38. Linear fits to tracker response.

Sixty instrument magnitude prediction models were compared using the 4,319 BST1 instrument magnitude results summarized in Table 19. Visual, blue, passband 1, passband 2, and passband 3 magnitudes were used as model inputs. Passband 3 magnitudes were expected to perform best as they are flight instrument magnitudes from RXTE and SKY2000. Passband 1 and 2 magnitudes were expected to perform next best. They correspond to astronomical red and infrared magnitudes, where star tracker response is typically strongest. Models with and without a color term were evaluated. The color term was an integer s representing star spectral class. An example model for instrument magnitude m without a color term and with visual magnitude m_V and blue magnitude m_B terms is shown in Equation (168).

$$m = c_0 + c_1 m_V + c_2 m_B \tag{168}$$

The same example model but including a color term s is shown in Equation (169).

$$m_i = c_0 + c_1 s + c_2 m_v + c_3 m_b \tag{169}$$

The information contained in the color term was mostly redundant if more than one passband magnitude term was included in the model since the difference of two passband magnitudes effectively characterizes color.

Table 23 shows the performance of the various models that were evaluated. Instrument magnitude prediction error was defined as the difference of an observed and predicted instrument magnitude. The model inputs are identified by V visual, B blue, 1 for passband 1, 2 for passband 2, and 3 for passband 3. Prediction errors for a particular model were calculated using all of the test stars for which SKY2000 included the necessary information. The RMS errors are shown in the table. The ratio in parentheses for each error gives the percentage of stars for which SKY2000 included the necessary information. As expected, passband 3 magnitudes performed the best. Passband 1 magnitudes performed second best and were available for fewer stars.

Table 23. Instrument magnitude prediction errors (RMS).

Inputs	Linear	Quadratic	Linear with s	Quadratic with s
V	0.54 (1.00)	0.51 (1.00)	0.37 (0.99)	0.35 (0.99)
B	0.76 (0.99)	0.72 (0.99)	0.46 (0.99)	0.42 (0.99)
1	0.15 (0.70)	0.15 (0.70)	0.14 (0.70)	0.14 (0.70)
2	0.38 (0.30)	0.38 (0.30)	0.24 (0.30)	0.23 (0.30)
3	0.07 (0.90)	0.07 (0.90)	0.07 (0.90)	0.07 (0.90)
V, B	0.36 (0.99)	0.34 (0.99)	0.34 (0.99)	0.32 (0.99)
V,1	0.15 (0.70)	0.13 (0.70)	0.14 (0.70)	0.13 (0.70)
V,2	0.13 (0.30)	0.13 (0.30)	0.13 (0.30)	0.13 (0.30)
V,3	0.07 (0.90)	0.07 (0.90)	0.06 (0.90)	0.06 (0.90)
B,1	0.15 (0.70)	0.13 (0.70)	0.14 (0.70)	0.13 (0.70)
B,2	0.15 (0.30)	0.15 (0.30)	0.15 (0.30)	0.15 (0.30)
B,3	0.07 (0.90)	0.07 (0.90)	0.07 (0.90)	0.07 (0.90)
1,2	0.13 (0.30)	0.13 (0.30)	0.13 (0.30)	0.13 (0.30)
1,3	0.06 (0.64)	0.06 (0.64)	0.06 (0.64)	0.06 (0.64)
2,3	0.04 (0.28)	0.04 (0.28)	0.04 (0.28)	0.04 (0.28)

Table 24 shows instrument magnitude prediction errors grouped by tracker, visual magnitude, and spectral class B, A, F, G, K, M . The instrument magnitude prediction model used for Table 24 was linear with passband 3 magnitude as input (the fifth row of Table 23). The number of test stars available to calculate each value is shown in parentheses. Very few dim blue stars were available, which demonstrates the smaller sensitivity of the trackers to blue light than to red light. The prediction errors for the RXTE tracker are zero because passband 3 magnitudes are in fact RXTE measured instrument magnitudes.

Table 24. Instrument magnitude prediction errors (RMS).

Star	Tracker	$V < 4$	$4 < V < 5$	$5 < V < 6$	$6 < V < 7$	$7 < V$
B	IST	0.04 (70)	0.05 (96)	0.06 (214)	0.16 (9)	-- (0)
	BST1	0.04 (83)	0.04 (124)	0.08 (139)	0.11 (9)	-- (0)
	BST2	0.03 (84)	0.05 (132)	0.06 (153)	0.12 (5)	-- (0)
	RXTE	0.00 (78)	0.00 (116)	0.00 (137)	0.00 (7)	-- (0)
A	IST	0.03 (54)	0.03 (119)	0.06 (319)	0.08 (25)	0.03 (3)
	BST1	0.02 (66)	0.03 (141)	0.06 (311)	0.05 (42)	0.02 (1)
	BST2	0.03 (70)	0.04 (146)	0.06 (275)	0.07 (48)	0.06 (1)
	RXTE	0.00 (60)	0.00 (128)	0.00 (288)	0.00 (34)	0.00 (1)
F	IST	0.04 (32)	0.04 (79)	0.06 (201)	0.17 (56)	0.01 (1)
	BST1	0.04 (44)	0.04 (89)	0.07 (205)	0.14 (74)	0.02 (1)
	BST2	0.03 (47)	0.04 (87)	0.07 (200)	0.15 (93)	0.03 (1)
	RXTE	0.00 (41)	0.00 (82)	0.00 (194)	0.00 (63)	0.00 (1)
G	IST	0.06 (21)	0.04 (58)	0.05 (161)	0.08 (133)	0.09 (2)
	BST1	0.06 (21)	0.03 (71)	0.04 (179)	0.06 (156)	0.06 (4)
	BST2	0.05 (24)	0.03 (64)	0.05 (180)	0.07 (167)	0.10 (2)
	RXTE	0.00 (18)	0.00 (63)	0.00 (163)	0.00 (146)	0.00 (1)
K	IST	0.03 (74)	0.03 (155)	0.09 (540)	0.07 (654)	0.12 (9)
	BST1	0.03 (100)	0.02 (211)	0.08 (602)	0.06 (696)	0.06 (35)
	BST2	0.03 (102)	0.03 (215)	0.08 (613)	0.06 (687)	0.07 (33)
	RXTE	0.00 (96)	0.00 (203)	0.00 (564)	0.00 (659)	0.00 (32)
M	IST	0.18 (9)	0.19 (34)	0.05 (82)	0.14 (185)	0.18 (102)
	BST1	0.05 (11)	0.06 (41)	0.04 (103)	0.05 (217)	0.17 (114)
	BST2	0.03 (10)	0.06 (41)	0.04 (107)	0.05 (214)	0.13 (113)
	RXTE	0.00 (11)	0.00 (39)	0.00 (99)	0.00 (211)	0.00 (113)

Table 25 compares the performance of three important instrument magnitude prediction models. The means and standard deviations of the prediction errors for the IST and BSTs are shown along with the number of test stars in parentheses. For a given tracker, each test star was included in the table once using the best model for which information was available in SKY2000. Passband 3 magnitudes result in significant prediction improvements.

Table 25. Comparison of three important instrument magnitude prediction models.

Model	IST	BST1	BST2
$1,3$	-0.00 ± 0.07 (2463)	-0.00 ± 0.06 (2800)	-0.00 ± 0.05 (2879)
$V,3$	0.00 ± 0.09 (1065)	0.00 ± 0.06 (1107)	0.00 ± 0.06 (1055)
V,B	0.00 ± 0.38 (298)	0.01 ± 0.40 (411)	0.01 ± 0.40 (460)

Two classes of stars are commonly associated with instrument magnitude prediction errors. When large measured minus predicted residuals are found for a particular star's instrument magnitude, there is usually a bright near-neighbor, or the star is variable. Examples from the ICESat results are given for both classes. Another source of errors is variation of tracker response due to aging and environmental effects. Tracker response is discussed last.

Near-neighbor stars generally cause negative instrument magnitude prediction errors, where the measured instrument magnitude of the star is smaller than its predicted value because of light from near-neighbors. Figure 39 shows an example. The IST acquired these stars regularly. They form the Trapezium open cluster in the Orion Nebula. There are at least five relatively bright stars within 30 arcseconds. At various times the attitude processor identified HD 37022 and HD 37023 and treated them as the guide star. In both cases the magnitude prediction errors were high due to the various other light sources.

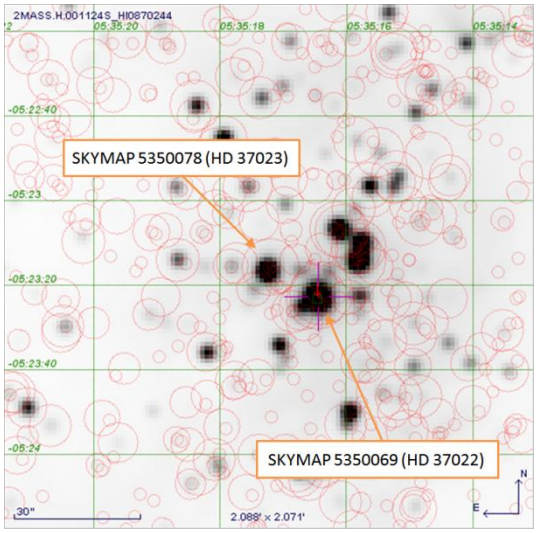

Figure 39. Stars with instrument magnitude prediction errors caused by near-neighbors.

Table 26 shows a set of stars whose instrument magnitude prediction errors were large for both BSTs. Table 26 demonstrates that positive errors are generally associated with variable stars, while negative errors are associated with both variable and non-variable stars. The non-variable stars with negative errors are generally associated with near-neighbors. In Table 26 the measured instrument magnitude is labeled m and the measured minus predicted instrument magnitude is labeled $\tilde{m} \equiv m - m_{predicted}$. Passband 3 magnitudes and models were available for all of these stars. Smithsonian Astrophysical Observatory (SAO) identifiers are given for use with astronomical databases. The first two stars in the table are the members of the binary pair shown above in Figure 35.

Table 26. Stars whose prediction errors were large for both BSTs.

SKYMAP	SAO	m BST1	m BST2	$\tilde{m}$ BST1	$\tilde{m}$ BST2	Note
15380094	140671	6.84	6.94	-0.80	-0.90	
15380095	140672	6.80	6.91	-0.77	-0.83	
16310033	84423	5.91	5.90	-0.77	-0.74	
4030090	169080	6.28	6.37	-0.48	-0.47	
13390077	100654	6.32	6.4	-0.38	-0.40	variable
3470095	168836	6.14	6.25	-0.38	-0.37	
3550050	56815	6.67	6.76	-0.34	-0.30	variable
10180019	178644	6.06	6.14	-0.27	-0.26	variable
13550141	258683	5.78	5.85	-0.27	-0.24	
22230017	34387	5.72	5.80	-0.25	-0.25	variable
14130055	29045	5.04	5.03	-0.29	-0.19	
10140	147042	3.51	3.54	-0.24	-0.23	variable
20170002	125646	6.24	6.33	-0.24	-0.23	
13470039	252448	5.14	5.20	-0.23	-0.22	variable
16040068	159665	4.57	4.65	-0.21	-0.22	
10340162	178993	6.51	6.61	-0.20	-0.22	
2020164	110291	4.52	4.58	-0.21	-0.21	
23050063	191638	6.40	6.49	-0.22	-0.19	variable
14560071	206112	5.91	5.99	-0.19	-0.22	
10430073	118448	5.83	5.90	-0.20	-0.20	
10210005	15147	6.15	6.24	0.18	0.18	variable
510044	11430	5.05	5.12	0.19	0.18	variable
16350003	17155	5.61	5.69	0.19	0.19	variable
13490099	224471	3.83	3.85	0.21	0.18	variable
22250055	127520	5.29	5.35	0.20	0.21	variable

Table 26 (continued)

16270002	159918	4.47	4.53	0.2	0.23	variable
23560031	192250	6.33	6.41	0.21	0.23	variable
8290136	135976	5.05	5.12	0.29	0.23	variable
22550003	108255	5.97	6.05	0.25	0.27	variable
23000016	35039	4.85	4.87	0.33	0.38	variable

Variable stars cause both positive and negative instrument magnitude prediction errors. Figure 40 shows BST2 instrument magnitudes for the Cepheid variable Mekbuda (Zeta Gemini, SKYMAP 7040034, HD 52973). The SKY2000 values for the variability max and min visual magnitudes are 3.62 and 4.18, the visual magnitude is 4.01, and the period is 10.15 days. The variability amplitude is significantly larger than the prediction uncertainty of about 0.06 1σ for models including a passband 3 term. The instrument magnitude prediction error $\tilde{m} \equiv m - m_{predicted}$ varies periodically with the star brightness, in this case between approximately $\tilde{m} = -0.15$ and $\tilde{m} = +0.15$.

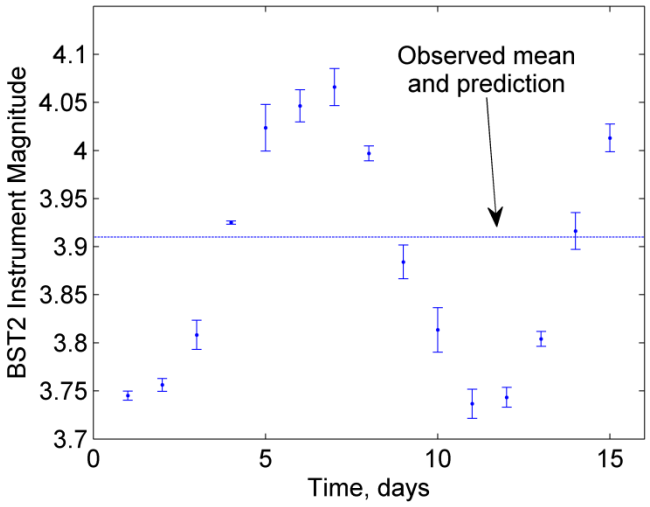

Figure 40. BST2 instrument magnitudes for the Cepheid variable Mekbuda.

Table 27 shows variable stars that were found to have large prediction errors in the instrument magnitude results. The values of the predicted instrument magnitude $m_{predicted}$ and the prediction error $\tilde{m} \equiv m - m_{predicted}$ are given. The last two columns of the table show the variability amplitude and period information available in SKY2000. Henry Draper (HD) identifiers are given for use with astronomical databases.

Table 27. Variable stars with large prediction errors.

SKYMAP	HD	$m_{predicted}$	$\tilde{m}$	Amplitude	Period (days)
2530146	18242	4.928	1.109	9.6	407.6
23430138	222800	4.186	-0.3	6.6	387
9320044	82901	4.052	1.111	6.6	308.7
19060091	177940	4.553	-0.555	6.5	284.2
21350031	206362	6.09	-0.691	5.5	486.8
13490007	120285	3.185	0.403	3.9	361
7130116	56096	2.901	0.914	3.6	140.6
18380073	172171	4.652	-0.965	3.3	328.9
8290136	71887	5.053	0.29	3.2	290
10070209	88028	5.524	-0.277	2.3	780
16350003	150077	5.614	0.193	2.3	78
22230017	212466	5.806	-0.259	2.1	346
23590013	224583	5.969	-0.562	2	141
6050169	41698	4.645	-0.406	1.6	89
8580035	76734	5.774	-0.689	1.5	60
13470039	119796	5.146	-0.231	1.3	--
8240086	70938	4.936	0.246	1.3	--
18500232	174638	4.021	-0.211	1.1	12.9
6250055	44990	5.978	-0.255	1	27
3550050	24534	6.671	-0.345	1	--

Table 27 (continued)

22030149	209598	4.684	-0.227	0.9	929.3
16010041	142941	6.463	-0.282	0.9	6.3
16270002	148184	4.536	0.237	0.8	--
23000016	217476	4.879	0.388	0.8	--
22550003	216724	6.056	0.276	0.7	--
20510095	198726	5.9	0.292	0.7	4.4
23050063	218074	6.402	-0.226	0.7	--
11450105	102159	5.451	-0.254	0.6	42
13490099	120324	3.747	0.248	0.6	--
3260092	21242	6.441	0.319	0.4	6.4
10180019	89353	6.066	-0.27	0.4	--
7520023	64052	4.962	-0.259	0.3	35
22250055	212571	5.353	0.213	0.3	--
15380045	139608	4.547	-0.275	0.3	--
2590085	18482	5.649	-0.197	0.2	--
7260238	58978	6.425	-0.221	0.2	--

Tracker response can vary over time due to aging effects, or environmental factors such as background light from the sun and moon. Table 28 shows the variations over time of measured instrument magnitudes for a set of stars that were routinely measured. The earliest measurements of individual stars were used to define reference values and differenced with later measurements. Statistics for the tables below were calculated using two orbital revolutions from 228 days with 457,438 tracker passes of 6,404 unique stars. The number of stars used is indicated in parentheses.

For all three trackers the mean differences from the reference values appear to be zero-mean variations and not significant compared to the uncertainties. This suggests that

variation over time of the tracker responses did not cause significant effects. This conclusion was called into doubt by other types of evidence however. Some evidence was seen of small decreases over time of the measured instruments magnitudes for individual stars.

Table 28. Variations of magnitudes over time for groups of stars due to tracker aging.

Time period	IST	BST1	BST2
2003 to 2004	-0.017 ± 0.045 (43)	-0.002 ± 0.046 (111)	-0.016 ± 0.043 (112)
2003 to 2005	0.005 ± 0.032 (46)	0.010 ± 0.032 (42)	0.011 ± 0.030 (53)
2003 to 2006	-0.002 ± 0.040 (56)	-0.016 ± 0.035 (218)	-0.034 ± 0.059 (222)
2003 to 2006	-0.015 ± 0.057 (146)	-0.006 ± 0.028 (176)	0.021 ± 0.023 (169)
2003 to 2007	-0.011 ± 0.031 (38)	0.007 ± 0.021 (52)	0.031 ± 0.028 (47)

The LRS output brightness counts, not instrument magnitudes. Transformation from counts to instrument magnitudes was performed internally by the other three trackers. The LRS brightness counts were converted to instrument magnitudes using the standard astronomical equation and a reference star. The reference values were an instrument magnitude of 3.68 and LRS brightness counts of 1500, so the LRS instrument magnitude was given by Equation (170).

$$m = 3.68 + 2.5 log\left(1500 / counts\right) \tag{170}$$

Figure 41 shows the differences between LRS and IST instrument magnitudes for the calibration stars. The differences before correction of the LRS values are shown in red, and after correction in blue. LRS instrument magnitudes were corrected using Equation (171).

$$m_{corrected} = m - \left(.0207 m^2 - .0618 m - .0546\right) \tag{171}$$

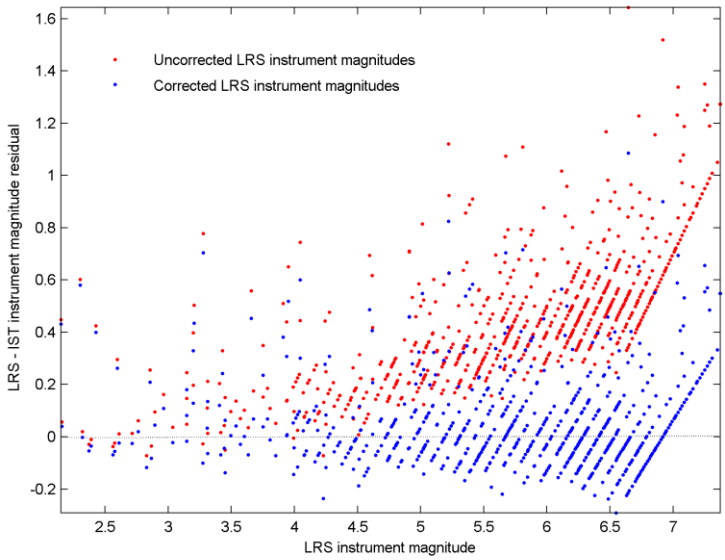

Figure 41. LRS instrument magnitude residuals before correction (red) and after correction (blue).

The trend in the uncorrected LRS instrument magnitudes may have been related to nonlinearities in the LRS brightness counts. The LRS had a relatively small 0.5° field of view. With typical defocusing to improve sub-pixel centroiding, star light appears to have been partially cut-off at the edges of the field of view so that brightness counts varied strongly with position. Figure 42 shows all of the instrument magnitude measurements in the dataset for a typical star (SKYMAP 300127). The measurements were collected from multiple passes which were widely separated in time. The time intervals separating different passes were removed so that the measurements appear to be continuous in time. Individual LRS passes of the star are apparent because of the position dependent variations of the LRS instrument magnitudes.

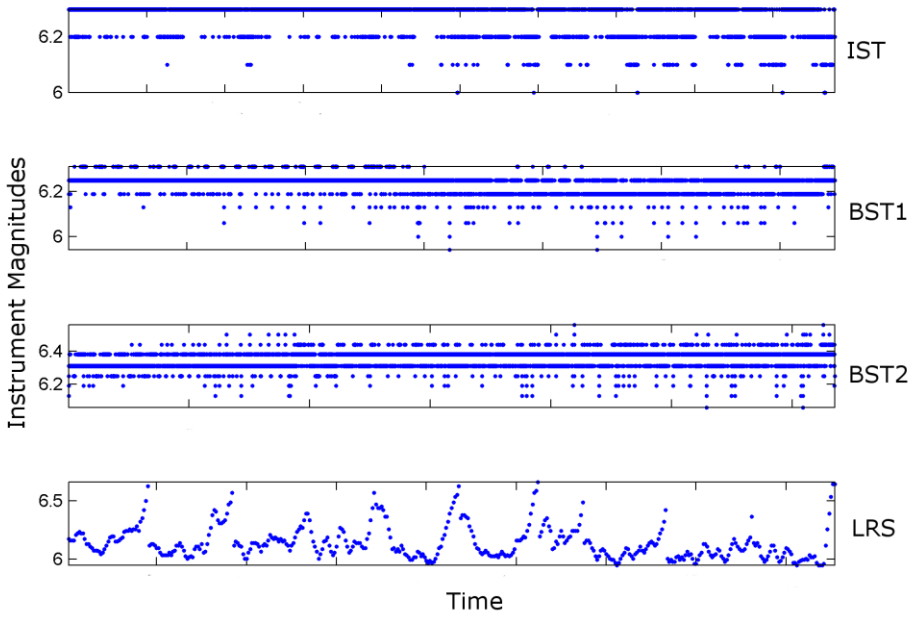

Figure 42. Instrument magnitude measurements from multiple passes of a typical star.

Because of the variations of the instrument magnitude measurements demonstrated by Figure 42, particularly from the LRS, a robust statistic that could be applied identically for all four trackers was preferable over the mean value. The trimmed mean[131] and Winsorized mean[131] were evaluated. The median value was the simplest alternative with no tunable parameters that could introduce tracker dependencies.

VI. Alignment Results

The state results output by the filter were composed of three types of information forming three time-series with approximately 1 Hz sampling frequencies. The time-series represented the spacecraft body frame attitude, the four tracker alignments, and the star position residuals, as summarized in Table 29.

Table 29. State results output by the filter.

Quantity	Representation
Body attitude changes	Small correction rotations of the body frame
Overall state	Pointing vectors in the body and celestial frames
Star residuals	Small error rotations in the body and celestial frames

The attitude was represented by its variations over time, expressed in the body frame. The absolute attitude in the celestial frame was less significant in this case than the corrections made by the filter update phase, and was recoverable from the state results. The overall filter state was equivalent to four tracker pointing vectors in the celestial frame, representing the combined alignment and attitude states. The pointing vectors were expressed relative to both the body and celestial frames. The star residuals were an empirical measure of the uncertainties in the tracker pointing vectors. If the filter states resulted in an incorrect tracker pointing vector, the measurement residuals for that tracker were large. If the pointing vectors were accurate, the residuals reflected measurement noise.

a. Uncertainties

Uncertainties in the tracker pointing vectors were estimated directly from the star pass residuals described in Section IVe. In some configurations of the filter it was possible for the alignment and attitude states to contain drifts that cancelled one another in the pointing vectors. This is referred to as attitude drift because the attitude state was shared

by all four pointing vectors. If there was attitude drift, the uncertainties in the individual alignment and attitude states were larger than the pointing vector uncertainties. In this sense the pointing vector uncertainties were lower-bounds for the individual alignment and attitude uncertainties. Pointing vector uncertainties are discussed first, followed by alignment and attitude uncertainties.

Table 30 shows uncertainties for the tracker pointing vectors. They were estimated as the standard deviations of the pass residuals. For a particular alignment coordinate, all non-outlier pass residuals from the 244 normal granules were used. The pointing vector uncertainties combined the alignment and attitude uncertainties, and the attitude uncertainties were shared by all four trackers. When there was no attitude drift, 0.98 arcseconds 1σ was an upper-bound on the attitude uncertainty in the north coordinate, and 0.87 arcseconds 1σ was an upper-bound on the attitude uncertainty in the west coordinate.

The small pointing uncertainties are a result of simultaneous use of multiple stars and trackers for measurement updates. They are smaller than the tracker measurement noise values shown in Section Va because of averaging over large numbers of measurements in each pass residual, and they reflect the fact that the more simultaneous stars and trackers used to update the filter, the lower the sensitivity to noise in the individual star measurements.

Table 30. Uncertainties (1σ) for tracker pointing vectors.

Alignment coordinate		Sample size	1σ, arcseconds
IST	body north	142052	1.56
IST	body west	138764	1.04
LRS	body north	2686	2.54
LRS	body west	3433	1.75
BST1	body north	145501	0.98
BST1	body west	144302	0.87
BST2	body north	150950	1.26
BST2	body west	149456	0.90

In all cases the uncertainties are larger in the north coordinates than the west coordinates, and larger for the GLAS trackers than for the bus trackers. This agrees with the alignment plots below, which show more variation of the alignment north coordinates, and more variation of the GLAS tracker alignments. The bus trackers were relatively stable compared to the GLAS trackers.

Both tracker alignment states and error signals were represented by quantities near zero. The alignment states were small deviations from reference values, and the error signals were estimates of small and approximately zero mean pass residuals. It was useful to plot the alignments and error signals together, as shown in Figure 43. Spikes in the error signals indicate increased uncertainty in the filter states. In this case high frequency alignment variations due to an ocean scan maneuver are correlated with spikes in the error signals. The problem with this type of plot is that errors in the body frame attitude state can counteract errors in the alignment states. The fact that an error signal is zero does not mean that individual states are accurate, only that the tracker pointing vector and combined alignment and attitude states are accurate.

The LRS was unique in several ways. It was deactivated during daylight because of glare, so LRS attitude states are constant for large intervals. Even when activated, the LRS made relatively sparse measurements, so the attitude states and resulting pass residuals and error signals are less continuous for the LRS than for the other trackers. As a result, the LRS plots are very different than the plots for the other three trackers. They are effectively lower resolution. This is expected because the LRS was designed specifically for higher resolution measurements of single stars, with a direct tradeoff in lower resolution for overall attitude and alignment estimates.

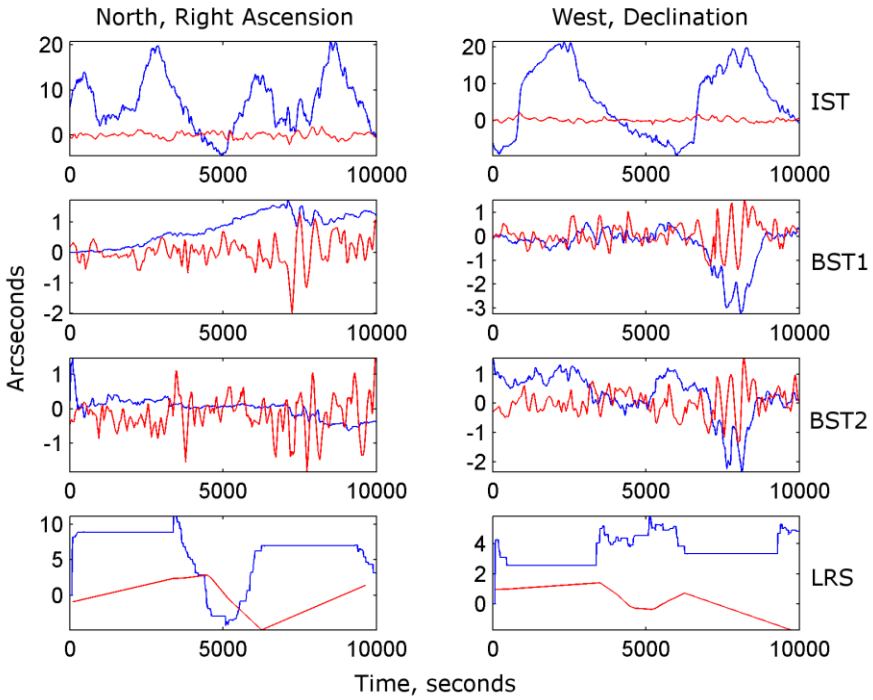

Figure 43. Alignments (blue) and error signals (red) for a single granule

Figure 44 shows the alignments for 2003 campaign 2A. It was a useful test case because there were two commanded GLAS temperature changes. The temperature changes resulted in two alignment step changes, effectively dividing campaign 2A into three periods 2A1, 2A2, and 2A3. The two step changes are clear in the IST body west coordinate, where the curves are grouped in three clusters. The basic set of subfigures in

Figure 44 is comprised of four rows and two columns, and is duplicated side-by-side for granules without maneuvers on the left, and granules with maneuvers on the right. Each curve in a subfigure represents an alignment coordinate for a single granule over a 10,000 second time-span. The curves are color coded with blue curves earlier in time and red curves later in time. Color represents a longer time scale of days rather than seconds. Since the same 10,000 second section was taken from each granule, the orbital positions are aligned in all of the curves shown in the subfigures. If $t = 0$ seconds is the ascending equator crossing for one of the curves, then the same is true for all of the curves.

The variations of the GLAS trackers are large, approximately 50 arcseconds. In the first period (blue) the IST body west coordinates were centered near +10 arcseconds, and in the third period (red) they were centered near -20 arcseconds. The two step changes are rapid, but one of the granules happened to fall during the second step change and appears as the single purple curve between the second and third periods in the granules without maneuvers. These results agree with the results later in this chapter, where it is clear from the long time scale results that there were large variations of the body north and body west coordinates of the GLAS trackers. The variations of the bus trackers were roughly an order of magnitude smaller, approximately 5 arcseconds. The significance of these variations can be judged by comparing them to the tracker pointing uncertainties, which range up to 1.6 arcseconds 1σ for the IST, and up to 1 arcseconds 1σ for BST1. In effect the alignment variations of the GLAS trackers had a high signal to noise ratio of about 50/1.6 while the bus trackers had a low signal to noise ratio of about 5/1.

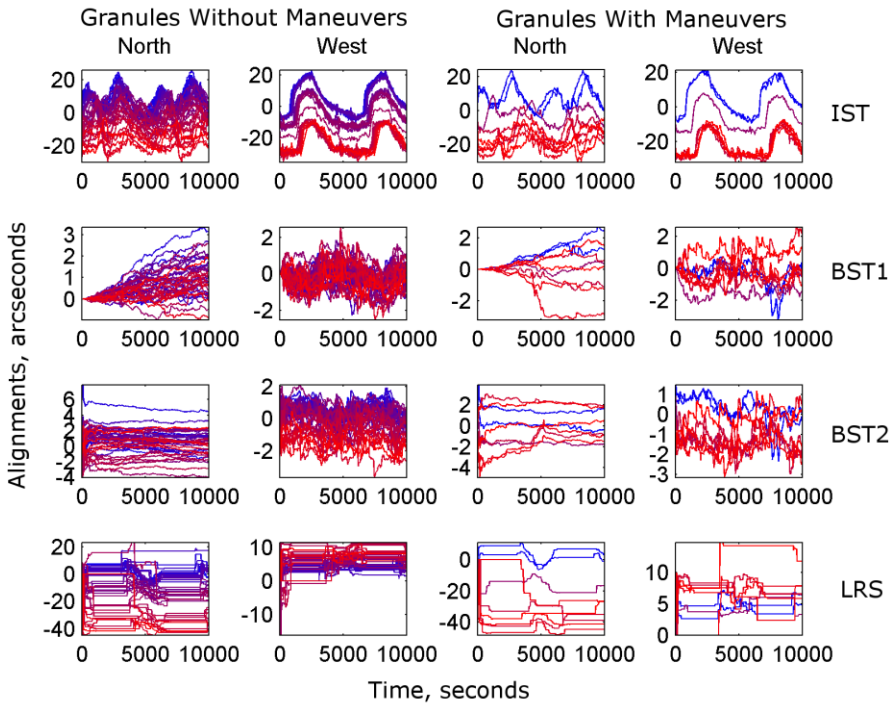

Figure 44. 2003 campaign 2A alignment states.

The bus tracker north coordinates in Figure 44 raise questions about the uncertainties in the individual attitude and alignment states. The curves vary significantly and are less consistent than the other coordinates. Their magnitudes are near the pointing vector uncertainty level, and it appears they contain drifts with a magnitude of a few arcseconds. In the BST1 body north coordinates with maneuvers there is a case with a clear step change caused by a maneuver. If the alignment states drifted, then they were counteracting corresponding drifts in the attitude in order to minimize the effects on the tracker pointing vectors. When there is such an attitude drift of a few arcseconds, it is less significant for the GLAS trackers, which have alignment variations an order of magnitude larger, demonstrating that the significance of an attitude drift depends on its relative scale. In practice, attitude drift was less significant for the GLAS trackers, and more significant for the bus trackers. Attitude drift can be prevented by holding the BST1 alignment constant, which effectively redefines the body frame as the BST1 frame instead of the gyro frame. The disadvantage is that BST1 alignment variations are not

estimated. Since the alignment variations of the bus trackers were relatively small, this was an acceptable trade-off.

The term attitude drift is used here to cover slow changes over time, rapid changes during initial convergence of the attitude states, and rapid step changes during maneuvers. The effect on the tracker pointing vectors of attitude drift is counteracted by opposing drifts of the tracker alignment states. Attitude drift can be caused by defining the body frame using an instrument that does not make direct attitude measurements. In practice, it occurred when the gyro frame was defined to be the body frame. Gyros measure angular rate, but do not make direct attitude measurements. Propagation error is possibly a better term for these errors since they occur during the filter propagation phase. They can grow gradually over time in a random-walk fashion when there are not maneuvers, as suggested by the term drift. They can grow rapidly during maneuvers because the propagation phase has to track more complex rotation.

The ideal situation was for the body frame to be defined as the gyro frame and for all of the tracker alignment states to be free to vary relative to it. If the initial attitude state for the body frame and the gyro measurements were good, then the attitude state would follow the true body frame attitude and the star measurement residuals would be used to correct the tracker alignment states and make relatively small corrections to the attitude state. Because the gyro unit made rate measurements, not direct attitude measurements, there was the possibility of ambiguity between the alignment and attitude states. An arbitrary drift could be present in the attitude if corresponding alignment drifts cancelled its effects on the tracker pointing vectors.

In practice the actual filter runs were not ideal. The initial attitude for the body frame contained errors, and the gyro measurements and measurement model were not perfect. The results below demonstrate that when using the gyro frame as the body frame there was detectable drift in the attitude states, at the arcsecond or tens of arcseconds level. The drift could be prevented by holding the BST1 alignment constant, which effectively

redefined the body frame as the BST1 frame instead of the gyro frame, with the disadvantage that BST1 alignment variations were not estimated.

Filter 1 denotes the filter configuration with the BST1 alignment free and the body frame defined as the gyro frame. Filter 2 denotes the filter configuration with the BST1 alignment held constant so that the body frame is effectively defined as the BST1 frame. The difference between the IST alignment states from Filter 1 and Filter 2 was a direct estimate of the attitude drift in Filter 1. The large IST alignment orbital variation, on the order of fifty arcseconds, provided a test signal with a high signal to noise ratio, as demonstrated below.

Figure 45 shows the Filter 1 alignment states for the 244 normal granules in the dataset. The BST1 alignment states were free to vary, but played a special role in the initialization and convergence of each filter run. The BST1 alignment covariance was kept small at the beginning of each filter run in order to make the filter more robust to errors in the initial conditions and to reduce the effects of attitude drift while the other tracker alignment states converged. One effect was that the BST1 alignment variations began relatively slowly. The IST alignment variations are relatively large, both on orbital and longer time scales, and clustering by campaign is clear in the IST west coordinates. For all of the trackers, the alignment variations in the north coordinate are relatively large compared to those in the west coordinate. The LRS in particular has alignment variations in the north coordinate that are comparable to the IST variations. The spacecraft was rotating about the body north axis and the stars had an apparent rate of 223 arcseconds per second in the body west direction. Figure 46 shows the alignments for Filter 2 with the BST1 alignment held constant to prevent attitude drift. The two figures are nearly indistinguishable except for the vertical scale on the BST1 subfigures, demonstrating that attitude drift had small, second-order effects on the IST, LRS, and BST1 alignments.

The three peaks in the bus tracker west coordinates are caused by ocean scan maneuvers. During maneuvers, errors in the filter propagation phase accumulate in the attitude state

as a type of attitude drift. These errors can be reduced by improving the gyro measurements and measurement model, as discussed below.

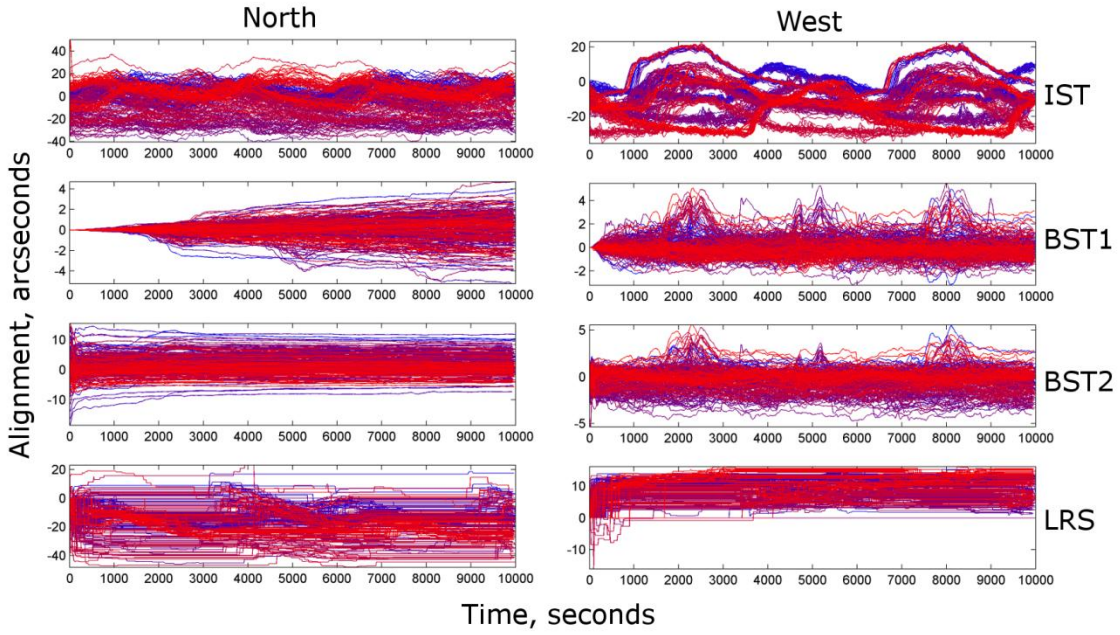

Figure 45. Filter 1 alignments for all granules with all trackers free.

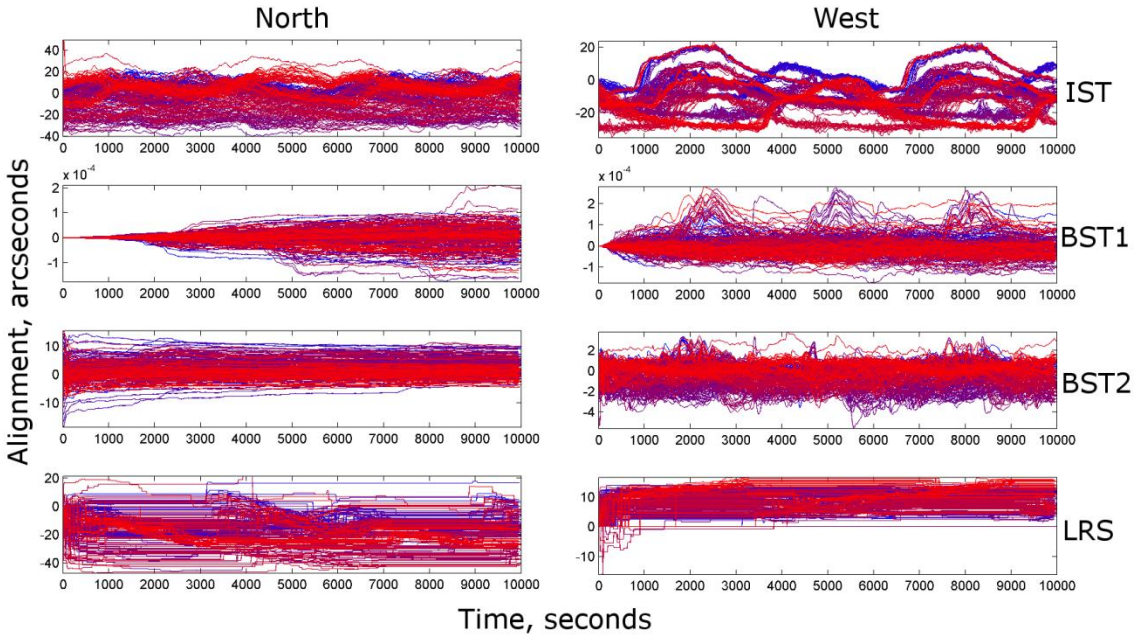

Figure 46. Filter 2 alignments for all granules with BST1 held nearly constant (10^{-4} arcseconds) so effectively defined as the body frame.

The following two figures demonstrate the effects of attitude drift. Figure 47 shows the IST alignment differences between Filter 1 and Filter 2 for 28 granules. 28 curves are superimposed in each subfigure. The difference Filter 1 minus Filter 2 is shown on the right. The Filter 1 and Filter 2 subfigures are almost indistinguishable at this scale, just as Figure 45 and Figure 46 are nearly indistinguishable. However, the Filter 1 minus Filter 2 subfigures show that there were systematic differences on the order of two or three arcseconds. It will be demonstrated in Figure 48 that these systematic differences match the drifts in the free BST1 alignment in Filter 1. The same drifts appear in both the IST and BST1 alignments because they are counteracting drifts in the attitude.

Figure 48 superimposes the IST Filter 1 minus Filter 2 differences from Figure 47 with similar differences for the BST1 alignment. As discussed above, in Filter 1 the BST1 alignment states were free to vary. In Filter 2 they were effectively held constant at zero. In both Filter 1 and Filter 2 the BST1 alignments played a special role in the initialization and convergence of each filter run. The BST1 alignment covariance was kept small at the beginning of each filter run. As a result, the BST1 alignment variations began relatively slowly, this is particularly apparent in the north coordinate where they gradually diverge from zero. The Filter 1 minus Filter 2 differences for the IST match those for BST1. In Filter 1 the free BST1 alignments can drift along with a counteracting drift in the attitude such that they cancel each other in the BST1 pointing vectors and measurements residuals. The attitude drift directly affects the IST alignments so the same drifts appear in both the IST and BST1 alignments.

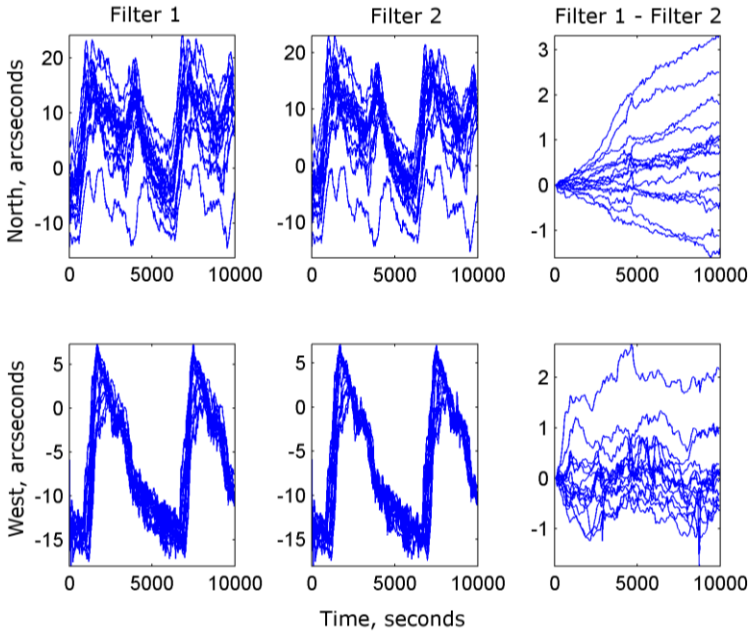

Figure 47. IST alignment differences between Filter 1 and Filter 2 for 28 granules. The difference Filter 1 minus Filter 2 is shown on the right.

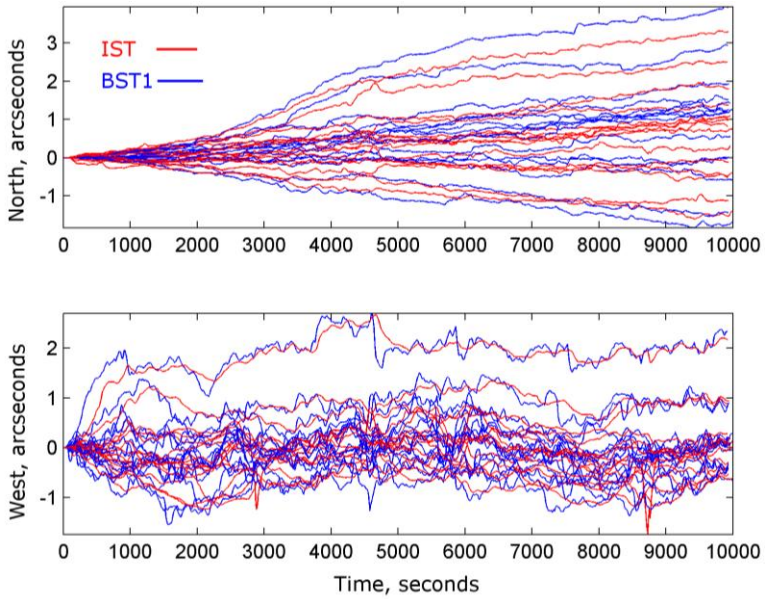

Figure 48. IST and BST1 alignment differences between Filter 1 and Filter 2 for 28 granules. The same drifts appear in both the IST and BST1 alignments, counteracting drifts in the attitude.

The most significant effect of attitude drift was the need for two filter configurations, Filter 1 and Filter 2. Filter 2 prevented attitude drift by holding the BST1 alignment constant, effectively redefining the BST1 frame as the body frame instead of the gyro frame. The results from Filter 2 for the IST, LRS, and BST2 were not qualitatively different than those from Filter 1. Essentially there was increased consistency of the relatively small BST2 alignment variations.

The BST1 alignments were held constant during the initial convergence period in both Filter 1 and Filter 2. Filter 1 runs began with a small initial covariance for the BST1 alignment and the process noise was allowed to gradually increase the uncertainty to levels where the BST1 alignment began to vary. This is apparent in the figures where the BST1 north and west coordinates, particularly the north coordinate, only gradually change from their initial values of zero. To reconfigure Filter 1 as Filter 2, the only change was to set the process noise small for the BST1 alignment. With both the initial covariance and process noise set small, the BST1 alignment was effectively removed from the filter state.

Holding BST1 constant at the beginning of filter runs was an ad hoc method to make the filter more robust to errors in the initial conditions, particularly the initial attitude state. In the 244 normal granules, initial conditions were the primary factor in attitude drift at the beginning of filter runs. After initial filter convergence, maneuvers were the primary factor, as discussed in the next subsection. Temporarily preventing attitude drift by holding BST1 constant decreased the sensitivity to errors in the initial conditions.

Figure 49 shows the alignment results for the bus trackers in five problem granules where there were significant initial convergence problems due to poor initial conditions. The behavior was similar for both Filter 1 and Filter 2. The BST2 north coordinates jump to unrealistic values. In order for the filter to identify stars and make usable star predictions, the attitude state must drift to counteract the effects of the alignments on the tracker pointing vectors.

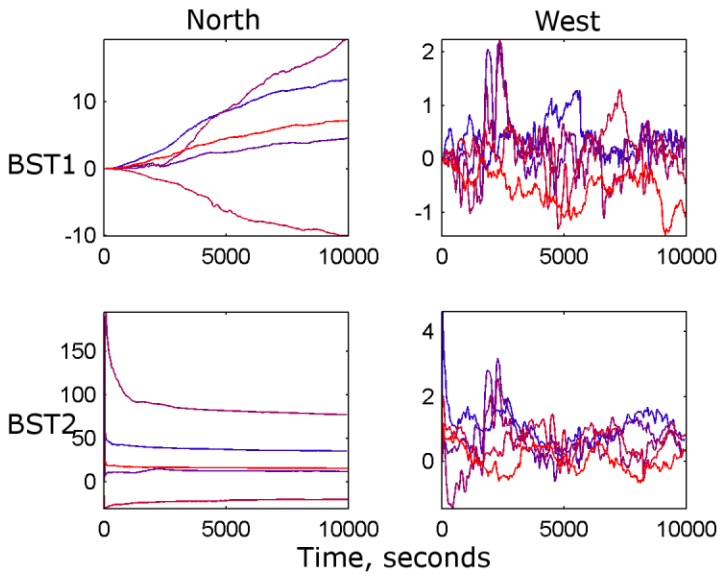

Figure 49. Problem granules with poor initial convergence of the BST2 north coordinate.

Maneuvers caused significant attitude drifts in eleven problem granules. The standard maneuver was an ocean scan lasting 1000 seconds. A related maneuver was an around world scan with larger angular rate variations and covering a complete orbital revolution. There were also intermittent non-scan maneuvers. Ocean scans affected the results in 91 of the 244 normal granules. Around the world scans and non-scan maneuvers resulted in problem granules.

Figure 50 shows the angular rates from a problem granule with both an ocean scan and an around the world scan. The alignment results for four similar problem granules are shown on the right, demonstrating the effects of both ocean scans and around the world scans. The ocean scan covers about 1000 seconds and its amplitude is about 400 arcseconds per second peak-to-peak. The around the world scan extends beyond the end of the granule to cover an orbital revolution and its amplitude is about 500 arcseconds peak-to-peak. The ocean scan does have a significant effect on the alignment results, the west coordinates change from their steady state values and oscillate with the angular rates, but return to the steady state values when the ocean scan ends. The BST2 north coordinate has different steady state values before and after the ocean scan. This is evidence that the attitude state

has drifted. The around the world scan has a similar effect but lasts longer and has larger oscillations. The alignments continue diverging from their steady state values while the around the world scan continues, and clearly oscillate along with the angular rates. The attitude state must drift to counteract the alignments.

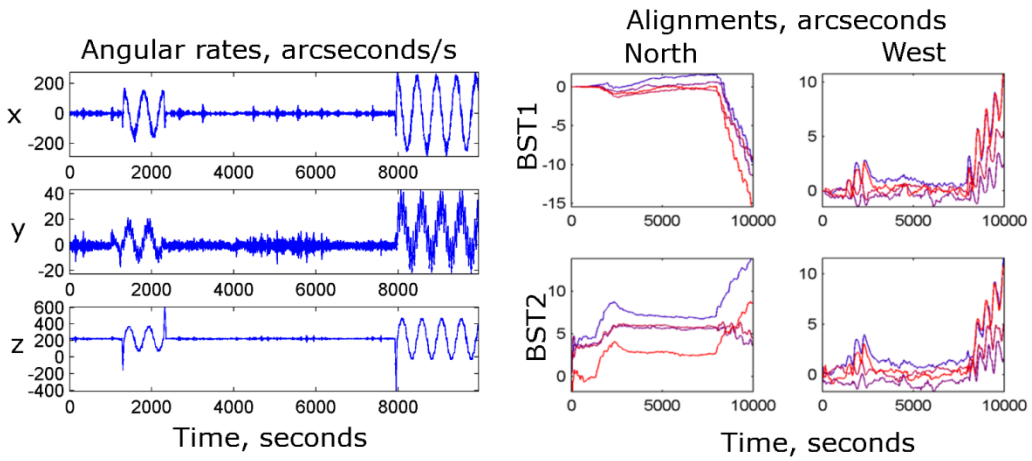

Figure 50. Problem granules with ocean scans and around the world scans.

Figure 51 shows the angular rates from one of three problem granules caused by non-scan maneuvers. The non-scan maneuver took place near $t = 5000$ seconds in two of the granules, and near $t = 8000$ seconds in the third granule. In all three granules the angular rate histories during the non-scan maneuvers were similar. The maneuvers were largely yaws about the zenith direction. This differed from the ocean scans and around the world scans where yaw was relatively small. The effects of non-scan versus scan maneuvers on the alignment results were different, as shown by comparing the right sides of Figure 50 and Figure 51. One characteristic of the alignment results in Figure 51 is that there are two steady state alignment values, one before the maneuver and another after the maneuver, for both north and west coordinates and for both BST1 and BST2. The maneuvers caused step changes of the attitude drifts, which were counteracted by the alignments.

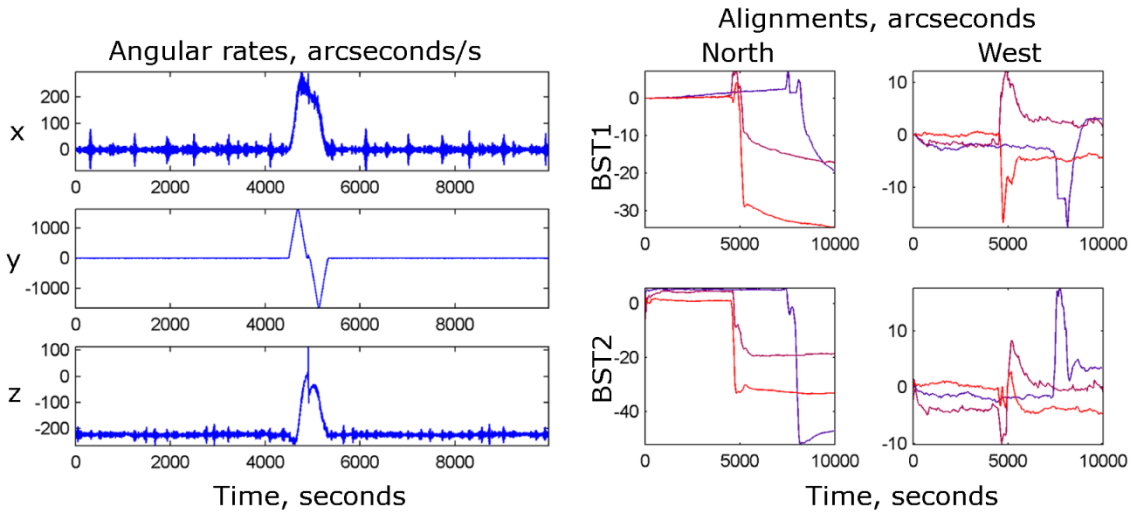

Figure 51. Problem granules with non-scan maneuvers.

Attitude drifts during maneuvers demonstrate the importance of the gyro measurement model and gyro propagation of the attitude state when the angular rates are varying. In the ideal case, with perfect gyro measurements and Filter 1 tuning, attitude propagation would track the true attitude perfectly. The fact that significant attitude drifts appeared in Filter 1 during maneuvers suggests that improvements are possible in the use of the gyros.

The small pointing uncertainties demonstrate that the combined filter states are accurate, but the individual alignment states are of interest here and attitude drift increases the alignment uncertainties in the Filter 1 results. Attitude drift was on the order of a few arcseconds over the 10,000 second filter runs when there were not maneuvers, which is relatively small in comparison to the roughly 50 arcsecond alignment variations of the GLAS trackers. On the other hand, the uncertainty from attitude drift was on roughly the same scale as the bus tracker alignment variations. As a result, the overall approach to interpreting the alignment results focuses on the GLAS trackers. The emphasis is also on Filter 2 results. Since the Filter 1 results are evidence that the bus tracker variations are small, the fact that BST1 alignments are not estimated by Filter 2 is an acceptable trade for reduced attitude drift.

b. Alignments

The overall results for the dataset are represented by plots of the alignment variations. One orbital revolution was extracted from each day and the alignment states were plotted sequentially day by day. The sequence could be extended over arbitrary time periods. Figure 52 is an example. Here the body north alignment states for the IST and LRS are plotted for the first four days of 2003 campaign 2A. Only four days are shown so that orbital variations are clearly visible, but the real value of this type of figure is for plotting many days. When all 244 days in the dataset are included, the orbital signals are no longer resolvable, but systematic variations of the alignments over long time scales are apparent. There is evidence of correlation between the IST and LRS alignment variations in Figure 52 during the periods where the LRS alignments are not constant while the LRS was deactivated in daylight. IST and LRS correlations on orbital and longer time scales are an important question in the following discussion.

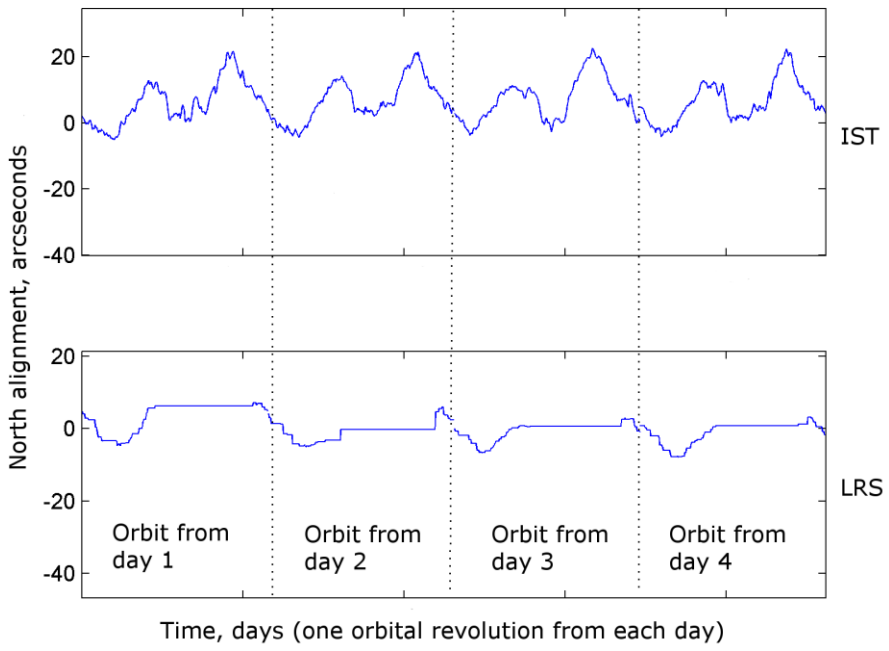

Figure 52. Body north alignments on a daily time scale.

Figure 53 shows the Filter 2 (BST1 constant) alignment variations of the GLAS trackers over long time scales, and represents the primary alignment results. One revolution from each of the 244 normal granules is shown. At this scale the individual orbital variations are only apparent as high frequency fluctuations. The relative amplitudes of the orbital variations and long term trends in the alignments can be estimated directly from the figure. The orbital variations are represented by the high frequency variations or thickness of the curves. The orbital variation amplitudes are 20 to 30 arcseconds for the IST. Parts of the LRS orbital variations were cut off because the LRS was deactivated in daylight. The portions available have smaller amplitudes than the IST.

There is strong evidence of correlation in the IST and LRS body north coordinates. A simple explanation is that the GLAS tracker alignments were not independent in the body north coordinates because GLAS alignment was varying. Both trackers were attached to the GLAS optical bench and their alignment correlations reflect optical bench motion. The evidence also indicates the GLAS alignment was more stable in the body west coordinate. There is less correlation in the body west coordinates of the trackers.

In the 2003 campaign there were two commanded GLAS temperature changes, resulting in two alignment step changes separating three nearly steady state periods. In effect, the two temperature changes divided campaign 2A into three sub-campaigns 2A1, 2A2, and 2A3. The temperature changes are clear in the body west coordinates of the GLAS trackers, demonstrating that rapid changes of the alignments were possible.

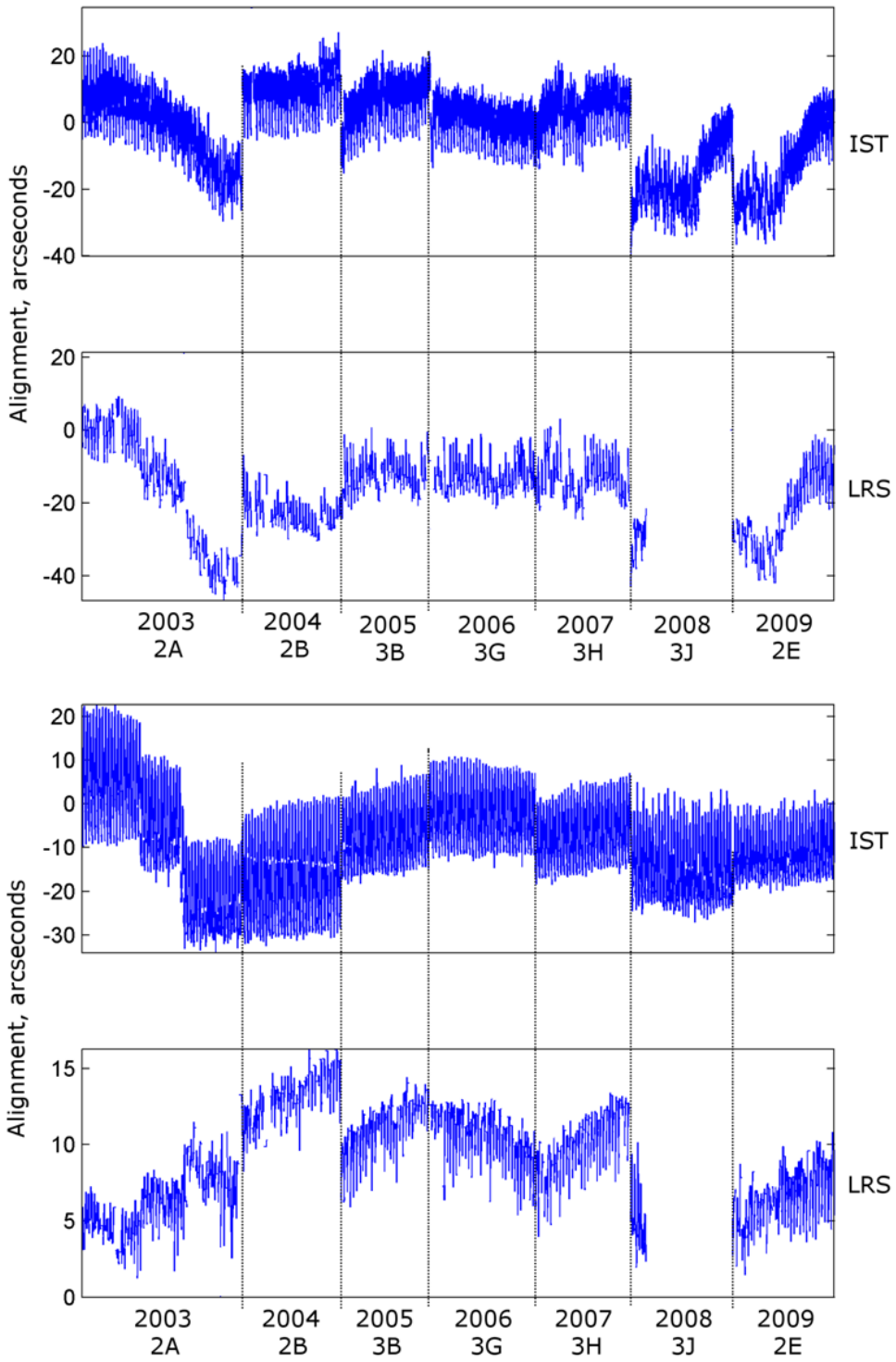

Figure 53. Body north (top) and body west (bottom) alignments.

Figure 54 shows the Filter 2 alignments for BST2, along with the GLAS trackers for comparison. BST2 is representative for the bus trackers. In Filter 2 the BST1 alignment was held constant and the BST1 frame was effectively defined as the body frame to prevent attitude drift. In effect, the alignments of the IST, LRS, and BST2 were estimated relative to BST1. The BST2 alignment variations were roughly an order of magnitude smaller than the GLAS trackers. The scale of the vertical axes is smaller for the BST2 plots than the GLAS tracker plots.

One similarity between the GLAS trackers and BST2 is that there was more variation of the body north coordinates than the body west coordinates. There is also evidence of a small linear trend in the BST2 body north coordinates, in addition to variations within each campaign.

There are more prominent jumps or inconsistencies from day to day for BST2, particularly during campaigns in which ocean scans were more frequent. Because the BST2 alignment variations were small, inconsistencies caused by attitude drift and ocean scan maneuvers are more apparent. In effect the signal to noise ratio for the BST2 alignments is lower than for the GLAS tracker alignments, resulting in noisier plots. There were frequent ocean scans in the 2008 and 2009 campaigns, and high frequency jumps in the BST2 alignments were a direct result. There is a strong correlation between the number of ocean scan granules in a campaign, shown in Table 4 in Section IIId, and the number of inconsistencies in the BST2 coordinates.

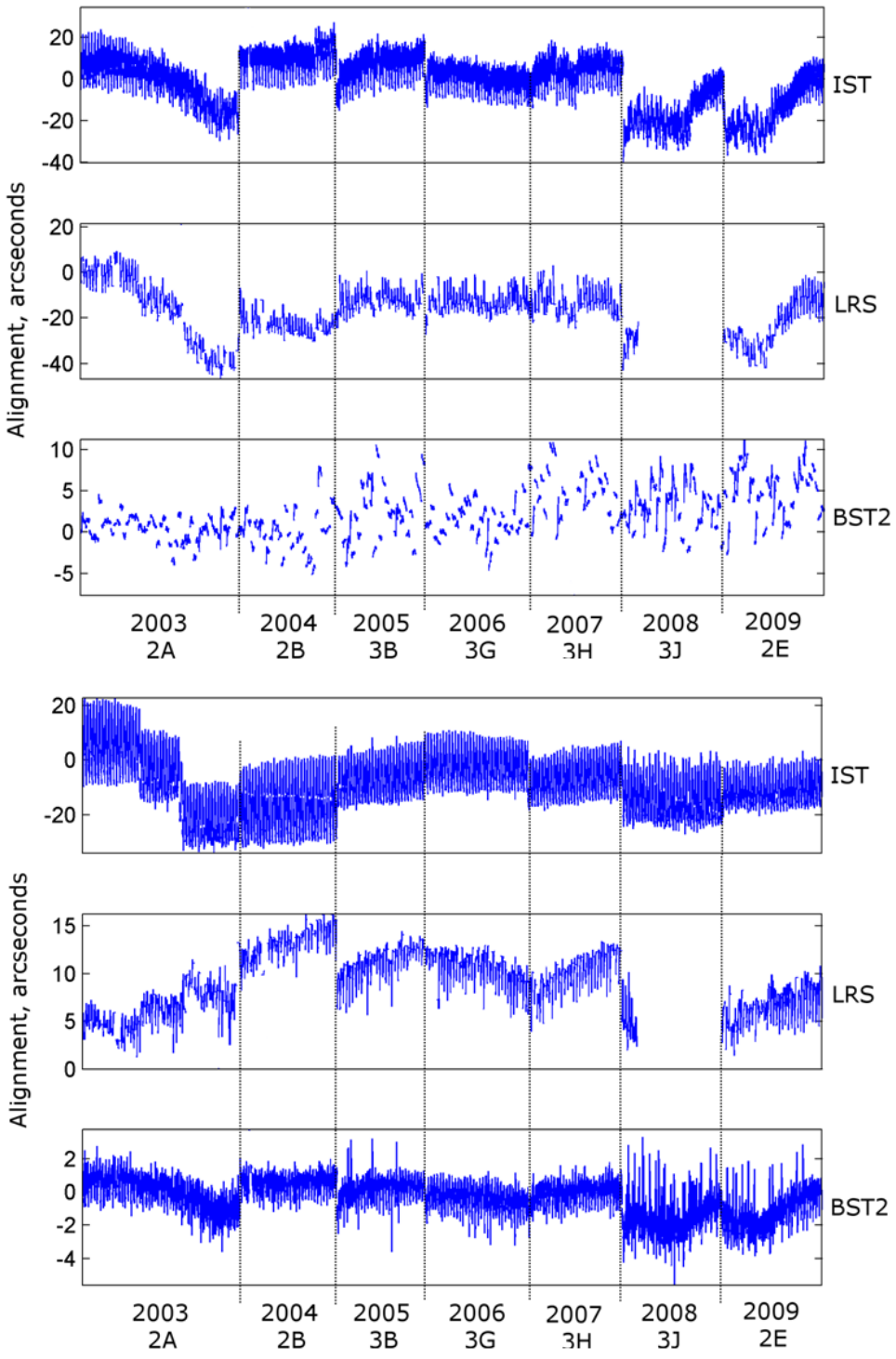

Figure 54. Body north (top) and body west (bottom) alignments.

The IST, LRS, and BST2 alignments are superimposed in Figure 55 for comparison. A constant ten arcsecond bias has been removed from the IST body north coordinates so that correlations with the LRS are more apparent. When viewed at the same scale, the BST2 alignment variations clearly have a different character than the GLAS trackers. A gradual linear trend in the BST2 body north coordinate is apparent, possibly an effect of aging on the BSTs and their mountings.

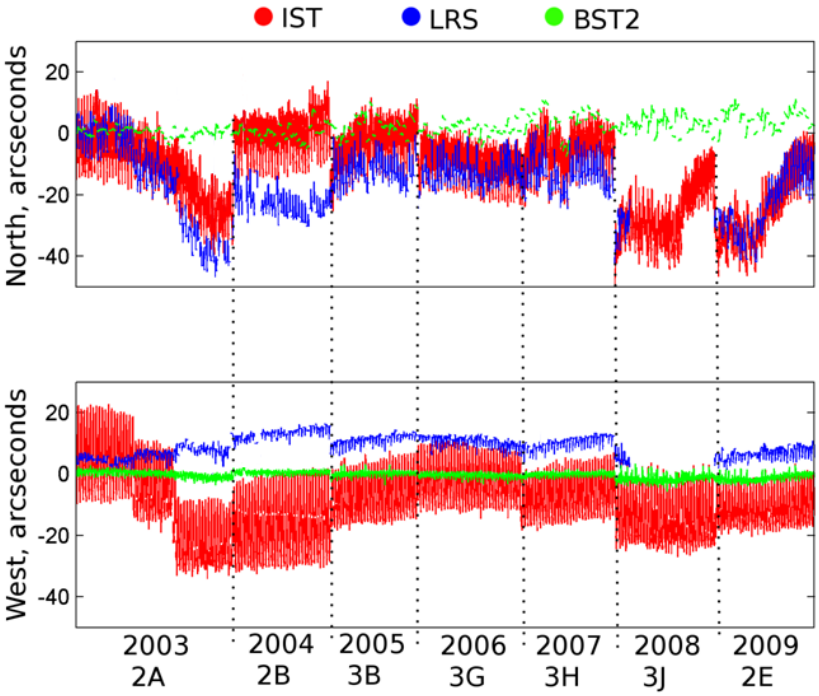

Figure 55. Superimposed alignments for IST, LRS, and BST2 in body north and body west coordinates.

The GLAS tracker body north coordinates have large orbital variations, apparent in the amplitude of the high frequency variations in Figure 55, and large trends over campaign time scales, particularly in 2003, 2008, and 2009. The long term trends of the GLAS tracker body north coordinates are generally consistent, but 2004 is an exception demonstrating that there were also significant independent motions between the IST and LRS. There is little evidence of correlation in the body west coordinates. The body west

variations of the IST were large both on orbital and longer time scales, while the variations of the LRS was relatively small.

To summarize, the BSTs were relatively stable and provided a practical reference against which GLAS tracker motion could be characterized. There was independent motion between the GLAS trackers, particularly in the body west coordinates, where IST motion was large and LRS motion was small. More importantly, there was correlated motion of the GLAS trackers in the body north coordinates. The simplest explanation is that correlated motion of the GLAS trackers was caused by motion of the GLAS optical bench relative to the bus. The discussion below focuses on evidence for inferring that the correlated IST and LRS pointing variations were caused by GLAS optical bench pointing variations.

The three quantities underlying the following discussion are Θ_{GLAS}, Θ_{IST} and Θ_{LRS} representing the true pointing of the GLAS optical bench, IST, and LRS in the spacecraft body north direction. They are assumed to be time varying, and three derived quantities θ_{GLAS}, θ_{IST} and θ_{LRS} are defined in equations (172) to (174) using the expected value function $E(\ )$. They represent the true variations of the GLAS optical bench, IST, and LRS pointing in the spacecraft body frame north direction. In sailboat attitude mode they are approximately equivalent to cross-track pointing variations.

$$\theta_{GLAS} \equiv \Theta_{GLAS} - E\left(\Theta_{GLAS}\right) \tag{172}$$

$$\theta_{IST} \equiv \Theta_{IST} - E\left(\Theta_{IST}\right) \tag{173}$$

$$\theta_{LRS} \equiv \Theta_{LRS} - E\left(\Theta_{LRS}\right) \tag{174}$$

In practice, estimated values $\hat{\theta}_{GLAS}$, $\hat{\theta}_{IST}$ and $\hat{\theta}_{LRS}$ are available, not the true values θ_{GLAS}, θ_{IST} and θ_{LRS}. $\hat{\theta}_{IST}$ and $\hat{\theta}_{LRS}$ are estimated directly by the alignment filter. $\hat{\theta}_{GLAS}$ has to be inferred from $\hat{\theta}_{IST}$ and $\hat{\theta}_{LRS}$. The method used here is to assume that $\hat{\theta}_{GLAS}$ is nearly equal to the correlated portions of $\hat{\theta}_{IST}$ and $\hat{\theta}_{LRS}$. In other words, synchronized motion of the IST and LRS is assumed to be caused by motion of the optical bench.

Figure 56 shows $\hat{\theta}_{IST}$ and $\hat{\theta}_{LRS}$ results from alignment filtering. The large difference $\hat{\theta}_{IST} - \hat{\theta}_{LRS}$ between the IST and LRS during 2004 demonstrates that there was independent, uncorrelated north motion of the IST relative to the LRS. Independent motion is also demonstrated by the changes of the difference $\hat{\theta}_{IST} - \hat{\theta}_{LRS}$ during 2003, where the LRS north coordinate drops faster than the IST. Relative motion and variations of the difference $\hat{\theta}_{IST} - \hat{\theta}_{LRS}$ are discussed below.

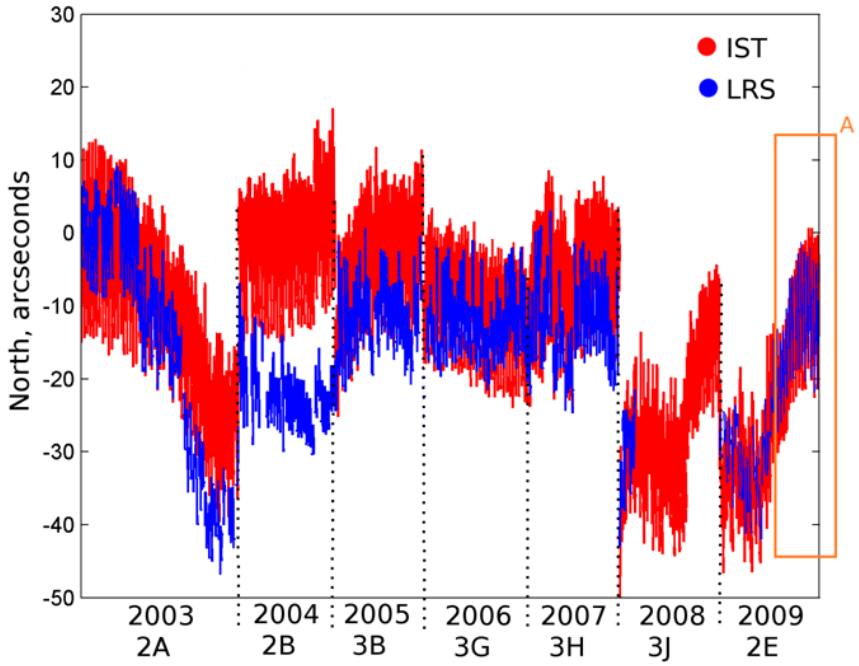

Figure 56. GLAS tracker body north coordinates $\hat{\theta}_{IST}$ and $\hat{\theta}_{LRS}$.

There are areas in Figure 56 where the IST and LRS correlation is particularly strong. An example is the area enclosed in the box labeled A. It raises the question of how strong the correlation is on shorter time scales. Figure 57 shows an expanded view. The vertical scale is the same, but the horizontal time scale has been decreased so that individual days and orbits are visible. One orbit from each day is shown in sequence for fifteen days. The repeated pattern of the orbital variations in $\hat{\theta}_{IST}$ and $\hat{\theta}_{LRS}$ make the boundaries between adjacent days apparent. Vertical lines have been added to make the boundaries clearer.

The variations have two peaks per orbit, one during the day side and one during the night side. $\hat{\theta}_{LRS}$ is constant during the day side, where the LRS was not tracking stars. During the night side peak there is a strong match between $\hat{\theta}_{IST}$ and $\hat{\theta}_{LRS}$. There is also a strong trend over the fifteen days shown, with $\hat{\theta}_{IST}$ and $\hat{\theta}_{LRS}$ increasing from around -20 arcseconds at the beginning to around -10 arcseconds near the middle of the plot.

Figure 57 is evidence that $\hat{\theta}_{IST}$ and $\hat{\theta}_{LRS}$ were correlated on orbital times scales, as well as on the longer time scales of Figure 56. With the assumption that $\hat{\theta}_{GLAS}$ was nearly equal to the correlated portions of $\hat{\theta}_{IST}$ and $\hat{\theta}_{LRS}$, this implies that $\hat{\theta}_{GLAS}$ varied significantly over each orbit. In sailboat mode $\hat{\theta}_{GLAS}$ was approximately equivalent to the GLAS cross-track pointing, so Figure 57 implies a roughly ten to fifteen arcsecond orbital variation of the GLAS cross-track pointing. A one arcsecond change of laser pointing results in three meters of cross-track motion in the ground spot location, so Figure 57 implies a roughly thirty to fifty meter cross-track orbital variation in the path of the ground spots.[96]

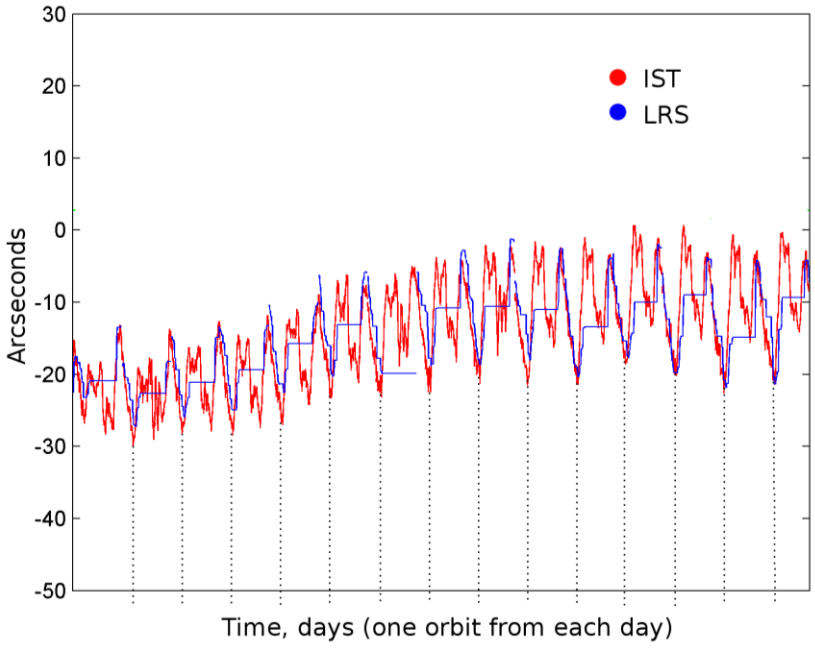

Figure 57. GLAS tracker body north coordinates $\hat{\theta}_{IST}$ and $\hat{\theta}_{LRS}$ over orbital time scales.

There is a close match between $\hat{\theta}_{IST}$ and $\hat{\theta}_{LRS}$ in Figure 57 during the periods when there is LRS data. The difference $\hat{\theta}_{IST} - \hat{\theta}_{LRS}$ is small and nearly constant during these periods. This is surprising because there was evidence of significant relative motion between the IST and LRS during at least some periods, with variations of $\hat{\theta}_{IST} - \hat{\theta}_{LRS}$ on the order of twenty arcseconds. The strongest evidence for variations of $\hat{\theta}_{IST} - \hat{\theta}_{LRS}$ was provided early in the mission by a reference signal from the Collimated Reference Source (CRS), which directly tied the IST reference frame to the LRS reference frame. The CRS signal failed early on, but was available during L2A. It provided a direct measure of the relative motion between the IST and LRS, and the difference $\hat{\theta}_{IST} - \hat{\theta}_{LRS}$. A plot of the CRS results for L2A day 270 (2003.09.27) is shown on the left side of Figure 58.[132] The right side of the figure shows an analogous plot from the alignment filter states. The horizontal axis is directly equivalent to $\hat{\theta}_{IST} - \hat{\theta}_{LRS}$. The effective resolution is low because of the sparse LRS star measurements, and only half of the orbit is usable because the LRS was deactivated on the day side.

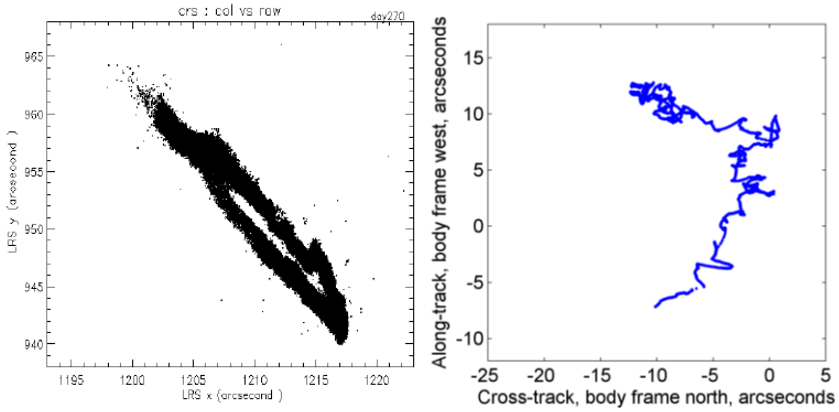

Figure 58. Motion of the IST relative to the LRS from CRS data (left) and alignment filter results (right). Both plots are thirty by thirty arcseconds. The horizontal axis of the right plot represents $\hat{\theta}_{IST} - \hat{\theta}_{LRS}$.

Figure 58 is evidence that the alignment filter was able to resolve and track the relative motions between the IST and LRS. The intermittent nature of the LRS measurements made this difficult, but the magnitude of the effect in the filter results agrees with the

direct measurements from the CRS. Taken together, Figure 57 and Figure 58 are evidence that there was significant relative motion between the IST and LRS on orbital time scales, and that the magnitude was larger at the beginning of the mission.

Orbital variations of the alignments are represented by sets of plots organized by campaign, starting with 2003. Figure 59 shows the Filter 1 alignments and error signals for a typical 2003 campaign 2A granule, 2003.09.29 granule GLA04_ 031_1102_ 029_0019_ 0_01_000.

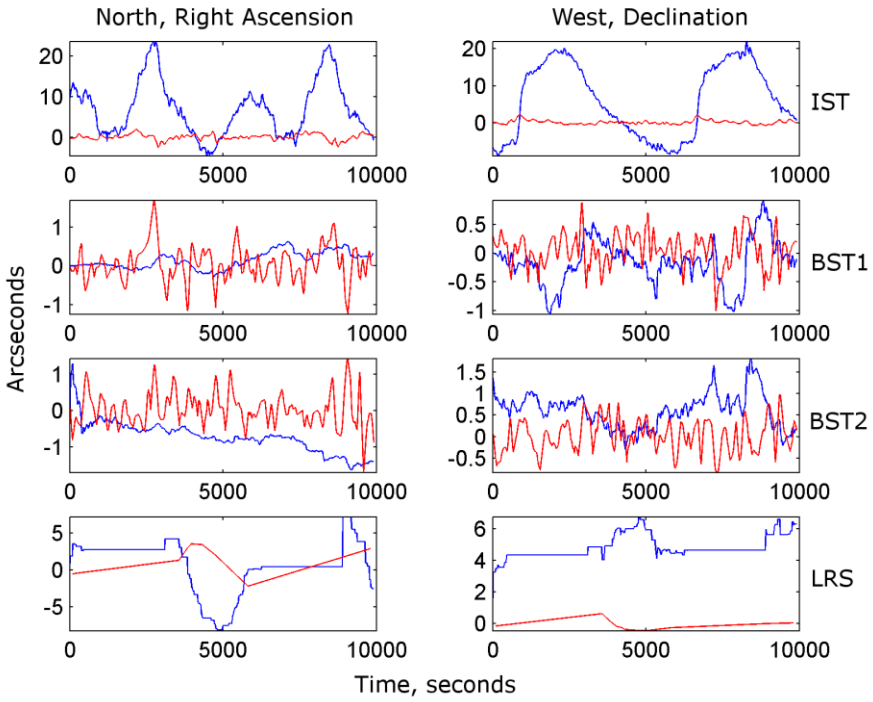

Figure 59. Alignments (blue) and error signals (red) for a typical 2003 campaign 2A granule.

Figure 60 show the Filter 1 and Filter 2 orbital and campaign results for 2003 campaign 2A. Comparing the Filter 1 and Filter 2 plots, the BST2 north coordinates for granules with maneuvers are similar. In both, there is a granule where an ocean scan caused an alignment change. This demonstrates that both Filter 1 and Filter 2 are affected by maneuver errors during the filter propagation phase, which is classified here as a type of attitude drift. The BST2 west coordinates from Filter 2 are more consistent than those from Filter 1, and show evidence of a small orbital variation of the BST2 alignment on

the order of a few arcseconds. This evidence of a BST2 orbital variation appears to be the practical advantage provided by Filter 2 over Filter 1.

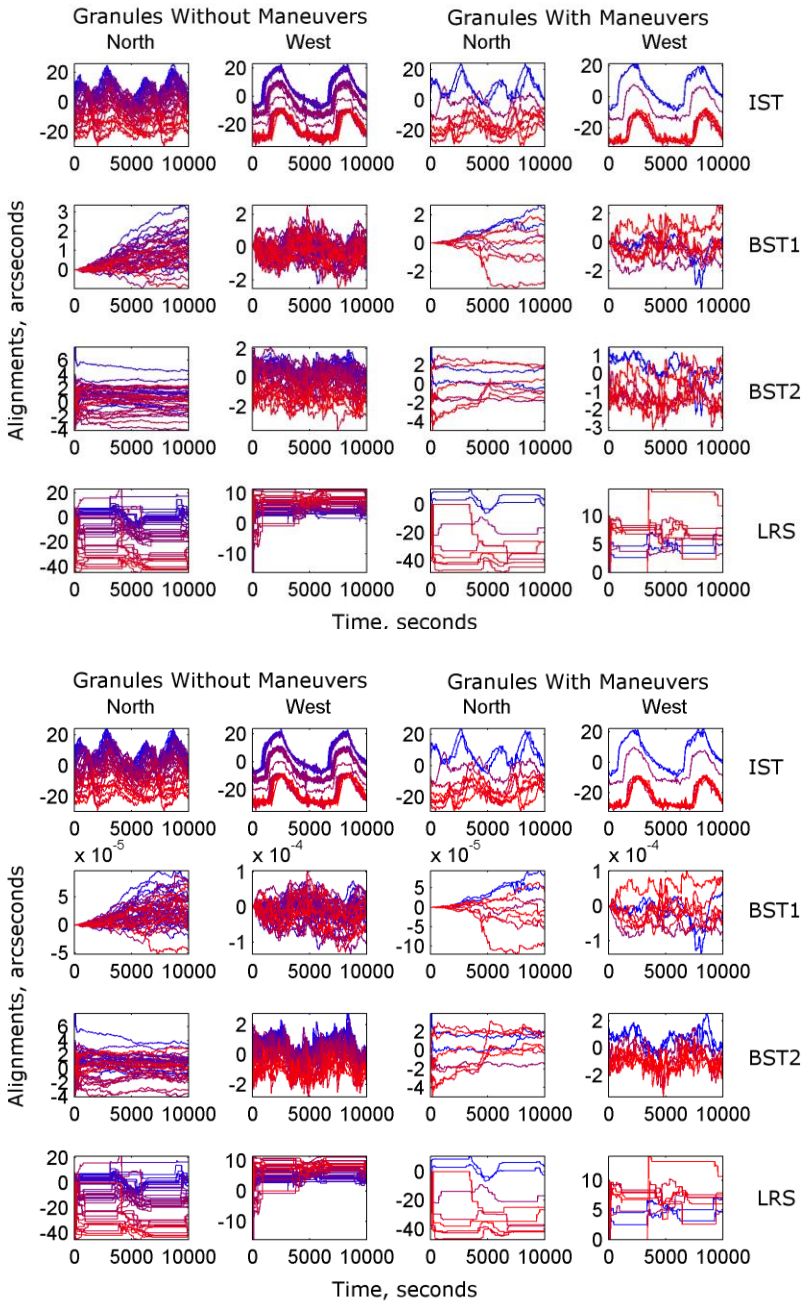

Figure 60. 2003 campaign 2A alignment states from Filter 1 (top) and Filter 2 (bottom).

Figure 61 shows the Filter 1 alignments and error signals for a typical 2004 campaign 2B granule, 2004.02.23 granule GLA04_031_ 2107_002_ 0007_0_ 01_000.

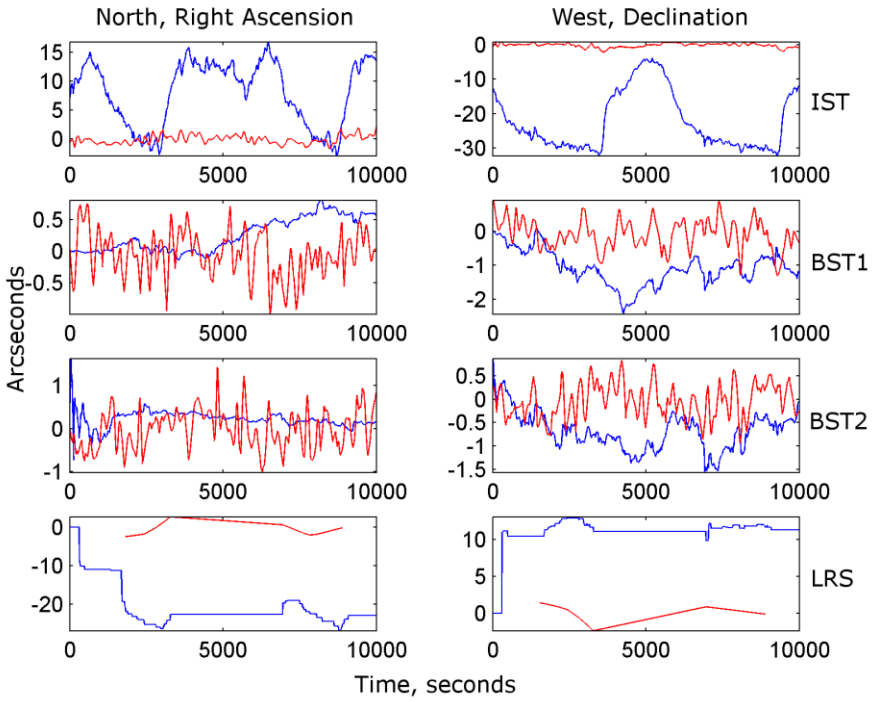

Figure 61. Alignments (blue) and error signals (red) for a typical 2004 campaign 2B granule.

Figure 62 show the Filter 1 and Filter 2 orbital and campaign results for 2004 campaign 2B. There is evidence of a small orbital variation of the BST2 alignments, particularly in the Filter 2 results. Small step changes of the bus tracker north alignments in the granules with maneuvers indicate propagation errors during ocean scans.

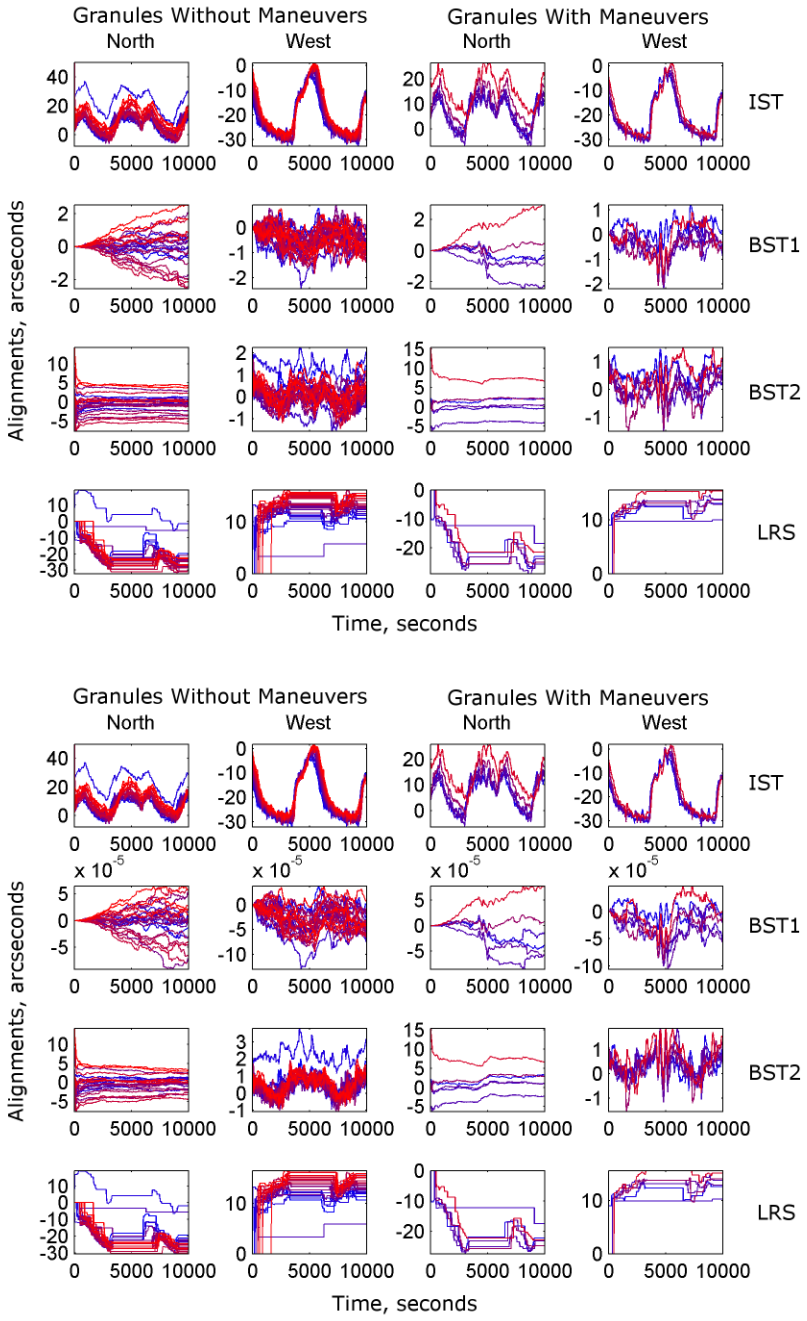

Figure 62. 2004 campaign 2B filter alignment states from Filter 1 (top) and Filter 2 (bottom).

Figure 63 shows the filter 1 alignments and error signals for a typical 2005 campaign 3B granule (2005.02.18 granule GLA04_031_ 2111_001_ 1265_0_ 01_000).

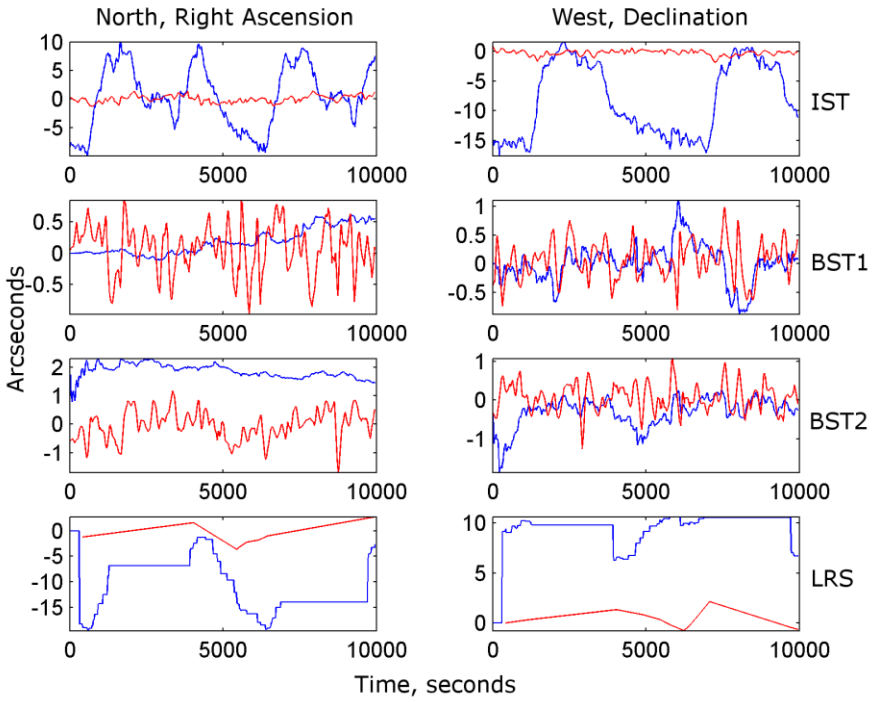

Figure 63. Alignments (blue) and error signals (red) for a typical 2005 campaign 3B granule.

Figure 64 show the Filter 1 and Filter 2 orbital and campaign results for 2005 campaign 3B. A relatively large number of the granules contained maneuvers, resulting in the increased inconsistencies noted above in Figure 54. The BST2 north coordinates appear to be grouped or quantized. This structure is not apparent in the long time scale plots of Figure 54. It affects both granules with and without maneuvers, and only appears in this campaign.

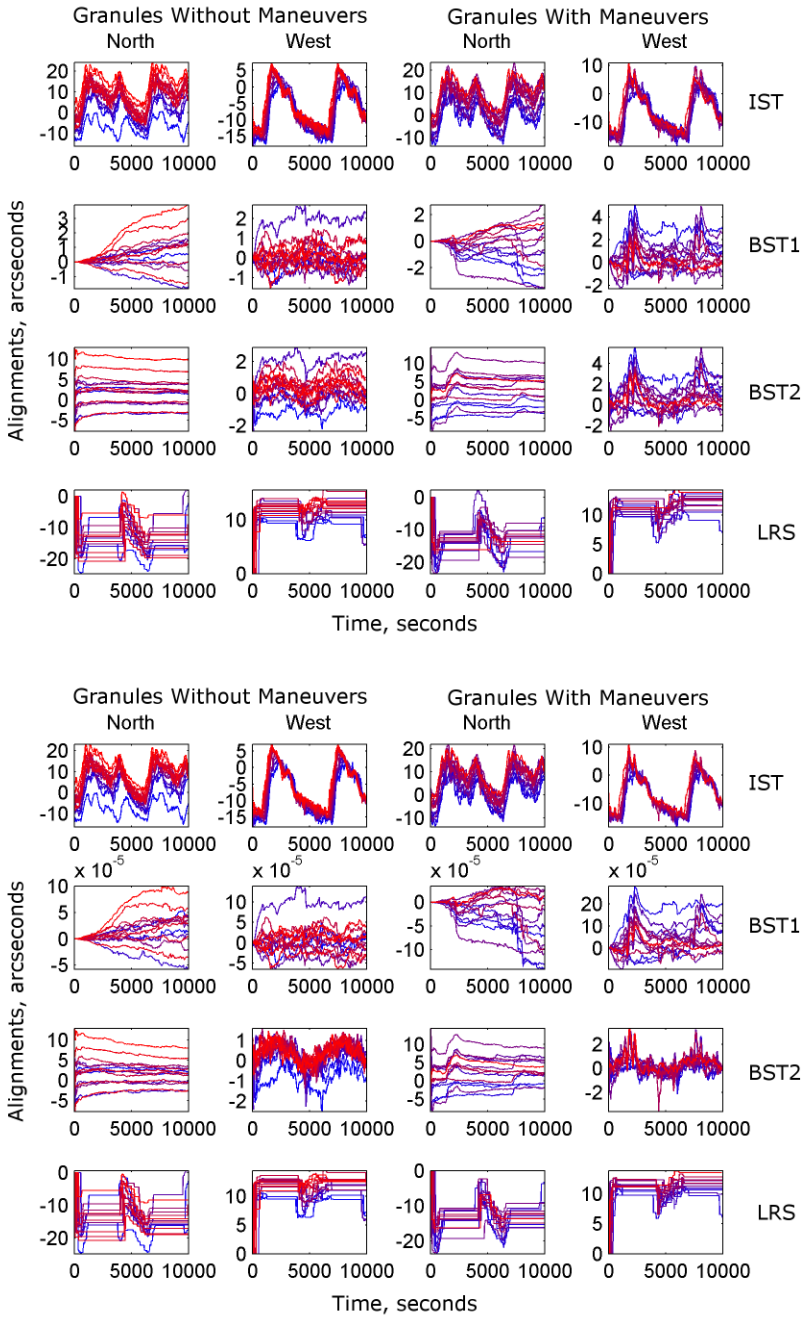

Figure 64. 2005 campaign 3B alignment states from Filter 1 (top) and Filter 2 (bottom).

Figure 63 shows the Filter 1 alignments and error signals for a typical 2006 campaign 3G granule (2006.10.26 granule GLA04_031_ 2117_001_ 1291_0_ 01_000).

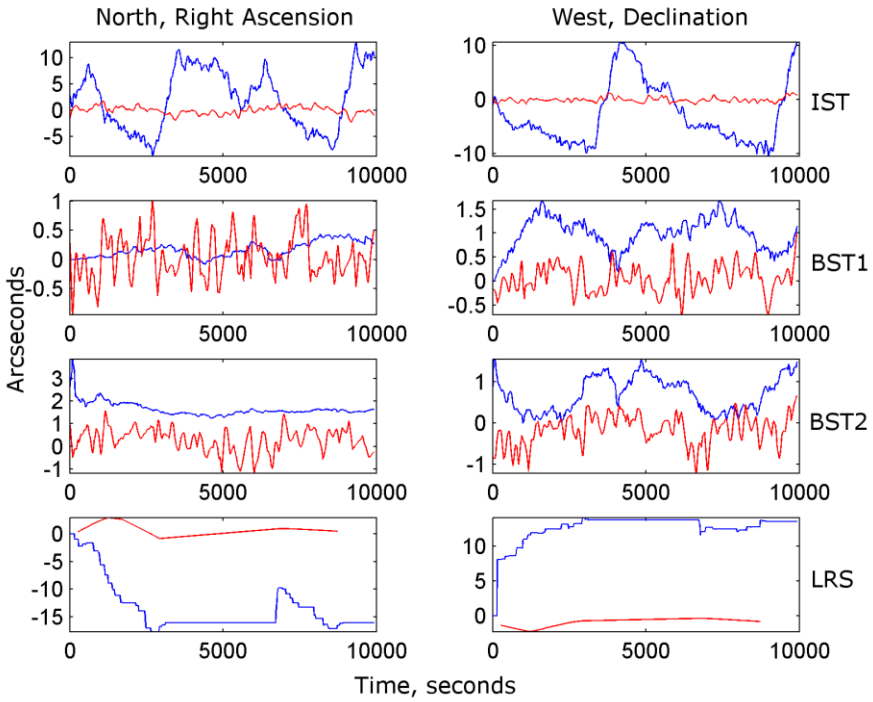

Figure 65. Alignments (blue) and error signals (red) for a typical 2006 campaign 3G granule.

Figure 66 show the Filter 1 and Filter 2 orbital and campaign results for 2006 campaign 3G. The BST2 west alignments from Filter 2 are more consistent than those from Filter 1. This demonstrates both the scale of attitude drift effects, and the ability of the alignment filter to resolve orbital variations of a few arcseconds. The fact that the BST2 variations are consistent and small in the Filter 2 results is evidence that the bus trackers are stable relative to each other. Similarly, the results from Filter 1 and Filter 2 together are evidence that the bus trackers are stable relative to the spacecraft body frame.

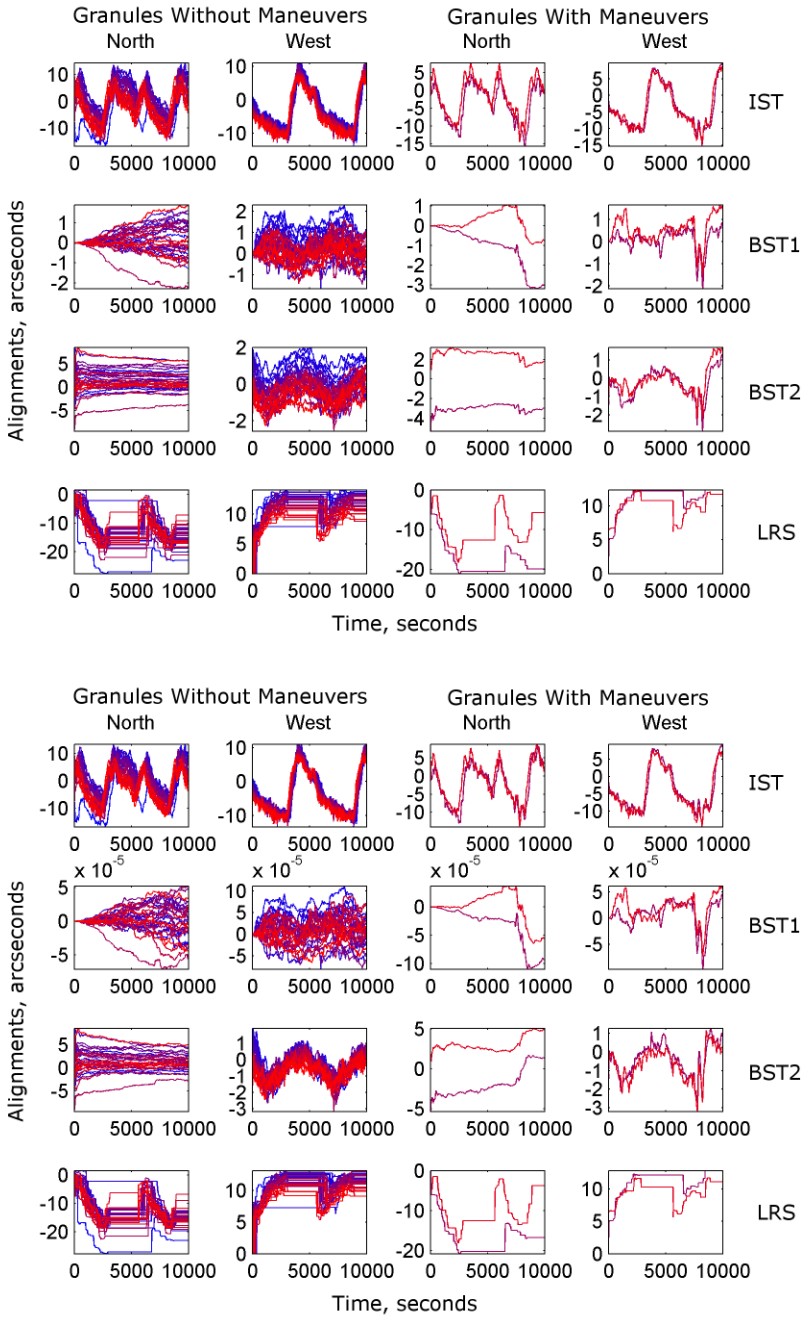

Figure 66. 2006 campaign 3G alignment states from Filter 1 (top) and Filter 2 (bottom).

Figure 67 shows the Filter 1 alignments and error signals for a typical 2007 campaign 3H granule (2007.03.18 granule GLA04_031_ 2119_002_ 0015_0_ 01_000).

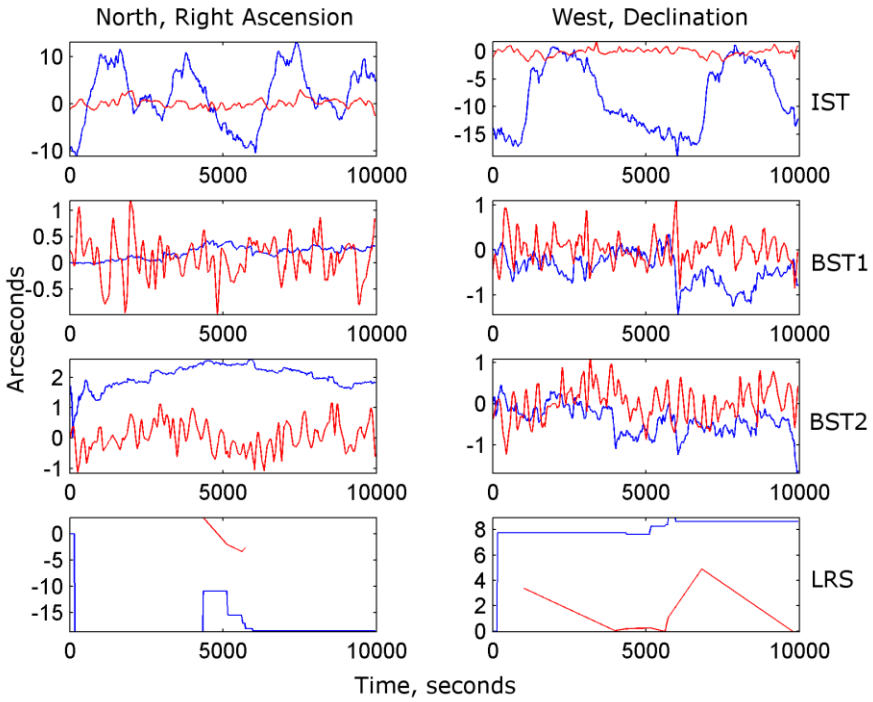

Figure 67. Alignments (blue) and error signals (red) for a typical 2007 campaign 3H granule.

Figure 68 show the Filter 1 and Filter 2 orbital and campaign results for 2007 campaign 3H. Like the 2006 campaign, the BST2 west alignments from Filter 2 are more consistent than those from Filter 1. The 2006 and 2007 campaigns have many similar characteristics, this is apparent in Figure 54 as well. They were treated as reference cases.

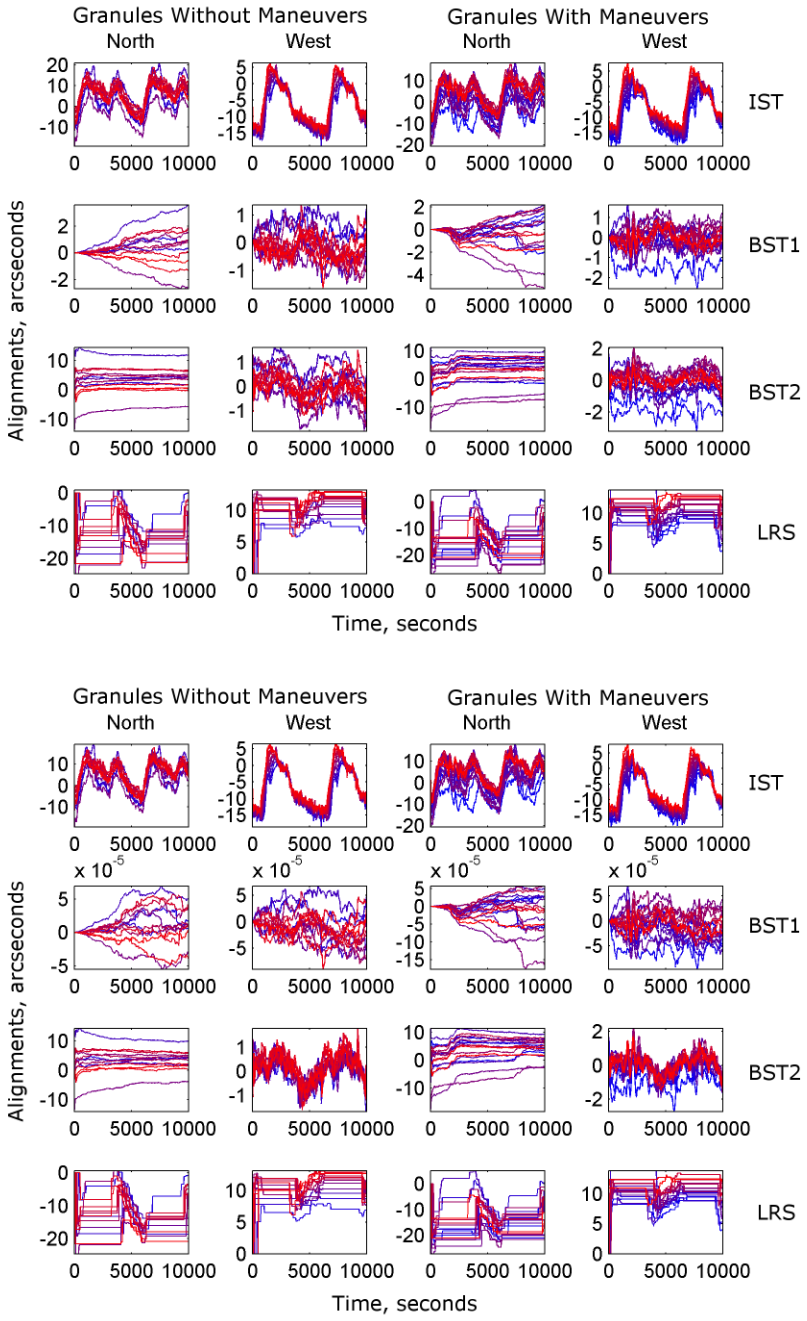

Figure 68. 2007 campaign 3H alignment states from Filter 1 (top) and Filter 2 (bottom).

Figure 69 shows the Filter 1 alignments and error signals for a typical 2008 campaign 3J granule (2008.02.18 granule GLA04_031_ 2123_001_ 1285_0_ 01_000).

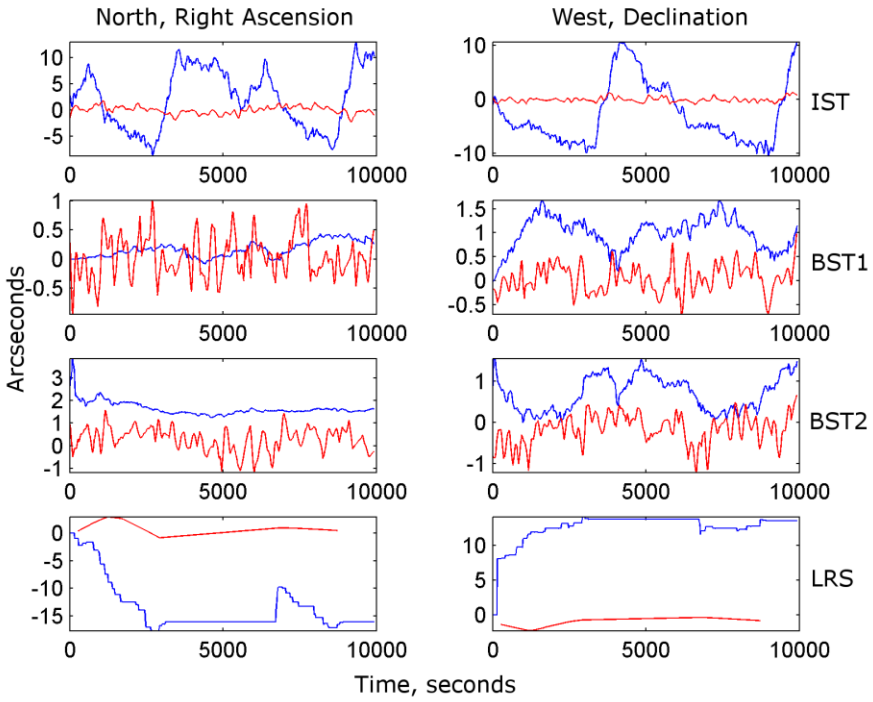

Figure 69. Alignments (blue) and error signals (red) for a typical 2008 campaign 3J granule.

Figure 70 show the Filter 1 and Filter 2 orbital and campaign results for 2008 campaign 3J. The BST2 north coordinates for this campaign are a clear example of the effects of ocean scans. There is a step change of the north coordinates in the maneuvers with granules. After the maneuver the attitude error shrinks because BST1 defines the body frame, but it is apparent here that the BST2 north coordinate remains near its last value during the maneuver. This indicates that the BST2 north coordinate is not sensitive enough to measurements after the maneuver. There should be more uncertainty in the BST2 north coordinate, via process noise, so that it continues to track the measurements.

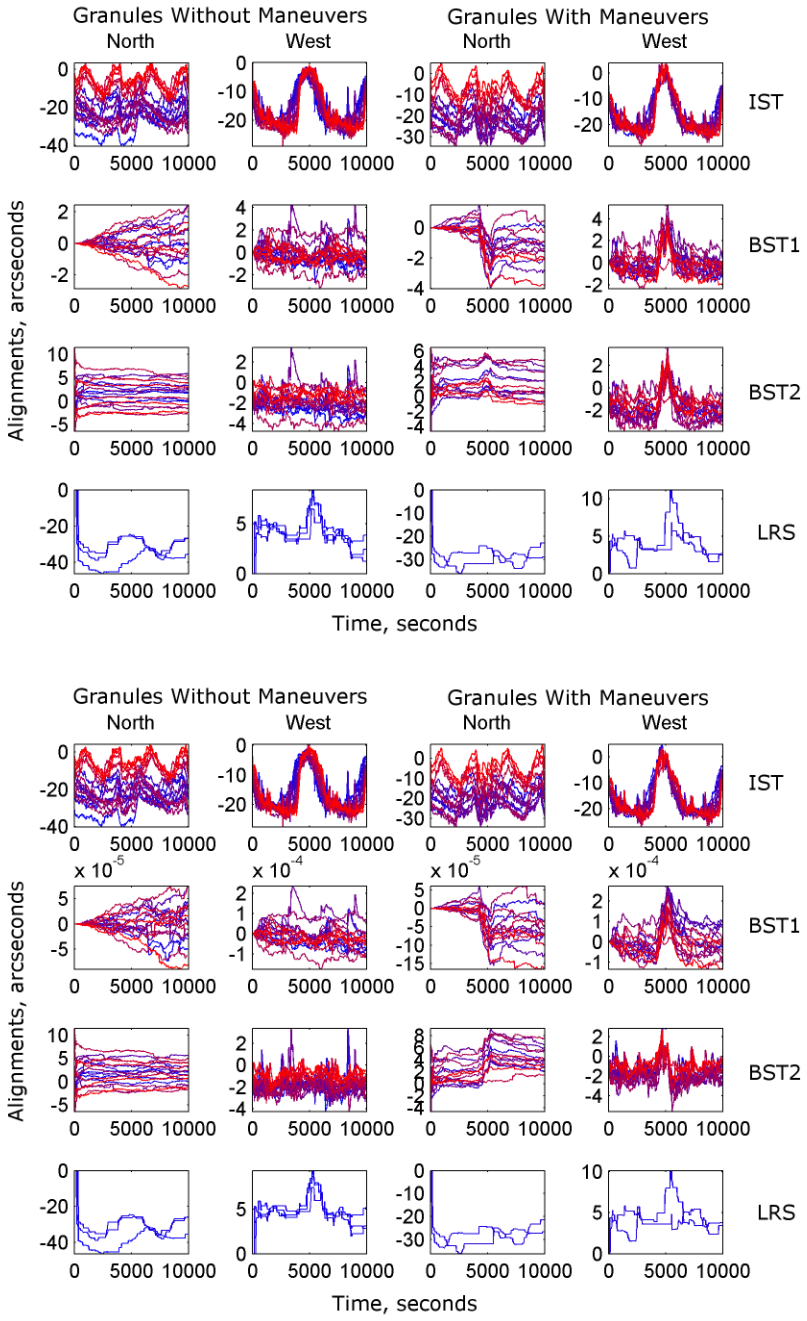

Figure 70. 2008 campaign 3J alignment states from Filter 1 (top) and Filter 2 (bottom).

Figure 71 shows the Filter 1 alignments and error signals for a typical 2009 campaign 2E granule (2009.03.29 granule GLA04_031_ 2129_002_ 0223_0_ 01_000).

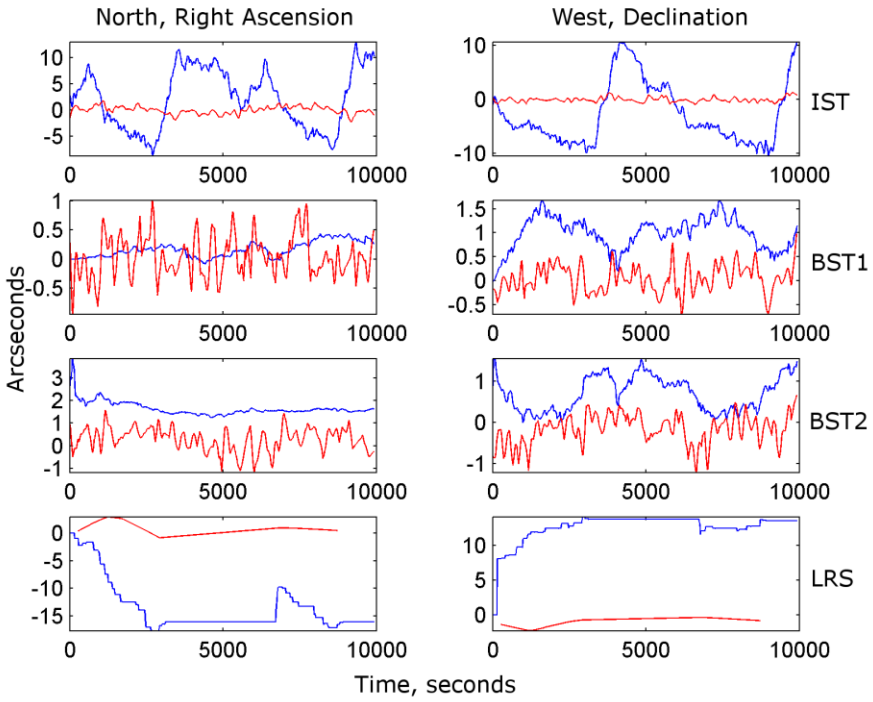

Figure 71. Alignments (blue) and error signals (red) for a typical 2009 campaign 2E granule.

Figure 72 show the Filter 1 and Filter 2 orbital and campaign results for 2009 campaign 2E. There were frequent ocean scan maneuvers and relatively few granules without maneuvers. The effects of ocean scans on the bus tracker alignments are clear in their west coordinates. There are two peaks with amplitudes of three or four arcseconds, corresponding to ocean scans early or late in the granules. The north coordinates contain the same type of step change as seen in the 2008 campaign, but the vertical scale is larger here and the changes are not as visible.

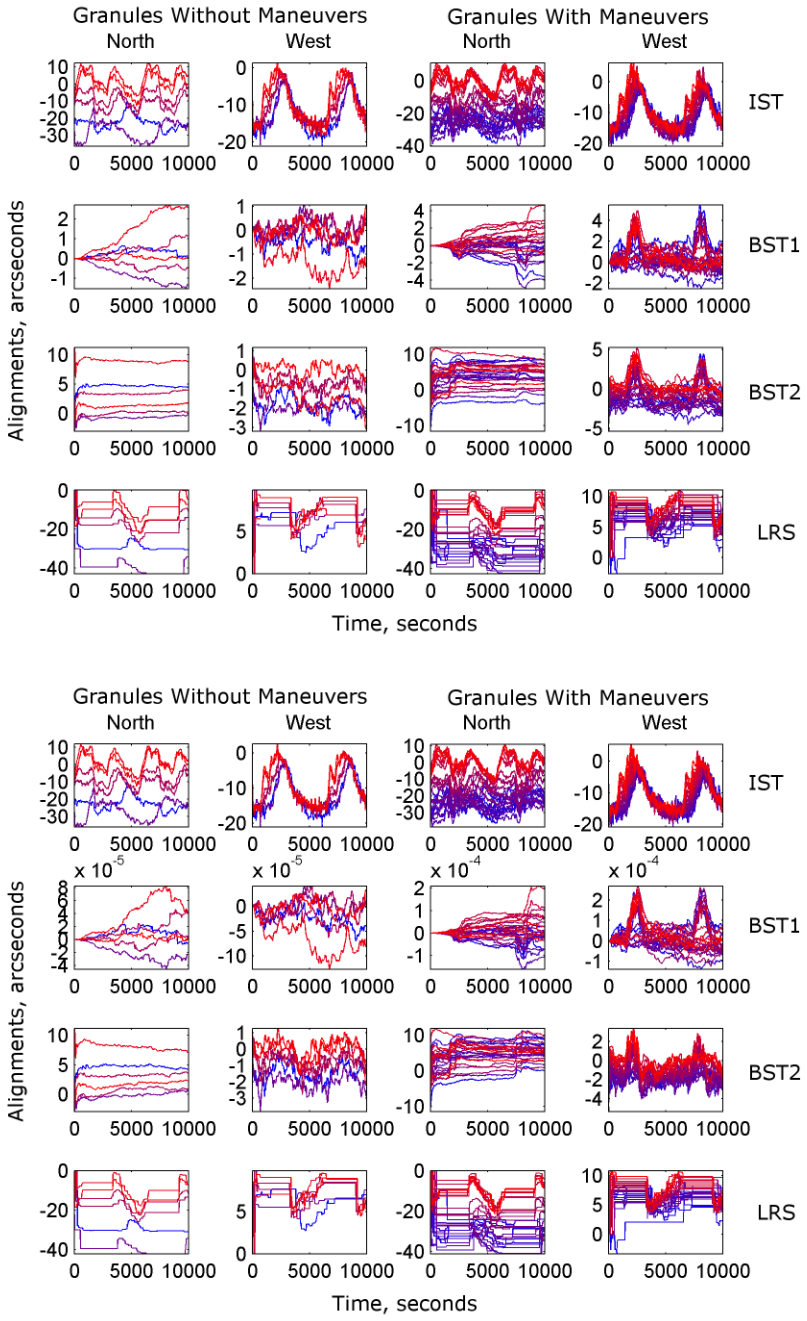

Figure 72. 2009 campaign 2E alignment states from Filter 1 (top) and Filter 2 (bottom).

VII. Conclusion

The alignment filter results were evidence for significant IST and LRS pointing variations over both orbital and campaign time scales, and evidence that the variations were partially correlated. It was previously known that there were orbital variations of IST pointing relative to the LRS. This fact was directly observed early in the mission while the reference signal from the CRS was available. It was also known that propagating an IST attitude forward in time using gyro data alone allowed the IST relative motion to be reconstructed by comparison with the results from a filter using both gyro propagation and IST measurement updates.[96, 132-136] It was believed that LRS pointing was as stable as BST pointing and evidence of significant LRS pointing variations was a new result. The data fusion inherent in alignment filtering made it practical to extract more information from the sporadic LRS measurements.

The simplest explanation was that the correlated variations of the IST and LRS body north coordinates reflected motion of the GLAS optical bench relative to the bus, and independent variations of the IST and LRS coordinates reflected changes in their individual attachments to the optical bench. This was necessarily an inference. The only available measurements sensitive to GLAS alignment were star tracker data, gyro data, and possibly results concerning the ground track of the GLAS laser spots. Careful use of the SIRU data to reduce gyro propagation errors provided an independent fifth measured reference frame, in addition to the four tracker frames. The SIRU defined the body frame and the alignment filter estimated the tracker alignments relative to it. This filter configuration was used for validation and may be capable of producing new results. Correlations between the IST and LRS pointing variations and the GLAS laser spot ground track were also possible. A one arcsecond change in GLAS pointing was equivalent to a three meter change of laser spot geolocation. A twenty arcsecond or sixty meter orbital variation may be detectable in the geolocation and ground track results.

Small empirical uncertainties for the filter results demonstrated that the alignment filter was successful in simultaneously keeping the four estimated tracker pointing vectors near their true positions on the celestial sphere. This was primarily a reflection of the characteristics of the star measurements, the IST and BSTs provided high information bandwidth and accuracy. During normal ICESat science operations without maneuvers, small corrections of deterministic tracker measurement errors was the remaining practical route to improved alignment filter performance. Improvements were possible in handling gyro drift over long time scales, but these improvements would not directly affect the tracker pointing vectors during normal science operations.

Attitude drifts observed in the Filter 1 results demonstrated that the idealistic alignment filter configuration with all of the trackers free was in a sense equivalent to dealing with maneuvers. Gyro measurements and the filter propagation phase became more significant. If the gyros were perfect, there would have been no attitude drift or maneuver error during propagation. Correction of deterministic gyro errors via the gyro measurement model improved filter performance during maneuvers and in the Filter 1 configuration. An interesting side effect of fusing the data from multiple trackers was that in many cases attitude drift and maneuver errors were directly detectable because they caused simultaneous variations in the alignments and residuals.

The small bus tracker alignment variations were more of a challenge for the filter than the large GLAS tracker variations. The bus tracker orbital variations were on the same scale as both the overall uncertainties and the effects of attitude drift. There were cases where the filter covariance in the bus tracker alignment states became too small, so that the states did not respond to new measurements. When an error was introduced in the alignments by a maneuver, the alignments did not return to their previous values after the maneuver completed. This behavior can be corrected by better tuning of the filter covariance via the process noise.

VIII. Appendix

a. Scaled Tangent Coordinates for Unit Vectors

A linear two-component representation is useful for describing the difference between a pair of three-component unit vectors having the same origin and nearly the same direction. The general method is referred to here as scaled tangent coordinates. Three-component unit vectors are represented as a two-component vector on a linear coordinate plane using scaled tangents. Usually a physically significant reference unit vector is used to define a coordinate frame in which a variable unit vector is expressed. The reference vector is used as the z axis of the coordinate frame and the variable unit vector is then expressed using scaled tangents in the coordinate frame x and y plane. The rotation of the x and y plane about the z axis is arbitrary and chosen to emphasis physically meaningful characteristics. For example in the celestial frame the coordinate plane is tangent to the celestial sphere and locally parallel to right ascension and declination. In the body frame the coordinate plane is oriented parallel to body frame north and west. The scaling of the x and y plane is usually defined such that at the origin a unit of distance is equivalent to a one arcsecond change in direction of the variable unit vector.

A tracker coordinate frame is defined by three orthogonal axes with the z axis along the optical axis and the x and y in the image plane. Tracker frame horizontal and vertical (h and v) coordinates are expressed using scaled tangents in the tracker frame x and y plane, with the z axis implicitly acting as the reference vector. The orientation of the x and y plane is defined by the direction of the image pixels.

A hardware dependent definition of h and v uses the tracker focal length f and the x and y position of the star image in the tracker frame relative to the origin as shown in Equations (175) to (177). The scaling factor k relates change of direction to distance.

$$k = 648000 / \pi \ \left[arcseconds / radian \right] \tag{175}$$

$$h = k\left(x / f \right) = k \tan \Theta_h \tag{176}$$

$$v = k\left(y/f\right) = k\tan\Theta_v \tag{177}$$

An equivalent definition of h and v is hardware independent. It replaces the hardware dependent parameters with similar triangles and the components of the unit vector representation as shown in Equations (178) and(179).

$$h = k\left(u_1/u_3\right) \tag{178}$$

$$v = k\left(u_2/u_3\right) \tag{179}$$

An angular representation Θ_h and Θ_v is used as the output format of the Ball CT-602 star trackers, as shown in Equations (180) and (181).

$$\Theta_h = \tan^{-1}\left(u_1/u_3\right) = \tan^{-1}\left(h/k\right) \tag{180}$$

$$\Theta_v = \tan^{-1}\left(u_2/u_3\right) = \tan^{-1}\left(v/k\right) \tag{181}$$

A star unit vector has a simple expression in terms of h and v as shown in Equation (182). In effect, an intermediate vector whose third component is defined equal to one is calculated and then normalized. This is equivalent to setting u_3 equal to one in Equations (178) and (179) leaving two equations for u_1 and u_2 and then normalizing. The unit constraint means there are effectively two degrees of freedom in the unit vector representation.

$$u = \begin{bmatrix} h/k & v/k & 1 \end{bmatrix}^T \Big/ \left(\left(h/k\right)^2 + \left(v/k\right)^2 + 1\right)^{1/2} \tag{182}$$

A two-component north and west coordinate system analogous to latitude and longitude was defined and used to express alignments. Figure 73 shows that GLAS was defined as the spacecraft north pole and the tracker pointing vectors were near the spacecraft equator. Near the spacecraft equator both the north and west coordinates have similar scaling and linearity. The gyro and body coordinate frame z axis pointed in the north

direction, the x axis pointed in the west direction, and the y axis was parallel to the zenith direction and the IST and LRS pointing vectors.

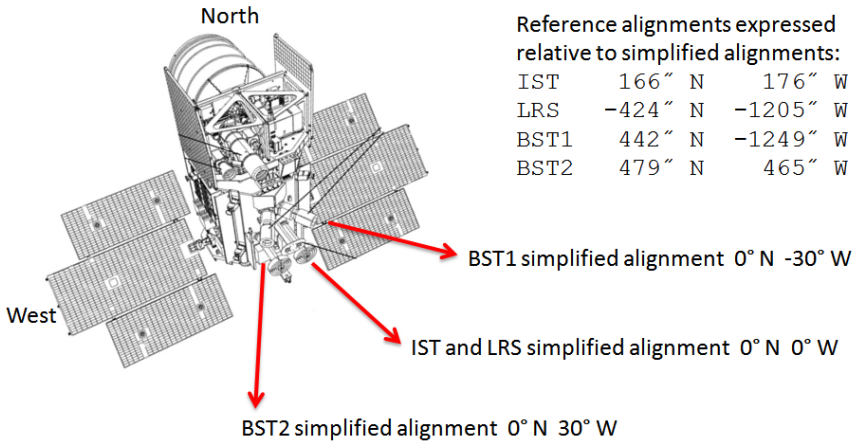

Figure 73. North and west coordinate system.

To express a tracker pointing vector in north and west coordinates, the reference vector for the scaled tangent coordinate frame is the reference pointing vector for the tracker, as shown in Figure 73. The coordinate frame x and y plane is oriented parallel to the north and west coordinates. Given a reference pointing vector u_{ref} and a unit vector pointing to the body frame north $u_{body\ north} = \begin{bmatrix} 0 & 0 & 1 \end{bmatrix}^T$, the u_x and u_y axes of the scaled tangent coordinate frame are expressed in the the body frame as shown in Equations

$$u_x = u_{body\ north} \times u_{ref} \tag{183}$$

$$u_y = u_{ref} \times u_x \tag{184}$$

$$u_z = u_{ref} \tag{185}$$

Celestial frame coordinates use the catalog position of a star as the reference vector and define a plane tangent to the sky with coordinate axes locally parallel to right ascension and declination. Given a catalog unit vector for the star $u_{catalog}$ and a unit vector pointing to the celestial north pole $u_{north} = \begin{bmatrix} 0 & 0 & 1 \end{bmatrix}^T$, the u_x and u_y axes of the tangent plane are expressed in the celestial frame as shown in Equations (186) and (187).

$$u_x = u_{north} \times u_{catalog} \tag{186}$$

$$u_y = u_{catalog} \times u_x \tag{187}$$

$$u_z = u_{catalog} \tag{188}$$

Measured star unit vectors are rotated from the tracker frame to the inertial frame using the filter attitude and alignment states and represented relative to the tangent plane axes. If the measured unit vectors all point along the $u_{catalog}$ axis, then the measured minus predicted residuals are zero.

b. Three-component Rotation Representations

A three-component rotation a can be represented as an Euler Axis and Angle also known as a rotation vector a_ϕ, a Gibbs Vector also known as Rodriques Parameters a_g, Modified Rodriques Parameters a_p, or twice the vector part of a quaternion a_q.[10] Euler Angles (roll, pitch, yaw) are another three-component representation but are not included in the following discussion.

To second-order these representations are equivalent when transforming to a quaternion representation. This is a common operation for the small-angle rotations dealt with in the MEKF attitude filter and the alignment filter, where the attitude errors and alignment states are represented as three-component rotations. To transform to rotation matrix representation, they are first converted to a normalized quaternions as an intermediate step, insuring an orthogonal rotation matrix result.

A quaternion giving a first-order approximation to all three-component rotation representations a is shown in Equation (189).

$$q(a) \approx \begin{bmatrix} a/2 \\ 1 \end{bmatrix} \tag{189}$$

A second-order approximation is given by Equation (190). In practice both approximations should be normalized $q = q/norm(q)$ before use.

$$q(a) \approx \begin{bmatrix} a/2 \\ 1 - a^2/8 \end{bmatrix} \tag{190}$$

Exact equations for the four rotation representations are given by Markley.[10]

c. Gyro Calibration Maneuvers

To improve the gyro measurement model, gyro calibration parameters were estimated from gyro calibration maneuvers performed three times during the mission. Gyro calibration is a large topic and a summary is included here in order to document the results.

Table 31 summarizes the GLA04 granules containing calibration maneuvers. The times t_1 and t_2 give boundaries within the granules, expressed in seconds. The time and granule name information for the first maneuver is uncertain. It does describe a maneuver found on the day in 2003 when a calibration maneuver was performed, but it appears that either it is the wrong maneuver, or the maneuver was not well designed for gyro calibration. This discussion below focuses on the second and third maneuvers.

Table 31. SIRU calibration maneuvers.

Date	t_1	t_2	GLA04 granule
2003.02.25	10200	11500	GLA04_008_1102_002_0019_0_02
2008.07.01	7300	8700	GLA04_029_2123_003_0583_0_01
2010.05.07	7600	8700	GLA04_032_2133_002_1101_0_01

The objective of the calibration maneuvers was data for estimating gyro calibration parameters. When the angular rate is constant, all gyro calibration parameters are absorbed in the gyro rate bias vector b which is estimated as three of the six states in the MEKF attitude filter. When the angular rate vary, additional gyro calibration parameters beyond b for more sophisticated gyro measurement models are useful.

Figure 74 and Figure 75 show the second and third calibration maneuvers. The angular rates are expressed in the gyro frame. The y axis pointed towards the zenith and the z axis pointed along the GLAS to bus axis (body frame north). Each figure includes a quality value from 0 to 1. For the angular rate vector ω, Q was calculated using Equation (191).[7]

$$Q = rcond\left(\int_{t_1}^{t_2} \omega\omega^T dt\right) \tag{191}$$

The quality parameter Q was developed by Pittelkau.[7]

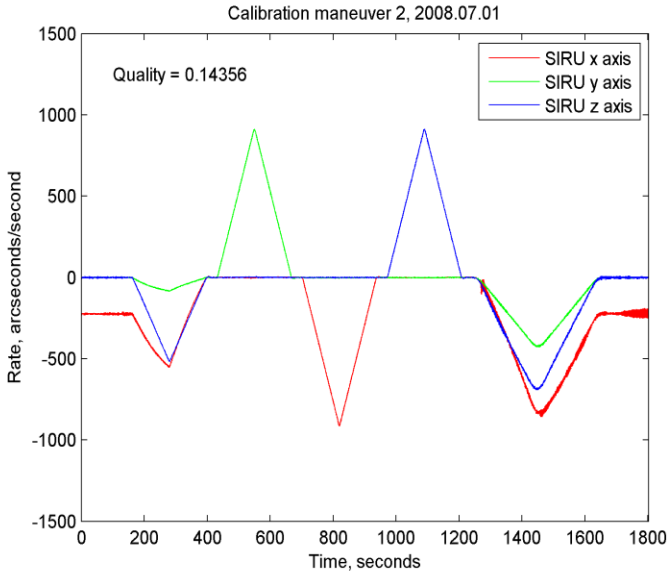

Figure 74. SIRU calibration maneuver 2.

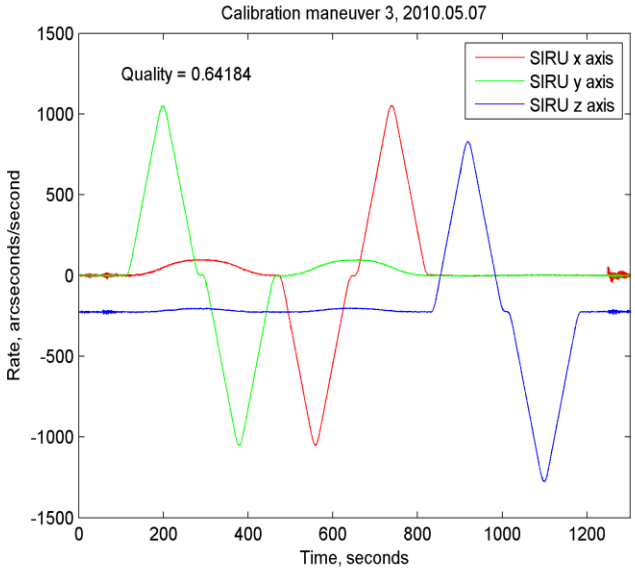

Figure 75. SIRU calibration maneuver 3.

Gyro calibration maneuver 3 had the highest quality parameter and its analysis is described here. Figure 76 shows the gyro sense-axes measured rates ω_{gyros} (or ω_{meas}) output by the gyro. Only three of the four sense-axes were active during the mission, one was kept inactive as a spare. If all four sense-axes had been active then ω_{gyros} would have had four components and there would have been four curves plotted in Figure 76.

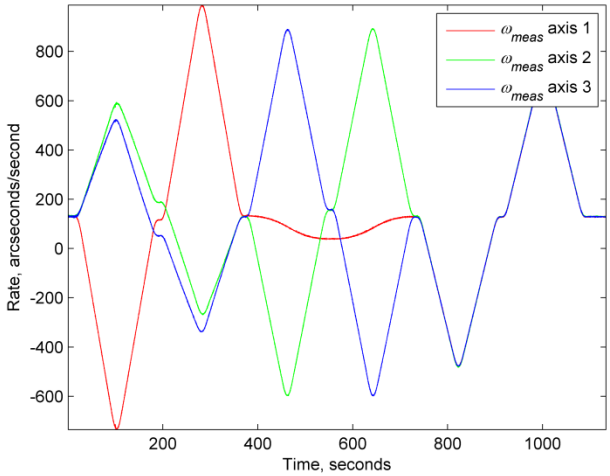

Figure 76. Gyro sense-axes measured rates for SIRU calibration maneuver 3.

Figure 77 shows the body rates ω_{body} calculated using the gyro measurement model for the gyro sense-axes measured rates ω_{gyros} shown in Figure 76. The gyro measurement model is shown in Equations (192) to (194). It included calibration parameters for symmetric scale factor errors Λ, asymmetric scale factor errors M, and sense-axes misalignments Δ_u, Δ_v.[6] If all of the gyro calibration parameters were equal to zero then Equation (192) reduced to the simplest possible gyro model $G = W^T$.

$$G = \left(I - \Lambda - M\right)\left(W - U\Delta_v - V\Delta_u\right)^T \tag{192}$$

$$\omega_{gyros} + b = G\omega_{body} \tag{193}$$

$$\omega_{body} = \left(G^T G\right)^{-1} G^T \left(\omega_{gyros} + b\right) \tag{194}$$

W, U, V were geometry matrices defining the ideal sense-axes geometry relative to the gyro unit reference frame. They defined orthogonal coordinate frames with *w*, *u*, and *v* unit vectors at each of the gyro sense-axes. The W matrix was the same as in Equation (44) and defined the directions of the sense-axes. The U and V matrices defined the other two orthogonal unit vectors for each sense-axis. The essentially arbitrary U and V matrices were computed using matrix decomposition methods.[42, 45]

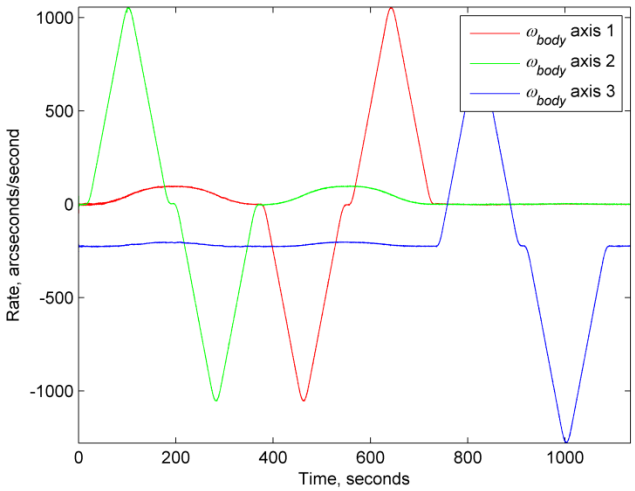

Figure 77. Body rates from the gyro measurement model for SIRU calibration maneuver 3.

The symmetric scale factor matrix Λ and asymmetric scale factor matrix M were defined by Equations (195) and (196).[42] λ_i and m_i were vectors of scale factor parameters, one for each gyro sense-axis. These parameters were dimensionless real-numbers within the filter, but for input and output were converted to units of parts per million ($ppm = 10^{-6}$).

$$\Lambda = diag\left(\lambda_i\right) \tag{195}$$

$$M = diag\left(sign\left(\omega_{gyro}\right) m_i\right) \tag{196}$$

The Δ_u, Δ_v sense-axes misalignment matrices were defined by equations (197) and (198). Within the filter u_i and v_i were vectors of angles with units of radians and were converted to arcseconds for input and output.

$$\Delta_u = diag\left(u_i\right) \tag{197}$$

$$\Delta_v = diag\left(v_i\right) \tag{198}$$

Table 32 shows the gyro calibration parameters estimated using calibration maneuver 3. The more sophisticated gyro measurement model using all of these parameters had a significant effect when the angular rate was varying during a maneuver. When the angular rate was constant, the effects of these parameters were absorbed in the gyro rate bias b which was estimated as part of the attitude filter state.

Table 32. Gyro calibration parameters estimated using SIRU calibration maneuver 3.

Parameter	*sense - axis x*	*sense - axis y*	*sense - axis z*
b (arcsec / s)	-0.64	-0.54	0.27
λ (ppm)	-366	-1696	1547
m (ppm)	361	14	-147
u (arcsec)	6	-49	-2
v (arcsec)	-51	-14	-31

IX. References

1. Smith, N., Bae, S. and Schutz, B. E., "Biased Star Tracker Measurements of Forty-Nine Stars from Flight Data", *Journal of Spacecraft and Rockets*, Volume 47, Number 6, 2010.
2. Smith, N., Fowell, R., Bae, S. and Schutz, B. E., "Improved Star Tracker Instrument Magnitude Prediction From ICESat Flight Telemetry", Paper AAS 11-086, AAS Guidance and Control Conference, *Advances in the Astronautical Sciences*, Volume 141, Pages 639-654, Univelt, 2011.
3. Sande, C., Brasoveanu, D., Miller, A. C., Home, A. T. and Tracewell, D., "Improved Instrumental Magnitude Prediction Expected from Version 2 of the NASA SKY2000 Master Star Catalog", AAS 98-362, AAS Space Flight Dynamics, *Advances in the Astronautical Sciencs*, Volume 100, Pages 765-778, Univelt, San Diego, 1998.
4. Sande, C. B., Warren, W. H. and Tracewell, D. A., "Recent Enhancements to and Future Plans for the SKY2000 Star Catalog", *Journal of the American Association of Variable Star Observers*, Volume 29, Number 2, 2000.
5. Sande, C., Ottenstein, N., Tracewell, D. and Oza, D., "SKYMAP Requirements, Functional, and Mathematical Specifications", Report No. CSC-96-932-24, Computer Sciences Corporation, Report CSC-96-932-24, Falls Church, Virginia, 1999.
6. Pittelkau, M. E., "Attitude Determination and Calibration with Redundant Inerital Measurement Units", AAS 04-116, AAS Space Flight Mechanics Meeting, *Advances in the Astronautical Sciences*, Volume 119, Pages 229-248, Univelt, 2005.
7. Pittelkau, M. E., "Survey of Calibration Algorithms for Spacecraft Attitude Sensors and Gyros", AAS 07-295, AAS Astrodynamics Specialist Conference, *Advances in the Astronautical Sciences*, Volume 129, Univelt, San Diego, 2007.
8. Wahba, G., "A Least Squares Estimate of Spacecraft Attitude", *SIAM Review*, Volume 7, Number 3, 1965.
9. Lefferts, E. J., Markley, F. L. and Shuster, M. D., "Kalman Filtering For Spacecraft Attitude Estimation", *Journal of Guidance, Control, and Dynamics*, Volume 5, Number 5, 1982.

10. Markley, F. L., "Attitude Error Representation for Kalman Filtering", *Journal of Guidance, Control, and Dynamics*, Volume 26, Number 2, 2003.
11. Potter, J. E. and Vander Velde, W. E., "Optimum Mixing of Gyroscope and Star Tracker Data", *Journal of Spacecraft and Rockets*, Volume 5, Number 5, 1968.
12. Sabroff, A. E., "Advanced Spacecraft Stabilization and Control Techniques", *Journal of Spacecraft and Rockets*, Volume 5, Number 12, 1968.
13. Pauling, D. C., Jackson, D. B. and Brown, C. D., "SPARS Algorithms and Simulation Results", Aerospace Corporation Symposium on Spacecraft Attitude Determination, *Aerospace Corporation Conference Proceedings*, Volume TR-006, Pages 293-317, Aerospace Corporation, El Segundo, CA, 1969.
14. Toda, N. F., Heiss, J. L. and Schlee, F. H., "SPARS: The System, Algorithms, and Test Results", Aerospace Corp. Report TR-006 (5306-12), Proceedings of the Symposium on Spacecraft Attitude Determination, Pages 361-370, 1969.
15. Farrell, J. L., "Attitude Determination by Kalman Filtering", *Automatica*, Volume 6, Number 3, 1970.
16. Murrell, J. W., "Precision Attitude Determination for Multimission Spacecraft", AIAA 78-1248, AIAA Guidance and Control Conference, Palo Alto, CA, 1978.
17. Junkins, J. L. and Strikwerda, T. E., "Autonomous Attitude Estimation Via Star Sensing and Pattern Recognition", NASA Flight Mechanics and Estimation Theory Symposium, *NASA Conference Proceedings*, Pages 127-148, NASA, 1979.
18. Pittelkau, M. E., "Rotation Vector in Attitude Estimation", *Journal of Guidance, Control, and Dynamics*, Volume 26, Number 6, 2003.
19. desJardins, R., "In-Orbit Startracker Misalignment Estimation on the OAO", NASA TM-X-63681 Symposium on Spacecraft Attitude Determination, El Segundo, CA, 1969.
20. desJardins, R., "MESS (Misalignment Estimation Software System) for In-Flight Alignment and Calibration of Spacecraft Attitude Sensors", AAS 71-357, AAS Astrodynamics Conference, Ft. Lauderdale, FL, 1971.
21. Davis, W., Hashmall, J., Garrick, J. and Harman, R., "Postlaunch Calibration of Spacecraft Attitude Instruments", AAS Symposium on Advances in the Astronautical Sciences, *Advances in the Astronautical Sciences*, Volume 84, Pages 1085-1099, Univelt, San Diego, 1993.

22. Davis, W. S., Hashmall, J. A., Garber, A. R., Kang, H. K. and Zsoldos, J. M., "In-Flight Calibration of Alignment and Field Of View Distortion for Spacecraft Attitude Sensors", AAS Astrodynamics Conference, *Advances in the Astronautical Sciences*, Volume 90, Pages 47, Univelt, San Diego, 1995.
23. Hashmall, J., Davis, W. and Harman, R., "Attitude Accuracy Consequences of On-Orbit Calibration of the Extreme Ultraviolet Explorer Attitude Sensors by the Flight Dynamics Facility at Goddard Space Flight Center", AAS 93-103, AAS Space Flight Mechanics Meeting, *Advances in the Astronautical Sciences*, Volume 82, Pages 59-78, Univelt, 1993.
24. Hashmall, J., Rowe, J. and Sedlak, J., "Spacecraft Attitude Sensor Calibration From On-Orbit Experience", IEEE Digital Avionics Systems Conference, *IEEE Conference Proceedings*, IEEE, New York, NY, 1997.
25. Hashmall, J. and Sedlak, J., "New Attitude Sensor Alignment Calibration Algorithms", IAF International Astronautical Federation Committee on Space Research (IAF COSPAR) World Space Congress, Houston, TX, 2002.
26. Lopes, R. V. F. and Shuster, M. D., "Parameter Interference in Distortion and Alignment Calibration", *Journal of the Astronautical Sciences*, Volume 51, Number 3, 2003.
27. Pitone, D. S. and Shuster, M. D., "Attitude Sensor Alignment Calibration for the Solar Maximum Mission", NASA Flight Mechanics Estimation Theory Symposium, *Proceedings of the NASA Flight Mechanics and Estimation Theory Symposium*, NASA, 1990.
28. Sedlak, J. and Hashmall, J., "Automated Attitude Sensor Calibration: Progress and Plans", AIAA 2004-4854, AIAA Astrodynamics Specialist Conference, Providence, RI, 2004.
29. Shuster, M. D., Chitre, D. M. and Niebur, D. P., "In-Flight Estimation Of Spacecraft Attitude Sensor Accuracies And Alignments", *Journal of Guidance, Control, and Dynamics*, Volume 5, Number 4, 1982.
30. Shuster, M. D. and Lopes, R. V. F., "Parameter Interference In Distortion And Alignment Calibration", AAS 94-186, AAS Spaceflight Mechanics Meeting, *Advances in the Astronautical Sciences*, Volume 87, Pages 595-611, Univelt, San Diego, 1994.

31. Shuster, M. D., Pitone, D. S. and Bierman, G. J., "Batch Estimation Of Spacecraft Sensor Alignments. I. Relative Alignment Estimation", *Journal of the Astronautical Sciences*, Volume 39, Number 4, 1991.
32. Sedlak, J., Welter, G. and Ottenstein, N., "Towards Automating Spacecraft Attitude Sensor Calibration", IAC 03-U.4.03, International Astronautical Congress, Bremen, Germany, 2003.
33. Welter, G., "A Recursive Filter Approach to Onboard Gyro Calibration", Computer Sciences Corporation, Report CSC-5569-04, 2003.
34. Gray, C. W., Herman, L. K., Kolve, D. I. and Westerlund, G. L., "On-Orbit Attitute Reference Alignment and Calibration", AAS 90-042, AAS Guidance and Control Conference, *Advances in the Astronautical Sciences*, Volume 72, Pages 275-292, Univelt, San Diego, 1990.
35. Li, R., Needelman, D., Fowell, R., Tsao, T.-C. and Wu, Y.-W., "Reusable Stellar Inertial Attitude Determination (SIAD) Design For Spacecraft Guidance, Navigation & Control", AIAA 2005-5928, AIAA Guidance, Navigation, and Control Conference, San Francisco, CA, 2005.
36. Li, R. and Wu, Y.-W., "Absolute and Relative Attitude Determination for Multiple Payloads On Spacecraft", AIAA 2006-6048, AIAA Guidance, Navigation, and Control Conference, Keystone, CO, 2006.
37. Wu, Y.-W. and Li, R., "Star Tracker Error Characteristics and Their Compensation Techniques", Proceedings NASA-CP-2003-212246, Proceedings of the NASA Goddard Flight Mechanics Symposium, *NASA-CP-2003-212246*, 2003.
38. Davis, S. and Lai, J., "Attitude Sensor Calibration for the Ocean Topography Experiment Satellite (TOPEX)", SPIE Space Guidance, Control and Tracking Conference, *SPIE Proceedings*, Volume 1949, Pages 80-91, SPIE, Bellingham, WA, 1993.
39. Zanardi, M. C. and Shuster, M. D., "Batch, Sequential, and Hybrid Approaches to Spacecraft Sensor Alignment Estimation", *Journal of the Astronautical Sciences*, Volume 51, Number 3, 2003.
40. Pittelkau, M. E., "Kalman Filtering for Spacecraft System Alignment Calibration", *Journal of Guidance, Control, and Dynamics*, Volume 24, Number 6, 2001.
41. Pittelkau, M. E., "Everything Is Relative In Spacecraft System Alignment Calibration", *Journal of Spacecraft and Rockets*, Volume 39, Number 3, 2002.

42. Pittelkau, M. E., "Calibration and attitude determination with Redundant Inertial Measurement Units", *Journal of Guidance, Control, and Dynamics*, Volume 28, Number 4, 2005.
43. Pittelkau, M. E., "General Definition of Relative Misalignment", AAS 08-289, AAS F. Landis Markley Astronautics Symposium, *Advances in the Astronautical Sciences*, Volume 132, Univelt, San Diego, 2008.
44. O'Shaughnessy, D. and Pittelkau, M. E., "Attitude Sensor and Gyro Calibration for Messenger", NASA International Symposium on Space Flight Dynamics, *NASA Conference Proceedings*, Volume NASA CP-2007-214158, NASA, 2007.
45. Pittelkau, M. E., "RIMU Misalignment Vector Decomposition", AIAA 2004-4856, AIAA Astrodynamics Specialist Conference, Providence, RI, 2004.
46. Pittelkau, M. E., "Observability and Calibration of a Redundant Inertial Measurement Unit (RIMU)", AAS 05-105, AAS Space Flight Mechanics Meeting, *Advances in the Astronautical Sciences*, Volume 120, Pages 71-84, Univelt, 2005.
47. Pittelkau, M. E., "Cascaded and Decoupled RIMU Calibration Filters", *Journal of the Astronautical Sciences*, Volume 54, Number 3 & 4, 2006.
48. Pittelkau, M. E., "Advances in Attitude Determination with Redundant Inertial Measurement Units", AAS 06-110, AAS Space Flight Mechanics Meeting, *Advances in the Astronautical Sciences*, Volume 124, Pages 163-178, Univelt, 2006.
49. Pittelkau, M. E. and O'Shaughnessy, D., "Gyro Misalignment Decomposition Applied To Messenger Calibration", AAS 09-203, AAS Spaceflight Mechanics Meeting, *Advances in the Astronautical Sciences*, Volume 134, Univelt, San Diego, 2009.
50. Bayard, D. S., "An Overview of the Pointing Control System for NASA's Space Infra-Red Telescope Facility (SIRTF)", AIAA 2003-5832, AIAA Guidance, Navigation, and Control Conference, Austin, TX, 2003.
51. Bayard, D. S., "Advances in Precision Pointing Control for the NASA Spitzer Space Telescope", AAS 04-071, AAS Guidance and Control Conference, *Advances in the Astronautical Sciences*, Volume 118, Pages 527-547, Univelt, San Diego, 2004.
52. Bayard, D. S. and Kang, B. H., "A High-Order Kalman Filter for Focal Plane Calibration of NASA's Space Infrared Telescope Facility (SIRTF)", AIAA 2003-5824, AIAA Guidance, Navigation, and Control Conference, Austin, TX, 2003.

53. Bayard, D. S., Kang, B. H., Brugarolas, P. B. and Boussalis, D., "An Integrated Optimal Estimation Approach to Spitzer Space Telescope Focal Plane Survey", SPIE Optical, Infrared, and Millimeter Space Telescopes, *SPIE Proceedings*, Volume 5487, SPIE, Bellingham, WA, 2004.
54. Bayard, D. S., Kang, B. H., Brugarolas, P. B. and Broussalis, D., "Focal Plane Calibration of the Spitzer Space Telescope", *IEEE Control Systems*, Volume 29, Number 6, 2009.
55. Lai, K., Crassidis, J. L. and Harman, R., "In Space Spacecraft Alignment Calibration Using the Unscented Kalman Filter", AIAA 2003-5563, AIAA Guidance, Navigation and Control Conference, Austin, TX, 2003.
56. Lam, Q. M., Woodruff, C., Ashton, S. and Martin, D., "Noise Estimation for Star Tracker Calibration and Enhanced Precision Attitude Determination", IEEE Information Fusion Conference, *IEEE Conference Proceedings*, Pages 235-242, IEEE, New York, NY, 2002.
57. Lam, Q. M., Welch, R. and Lee, Y., "Performance Enhancement of the Stellar Inertial Attitude Determination System Via System Optimization Techniques", Hughes Space and Communications, 1997.
58. Liebe, C. C., "Accuracy performance of star trackers - A Tutorial", *IEEE Transactions on Aerospace and Electronic Systems*, Volume 38, Number 2, 2002.
59. Haley, D. R., "Precision Attitude Estimation With Star Trackers: Experience, Error Models and Their Interpretation", AAS 99-433, AAS Astrodynamics Specialist Conference, *Advances in the Astronautical Sciences*, Volume 103, Pages 2055-2066, Univelt, 1999.
60. Haley, D. R., Strikwerda, T. E., Fisher, H. L. and Heyler, G. A., "Attainable Pointing Accuracy With Star Trackers", AAS 98-072, AAS Guidance and Control Conference, *Advances in the Astronautical Sciences*, Volume 98, Pages 593-604, Univelt, 1998.
61. Griffith, T. D., Singla, P. and Junkins, J. L., "Autonomous On-orbit Calibration Approaches for Star Tracker Cameras", AAS 02-102, AAS Space Flight Mechanics Meeting, *Advances in the Astronautical Sciences*, Volume 112, Pages 39-57, Univelt, San Diego, 2002.
62. Singla, P., Griffith, T. D., Crassidis, J. L. and Junkins, J. L., "Attitude determination and autonomous on-orbit calibration of star tracker for the gifts mission", AAS 02-

101, Spaceflight Mechanics 2002, *Advances in the Astronautical Sciences*, Volume 112, Pages 19-38, 2002.

63. Singla, P., Kamesh, S., Griffith, T. D. and Junkins, J. L., "Autonomous Focal Plane Calibration by an Intelligent Radial Basis Function Network", AAS 04-119, AAS Space Flight Mechanics Meeting, *Advances in the Astronautical Sciences*, Volume 119, Pages 275-300, Univelt, San Diego, 2004.
64. Pal, M. and Bhat, M. S., "Star Camera Calibration Combined with Independent Spacecraft Attitude Determination", IEEE Control Systems Society American Control Conference, *IEEE Conference Proceedings*, IEEE, New York, NY, 2009.
65. Fowell, R. A., Smith, N., Bae, S. and Schutz, B. E., "Bad Stars", AAS 09-012, AAS Guidance and Control Conference, *Advances in the Astronautical Sciences*, Volume 133, Pages 20-36, Univelt, San Diego, CA, 2009.
66. Lauer, M., Jauregui, L. and Kielbassa, S., "Operational Experience with Autonomous Star Trackers on ESA Interplanetary Spacecraft", Proceedings NASA-CP-2007-214158, Proceedings of the 20th International Symposium on Space Flight Dynamics, *NASA-CP-2007-214158*, 2007.
67. McCutcheon, B., "FHST Near Neighbor Problems and Integrated Magnitude Spoilers", STSCI, 2000, Unpublished.
68. Sande, C., Natanson, G. and Tracewell, D., "Effects of Uncataloged Near-Neighbor Stars on CCDST Operation", Proceedings NASA-CP-2005-212789, Proceedings of the NASA Goddard Flight Mechanics Symposium, 2005.
69. Ju, G. and Junkins, J. L., "Overview of Star Tracker Technology and its Trends in Research and Development", AAS 03-285, AAS John L. Junkins Astrodynamics Symposium, *Advances in the Astronautical Sciences*, Volume 115, Pages 461-478, Univelt, San Diego, 2003.
70. Carrou, J.-P., Manon, F. and CNES, *Spaceflight Dynamics*, Cepadues Editions, Toulouse, France, 1995.
71. Kudva, P. and Throckmorton, A., "Preliminary star catalog development for the Earth Observation System AM1 (EOS-AM1) mission", *Journal of Guidance, Control, and Dynamics*, Volume 19, Number 6, 1996.
72. Van Bezooijen, R. W. H., Degen, L. and Nichandros, H., "Guide Star Catalog for the Spitzer Space Telescope Pointing Calibration and Reference Sensor", SPIE

Proceedings Vol. 5487, Optical, Infrared, and Millimeter Space Telescopes, *Proceedings of the SPIE*, Volume 5487, Pages 253-265, 2004.

73. Batten, A., Marc, X., McDonald, A. and Schutz, A., "The Use Of The Hipparcos and Tycho Catalogues In Flight Dynamics Operations At ESO", ESA Hipparcos Conference, *ESA Conference Proceedings*, Volume SP-402, Pages 191-194, ESA, 1997.
74. Tracewell, D., "NASA Goddard Flight Dynamics Facility Star Catalogs", 2011, Internet URL: https://wakata.nascom.nasa.gov//dist/generalProducts/attitude/ATT_SKYMAP.html (Archived by WebCite® at http://www.webcitation.org/5bfVD1j6s).
75. Sande, C., "SKYMAP Sources and Data Representations, Version 5 Revision 4", 2006, Internet URL: https://wakata.nascom.nasa.gov//dist/generalProducts/attitude/SKYMAP_Sources_and_Data_Representation_V5R4.pdf (Archived by WebCite® at http://www.webcitation.org/5bh24j8Zv).
76. Sodano, "Delivery of Updated Star Catalog for RXTE, Attachment: Delivery Documentation for the Updated RXTE Onboard", 2002, Internet URL: http://fdf.gsfc.nasa.gov/dist/generalProducts/attitude/ATT_rxte_osc6_delivery.pdf (Archived by WebCite® at http://www.webcitation.org/5bcWeK8Fy).
77. Anonymous, "NASA Flight Dynamics Facility Delivery Documentation for the Updated RXTE Star Catalogs", 2000, Internet URL: https://wakata.nascom.nasa.gov//dist/generalProducts/attitude/ATT_RXTE_StarCatalog_delivery.pdf (Archived by WebCite® at http://www.webcitation.org/5c1WERVgC).
78. Landi, A., Boldrini, F. and Procopio, D., "Mars Express and Rosetta Autonomous STR: in Flight Experience", ESA Guidance, Navigation and Control Systems Conference, *ESA Conference Proceedings*, Volume SP-606, Pages 683-689, European Space Agency, 2005.
79. Nadelman, M. S., Karl, J. B. and Hallock, L., "Fixed-Head Star Tracker Attitude Updates On The Hubble Space Telescope", Computer Sciences Corporation, Report N94-35605, 1994.
80. Davenport, P., "The Approximation of Stellar Energy Distributions and Magnitudes from Multi-Color Photometry", NASA, Report TM X-63185, 1968.

81. Johnson, H. L. and Morgan, W. W., "Fundamental stellar photometry for standards of spectral type on the revised system of the Yerkes spectral atlas", *Astrophysical Journal*, Volume 117, Number 3, 1953.
82. Singh, V., Pullaiah, D., Rao, S., Shashikala, T. H., Rao, G. N., Jain, Y. K. and Alex, T. K., "Generation and Validation of On-board Star Catalog for Resourcesat I Star Tracker", AIAA 2004-5391, AIAA Astrodynamics Specialist Conference, Providence, Rhode Island, 2004.
83. Barry, K., Hindman, M. and Yates, R., "Application of Flight Data to Space Shuttle CCD Star Tracker Catalog Design", AAS 93-015, AAS Guidance and Control Conference, *Advances in the Astronautical Sciences*, Volume 81, Pages 57-71, Univelt, San Diego, 1993.
84. Gomes, N. M., Fouquet, M. and Steyn, W. H., "Astrolabe - A Low Cost Autonomous Star Camera", ESA Small Satellite Systems and Services Conference, *ESA Conference Proceedings*, Volume SP-587, ESA, 1998.
85. Strunz, H. C., Baker, T. and Ethridge, D., "Estimation of Stellar Instrument Magnitudes", Space Guidance, Control, and Tracking Conference, *SPIE Conference Proceedings*, Volume 1949, SPIE, Bellingham, WA, 1993.
86. Anonymous, "NASA Flight Dynamics Facility Delivery Documentation for the SKYMAP Aqua Star Catalog", 2002, Internet URL: https://wakata.nascom.nasa.gov//dist/generalProducts/attitude/ATT_Aqua_Star Catalog_delivery_041002.pdf (Archived by WebCite® at http://www.webcitation.org/5brwUCF7J).
87. Kruijff, M., Heide, E. v. d., Boom, C. W. d. and Heiden, N. v. d., "Star Sensor Algorithm Application and Spin-Off", IAC 03-A.5.03, International Astronautical Congress, Bremen, Germany, 2003.
88. NASA, "Blinking Star Explains Mystery Aboard Galileo", 2001, Internet URL: http://spaceflightnow.com/news/n0103/22galblink/ (Archived by WebCite® at http://www.webcitation.org/5bs6M5fLs).
89. Anonymous, "Hubble Space Telescope Daily Report #2821", STSCI, 2001, Unpublished.
90. Baskill, D., "RXTE Bad Star Report", 2002, Internet URL: Original web page no longer online (Archived by WebCite® at http://www.webcitation.org/5bcU3Goef).

91. Markwardt, C., "RXTE Attitude Anomaly of September 6-12, 2000", 2001, Internet URL: http://lheawww.gsfc.nasa.gov/users/craigm/xteatterr/ (Archived by WebCite® at http://www.webcitation.org/5bcVR9JSG).
92. Jayaraman, P., Fischer, J. and Mathias, L., "Star Tracker Operational Usage In Different Phases Of The Mars Express Mission", AIAA 2006-5930, AIAA SpaceOps 2006 Conference, Rome, Italy, 2006.
93. Bucher, S. and Martin, E., "Chandra Attitude Disturbance", 2003, Unpublished.
94. Kirschner, S., Sedlak, J., Challa, M., Nicholson, A., Sande, C. and Rohrbaugh, D., "Submillimeter Wave Astronomy Satellite (SWAS) Launch and Early Orbit Support Experiences", 1999, Internet URL: http://ntrs.nasa.gov/archive/nasa/casi.ntrs.nasa.gov/19990039118_1999050118.pdf. Accessed: 2011-08-24. (Archived by WebCite® at http://www.webcitation.org/61AjRVhyS).
95. Schutz, B. E., "Geolocation for the ICESat Laser Altimeter", AAS 05-011, AAS Guidance and Control Conference, *Advances in the Astronautical Sciences*, Volume 121, Pages 127-142, Univelt, San Diego, 2005.
96. Schutz, B. E., Bae, S., Smith, N. and Sirota, J. M., "Precision Orbit And Attitude Determination For ICESat", Paper AAS 08-305, F. Landis Markley Astronautics Symposium, Cambridge, Maryland, 2008.
97. Yoon, S., Bae, S. and Schutz, B. E., "High Frequency Attitude Motion Of ICESat", AAS 05-108, AAS Space Flight Mechanics Meeting, *Advances in the Astronautical Sciences*, Volume 120, Pages 117-131, Univelt, San Diego, 2005.
98. Schutz, B. E., Zwally, H. J., Shuman, C. A., Hancock, D. and DiMarzio, J. P., "Overview of the ICESat Mission", *Geophysical Research Letters*, Volume 32, Number 21, 2005.
99. Zwally, H. J., Schutz, B. E., Bentley, J., Bufton, T., Herring, J., Minster, J., Spinhirne, J. and Thomas, R., 2003, updated 2011, *GLAS/ICESat L1A Global Laser Pointing Data V031. Boulder, CO: National Snow and Ice Data Center. Digital media*, Boulder, CO, National Snow and Ice Data Center, Digital media.
100. Anonymous, "GLA04-01 Product Format", 2003, Internet URL: http://wffglas.wff.nasa.gov/v54_products/home.html?ht_action=view_format&ht_obj_key=4982 (Archived by WebCite® at http://www.webcitation.org/5c330VKMe).

101. Anonymous, "GLA04-02 Product Format", 2003, Internet URL: http://wffglas.wff.nasa.gov/v54_products/home.html?ht_action=view_format&ht_obj_key=4983 (Archived by WebCite® at http://www.webcitation.org/5c33HVvFq).
102. Anonymous, "GLA04-03 Product Format", 2003, Internet URL: http://wffglas.wff.nasa.gov/v54_products/home.html?ht_action=view_format&ht_obj_key=4984 (Archived by WebCite® at http://www.webcitation.org/5c33fnFtP).
103. Anonymous, "GLA04-04 Product Format", 2003, Internet URL: http://wffglas.wff.nasa.gov/v54_products/home.html?ht_action=view_format&ht_obj_key=4985 (Archived by WebCite® at http://www.webcitation.org/5c33yVEXo).
104. Anonymous, "GLA04-05 Product Format", 2003, Internet URL: http://wffglas.wff.nasa.gov/v54_products/home.html?ht_action=view_format&ht_obj_key=4986 (Archived by WebCite® at http://www.webcitation.org/5c34IbXe1).
105. Anonymous, "GLA04-06 Product Format", 2003, Internet URL: http://wffglas.wff.nasa.gov/v54_products/home.html?ht_action=view_format&ht_obj_key=4987 (Archived by WebCite® at http://www.webcitation.org/5c34ZpzKf).
106. Savage, P. G., "Strapdown Inertial Navigation Integration Algorithms Design Part 1: Attitude Algorithms", *Journal of Guidance, Control, and Dynamics*, Volume 21, Number 1, 1998.
107. Crassidis, J. L. and Junkins, J. L., *Optimal Estimation Of Dynamic Systems*, Chapman & Hall CRC, Boca Raton, FL, 2004.
108. Jazwinski, A. H., *Stochastic Processes and Filtering Theory*, Dover Publications, Mineola, NY, 2007.
109. Grewal, M. S. and Andrews, A. P., *Kalman Filtering Theory and Practice Using MATLAB*, John Wiley & Sons, Hoboken, NJ, 2008.
110. Pittelkau, M. E., "Attitude Sensor and Gyro Calibration: Gyroscopes", 2010, Unpublished.

111. Lam, Q. M., Stamatakos, N., Woodruff, C. and Ashton, S., "Gyro Modeling and Estimation of Its Random Noise Sources", AIAA 2003-5562, AIAA Guidance, Navigation, and Control Conference, Austin, TX, 2003.
112. Pittelkau, M. E., "Attitude Determination by Kalman Filtering", 2010, Unpublished.
113. Anonymous, "ICESat SIRU Configuration", Ball Aerospace, 2003, Unpublished.
114. Hanlon, P. D. and Maybeck, P. S., "Multiple-Model Adaptive Estimation Using a Residual Correlation Kalman Filter Bank", *IEEE Transactions on Aerospace and Electronic Systems*, Volume 36, Number 2, 2000.
115. Wu, Y.-W. and Li, R., "Star Tracker Error Characteristics and Their Compensation Techniques", NASA, Report CP-2003-212246, 2003.
116. Smith, N., "Localized Distortion Estimation and Correction for the ICESat Star Trackers", Thesis, University of Texas at Austin, Austin, May 2006.
117. Bissell, C. C. and Chapman, D. A., *Digital Signal Transmission*, Cambridge University Press, Cambridge, England, 1992.
118. Bevington, P., *Data Reduction and Error Analysis for the Physical Sciences*, McGraw-Hill Science Engineering Math, New York, NY, 2002.
119. Cleveland, W. S., "Robust Locally Weighted Regression and Smoothing Scatterplots", *Journal of the American Statistical Association*, Volume 74, Number 368, 1979.
120. Cleveland, W. S. and Devlin, S. J., "Locally-Weighted Regression: An Approach to Regression Analysis by Local Fitting", *Journal of the American Statistical Association*, Volume 83, Number 403, 1988.
121. Shuster, M. D., "Stellar Aberration and Parallax: A Tutorial", *Journal of the Astronautical Sciences*, Volume 51, Number 4, 2003.
122. Thomas, V. C., Blue, R. C. and Procopio, D., "Cassini Stellar Reference Unit Performance Test Approach and Results", Cassini/Huygens A Mission to the Saturnian Systems, *SPIE Proceedings*, Volume 2803, SPIE, Bellingham, WA, 1996.
123. Zacharias, N. and Dorland, B., "The Concept of a Stare-mode Astrometric Space Mission", *Publications of the Astronomical Society of the Pacific*, Volume 118, Number 848, 2006.
124. Adorf, H.-M., Lemson, G., Voges, W., Enke, H. and Steinmetz, M., "Astronomical Catalogues Simultaneous Querying and Matching", ASP Astronomical Data

Analysis Software and Systems, *ASP Conference Proceedings*, Volume 314, Astronomical Society of the Pacific, Seattle, WA, 2004.

125. Markley, F. L., "Attitude Determination using Vector Observations and the Singular Value Decomposition", *Journal of the Astronautical Sciences*, Volume 36, Number 3, 1988.
126. Bonnarel, F., Fernique, P., Bienaymé, O., Egret, D., Genova, F., Louys, M., Ochsenbein, F., Wenger, M. and Bartlett, J. G., "The ALADIN interactive sky atlas. A reference tool for identification of astronomical sources.", *Astronomy and Astrophysics Supplement*, Volume 143, 2000.
127. Anonymous, "OBC subset of the Aura Star Catalog", 2004, Internet URL: https://wakata.nascom.nasa.gov//dist/generalProducts/attitude/ATT_aura_alp_obc_subset.cat.gz (Archived by WebCite® at http://www.webcitation.org/5c1XPSkyo).
128. Anonymous, "Aura Star Catalog", 2004, Internet URL: https://wakata.nascom.nasa.gov//dist/generalProducts/attitude/ATT_aura_alp.cat.gz (Archived by WebCite® at http://www.webcitation.org/5c1Xf8AfE).
129. Anonymous, "Aura Star Catalog with OBC identifiers in place of SKYMAP numbers", 2004, Internet URL: https://wakata.nascom.nasa.gov//dist/generalProducts/attitude/ATT_aura_alp_obc_ids.cat.gz (Archived by WebCite® at http://www.webcitation.org/5c1XxPKM0).
130. Gramling, C., "Flight Dynamics Analysis Branch End of Fiscal Year 2003 Report", NASA, Report TM-2004-212747, 2004.
131. Huber, P. J., *Robust Statistics*, John Wiley & Sons, Hoboken, NJ, 1981.
132. Bae, S., Webb, C. and Schutz, B. E., "Star Tracker Misalignment Calibration for the ICESat Mission", AAS 06-107, AAS/AIAA Space Flight Mechanics, *Advances in the Astronautical Sciences*, Volume 124, Pages 113-124, Univelt, 2006.
133. Bae, S. and Schutz, B. E., "Precision attitude determination using gyro and star tracker data with a batch least squares estimator", *Advances in the Astronautical Sciences*, Volume 123 I, Pages 175-182, Univelt Inc., San Diego, CA 92198, United States, 2006.

134. Sirota, J. M., Bae, S., Millar, P., Mostofi, D., Webb, C., Schutz, B. and Luthcke, S., "The Transmitter Pointing Determination In The Geoscience Laser Altimeter System", *Geophysical Research Letters*, Volume 32, Number 22, 2005.
135. Bae, S., Webb, C. and Schutz, B., "GLAS PAD Calibration Using Laser Reference Sensor Data", AIAA/AAS Astrodynamics Specialist Conference, *Collection of Technical Papers - AIAA/AAS Astrodynamics Specialist Conference*, Volume 1, Pages 302-311, American Institute of Aeronautics and Astronautics Inc., Reston, VA 20191, United States, 2004.
136. Bae, S., Magruder, L., Ricklefs, R., Webb, C., Yoon, S. and Schutz, B., "ICESat/GLAS Precision Attitude Determination For Early Laser Operation", AAS/AIAA Space Flight Mechanics Meeting, *Advances in the Astronautical Sciences*, Volume 119, Pages 263-274, Univelt Inc., San Diego, CA 92198, United States, 2004.